Physico-Chemical Material Development for the Manufacturing of Thermoelectric Generators

VON DER NATURWISSENSCHAFTLICHEN FAKULTÄT
DER GOTTFRIED WILHELM LEIBNIZ UNIVERSITÄT HANNOVER

ZUR ERLANGUNG DES GRADES

Doktor der Naturwissenschaften
(Dr. rer. nat.)

genehmigte Dissertation

von

Mario Wolf, M. Sc.

2021

Referent: apl. Prof. Dr. rer. nat. habil. Armin Feldhoff

Korreferent 1: Prof. Dr.-Ing. Ludger Overmeyer

Korreferent 2: Prof. Dr. Theodora Kyratsi

Tag der Promotion: 24.09.2021

Preface

The propounded thesis includes the results that were achieved in the past four years during my work as a research associate in the group of Prof. Dr. Armin Feldhoff at the Institute of Physical Chemistry and Electrochemistry of the Gottfried Wilhelm Leibniz University Hannover. Financially, this work was granted by the German Research Foundation (project number 325156807) in a cooperation of the Institute of Physical Chemistry and Electrochemistry and the Hannover Institute for Integrated Production. Cooperation partners at the Institute for Integrated Production were Prof. Dr.-Ing. Ludger Overmeyer and Dipl.-Ing. Marvin Abt. My research was done under the guidance of Prof. Dr. Armin Feldhoff.

During the four years, I contributed to 10 peer-reviewed publications and 13 conferences with talks or posters. Within this thesis, seven selected articles are presented. Here, I am the first and corresponding author in six of these. In the following, my contributions to the included articles are described in detail.

The first two articles are presented within the introductory chapter 1, as they present a review about the state of thermoelectric materials for high-temperature applications and a theoretical work concerning working points of thermoelectric generators based on finite-elemente method simulations, respectively. Within the review *High Power Factor vs. High zT - A Review of Thermoelectric Materials for High-Temperature Application*, I contributed in the revitalization of Ioffe plots for comparison of thermoelectric properties of various materials and carried out the literature research and visualization of several material classes. The manuscript was partly written by me, while some chapters were written by my colleague M. Sc. Richard Hinterding. It was revised by Prof. Dr. Armin Feldhoff. The concept of the second article, entitled *Geometry Optimization of Thermoelectric Modules: Deviation of Optimum Power Output and Conversion Efficiency*, was drawn by Prof. Dr. Armin Feldhoff, while I supervised the simulations and carried out the interpretation and visualization of the results. The simulations were carried out by M. Sc. Alexey Rybakov and the manuscript was originally written by me and revised by the co-authors.

In chapter 2, two articles are presented focussing on material development for thermoelectric energy conversion. The first article, *Low Thermal Conductivity in Thermoelectric Oxide-Based Multiphase Composites*, was a result of the experimental work of a student, B. Sc. Kaan Menekse. The article describes multiphase composite materials based on calcium cobaltite (CCO) to achieve very low values of the thermal conductivity by the introduction of heteromaterial interfaces. Here, I developed the experimental basis and supervised the student's work. The analysis of the thermal properties was done in cooperation with Prof. Dr. Oliver Oeckler (Leipzig University). I wrote the original draft of the manuscript, which was revised by the co-authors. The second article, *Cu-Ni Based Alloys as Potent Thermoelectric Materials for High Power*

Output, was conceived in a cooperation with the Institute of Materials Science at the Hannover Centre of Production Technology, namely Dr. Gregory Gerstein and Prof. Dr.-Ing. Hans Jürgen Maier. In this article, Cu-Ni based alloys are presented as a promising and mostly overlooked thermoelectric material to reach a high power output. The conception of this work arose from the analysis of thermoelectric materials in the context of the aforementioned review and the first article within this chapter. The experimental work was carried out by two student apprentices, M. Sc. Timon Steinhoff and B. Sc. Jan Flormann. I supervised and coordinated their experimental work and thermoelectric measurements as well as carried out the interpretation of the obtained results. The original draft of the manuscript was written by B. Sc. Jan Flormann and me in equal shares.

Chapter 3 contains the three remaining articles about processing of thermoelectric materials on the example of CCO. All of these articles were developed within a cooperation with the Hannover Institute for Integrated Production and the Hannover Institute of Transport and Automation Technology at the Hannover Centre of Production Technology, namely Prof. Dr.-Ing. Ludger Overmeyer and Dipl-Ing. Marvin Abt. The first article, *Combined Spray-Coating and Laser Structuring of Thermoelectric Ceramics*, describes the preparation and design of CCO layers utilizing spray-coating and laser structuring. Here, I contributed by developing the spray-coating ink based on CCO. Additionally, the microstructural analysis via scanning electron microscope and the thermoelectric characterization, including measurement of the electrical conductivity and the Seebeck coefficient, were done by me. The original draft was written by the first author, Dipl.-Ing. Marvin Abt and revised by me and the other co-authors. Within the second article, *Ceramic-Based Thermoeletric Generator Processed via Spray-Coating and Laser Structuring*, the production of CCO layers was transferred to a functional thermoelectric generator by combining it with a silver layer on the back side and contacting the respective structures. Here, I carried out the measurement, interpretation and visualization of the microstructure, X-ray diffraction analysis and the thermoelectric power output of the generator prototype. The original draft was written by me and revised by the co-authors. The third article, *Laser sintering process of thermoelectric $Ca_3Co_4O_9$ as promising optimization for TEG processing*, introduces the concept of laser sintering as a promising alternative to thermal sintering of CCO layers. Here, the experimental work was implemented by Dipl.-Ing. Marvin Abt and the microstructure analysis was carried out by B. Sc. Lena Rehder. I supervised the work and did the measurement and interpretation of the X-ray diffraction analysis and the thermoelectric measurements. The original draft of the manuscript was written by me and revised by all co-authors.

First of all, I would like to deeply thank Prof. Dr. Armin Feldhoff for supervising the presented thesis as a tutor. He always provided me with help and advice and carried out some of the transmission electron microscope analyses included in the articles. His revisions of the experimental work and the manuscript drafts were always productive and helpful.

Furthermore, I would like to thank the partners at the Hannover Institute of Integrated Production and Hannover Institute of Transport and Automation Technology, Prof. Dr.-Ing. Ludger Overmeyer and Dipl.-Ing. Marvin Abt, for the productive collarboration, which resulted in three of the included articles. The cooperation was always constructive and professional. In similar terms, I am grateful to Prof. Dr. Oliver Oeckler for the smooth cooperation also resulting in a mutual article. Then,

Abstract

The thermoelectric effect can be utilized for direct conversion of thermal energy into usable electrical energy. Due to the high amount of wasted energy in several big industrial fields, applications at elevated temperatures are desired to utilize the otherwise wasted energy. This thesis focuses on the two main research fields: The thermoelectric material research and the production technology of thermoelectric generators.

Until now, thermoelectric materials have been mostly evaluated in terms of their figure of merit, meaning their resulting efficiency. In this work, the arising concept of focussing on a high power factor instead is further analysed. A presented review of thermoelectric materials for high-temperature applications describes the desired multiparameter optimization of materials and compares various material classes. As a result, different concepts to optimize either the figure of merit or the power factor are investigated: To optimize the figure of merit, a hybrid material combining different classes of materials to gain synergistic effects was designed. The prepared hybrid material showed an exceptionally low thermal conductivity due to the introduced heteromaterial interfaces, proving the concept for optimization of the figure of merit. For an optimization of the power factor, Cu-Ni alloys were prepared, which shows an inferior figure of merit but a very high power factor. The alloys were prepared from nanoparticles and alloyed with heavier elements, resulting in an increase in both the power factor as well as the figure of merit for low amounts.

The manufacturing of TEGs also shows a big optimization potential, as the costs of the production are accountable for a big share in the overall costs. For this, a new manufacturing route was developed, which combines fast and scalable production technologies with laser-based processes to design a rigid TEG for application at elevated temperatures. The CCO and the counterpart Ag layer were prepared via spray-coating and the final design was arranged by using a CO_2 laser. A designed TEG prototype reached a maximum electrical power output of 1.6 μW cm^{-2} at a hot-side temperature of 673 K and a temperature difference of 100 K. The developed manufacturing route allows precise control over several parameters such as layer thickness and exact geometry. Finally, the uprising concept of laser-induced processes, e.g., for sintering of materials, was investigated via laser treatment of a spray-coated CCO layer. By utilization of a CO_2 laser, an initial sintering of the CCO layer could be observed, which opens a pathway to further investigations of this concept. The combination of laser treatment and thermal sintering showed an increase in electrical conductivity compared to an only thermally sintered CCO layer, making it promising to be included in rapid production technology for thermoelectric films.

Keywords: Thermoelectricity; Energy Harvesting; Power Factor; Thermoelectric Oxides; Additive Manufacturing; Thermoelectric Generator

Zusammenfassung

Der thermoelektrische Effekt kann zur direkten Umwandlung von thermischer in elektrische Energie genutzt werden. Aufgrund der großen Menge Abwärme in vielen Industriebereichen ist die Anwendung dieses Effekts hier vielversprechend, um die Gesamteffizienz der Energiewandlung zu erhöhen. Diese Arbeit konzentriert sich auf die zwei Hauptforschungsfelder: Die Erforschung und Verbesserung thermoelektrischer Materialien und die Produktionstechnologie von thermoelektrischen Generatoren (TEGs).

Bislang wurden thermoelektrische Materialien vor allem hinsichtlich ihrer resultierenden Effizienz bei der Energieumwandlung bewertet. In dieser Arbeit wird hingegen das Konzept, sich stattdessen auf den Leistungsfaktor zu fokussieren, weiter untersucht. Ein Review zu thermoelektrischen Materialien für Hochtemperaturanwendungen beschreibt dies und vergleicht verschiedene im Fokus stehende Materialklassen sowohl hinsichtlich der Effizienz als auch des Leistungsfaktors. Als Ergebnis dieser Diskussion werden verschiedene Konzepte zur Optimierung von Materialien untersucht: Zur Optimierung der Effizienz wurde ein Hybridmaterial entwickelt, dass verschiedene Klassen von Materialien kombiniert, um synergetische Effekte zu erzielen. Das entwickelte Hybridmaterial zeigte aufgrund der geschaffenen Heteromaterial-Grenzflächen eine außergewöhnlich niedrige thermische Leitfähigkeit. Dadurch eignet sich dieses Konzept besonders wenn eine hohe Effizienz erreicht werden soll. Für eine Optimierung der elektrischen Leistung wurden Cu-Ni-Legierungen als vielversprechende Materialien untersucht. Die Cu-Ni Legierungen wurden aus Nanopartikeln hergestellt und mit schweren Elementen legiert, wodurch sowohl der Leistungsfaktor als auch die Effizienz bei geringen Dotierungsmengen gesteigert werden konnte.

Auch bei der Herstellung von TEGs besteht ein Optimierungspotenzial, da die Prdouktionskosten einen großen Anteil an den Gesamtkosten ausmachen. Hierfür wurde eine Fertigungsroute entwickelt, die schnelle und skalierbare Produktionstechnologie mit laserbasierten Prozessen kombiniert. Die Schichten wurden durch Sprühbeschichtung hergestellt und das Design anschließend durch den Einsatz eines CO_2-Lasers strukturiert. Der entworfene TEG-Prototyp erreicht eine maximale elektrische Leistung von 1,6 μW cm^{-2}. Die entwickelte Herstellungsroute erlaubt eine präzise Kontrolle über die Schichtdicke und die exakte Geometrie. Schließlich wurde das Konzept laserinduzierter Prozesse für thermoelektrische Anwendung, z.B. zum Sintern, anhand einer Laserbehandlung einer gesprühten CCO Schicht untersucht. Durch den Einsatz eines CO_2-Lasers konnte hierbei eine beginnende Versinterung der CCO-Schicht beobachtet werden. Die Kombination aus Laser- und thermischer Behandlung zeigte eine Erhöhung der elektrischen Leitfähigkeit, was das Potenzial dieses Konzept in der Herstellung von thermoelektrischen Materialien und Generatoren integriert zeigt.

Stichworte: Thermoelektrizität; Energy Harvesting; Leistungsfaktor; Thermoelektrische Oxide; Additive Fertigung; Thermoelektrischer Generator

Abbreviations

AM	additive manufacturing
CCO	$Ca_3Co_4O_9$, calcium cobaltite
CNTs	carbon nanotubes
CS	conventional sintering
CW	continuous wave
DOS	density of states
EDTA	ethylenediaminetetraacetic acid
EDXS	energy-dispersive X-ray spectroscopy
FEM	finite elemente method (simulations)
HH	half-Heusler
HP	hot pressing
LBM-M	laser beam melting of metals
LBM-P	laser beam melting of polymers
LTCC	low temperature co-fired ceramic
MCEP	maximum conversion efficiency point
MEPP	maximum electrical power point
PANI	polyaniline
PEDOT:PSS	poly(3,4-ethylenedioxythiophene)polystyrene sulfonate
PGEC	phonon glass - electron crystal
SEM	scanning electron microscope
SPS	spark-plasma sintering
TEG	thermoelectric generator
TEM	transmission electron microscope

TRL	technology readiness level
XRD	X-ray diffraction

Contents

1. Introduction

The topic of energy supply is a very important field these days with an ever increasing importance and demand. In recent years, more and more interest arose in research and expansion of green and renewable energy. Simultaneously, the demand on electrical energy also rises from year to year. Figure 1.1 shows the statistic of the world's electricity generation from various sources from 1990 to 2018 [1]. Here, the main sources of electricity generation are fossil fuels and nuclear power, with increasing values of renewable energies like solar or wind in recent years. However, all ways of electricity generation are based on conversion processes, which always are accompanied by a huge amount of wasted energy due to the losses of the conversion processes. A good example is the conversion of thermal energy into mechanical energy (e.g., a combustion engine) which is limited by the Carnot efficiency, where a maximum conversion efficiency of 100 % can never occur with limited hot- and cold-side temperatures. Usually, most processes do not exceed a conversion efficiency of 50 % (e.g., combustion engine 20-50 % [2]). As a result, more than half of the total energy supply cannot be used sufficiently. In 2019, the United States energy consumption report states, that 67.5 % of the total energy remained unused as waste energy [3]. To tackle the world's increasing energy demand, reducing this amount of wasted energy is an important future task.

To achieve this reduction, energy conversion via *Energy Harvesting* may play a key role in the future. *Energy Harvesting* is a general term that combines various processes which are capable of the conversion of wasted energy into usable energy to increase the total efficiency sufficiently [4]. Due to the reliable energy supply (long-term energy supply without moving parts or limited lifetime), the use of *Energy Harvesting* systems is especially advantageous where a high amount of energy is wasted and where mainte-
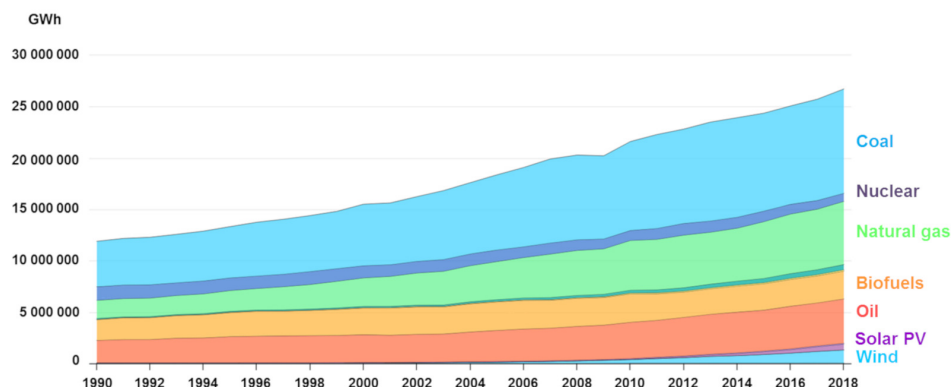

Fig. 1.1: Total global energy generation by source from 1990 to 2018 [1]. An increasing amount in the shares of renewable energies can be seen.
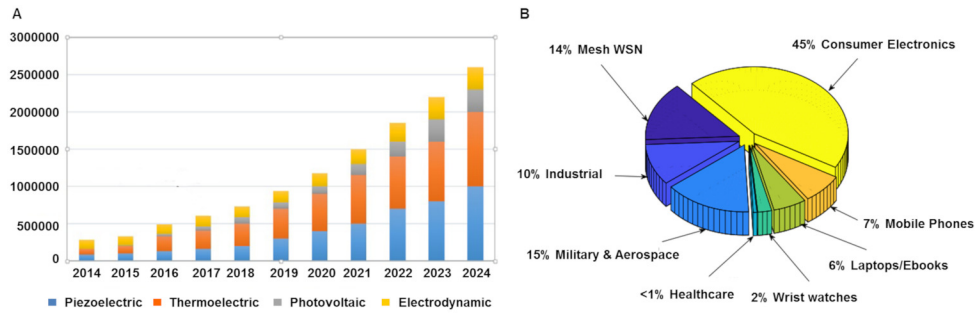
Fig. 1.2: Statistic stock market data of Energy Harvesting. A) Trend of total energy supply via Energy Harvesting from 2014 and predicted trend until 2024; B) Share of various application fields of Energy Harvesting in 2017. Reproduced from [5].

nance or a switching of batteries is complicated [4]. The most prominent examples are the direct conversion of solar energy into electrical energy via photovoltaics, mechanical pressure into electrical energy via piezoelectrics and thermal energy into electrical energy via thermoelectricity. Out of this, the photovoltaic energy conversion is already commercially established, reaching high conversion efficiencies of up to 25 % [5], which are comparable to the efficiency of a combustion engine. The costs of production and installation of photovoltaics can therefore be compensated by their energy supply in a reasonable amount of years. An even more promising method of *Energy Harvesting* is the direct conversion of thermal energy into electrical energy via thermoelectricity. Due to the nature of many conversion processes, the by far largest amount of wasted energy is in the form of heat, opening up a high number of possible applications for thermoelectric generators (TEGs). The thermoelectric energy conversion is based on the resulting potential difference of two dissimilar materials in a temperature gradient, the SEEBECK effect (after Thomas Johann Seebeck). Analogously, the inversion of this process, absorbing or releasing heat energy when an electrical current flows through an electrical interface (PELTIER effect, after Jean Charles Athanase Peltier) can be used in terms of cooling applications like refrigerators. Up to now the maximum conversion efficiency of those generators is fairly low, limiting a wide industrial application. However, there are already some niche application fields of thermoelectric energy conversion (in either direction) such as space exploration and consumer electronics. In Figure 1.2A, the trend of total energy supply via *Energy Harvesting* from 2014 up to now and the prediction of the trend until 2024 are shown [5]. Due to the increasing demand on energy supply, a strong increase is expected for all fields of *Energy Harvesting*. Figure 1.2B displays the respective shares in application of *Energy Harvesting* systems, where consumer electronics have the biggest share around 45 % followed by military and aerospace with 15 % and wireless sensor networks with 14 % [5]. For expansion of commercial application, both the improvement of materials as well as the manufacturing of TEGs needs to be further investigated to achieve better thermoelectric properties and to reduce the costs of TEG manufacturing. Within the context of this work, both of these aspects are analysed and new concepts are presented.

1.1 Basics of thermoelectricity

1.1.1 Thermoelectric parameters: Coupled fluxes

The effect of thermoelectric energy conversion is based on the coupling of thermal and electrical fluxes, which coined the term 'thermoelectric' effect. Here, an electrical flux density j_q is based on a transport of electrical charge q, which can be either electrons e^- or electron holes h^+. The corresponding potential of the electrical charge is the electrical potential φ. The flux density of thermal energy j_S is provided by the transport of entropy S with the corresponding thermodynamic potential being the absolute temperature T. The coupling of the respective fluxes in a thermoelectric material can be described by a basic transport shown in Equation 1.1:

$$\begin{pmatrix} j_q \\ j_s \end{pmatrix} = \begin{pmatrix} \sigma & \sigma \cdot \alpha \\ \sigma \cdot \alpha & \sigma \cdot \alpha^2 + \Lambda_{OC} \end{pmatrix} \cdot \begin{pmatrix} -\nabla\varphi \\ -\nabla T \end{pmatrix} \tag{1.1}$$

Via an approximation of constant gradients, the respective gradients can be substituted by the potential differences along the thermoelectric material with the length l ($\nabla\varphi \rightarrow -\Delta\varphi/l$ and $\nabla T \rightarrow -\Delta T/l$). Additionally, the local flux densities can be integrated to the current of electrical charge I_q and current of entropy I_S, when a thermoelectric material with a cross-sectional area A is assumed. Hence, the transport equation in its integral form is received (Equation 1.2) [6]. For a more detailed description of this transport equation, the reader is referred to the works of Feldhoff [6, 7], Fuchs [8] or Goupil et al. [9].

$$\begin{pmatrix} I_q \\ I_s \end{pmatrix} = \frac{A}{l} \begin{pmatrix} \sigma & \sigma \cdot \alpha \\ \sigma \cdot \alpha & \sigma \cdot \alpha^2 + \Lambda_{OC} \end{pmatrix} \cdot \begin{pmatrix} \Delta\varphi \\ \Delta T \end{pmatrix} \tag{1.2}$$

The coupling of the resulting fluxes of entropy I_S and charge I_q is therefore provided by a thermoelectric material tensor, consisting of three material parameters: The isothermal electrical conductivity σ, the SEEBECK coefficient α and the open-circuited entropy conductivity Λ_{OC}. Note, that the entropy conductivity Λ is here used as a more fundamental expression of the thermal conductivity of the material, which will be further discussed later (see page 7). Although the absolute temperature T does not explicitly occur within this description, it is implicitly within the materials parameters $\sigma(\mathrm{T})$, $\alpha(\mathrm{T})$ and $\Lambda(\mathrm{T})$.

Based on the thermoelectric material tensor in the transport equation, a dimensionless figure of merit $f = zT$ as a quality parameter for the thermoelectric energy conversion can be derived by a simple discussion of the tensor element M_{22} [10]. The resulting figure of merit is a function of the three material parameters and was firstly introduced by Ioffe in 1957 [11]:

$$f = zT := \frac{\sigma \cdot \alpha^2}{\Lambda_{OC}} \tag{1.3}$$

As a result of this quality criterion, the research on thermoelectric materials focuses on a high figure of merit zT, meaning a material is desired to have a high isothermal electrical conductivity σ, a high Seebeck coefficient α and a simultaneously low entropy conductivity Λ. As these material parameters are the fundamental parameters for the development of thermoelectric materials, they will be discussed in more detail in the following.

Isothermal electrical conductivity

The isothermal electrical conductivity of a material in its solid-state is a basic characteristic that is used to define different classes of materials. An electrical insulator exhibits an electrical conductivity less than 10^{-9} S cm^{-1}, whereby a metal exhibits an electrical conductivity higher than 10^2 S cm^{-1} [12]. A material with an electrical conductivity in between is referred to as a semiconductor. In textbooks, the electrical conductivity is often introduced using the nearly free electron model [12,13]. Here, the main assumption is an unhindered movement of electrons (or electron waves) within the atomic or ionic lattice resulting in a simple parabolic behavior of the electron wave energy with the respective wave vector. The model is widely used to describe the behavior of electrons in a metallic lattice. To describe the electrical conductivity of a semiconductor solid-state material and the appearance of an energy gap, this model is extended to include the periodicity of the lattice of the material and the resulting interaction with the electron transport. Due to occurring BRAGG reflection of the electron waves at the edges of the BRILLOUIN zones, the respective group velocity $\bar{\nu}$ has to vanish and the parabolic behavior splits into separate energy bands. In between, a forbidden band is formed which is referred to as the energy gap or band gap. The resulting bands are referred to as the conducting band and the valence band. For metals, both bands overlap and no energy gap occurs, which results in a high mobility of the electrons. A material, that exhibits a band gap of up to 4 eV is referred to as semiconductor, and with an even larger band gap as insulator. This description corresponds to the definition via the resulting electrical conductivity σ, which is based on the resulting full electronic band structure of the material. The resulting electrical conductivity σ is a function of the mobility of the charge carriers μ, the charge carrier concentration n and the elemental charge e based on the description of Drude [13]:

$$\sigma = n \cdot \mu \cdot z \cdot e \tag{1.4}$$

Both, the charge carrier concentration n as well as the charge carrier mobility μ are directly related to the electronic band structure of the material. The first is mainly determined by the density of states (DOS), which means the number of possible configurations for an electron following the PAULI principle, and the latter is defined by the curvature of the respective band (conduction band for electrons, valence band for electron holes). The charge carrier mobility μ is defined as a function of the elemental charge e, the median flight time of a charge carrier between collisions τ and the effective mass m^* [13]:

$$\mu = \frac{e \cdot \tau}{m^*} \tag{1.5}$$

It follows that the intrinsic electrical conductivity of a material is proportional to the charge carrier concentration n and antiproportional to the effective mass of the charge carriers m^*.

Another very important concept is the FERMI energy E_F, which is defined as the energy of the highest occupied state at 0 K [12]. For metals, E_F is located within the conduction band, as conduction and valence band overlap, whereas for semiconductors and insulators E_F is located in the middle of the effective band gap. However, for semiconductors E_F can strongly be influenced by the concept of doping, which introduces additional holes or electrons. Doping can effectively shift E_F towards the conduction or valence band, resulting in an extrinsic electrical conductivity of the

material. Influencing the electronic band structure of a material is a generally used concept of tuning the thermoelectric properties of promising materials, which is further described in section 1.1.3.

Seebeck coefficient

The SEEBECK coefficient α (in some cases also referred to as 'thermopower') describes the thermal induction of an electrical potential in a material. On the hot side of the material, the respective charge carriers have a higher mean velocity compared to the charge carriers on the cold side of the material. Hence, a diffusion of charge carriers to the cold side is induced, leading to an effective potential that can be detected [7]. The Seebeck coefficient α can therefore be described as an entropy S^* that is transported per charge q and is usually given in μV K^{-1}. Hereby, the sign of the Seebeck coefficient indicates the nature of the major charge carriers, effectively defining p- (for a positive Seebeck coefficient) and n-type (for a negative Seebeck coefficient) character of the materials.

The SEEBECK coefficient α is also closely related to the electronic band structure of the material, the DOS and the FERMI energy E_F [14] and therefore is interrelated with the isothermal electrical conductivity σ. Generally, the Seebeck coefficient of a material can be determined by the Mott formula (Equation 1.6) [15]:

$$\alpha = -\frac{\pi^2}{3e}k_B^2 T \frac{\partial ln(\sigma(E))}{\partial E}\bigg|_{E=E_F}$$ (1.6)

Here, k_B is the BOLTZMANN constant and E is the energy of the respective charge carriers. From this, the SEEBECK coefficient of a degenerated semiconductor can be derived as a function of its effective mass m^* and the charge carrier concentration n [16–18]:

$$\alpha_{degenerated} = \frac{S^*}{q} = \frac{k_B}{e}(\gamma + \frac{2}{3})\frac{\pi^2}{3}\frac{k_B}{E_F} = \frac{2}{3}(\frac{\pi}{3})^{\frac{2}{3}}(\gamma + \frac{2}{3})\frac{k_B^2 m^*}{e\hbar^2 n^{\frac{2}{3}}}$$ (1.7)

Here, $\hbar$ is the reduced PLANCK's quantum and γ a scattering factor depending on the scattering mechanism (-0.5 for acoustic phonons, 0 for neutral impurities and 1.5 for ionized impurities). It follows that for a degenerated conductor, the Seebeck coefficient α is proportional to m^* and antiproportional to n. This corresponds to the isothermal electrical conductivity described in the previous chapter, however, the dependencies are switched. When designing a thermoeletric material, this usually leads to an incoherent conflict, as an increase in electrical conductivity based on a higher charge carrier concentration or higher charge carrier mobility often leads to a decrease of the SEEBECK coefficient: The parameters are interlinked. In addition, tuning of m^* or n also influences the other parameter, which is a general challenge in thermoelectric material research. Although this derivation of the Mott formula is only valid for degenerated conductors (metals), it is also used as a good approximation for highly doped semiconductors [18] which are usually considered as promising thermoelectric materials.

Thermal conductivity

The thermal conductivity is the third crucial parameter in regard to thermoelectric energy conversion. Note that in the context of this work, the term 'thermal conductiv-

ity' is used as a general term. It can be described by the entropy conductivity Λ which defines the capability of a material to transport entropy. The entropy conductivity Λ is a more fundamental description of this transfer compared to the traditionally used heat conductivity λ[1]. In fact, the heat conductivity λ is based on the entropy conductivity Λ and the absolute temperature T [6]:

$$\lambda = \Lambda \cdot T \tag{1.8}$$

The entropy conductivity of a material is determined by measuring the thermal diffusivity D_{th}, the entropy capacity K_{p} and the density of the material ρ:

$$\Lambda = D_{\mathrm{th}} \cdot K_p \cdot \rho \tag{1.9}$$

The transport of thermal energy within a solid-state material is a complex process, as there are multiple transport processes involved. Under open-circuited conditions (vanishing electrical current), this transport is described by FOURIER's law, which also results from the transport Equation 1.1 [7,19]. The respective proportionality between the local thermal flux density and the temperature gradient, the entropy conductivity, is often treated as constant although it shows a temperature derivation. Based on the two main mechanisms of transport of thermal energy, the entropy conductivity can be split into the respective parts:

$$\Lambda = \Lambda_{\mathrm{ph}} + \Lambda_{\mathrm{el}} \tag{1.10}$$

Λ_{ph} describes the transport of entropy via lattice vibrations, the phonons, and Λ_{el} describes the transport of entropy via electronic conduction. Hereby, Λ_{el} is often described by the empirical WIEDEMANN-FRANZ relation (Equation 1.11), that proposes a linear dependency of the entropy conductivity on the electrical conductivity with the proportional factor being the Lorenz number L. For a degenerated conductor, the Lorenz number L is described by the Sommerfeld value $L = 2.45 \cdot 10^{-8}$ W Ω^{-1} K^{-2} [20].

$$L = \frac{\Lambda}{\sigma} \tag{1.11}$$

Equation 1.11, however, is only valid for very high concentrations of charge carriers, as stated by Ioffe [11], and can vary strongly for charge carrier concentrations lower than $2.5 \cdot 10^{19}$ cm^{-3}, which is the case for most semiconducting thermoelectric materials. Then, a deviating Lorenz number of $1.48 \cdot 10^{-8}$ W Ω^{-1} K^{-2} [20] can be found, here noted as L'. This can be seen in Figure 1.3, where the entropy conductivity Λ is shown as function of the electrical conductivity σ for a given temperature T. The value of the entropy conductivity Λ at vanishing electrical current corresponds to the lattice-based transport of thermal energy Λ_{ph}, but only when one type of charge carrier is present. At increasing electrical conductivity (i.e. increasing charge carrier concentration), the total thermal conductivity increases with a proportionality deviating from the SOMMERFELD value. Only at high electrical conductivity a Wiedemann-Franz behavior can be expected.

Independent of the exact interrelation, the thermal conductivity based on the transport of electrons Λ_{el} is therefore also coupled with the charge carrier concentration n, the mobility of the charge carriers μ and their effective mass m^{*}. In fact, the

---

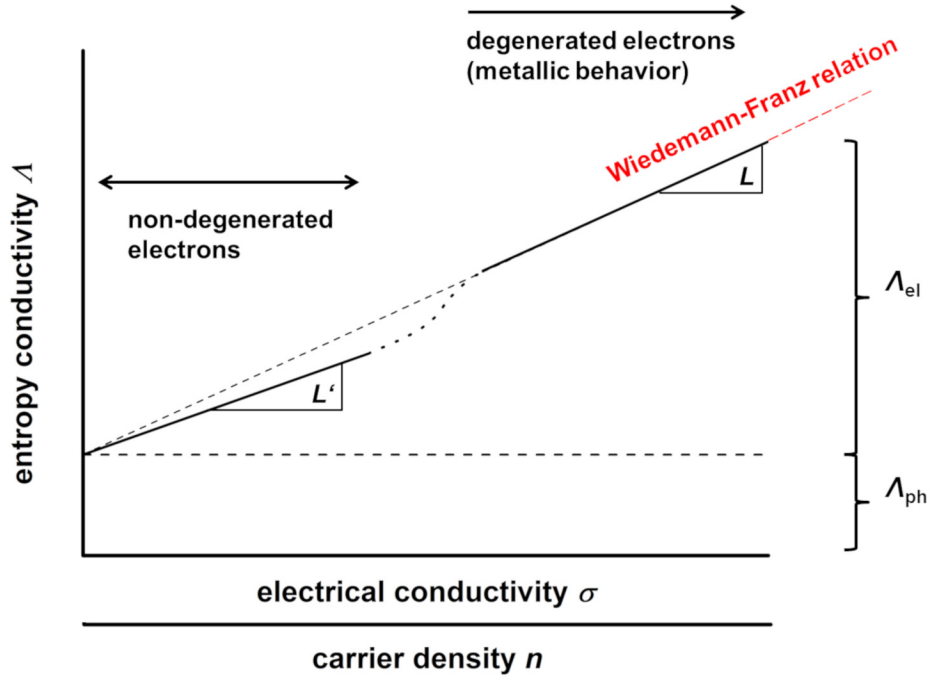[1]Note that in some literature the heat conductivity is also displayed as κ.

Fig. 1.3: Thermal conductivity Λ as a function of the electrical conductivity σ and the carrier density n of a semiconductor. Reproduced from [11]. Note that the correlation with the electrical conductivity is only valid when one type of charge carriers is present.

phonon-related thermal conductivity Λ_{ph} is also interrelated with the charge carrier mobility μ, as phonons and electron waves both are underlying similar scattering mechanism in a solid-state material with varying degrees of scattering [11]. This is important, because it makes it questionable to determine the share of Λ_{ph} and Λ_{el} from the measured values of Λ by applying WIEDEMANN-FRANZ behavior [20], as it is reported also for non-degenerated semiconducting materials, even if not only one type of charge carrier is present. Moreover, this interrelation between the thermal conductivity (Λ_{ph} and Λ_{el}), the electrical conductivity σ and the SEEBECK coefficient α is the crucial factor in designing thermoelectric materials, as tuning one of the parameters always also influences the other. Some ways to influence and tune the properties of thermoelectric materials are discussed in chapter 1.1.3.

1.1.2 Electrical power output vs. conversion efficiency

As already discussed, the figure of merit zT is the most used quality criterion for thermoelectric materials. It is directly correlated to the resulting energy conversion efficiency of the material η_{max} [6]:

$$\eta_{max} = \frac{T_{hot} - T_{cold}}{T_{hot}} \cdot \frac{\sqrt{1 + z\bar{T}} - 1}{\sqrt{1 + z\bar{T}} + 1} \tag{1.12}$$

Note, that $z\bar{T}$ is the median zT of the materials and the first term corresponds to the CARNOT efficiency η_{Carnot}. However, there is another important quality criterion for thermoelectric materials, namely the power factor $\sigma\alpha^2$, which evaluates the electrical power output of the material. The maximum electrical power output
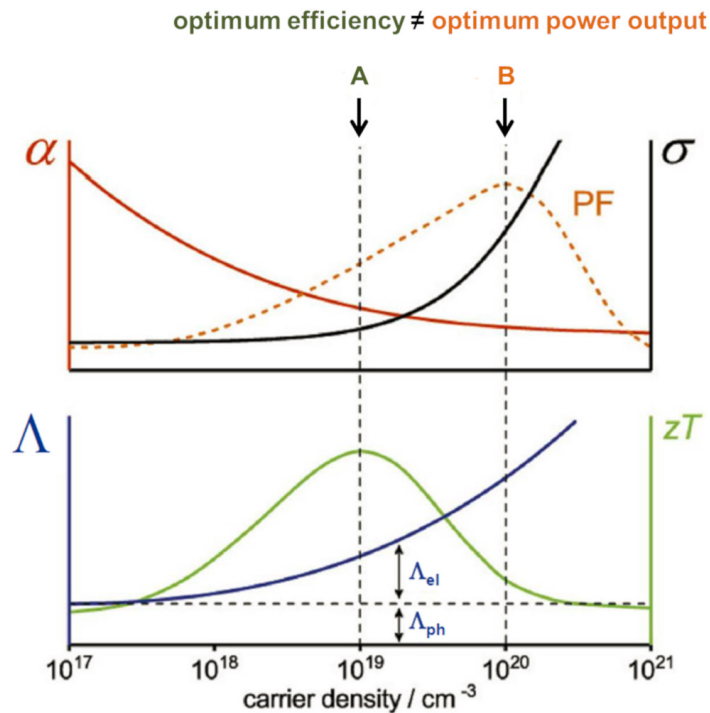
Fig. 1.4: Optimum power factor and conversion efficiency as a function of the carrier density. Reproduced from [22].

of a thermoelectric material $P_{el,max,mat}$ is a function of its power factor $\sigma\alpha^2$ and the temperature difference ΔT [21]:

$$P_{el,max,mat} = \frac{1}{4}\frac{A}{l}\sigma\alpha^2(\Delta T)^2 \qquad (1.13)$$

Therefore, the maximum electrical power output itself is not dependent on the figure of merit zT and also not on the thermal conductivity implicitly, but is a function of the temperature difference ΔT. Obviously, the thermal conductivity of the material has an influence on the temperature difference between hot and cold side, especially if passive cooling is applied.

The figure of merit zT describes the energy conversion efficiency, while the power factor correlates to the maximum electrical power output. As could be shown in the context of this work, this can result in various optimization strategies for materials and TEGs, aiming either for maximum energy conversion efficiency or maximum electrical power output. Also, analysing and comparing the power factor of various materials presents new promising materials for thermoelectric applications, which haven't been analysed yet due to their comparably low figure of merit zT. Various interesting thermoelectric materials including fairly new ones based on the optimization of the power factor are discussed in chapter 2.

The deviation of maximum power factor (i.e. power output) and maximum zT (i.e. energy conversion efficiency) can also be displayed by their interrelation with the charge carrier concentration n. As discussed before, all thermoelectric parameters are strongly influenced by the charge carrier concentration n and their mobility μ. This is shown in Figure 1.4, where the maximum power factor is located at a higher charge carrier concentration as the maximum zT. This is based on the entropy conductivity
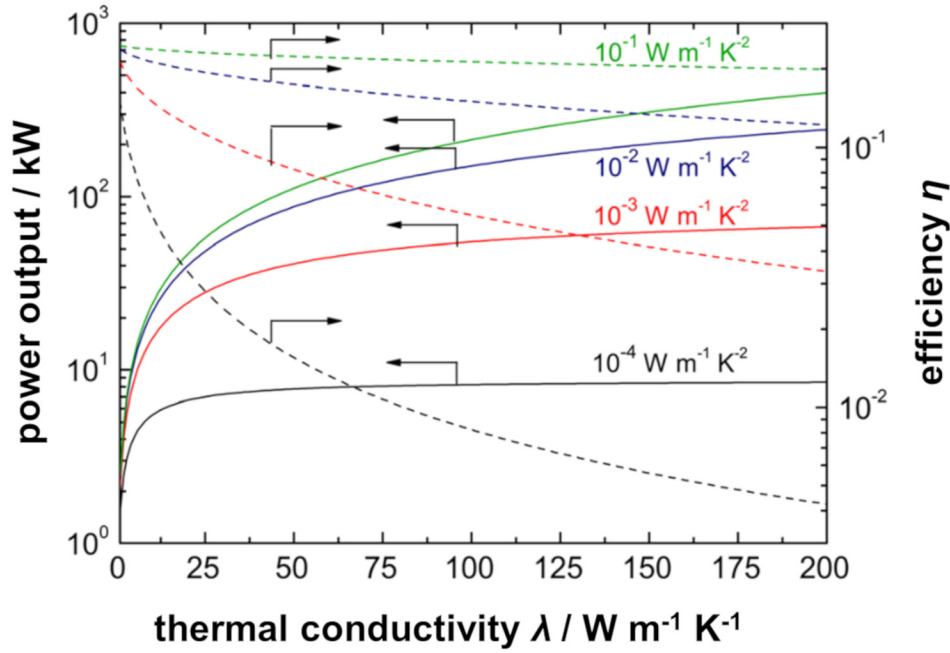
Fig. 1.5: Narducci plot: Electrical power output W (left axis) and energy conversion efficiency (right axis) as a function of the thermal conductivity λ for a power factor of 10^{-1} W m^{-1} K^{-2}, 10^{-2} W m^{-1} K^{-2}, 10^{-3} W m^{-1} K^{-2} and 10^{-4} W m^{-1} K^{-2} under the assumption of constant ΔT. Reproduced from [23].

Λ, which strongly influences the figure of merit zT and favours a lower carrier concentration compared to the optimum carrier concentration for the power factor, which is independent of the thermal conductivity. Therefore, designing a material for either a high energy conversion efficiency or a high electrical power output, by influencing the basic parameters such as the carrier concentration n, plays an important role.

Narducci also came up with the question 'Do we really need high figure of merit zT?' in his work from 2011 [23]. Figure 1.5 recaps his analyses to this topic by showing the electrical power output (left axis) and the energy conversion efficiency (right axis) as a function of the thermal conductivity. This also displays, that a high electrical power output can be achieved at a higher thermal conductivity or rather a higher power factor, as long as the ΔT over the material can be maintained. The findings therefore also show the importance of the power factor especially under fixed heat-flow conditions or a stable temperature difference, e.g., by active cooling, and denote the figure of merit zT a 'misleading' character in this context, as it is a multi-parameter optimization rather than optimizing just one.

Another way to display the variation of maximum power output and maximum energy conversion efficiency is by analysing the working points of the thermoelectric material: the maximum electrical power point (MEPP) and maximum conversion efficiency point (MCEP) [6]. The MEPP of a material is given at half the open-circuit voltage and half the short-circuit current and the resulting maximum electrical power output is determined according to Equation 1.13. However, the MCEP is a function of the figure of merit zT and thus depends on the thermoelectric material. This is shown in Figure 1.6 for some theoretical thermoelectric material with zT of 0.5, 1,
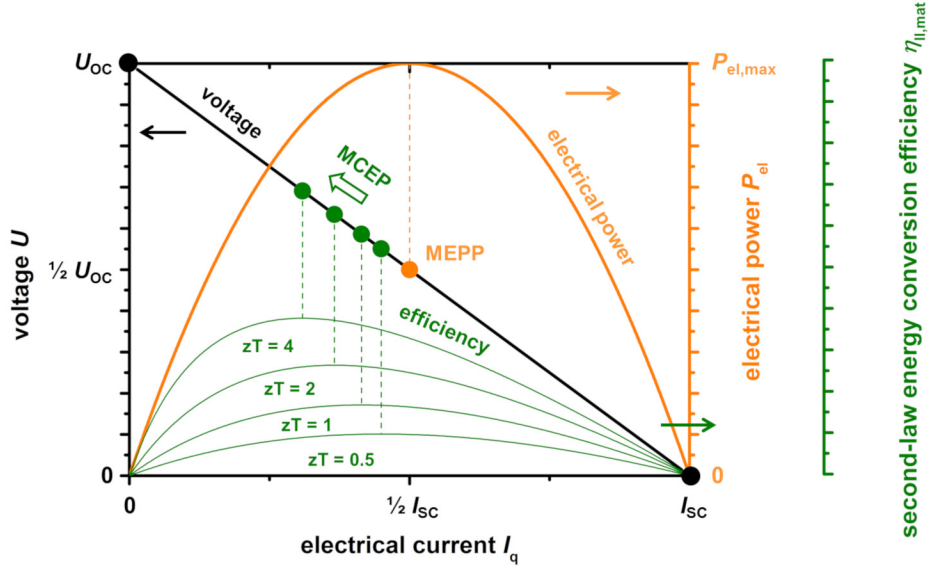
Fig. 1.6: U-I_q curve (left axis), P_{el}-I_q curve (right axis) and materials working points of theoretical thermoelectric materials with $zT = 0.5$, 1, 2 and 4. Reproduced from [6].

2 and 4. With increasing figure of merit zT, the MCEP drifts more and more apart from the MEPP. If operated at the MCEP, the resulting electrical power output of a thermoelectric material is therefore lower compared to the maximum electrical power output $P_{el,max}$ [6]:

$$P_{el,MCEP} = \frac{4\sqrt{1 + zT}}{(\sqrt{1 + zT} + 1)^2} \cdot P_{el,max} \tag{1.14}$$

Vice versa, the resulting conversion efficiency for a material operated at the MEPP is lower compared to the maximum conversion efficiency, corresponding to Equation 1.15.

$$\eta_{MEPP} = \frac{T_{hot} - T_{cold}}{T_{hot}} \cdot \frac{1}{2}\frac{zT}{zT + 2} \tag{1.15}$$

This also corresponds to the assertion of the Narducci plot (Figure 1.5) that shows this deviation of power output and conversion efficiency and postulates the overlap of MCEP and MEPP for $zT = 0$. For a given material, this means that the theoretical maximum electrical power output and the theoretical maximum conversion efficiency cannot be achieved simultaneously. This also indicates the possibility to achieve either a high conversion efficiency or a high electrical power output and showcases the importance to optimize either characteristic. This concept also opens a pathway for mostly overlooked materials which may exceed at one of the parameters and therefore can be promising for a certain application desired to have either a high conversion efficiency or a high power output.

1.1.3 Tuning of thermoelectric properties

The tuning of thermoelectric materials and their respective properties is in the focus of research ever since the uprising interest in this form of energy conversion. As discussed above, the interrelation of the main properties, the isothermal conductivity

σ, the SEEBECK coefficient α and the entropy conductivity Λ, is the crucial characteristic. Therefore, new approaches and special design of materials are required to further improve the thermoelectric properties of a promising material. In this section, various optimization strategies are introduced, including doping and band engineering of materials, nanostructuring as well as the concept of hybrid materials. Since all respective parameters are interlinked, the optimization strategies always influence all three parameters, which, however, may differ in intensity of the respective in- or decrease.

Doping and band engineering

Doping is a well-established method to influence the carrier concentration n and the effective mass m^* of a material by introducing additional states within the band gap. Although it only plays a minor role in the results related to this work, it is discussed here due to the importance of doping in tuning of thermoelectric properties.

Firstly, doping can strongly influence the carrier concentration n, as dopants usually are of higher or lower oxidation state than the ionic lattice. Via doping, additional electronic states are introduced and as a result, the FERMI energy E_F shifts towards the conduction band (for n-type doping) or the valence band (for p-type doping). This directly influences the isothermal electrical conductivity as well as the SEEBECK coefficient as discussed before. Obviously, the entropy conductivity is also influenced by doping: On one hand, an increasing carrier concentration n and therefore increasing isothermal electrical conductivity σ also increases the electron-related part of the entropy conductivity Λ_{el} as well as the phonon-related entropy conductivity Λ_{ph}, which counteracts the desired improvement of the zT value. On the other hand, dopants usually act as additional scattering points for phonons, also influencing Λ_{ph}. Overall, an optimum carrier concentration for thermoelectric materials (regarding a high zT) as a function of the temperature can be estimated [11], thus doping can be effectively used to design a material to match this characteristic.

Different doping techniques have been developed in the past decades: Conventional doping, graded doping and temperature-dependent doping [24]. Conventional doping describes a uniform doping process, where the resulting carrier concentration is more or less constant over a large temperature range. However, the mentioned optimum carrier concentration n^* increases with $T^{\frac{3}{2}}$ [11,24]. Graded doping introduces multiple segments including different dopants, where the temperature gradient alongside the material is considered and the resulting carrier concentration n varies accordingly. A third concept can be applied for specific dopants that show a strong temperature-dependent solubility in the material. By this, a temperature-dependent doping can be achieved, that results in a reversible solution process of the dopants when the material is in a temperature gradient. Due to the usually nearly linear temperature profile, this results in an also linear increase of the carrier concentration n with the temperature, which is a good approximation to the $T^{\frac{3}{2}}$ dependency of n with T (see Figure 1.7A).

A related topic is the precise design of the electronic band structure to tune the effective mass m^*. An interesting approach for this is band engineering in order to achieve band convergence, as shown in Figure 1.7B. By proper doping, a specific electronic band, e.g., a valence band, with an energy lower than the highest valence band (meaning a normally irrelevant band for electronic conduction) can be influenced to get closer to the highest energetic valence band (ΔE decreases and lastly
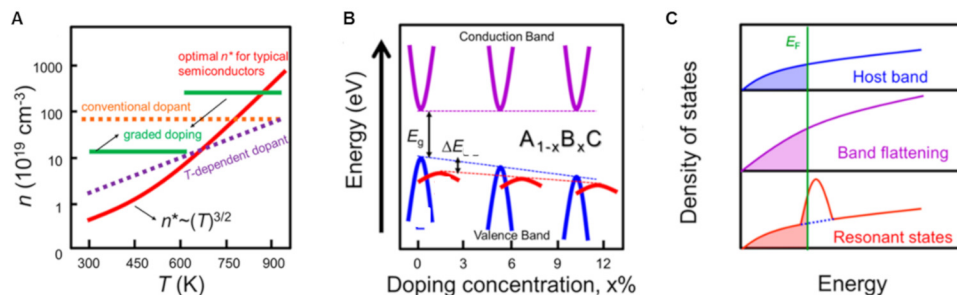
Fig. 1.7: A) Carrier concentration n as a function of the temperature T for various doping methods. The optimum carrier concentration n^* for a typical semiconductor is shown in red; B) Concept of band convergence via doping: The ΔE between the highest valence band and a lower valence band vanishes, effectively increasing the effective mass m^*; C) Concept of resonant levels to increase the DOS at the Fermi level E_F. Reproduced from [24].

vanishes). By achieving this band convergence, the number of equivalent degenerated valleys increases, effectively increasing the effective mass m^* [24]. The aim of this concept is increasing the Seebeck coefficient without significantly reducing the electrical conductivity [25]. Furthermore, the effective mass m^* can also be directly tuned by proper doping, as it can influence the curvature of the band (and therefore influences the charge carrier mobility μ). Here, the concept of resonant levels [26] is used for tuning the thermoelectric properties (Figure 1.7C), especially for materials whose application temperature is limited to lower temperatures up to room temperature. Resonant levels can occur due to the interrelation of electrons of the dopant and the conduction or valence band, increasing the DOS at that energy level as well as the effective mass m^* [24, 25]. The realization of band convergence or the introduction of resonant levels are therefore effective concepts to tune the power factor $\sigma\alpha^2$ [27].

Nanostructuring

The influence of doping on the thermal conductivity was already mentioned in the previous chapter. The general concept of doping can also be transferred from the atomic scale to the nanoscale or microscale by introducing grains, impurities or even porosity on the respective scale. This also leads to additional scattering centres for both, electron waves and phonons. This concept of structuring thermoelectric materials from the atomic scale up to the microscale is known as nanostructuring [28]. Figure 1.8 shows various ways to achieve random or ordered nanocomposites by their respective scale [29]. Due to this concept, very low values for the thermal conductivity could be achieved by combining various structuring methods on all scales. Analogously, this also influences the other parameters, as they are interlinked. This influence, however, is very complex, as every dopant, impurity, porosity etc. shows a varying effect, and therefore finding an optimum for the zT is the main focus of research.

A similar approach describes the 'phonon glass - electron crystal' (PGEC) concept [30]. The idea of this concept is a material featuring a crystal with a good electrical conductivity ('electron crystal'), featuring special cages or tunnels, where smaller impurities (compared to the cage or tunnel itself) can be incorporated, effectively scattering phonons, resulting in a low phonon mean free path ('phonon glass') [28].
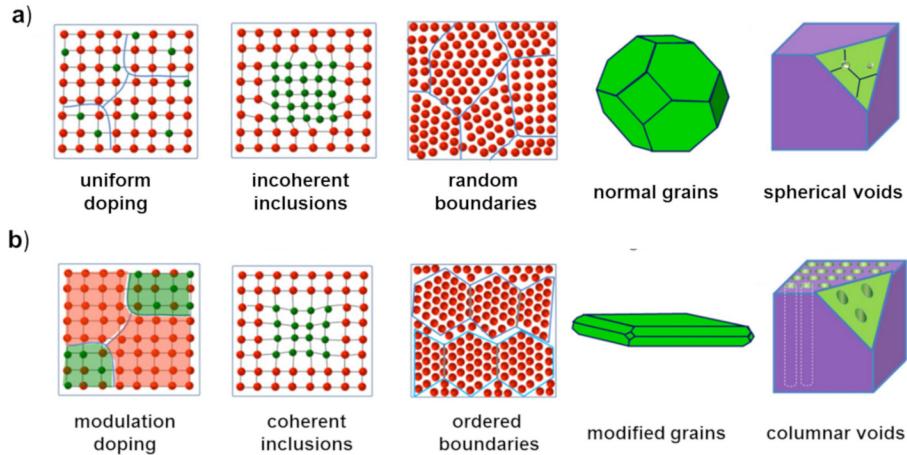
Fig. 1.8: Scheme of nanostructuring of thermoelectric materials from atomic doping to the microscale for a) random nanostructuring and b) ordered nanostructuring. Reproduced from [29].

The resulting strong decrease in thermal conductivity is based on the scattering of low frequency phonons, which carries more heat than high frequency phonons, at this 'rattling' impurities [27]. Famous examples of this concept are skutterudites, featuring empty cages that can be filled with smaller metallic cations, resulting in the described effect. By this, an exceptionally low heat conductivity down to 0.2 W m^{-1} K^{-1} could be achieved in multi-filled $CoSb_3$ [27].

Hybrid materials

A fairly new concept is the design of hybrid materials with enhanced thermoelectric properties. While doping usually means the introduction of other types of ions and nanostructuring mainly features the size and shape of the resulting crystals, hybrid materials are designed as a combination of completely different materials in order to achieve a beneficial synergy. The introduction of heteromaterial interfaces here again leads to additional scattering centres, reducing the phonon mean free path length. Additionally, the electrical conductivity and SEEBECK coefficient are also influenced by the nature of the combined materials. This has been investigated for various different combinations of materials [31]. WANG et al. compared an Ag-doping with an Ag-addition of the thermoelectric ceramic $Ca_3Co_4O_9$ (CCO), where both act beneficial for the power factor in a certain range of Ag amount [32]. In an included work, a hybrid material containing three different phases (ceramic, polymer and metallic phase) was designed, where it could be shown that a synergetic effect is gained because the electrical conductivity increases with the amount of metallic phase while the thermal conductivity further decreases due to the heteromaterial interfaces.

Due to the wide-ranging possibilities of material combinations and the complexity of this concept, further investigations for possible synergetic effects are required. In fact, it is not clear yet if a hybrid material can actually exceed the performance of pure materials. Back in 1991, BERGMAN et al. described theoretical limits for hybrid materials, stating that the figure of merit zT can never exceed the pure material [33]. This however, does not explicitly apply to the power factor $\sigma\alpha^2$, which has a similar relevance nowadays, and does not include possible effects on the nanoscale

[34]. Therefore, this is an interesting approach to design thermoelectric materials and tuning the power factor via synergetic effects or harshly reducing the thermal conductivity due to heteromaterial interfaces.

1.2   Thermoelectric material research

In this chapter, the basic idea behind the research for promising thermoelectric materials as well as a few examples, including some relevant thermoelectric materials for this work are introduced. For their application as thermoelectric materials, the defining material parameters were already discussed. As a result of the interrelation of the three defining parameters, the most promising materials are semiconductors or intermetallic phases, usually with a quite complex and often layered crystal structure. The most prevalent thermoelectric materials range from the commercially used bismuth telluride (Bi_2Te_3) [35] as well as other telluride- or selenide compounds [36–38], oxide-based ceramics [39, 40], intermetallic phases such as Zintl phases [41] and half-Heusler phases (HH) [42–44] and metal alloys such as SiGe [45]. Additionally, research on organic thermoelectric materials and hybrid materials became more relevant due to the introduction of electrically conducting polymers such as poly-3,4-ethylendioxythiophen polystyrene sulfonate (PEDOT:PSS) or polyanilin (PANI) [31, 46]. Within the literature, many investigations for the various materials and material classes have already been done, however, there are only a few works actually comparing different materials from various material classes and evaluating their performance in terms of energy conversion efficiency and power output. Therefore, as part of this work, a review about thermoelectric materials for high-temperature applications has been published, utilizing the Ioffe plots to compare and evaluate various materials. The review is included in section 1.2.5 as an overview of the different promising materials for respective applications including oxide ceramics, Zintl phases, half-Heusler phases and SiGe alloys.

1.2.1   Temperature stability of thermoelectric materials

A very important characteristic is the dependency of the thermoelectric materials and their properties on the desired application temperature. All material parameters exhibit a temperature dependency, often resulting in a maximum zT or power factor at a specific temperature. For example, Bi_2Te_3 shows a maximum zT near room temperature, while the zT decreases for higher and lower temperatures [4]. Additionally, every material is limited by its respective thermal stability in respect to the surrounding atmosphere. Therefore, different kinds of thermoelectric materials are needed, optimized for their respective application temperature. Figure 1.9 displays the temperature ranges of common thermoelectric materials and material classes. The commercially used Bi_2Te_3 and polymer-based materials like PEDOT:PSS are limited by their thermal stability and reach their respective optimum properties near room temperature. In the mid-temperature range (300 to 500 °C), PbTe-based materials as well as metal alloys and some intermetallic phases such as Zintl phases are the focus of research. For higher temperatures, oxide-based materials, half-Heusler intermetallic phases and SiGe alloys are promising materials. Obviously, the materials usually considered for mid- and high-temperatures may also be used for room temperature applications, however, their respective properties are inferior at this temperature. Note that some materials such as Zintl phases and SiGe alloys are usually characterized in inert gas atmosphere, as the thermal stability in air atmosphere is more limited.

Next to the aimed application field, the synthesis and preparation of thermoelectric materials also play an important role to control the resulting properties. The design
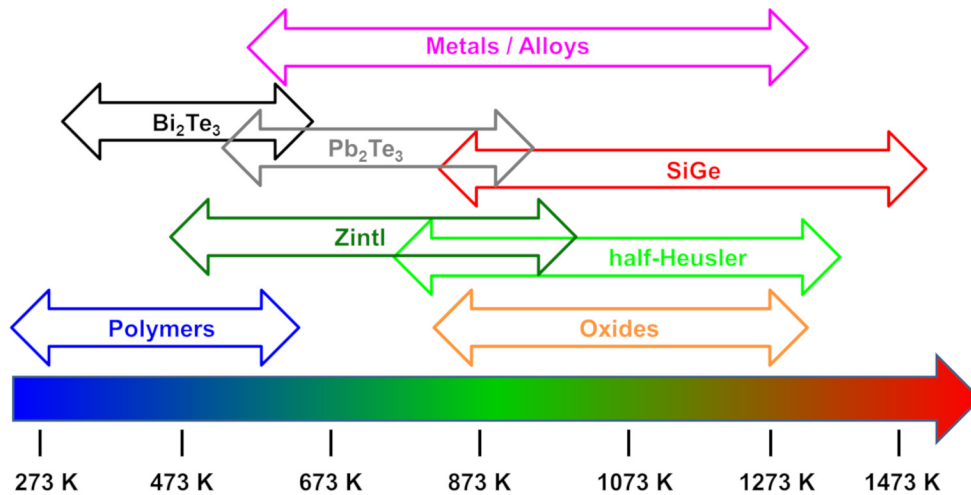
Fig. 1.9: Schematic temperature range and limitation of common thermoelectric materials and material classes. Different materials are suitable for certain temperature ranges, limited by their general thermal stability or their optimum thermoelectric properties. Note that some materials or material classes are only stable in vacuum or inert gas atmosphere at the displayed temperatures, e.g., SiGe alloys which are commonly used for space exploration.

of a thermoelectric bulk material often consists of calcination and sintering steps, including many varying parameters influencing the resulting nano- and microstructure of the material. The crystal size and shape used for preparation is also important, influencing the resulting microstructure in terms of grain boundaries and orientation, sometimes even resulting in an anisotropy of relevant properties. As this is very important for ceramic thermoelectric materials such as CCO, it will be discussed in detail later on (see page 19). Especially for organic thermoelectric materials, the preparation of thin films is in focus of research, where casting of the solution and the film preparation itself can be varied and investigated [36]. Naturally, the properties of thin films and bulk can differ widely, resulting in an increasing interest in thin films or layers of common thermoelectric materials. Furthermore, the tuning of the resulting properties of a material via doping, nanostructuring and band structure engineering adds several additional parameters to the thermoelectric material research. As a result, investigation and tuning of thermoelectric materials and new promising candidates is the main field of research in thermoelectric energy conversion.

Figure 1.10 shows Ioffe plots of type I (power factor $\sigma\alpha^2$ vs. electrical conductivity σ) and type II (entropy conductivity Λ vs. electrical conductivity σ) and the respective areas for the materials and material classes introduced before. An optimal material would exhibit a high power factor and a high electrical conductivity (top right in the Ioffe plot type I) and simultaneously a low thermal conductivity at a high electrical conductivity (bottom right in the Ioffe plot type II). However, as discussed before, the material parameters are linked to each other, meaning that materials that are located at a high power factor in the type I plot are usually also characterized by a high thermal conductivity in the type II plot. Hence, no material shows good characteristics in both plots. This also means, that for different desired properties, e.g., high power factor or high figure of merit, different materials may provide the best characteristic for a desired application. This can be further discussed by the

application temperatures for thermoelectric energy conversion. On the one hand there are many possible applications at or near room temperature like the electrical supply of a wrist watch via body heat [47]. However, the temperature differences that occur here and the amount of wasted heat energy are usually quite low. On the other hand, there are also interesting applications at high temperatures, where the amount of wasted heat energy is significantly larger. Therefore, solutions and tuning for applications at elevated temperature, e.g., in the automotive sector, for space exploration alongside radioisotope batteries or at industrial processes [48], are highly desired.
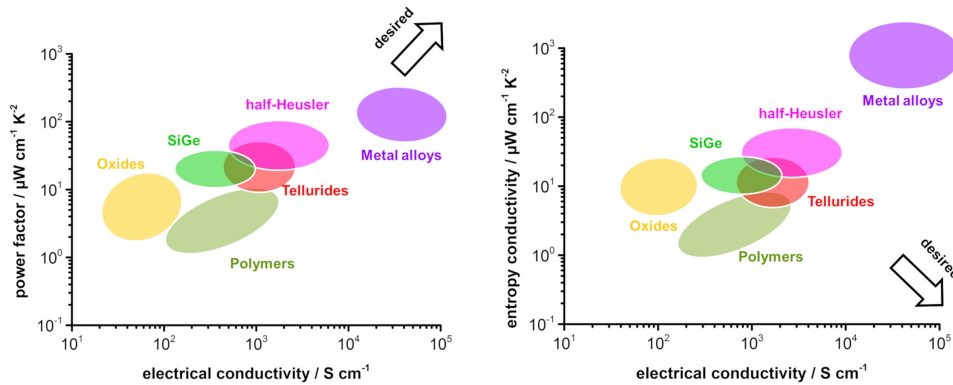

Fig. 1.10: Comparison of various thermoelectric material classes as A) Ioffe plot type I (power factor $\sigma\alpha^2$ vs. electrical conductivity σ and B) Ioffe plot type II (entropy conductivity Λ vs. electrical conductivity σ). A desired material is located in the top right in A and in the bottom right in B. Metal alloys and half-Heusler compounds show the highest power factor at high electrical conductivity while polymers and oxides exhibit the lowest thermal conductivity of the displayed materials. However, no material provides good characteristics in both.

1.2.2 Bi$_2$Te$_3$: The standard material

Doped Bi$_2$Te$_3$ is considered the standard material for thermoelectric energy conversion at room temperature. Remarkably, this material can be utilized as a *p*-type as well as a *n*-type material, simply by doping on the crystallographic Bi-site or Te-site, respectively. Most commonly, Se or Sb are used as dopants for both sites [49]. For nanostructured *p*-type Bi$_2$Te$_3$, zT values of 1.5 to 1.8 could be achieved [50, 51]. A related material is lead telluride (PbTe), which is characterized by similar properties, but reaches its peak performance at elevated temperatures around 300 to 400 °C. The crystal structure of Bi$_2$Te$_3$ is shown in Figure 1.11A. Bi$_2$Te$_3$ exhibits a hexahedral-layered crystal structure with stacked atomic layers bound via van-der-Waals interactions [36]. PbTe shows a cubic NaCl crystal structure [36]. Figure 1.11B gives a statistic on the research for thermoelectric materials. Here, the biggest share in thermoelectric applications relies on Bi$_2$Te$_3$ and Pb$_2$Te$_3$ for applications at room temperature or around 300 °C, respectively.

While Bi$_2$Te$_3$ compounds are as of yet unbeaten in thermoelectric performance at room temperature, it comes alongside a few major drawbacks:

- Application is limited by the relatively low thermal stability of the material.

- Reliance on toxic telluride-precursors, resulting in a costly and complex preparation process of materials and TEGs.

- Some metal-based materials like half-Heusler compounds reach even higher values of the power factor.

For lead telluride, the same drawbacks are true, the application is just shifted to slightly higher temperatures. Up to now, there is no competitive thermoelectric material to Bi_2Te_3 for near room temperature applications. For higher temperatures, various other kinds of materials are promising candidates like half-Heusler phases or oxides.
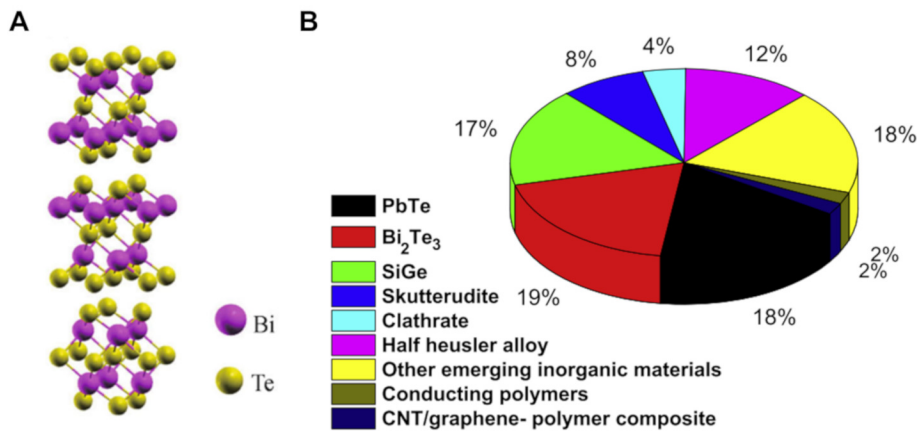

Fig. 1.11: A) shows the crystal structures of Bi_2Te_3. Reproduced from [49]. In B), contribution of various thermoelectric materials and material classes to thermoelectric technologies up to the year 2016 are shown. Reproduced from [36].

1.2.3 Oxide-based thermoelectric materials

Compared to the standard material Bi_2Te_3, oxide-based thermoelectric materials do not rely on toxic tellurides, although cobalt precursor can also be critical. Furthermore, the oxide-based materials show a much better chemical and thermal stability, e.g., up to 900 °C in air atmosphere for CCO. A good thermal stability in an air atmosphere can be highly beneficial, as promising applications are usually in air atmosphere (with the exception of space exploration) and some other thermoelectric materials in focus of research need inert gas atmosphere to operate at high temperatures. The major drawback of oxide-based materials are their comparatively low thermoelectric properties, reaching a power factor of 2 to 5 μW cm^{-1} K^{-2} and a figure of merit zT up to 0.4 to 0.6 [22].

Within the group of oxide-based thermoelectric materials, layered cobaltites are the most promising candidates as p-type materials. Na_xCoO_2 (NCO, x = 0.5 - 1) was first introduced as a pioneer compound in the group of layered cobaltites in the early 1990s. Later on, the related $Bi_2A_2Co_2O_9$ (A = alkaline metal) and $Ca_3Co_4O_9$ (CCO) compounds were in the focus of research. Within this group, CCO shows the best thermoelectric properties as well as the best thermal stability. All these compounds exhibit a hexagonal-layered crystal structure consisting of CdI$_2$-type CoO$_2$
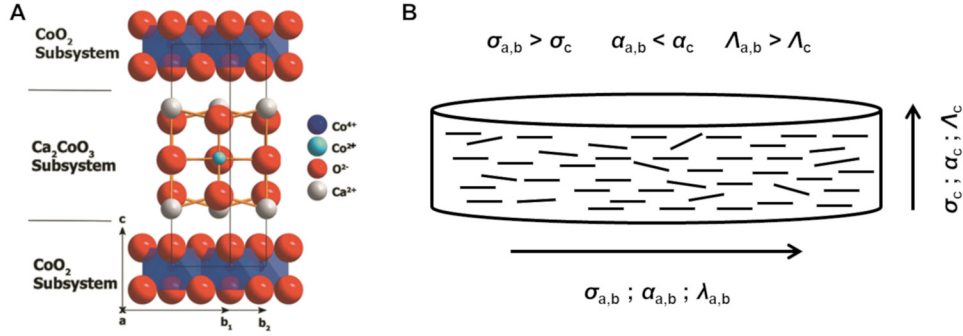
Fig. 1.12: A) Layered crystal structure of $Ca_3Co_4O_9$ (CCO) consisting of CoO_2 and $Ca_3Co_2O_6$ subsystems. Reproduced from [21]. As a result of the layered structure, the sintered ceramics usually show a higher electrical conductivity but at the same time higher thermal conductivity in the a,b-plane compared to the c-direction. In B), this resulting anisotropic behavior of sintered polycrystalline CCO ceramics is shown.

layers separated by a Na layer (for NCO), a rock-salt Ca_2CoO_3 layer (for CCO) or a $Bi_2A_2O_4$ layer (for $Bi_2A_2Co_2O_9$) [22]. The structure of CCO is shown in Figure 1.12A and corresponds to the PGEC concept discussed before, where the CoO_2 layers act as an electron crystal, while the Ca_2CoO_3 layers drastically reduce the thermal conductivity due to their role as phonon glass. As the oxide-based materials exhibit a relatively low power factor and electrical conductivity in combination with a very low thermal conductivity (compare Figure 1.10A and B) they can be categorized as materials for good energy conversion efficiency rather than high electrical power output. This, however, can additionally be tuned by different parameters such as doping and the preparation and sintering process.

Based on the layered crystal structure, CCO grows plate-like particles with a preferred growth in the *a,b*-direction up to 500 nm to several μm with a thickness of 20 to 100 nm up to 1 μm, both strongly depending on the preparation process. CCO can be synthesized in a sol-gel process, where Ca- and Co-precursors are complexed by ethylenediaminetetraacetic acid (EDTA) and calcinated within the process [52], resulting in platelets around 1 to 2 μm in the *a,b*-direction and a thickness of around 50 nm. Besides this, CCO can also be prepared via spray-pyrolysis, resulting in somewhat smaller particles, or via solid-state route for larger platelets [53]. Afterwards, the particles are sintered into a bulk ceramic. Here, different methods have been investigated, including conventional sintering (CS), spark-plasma sintering (SPS) and hot pressing (HP) [22, 54, 55]. A main difference of the sintering techniques is the resulting porosity of the ceramic, which significantly influences the final thermoelectric properties [56].

The layered crystal structure of CCO results in an anisotropic behavior, shown in Figure 1.12B. When CCO particles are sintered into a bulk ceramic, the platelets arrange perpendicular to the pressing direction. Hence, the electrical conductivity based on the CoO_2 layers is significantly larger in the *a,b*-direction, which leads to a higher power factor. However, the thermal conductivity is analogously higher in this direction. This anisotropic behavior results in a problematic characterization process, as all parameters have to be measured in the same direction to gain accurate values for the figure of merit zT.

For further tuning of the thermoelectric properties, various different dopants have

already been investigated, including several alkaline [57] and alkaline-earth metals [58] and heavier atoms such as Sm [59], Tb [60], Cr [61] or Cd [62] as well as co-doping with multiple elements [63]. Additionally, a few approaches to design hybrid materials based on CCO have been reported [21,64,65]. As n-type oxide-based materials, various materials can be utilized, like doped ZnO [66,67], $CaMnO_3$ [68–70] and $SrTiO_3$ [71–73], and have been widely investigated up to now. As the p-type CCO is in the focus of this work, the reader is referred to the review in section 1.2.5 for a detailed description of the n-type oxide based materials.

1.2.4 Metal-based thermoelectric materials

Metals generally show a very high electrical conductivity but simultaneously a very high thermal conductivity. Due to the resulting inferior figure of merit zT for most basic metallic system like elements or simple alloys, these materials have only played a minor role so far. Compared to the formerly discussed materials, metallic thermoelectric materials also show a good chemical and thermal stability and are less toxic and easier to process than tellurides or selenides. As promising metal-based thermoelectric materials, up to now mostly two different intermetallic phases, namely Zintl phases [41] and HH phases [44], are in focus of research. Zintl phases are semiconductors with a small band gap (< 1 eV), resulting in a medium power factor around 5 to 10 μW cm^{-1} K^{-2}. HH compounds XYZ (X,Y = transition metals; Z = main group element) are characterized by a cubic structure and a band gap around 0.5 eV. The resulting power factor around 20 to 50 μW cm^{-1} K^{-2} excels compared to all other materials discussed so far. Both phases consist of multiple elements and a quite complex structure, resulting in reasonable thermal conductivity and therefore a high figure of merit zT of up to 1.6 and 1.5 for Zintl phases and HH phases, respectively. Additionally, SiGe alloys are established high-temperature thermoelectric materials when used in vacuum, e.g., for energy supply of space exploration satellites and rovers. However, the evaluation of metallic materials for thermoelectric application is only based on the comparison of the zT and the resulting energy conversion efficiency of the materials.

As discussed before, the power factor and the resulting power output of a material may have the same significance as the conversion efficiency, especially for high temperature application where power output is more valuable than efficiency. As a result of this consideration, various other metallic materials may be promising for thermoelectric applications. A quite simple alloy, that drew some attention in recent years, is Isotan, a Cu-Ni alloys (55 % Cu, 45 % Ni). Based on Cu, one of the best electrically conducting metals, its electrical conductivity is very high, but, unlike Cu, it also provides a comparatively high Seebeck coefficient around -35 μV K^{-1} at room temperature (increasing up to -80 μV K^{-1} at elevated temperatures) [74]. Due to enhanced phonon scattering and the lower electrical conductivity compared to pure Cu, its resulting thermal conductivity is reasonably low (around 25 W m^{-1} K^{-1} at room temperature) [74]. However, only a few works about investigating and improving the thermoelectric properties of Cu-Ni-based alloys can be found, ranging from altering the material on the nanoscale via inclusion of carbon nano tubes (CNTs) or Al_2O_3 nanoparticles [75, 76] or via nanostructuring [74, 77, 78]. A comparison of the thermoelectric properties of the intermetallic phases, SiGe alloys, Isotan and Ag and Cu is shown in Table 1.1. The resulting figure of merit zT of Isotan is inferior to the established intermetallic phases due to the still pretty high thermal conductivity.

Table 1.1: Thermoelectric properties of various intermetalic phases and metal alloys. While Cu-Ni exhibits an inferior zT value, it has the highest power factor of the displayed materials. Compared to pure Ag or Cu, Cu-Ni also provides a much higher Seebeck coefficient and figure of merit zT

Material	T / K	σ / S cm^{-1}	α / μV K^{-1}	Λ / W m^{-1} K^{-2}	$\sigma\alpha^2$ / μW cm^{-1} K^{-1}	zT
Zintl [79]	700	180	290	0.73	15.1	1.45
HH [80]	1173	800	245	4.2	48	1.45
SiGe [81]	1173	520	245	2.8	31	1.3
Isotan [74]	600	19200	55	33	63	0.105
Ag / Cu	600	30000	7	400	15	0.002

The power factor, however, is comparable or even higher than the values reached by HH materials. Therefore, especially for applications that favor a high power output over the conversion efficiency, the much easier processable and less costly Isotan is an interesting alternative to the complex HH materials. Compared to the pure metals like Ag or Cu, Cu-Ni also exhibits a reasonable high figure of merit zT, reaching up to 0.18 at elevated temperatures [74, 78].

1.2.5 High power factor vs. high zT - A review of thermo-electric materials for high-temperature application

Mario Wolf, Richard Hinterding and Armin Feldhoff

entropy

MDPI

High Power Factor vs. High *zT*—A Review of Thermoelectric Materials for High-Temperature Application

Mario Wolf *, **Richard Hinterding** * and **Armin Feldhoff** *

Institute of Physical Chemistry and Electrochemistry, Leibniz University Hannover, Callinstraße 3A,
D-30167 Hannover, Germany

*   Correspondence: mario.wolf@pci.uni-hannover.de (M.W.); richard.hinterding@pci.uni-hannover.de (R.H.);
    armin.feldhoff@pci.uni-hannover.de (A.F.)

check for updates

Abstract: Energy harvesting with thermoelectric materials has been investigated with increasing attention over recent decades. However, the vast number of various material classes makes it difficult to maintain an overview of the best candidates. Thus, we revitalize Ioffe plots as a useful tool for making the thermoelectric properties of a material obvious and easily comparable. These plots enable us to consider not only the efficiency of the material by the figure of merit *zT* but also the power factor and entropy conductivity as separate parameters. This is especially important for high-temperature applications, where a critical look at the impact of the power factor and thermal conductivity is mandatory. Thus, this review focuses on material classes for high-temperature applications and emphasizes the best candidates within the material classes of oxides, oxyselenides, Zintl phases, half-Heusler compounds, and SiGe alloys. An overall comparison between these material classes with respect to either a high efficiency or a high power output is discussed.

Keywords: thermoelectric materials; energy harvesting; energy materials

1. Introduction

At a time when raw fossil materials are becoming scarcer and the demand for regenerative energies is relentlessly rising, the use of energy harvesting systems has gained an ever-increasing interest [1]. Regardless of whether it is from industrial processes, mechanical processes, or the transportation sector, the amount of wasted energy currently remains enormous. In 2017, the estimated energy consumption in the U.S. was shown to be approximately 67% wasted energy [2]. At this point, energy harvesting comes into play, converting even small amounts of wasted energy in the form of heat, light, vibration, or movement into usable energy [3]. Since most of this wasted energy is in the form of heat, the conversion of thermal energy to electrical energy via thermoelectric generators is an attractive solution. The associated energy conversion is based on the thermoelectric effect, which is the simplest way for direct energy conversion from dissipated heat into electrical energy.

Discovered by T.J. Seebeck in 1821, the first thermoelectric effect (Seebeck effect) describes the direct conversion of thermal energy into electrical energy, which Seebeck demonstrated by thermally inducing an electrical current by heating two different electrical conductors. Together with the Peltier effect (1834), which describes the heating or cooling effect of an electrical current in a thermocouple, and the work of W. Thomson on the thermoelectric effect in homogeneous conductors (Thomson effect), the basis of thermoelectricity was laid [4]. In the first half of the 20th century, the term 'figure of merit' was introduced, and the first theoretical approaches were made in designing a material with a high energy conversion efficiency. In 1957, A.F. Ioffe defined the figure of merit *zT* as a

function of the electrical conductivity, the Seebeck coefficient, and the thermal conductivity of the material [5]. However, thermoelectric energy conversion has been too inefficient for most applications for a long time. Theoretical descriptions of nanostructural engineering and superlattice structures paved the way to significantly improved zT values, which strongly increased research on thermoelectric materials in the mid 1990s [6]. Today, the improvement and development of thermoelectric materials still have the goals of gaining higher efficiencies and power outputs. Within this research field, various materials from wide-ranging material classes, such as metallics and intermetallics [7,8], oxide-based ceramics [9–11], chalcogenide compounds [12], and polymers [13] have been investigated. It is important to compare the efficiencies and resulting power outputs of these materials to draw the correct conclusions when actual generators for applications are manufactured. The purpose of this review is to convey descriptive comparisons, which is realized by two different types of Ioffe plots. These plots allow a direct comparison of the thermoelectric properties of different materials, which is vital for prospective research [14].

1.1. Thermoelectric Parameters

Discussing thermoelectricity requires an understanding of some fundamental parameters, which are briefly described in the following. Thermoelectric energy conversion is based on local coupling of fluxes of charge carriers and entropy. When a thermoelectric material is simultaneously exposed to local gradients of temperature (i.e., ∇T) and an electrochemical potential of charge carriers (i.e., $\nabla \frac{\tilde{\mu}}{q}$) the local flux densities of charge j_q and entropy j_s are given by the following transport equation [15]:

$$\begin{pmatrix} j_q \\ j_s \end{pmatrix} = \begin{pmatrix} \sigma & \sigma \cdot \alpha \\ \sigma \cdot \alpha & \sigma \cdot \alpha^2 + \Lambda \end{pmatrix} \cdot \begin{pmatrix} -\nabla \frac{\tilde{\mu}}{q} \\ -\nabla T \end{pmatrix}. \tag{1}$$

The thermoelectric material tensor, which appears here, is characterized by three material parameters: the isothermal electrical conductivity σ, the Seebeck coefficient α, and the electrically open-circuited entropy conductivity Λ. The latter is linearly related to the traditionally used heat conductivity λ via the absolute temperature T as described in Equation (2) [15–17]. In the context of this review, thermal conductivity is a generic term, that covers both entropy conductivity and heat conductivity. Here, it is advantageous to address the thermal conductivity by the more fundamental entropy conductivity, as we will see when comparing materials.

Considering entropy as a central primitive quantity of equal rank to electric charge comes with the benefit of an easy understanding of the physics of thermoelectricity. A local coupling of the fluxes of these substance-like quantities is described by Equation (1) [15]; this is in contrast to the cumbersome traditional approach, which introduces generalized forces and a kinetic matrix [18] instead of thermodynamic potential gradients and a material tensor. Naturally, for each substance-like quantity, a conductivity is assigned to the material. The material tensor is symmetric by principle, and an elaborate discussion of the reciprocity of Onsager coefficients is superfluous [15]. A further advantage is that the currents of thermal energy (heat) and electrical energy (or electrochemical energy), which accompany the fluxes of entropy and charge, can be treated separately. The entropy and charge fluxes allow us to consider energy conversion and its efficiency in a thermoelectric material apart from the device. When expressed with the entropy conductivity, the figure of merit zT in Equation (2) is purely a material parameter that depends only implicitly on temperature. Moreover, the appearance of two substance-like quantities in Equation (1) to be transported through a thermoelectric material allows for an integration of thermoelectricity into a broad picture of coupled transport processes (e.g., diffusion, viscous flow, entropy conduction and electric conduction) and benefits from analogies. A reader who is interested in more details is referred to the discussion about the properties of heat by Fuchs [19] and the comparative overview by Job and Rüffler [17].

The tensor element M_{22} in Equation (1) directly leads to parameters that describe the performance of a thermoelectric material. The most commonly used parameter is the dimensionless figure of merit zT, which describes the relation of the power factor $\sigma \alpha^2$ and the entropy conductivity Λ in Equation (2).

$$zT = \frac{\sigma \cdot \alpha^2}{\Lambda} = \frac{\sigma \cdot \alpha^2}{\lambda} \cdot T. \tag{2}$$

The figure of merit zT indicates the maximum achievable power conversion efficiency of a thermoelectric material [16]:

$$\eta_{\max} = \frac{\sqrt{1+zT}-1}{\sqrt{1+zT}+1} \cdot \eta_{\text{Carnot}}. \tag{3}$$

In contrast, the power factor $\sigma \alpha^2$ is proportional to the maximum achievable power output of a material and the temperature difference ΔT [20]:

$$P_{\text{el,max}} \propto \sigma \alpha^2 \cdot (\Delta T)^2. \tag{4}$$

For some applications, the power factor may have the same relevance as the efficiency described by the zT value. As shown in Figure 1a, for a thermoelectric material, the optimum efficiency and optimum power output as a function of the carrier density differ, leading to a possible optimization of one parameter for the desired properties or a special application.
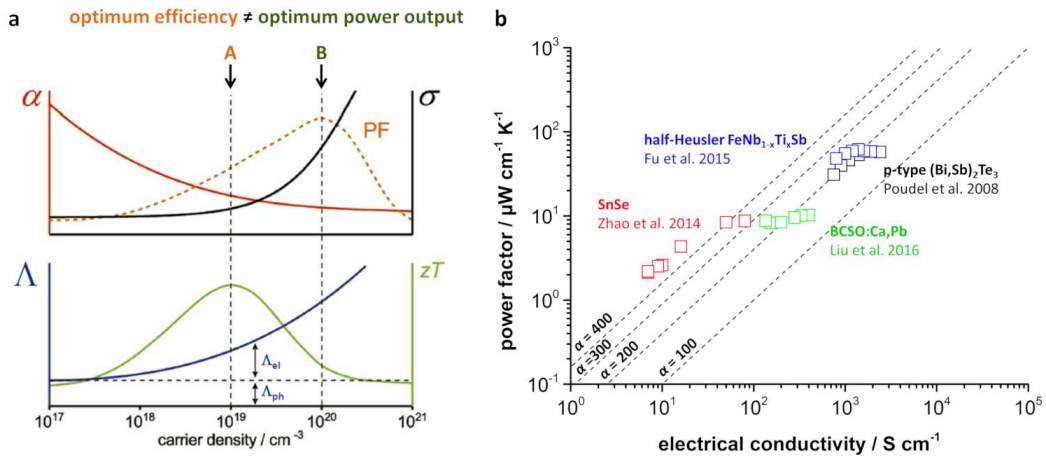

Figure 1. (**a**) Seebeck coefficient α, electrical conductivity σ, entropy conductivity Λ, and the resulting power factor $\sigma \alpha^2$ and zT value as a function of the charge carrier density; adapted from [20] with permission from Elsevier; (**b**) Type-I Ioffe plot of various reported high-zT materials [11,12,21,22]. Seebeck coefficient α is given in $\mu V\ K^{-1}$. Different data points for the same material refer to different temperatures.

Narducci [23] also emphasized that the figure of merit zT may be an inappropriate parameter to rate and compare different materials for some applications. Especially for applications at high temperature, the power factor $\sigma \alpha^2$ could be a better quality criterion. In this review, rather than just comparing the figure of merit zT, we will also look at the power output and the entropy conductivity of different materials by comparing them via Ioffe plots. We distinguish between a type-I Ioffe plot, which considers the power factor $\sigma \alpha^2$ as a function of the electrical conductivity σ, and a type-II Ioffe plot, which considers the entropy conductivity Λ as a function of the electrical conductivity σ. Figure 1b displays a type-I Ioffe plot of various reported materials from different classes with high figure of merit zT values. Although all of the shown materials exhibit exceptionally high zT values in their specific material class, the electrical conductivity σ as well as the power factor vary over several orders

of magnitude. Furthermore, type-II Ioffe plots will be vital for an in-depth comparison of different thermoelectric materials later on. Since the entropy conductivity can be displayed in the same unit and scale as the power factor, the type-II Ioffe plot enables an easy comparison of electrical and thermal properties and observable *zT* values.

1.2. Doping and Band Structure Engineering

A prevailing challenge when facing the improvement of a thermoelectric material is coupling all three relevant material parameters with each other, which can be managed to a certain degree. The most common approach to enhancing the performance of thermoelectric materials is doping, which can have a huge impact on the electrical conductivity, Seebeck coefficient, and thermal conductivity. Several parameters, such as carrier density, mobility, effective mass, and the band structure, are effectively influenced by proper doping.

Figure 1a shows an optimum carrier density for a balanced electrical conductivity and Seebeck coefficient at a given temperature, which varies between an optimum power factor and *zT* value. This means that adjusting the carrier density via doping is highly advised for either high power or high efficiency applications [23]. The dopant may influence the carrier density of a material by introducing defect-enabled mechanisms including point defects [1]. However, the optimum carrier density is temperature-dependent and increases approximately with $T^{3/2}$ [5]. Thus, either further material engineering is required or the carrier density needs to be optimized for a specific temperature range according to the application field.

Generally, the Seebeck coefficient decreases with increasing carrier concentration, as shown in Figure 1, and the electrical conductivity is oppositely coupled. However, the doping-induced convergence of valence or conduction bands to increased valley degeneracy has proven to increase the electrical conductivity while maintaining the Seebeck coefficient [24]. This is explained by the Seebeck coefficient being dominated by the smaller value of several bands. If degeneracy of several bands is achieved, the Seebeck coefficient is stable, but the electrical conductivity substantially rises [24,25]. Therefore, band convergence is an effective way to improve the power factor of a material.

Additionally, doping strongly influences the thermal properties of the material. The thermal conductivity expressed as entropy conductivity Λ was introduced in the tensor element M_{22} in Equation (1). Conventionally, the thermal conductivity is divided into a phonon contribution and an electronic contribution [5]. Influencing the phonon contribution to the thermal conductivity via scattering mechanisms is well investigated and can be divided into size-relevant dimensions. The atomic scale is influenced by single doping or cross substitution, which results in point defects within the crystal lattice. These defects effectively delay the phonon propagation by scattering when the lattice mismatch between the host and the dopant is sufficient and the mass difference as well as the dopant amount are high [26]. The next relevant dimension for scattering phonons is the nanoscale, which leads to so-called nanostructuring [27]. Nanoscaled defects can be introduced in-situ by forcing the precipitation of a second phase [28] or ex-situ by mixing the nanoscaled second phase with a host phase [29]. However, the phonon propagation within the second phase is rather unpredictable, making it difficult to design a proper system. Temperature stability is another issue since elevated temperatures may change the scale of the precipitates and diminish the achieved effect [27]. The main part of the thermal energy is propagated by short- and medium-wavelength phonons, which are effectively hindered by point defects and nanostructuring. The residual long-wavelength phonons can be influenced by defects in the range of a few micrometers or submicrometers, namely, the mesoscale. This effect is typically active for polycrystalline materials with mesoscale grains [30]. Additional phonon scattering may appear at heteromaterial interfaces of composite systems [31]. However, the electronic transport may be reduced by these grains, making a consideration of maximum power output vs. efficiency necessary. If the scattering of the phonons is achieved at all three length scales, the term all-scale hierarchical architecture is used [32]. Only a few studies achieve all-scale phonon scattering,

but when regarding the overall reduction of the phonon contribution to the thermal conductivity, decreases of more than 50% are possible [33].

While the phonon contribution to the thermal conductivity has been widely studied, the electronic contribution is not straightforward. For degenerate semiconductors with charge carriers of the same sign, the commonly used separation into both contributions fits well, and the Wiedemann–Franz relation $\Lambda = L_0 \cdot \sigma$ with the Sommerfeld value of the Lorenz number $L_0 = 2.4453 \cdot 10^{-8}$ W Ω / K^2 [34] can be applied to describe the electronic contribution. However, for nondegenerate semiconductors and especially for materials with charge carriers of both signs, the electronic contribution significantly increases, resulting in a deviation of the Sommerfeld value, as stated by Ioffe [5]. Thus, the relationship may lead to questionable results when applied to all kinds of thermoelectric materials and must be considered carefully. As a result, doping may have a nonnegligible influence on the electronic contribution to the thermal conductivity.

1.3. Thermoelectric Materials for High-Temperature Applications

As state-of-the-art materials for thermoelectric power conversion, bismuth telluride (Bi_2Te_3) and lead chalogenide PbX (X = S, Se or Te) compounds long exhibited the highest *zT* near room temperature and approximately 600 to 700 K, respectively [35]. However, due to the toxicity of telluride and lead, investigations into less toxic alternatives have attracted strong attention in recent years. Several promising materials or material classes have been reported since and have been discussed in detailed reviews, e.g., copper and tin chalcogenides [35], oxide-based materials [9,36], intermetallic compounds [8,37], and organic polymers [13,38]. Since each material typically has an optimum temperature range for its most efficient thermoelectric power conversion, the materials do not necessarily compete but complement each other with respect to a specific application. Figure 2 shows the *zT* values of several different thermoelectric material classes as a function of temperature. There are multiple promising alternatives for commercially used bismuth telluride at high operating temperatures.
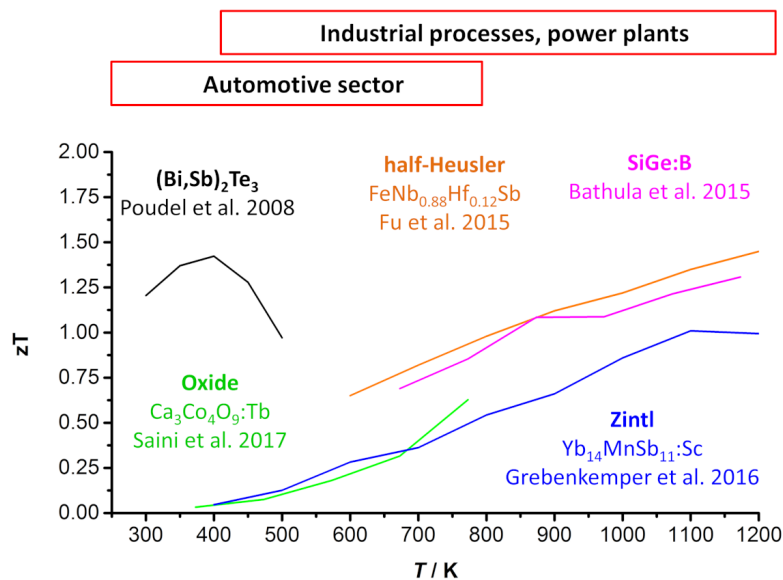

Figure 2. *zT* values as a function of temperature for several thermoelectric material classes [21,22,39–41]. While bismuth telluride shows the highest *zT* value at low temperatures, different kinds of materials are interesting for high-temperature applications.

In this review, we take a closer look at these promising materials for high-temperature applications (>700 K), e.g., power plants, industrial processes, and the automobile industry [20,42]. Therefore, oxide-based materials and several intermetallic compounds such as Zintl phases and half-Heusler compounds will be discussed and compared in terms of the power factor and the figure of merit zT. In this context, the focus is on the thermoelectric properties at the material level. Please note that the utilization of thermoelectric materials in a device comes alongside additional important tasks such as contact resistivity and the variation in thermoelectric properties in an applied temperature gradient. It has been emphasized that for a thermoelectric device, the average properties, such as the average zT, within the respective temperature range are the key parameters instead of the peak properties [43–45]. As mentioned, within this review, the discussed thermoelectric compounds will only be evaluated at their respective material level.

2. Oxides and Oxyselenides

2.1. Thermoelectric Oxides

Oxide-based thermoelectric materials generally exhibit an inferior zT compared to that of telluride and selenide compounds, but show a much higher chemical and thermal stability, thus allowing high operating temperatures and large temperature gradients [46]. Consequently, such materials are very promising for high-temperature applications in areas such as the automobile sector or industrial furnaces. Additionally, raw materials of such oxide-based ceramics are less toxic than other materials and therefore easier to process. The first works that predicted good thermoelectric properties in layered crystal structures [47] and the first report of Na_xCoO_2 [48] were published in the mid 1990s. Later, manganites and cobaltites, which show strong spin and orbital fluctuations in the d-electron system and a strong Jahn–Teller effect, became the focus of research [9]. Today, oxide-based thermoelectric materials represent a group of materials with good chemical and temperature stability. In general, oxide-based thermoelectric materials exhibit high Seebeck coefficients, but only a medium electrical conductivity and moderate thermal conductivity. By adjusting these parameters via nanostructuring, doping, and defect engineering, these materials can be tuned to reach high zT values up to 1. In this context, we will have a close look at p-type layered cobaltites (Na_xCoO_2, $Ca_3Co_4O_9$, $Bi_2Ca_2Co_2O_9$) and the most common n-type oxide-based materials (ZnO, $CaMnO_3$, $SrTiO_3$). As already mentioned, the focus of this work is on a comparison and evaluation of the power factor and the figure of merit zT. For a more detailed discussion of the physical properties of thermoelectric oxides, e.g., for oxide-based materials [9,36,49] or $BiCuSeO$ [49–51], the reader is referred to other review articles.

2.1.1. p-Type Layered Cobaltites

Since the discovery of Na_xCoO_2, several layered cobaltite compounds with analogous structures have been found. In addition to Na_xCoO_2, two other promising compounds, namely, $Ca_3Co_4O_9$ and $Bi_2A_2Co_2O_9$ (A = alkaline-earth metal), will be discussed. Figure 3 shows the crystal structures of these compounds. Na_xCoO_2 consists of a hexagonal-layered structure with CoO_2 sheets separated by disordered Na layers. In $Ca_3Co_4O_9$ and $Bi_2A_2Co_2O_9$ (A = alkaline-earth metal), the Na layer is replaced by Ca_2CoO_3 or $Bi_2A_2O_4$ substructures, respectively. In these structures, the CoO_2 sheets represent an electron-conducting layer, which is described as an 'electron crystal', while the salt-like separating layers work as a 'phonon glass' and reduce the thermal conductivity of the material, resulting in a high zT [1,46].

The thermoelectric parameters of these layered cobaltites are strongly influenced by the exact stoichiometry of the compound. In Na_xCoO_2, the amount of Na in the disordered phonon glass layer influences the phonon scattering and the electronic properties [52,53]. In $Bi_2A_2Co_2O_9$ (A = alkaline-earth metal), the thermoelectric properties can be influenced by the amount of Co [54]. The most investigated compounds of $Bi_2A_2Co_2O_9$ have A = Ca or Sr [55]. The practical use of

Na_xCoO_2 and $Bi_2A_2Co_2O_9$ is limited by the volatility of Na and Bi at high temperatures and the hygroscopicity of the compounds. Therefore, $Ca_3Co_4O_9$ represents the most interesting layered cobaltite for thermoelectric applications, especially at high operating temperatures. Due to its structure, which consists of electron conducting layers separated by nonconducting layers that cause phonon scattering, the thermoelectric properties of $Ca_3Co_4O_9$ are highly anisotropic. The in-plane direction is characterized by a high electrical conductivity within the CoO_2 layers, resulting in a high power factor $\sigma\alpha^2$. However, in the out-of-plane direction, the phonon scattering is very high, resulting in an even lower thermal conductivity.
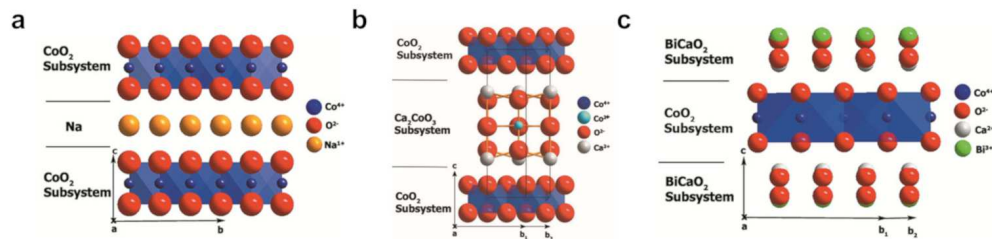

Figure 3. Crystal structures of (**a**) Na_xCoO_2, (**b**) $Ca_3Co_4O_9$ (CCO) and (**c**) $Bi_2Ca_2Co_2O_9$. Adapted from [10] with permission from Elsevier.

In general, the thermoelectric properties of bulk $Ca_3Co_4O_9$ can be strongly influenced by the parameters of the synthesis and the sintering method, which have a strong influence on the resulting density, grain size, and orientation of the material [56]. $Ca_3Co_4O_9$ can be synthesized via a solid-state mechanism or a sol-gel procedure. Krolicka et al. investigated the effect of these techniques on the structural and thermoelectric properties, and showed increased zT values in the sample prepared by the sol-gel route due to improved grain alignment [57]. The corresponding ceramics can be prepared by different sintering methods, such as spark plasma sintering (SPS) or pressureless sintering methods, all again leading to different grades of grain orientation and densification [56,58–60]. Bittner et al. showed that the porosity of a bulk $Ca_3Co_4O_9$ ceramic strongly influences the resulting thermoelectric parameters [61]. A high porosity leads to a reduced electrical conductivity and simultaneously decreased thermal conductivity, thus improving the figure of merit zT. Therefore, the porosity as well as the synthesis method is one way to tune such oxide-based materials for an increased power factor (dense ceramic) or zT (high porosity).

As mentioned before, doping and nanostructuring are common ways to tune the thermoelectric parameters of thermoelectric materials. Table 1 shows the figure of merit zT and the power factor $\sigma\alpha^2$ of several doped $Ca_3Co_4O_9$, Na_xCoO_2 and $Bi_2Ca_2Co_2O_9$ compounds. Here, Na_xCoO_2 exhibits the highest power factor, while $Ca_3Co_4O_9$ is the most promising layered cobaltite when high efficiency and therefore high zT is desired. A nanocomposite containing all three layered cobaltites discussed here is also included, showing promising synergistic effects in its thermoelectric properties as well as its thermal stability [10].

Overall, the thermoelectric properties of layered cobaltites, and all oxide-based materials in general, strongly depend on many parameters, such as the synthesis route, morphology of the crystals, doping, nanostructuring, texturing, and densification into a bulk material, thus leading to a possible control of tuning oxide-based thermoelectric materials to a high power factor $\sigma\alpha^2$ or a high zT value for different application fields. However, more research on the enhancement of the power factor is required to increase the potential of these materials for high-temperature applications.

Table 1. Dimensionless figure of merit zT and power factor $\sigma\alpha^2$ of p-type $Ca_3Co_4O_9$, Na_xCoO_2 and $Bi_2Ca_2Co_2O_9$ with different dopants.

Material	Dopant	T/K	zT	$\sigma\alpha^2/\mu W\ cm^{-1}\ K^{-2}$
$Ca_3Co_4O_9$	Cr [62]	1000 K	0.16	3.5
	Sm [63]	1000 K	0.15	2.4
	Tb [39]	1000 K	0.73	11.5
	K [64]	1000 K	0.22	2.85
	Cd [65]	1000 K	0.35	5.25
	Sr [66]	1000 K	0.22	3.95
	Na,W codopants [67]	1000 K	0.21	2.7
	La,Fe codopants [68]	1000 K	0.32	4.15
	NCO,BCCO nanocomposite [10]	1100 K	0.34	6.08
Na_xCoO_2	Ag,Au [69]	1000 K	0.4–0.5	13–15
	Ni [70]	1073 K	-	10.8
	Cu [71]	1000 K	-	15.5
	K, Sr, Y, Nd, Sm, Yb [72]	1000 K	0.36–0.5	6.8–7.3
$Bi_2Ca_2Co_2O_9$	Na [73]	900 K	-	2.1
	K [74]	1000 K	0.305	1.92
	Pb,La [75]	1000 K	-	1.6–2.2

2.1.2. *n*-Type Oxides

Around the same time as the first layered cobaltite compounds, other transition metal oxides were reported to have promising thermoelectric properties. Since then, the most studied oxide-based *n*-type materials have been the aforementioned ZnO, as well as $SrTiO_3$ and $CaMnO_3$. ZnO exhibits a hexagonal wurtzite structure with a large direct band gap of 3.44 eV [76], $SrTiO_3$ has a cubic perovskite structure and is also characterized by a large band gap of 3.25 eV [77] and $CaMnO_3$ crystallizes in an orthorhombic perovskite structure with an indirect band gap of 0.7 eV [78]. All these materials are characterized by a high Seebeck coefficient and a very low electrical conductivity due to a low carrier concentration without doping [9].

Based on the large band gap of undoped ZnO, increasing the carrier density by doping and defect engineering is used to ensure good thermoelectric properties. For ZnO, doping with Al has been widely studied and shows the highest zT values from 0.3 to 0.45 with moderate power factor values of approximately 5–8 $\mu W\ cm^{-1}\ K^{-2}$ thus far [79–81]. Again, the synthesis parameters as well as the morphology of the crystals strongly influence the resulting thermoelectric parameters. Han et al. reported, that the zT value of ZnO with nanoparticle morphology is 1.5 times higher than that of a platelet-shaped morphology [82]. In addition to doping, defect engineering is another promising way to enhance the thermoelectric properties, as shown by Tian et al.; by increasing the Al solubility and therefore the carrier concentration and electrical conductivity, the thermal conductivity decreases due to introduced defects [83]. Undoped $SrTiO_3$ also has a very large band gap, making it electrically insulating. However, by electron doping with group III elements (mostly lanthanides) on the Sr sites or group V elements (Nb, Ta) on the Ti sites, a strong increase in carrier density (up to approximately 10^{20} cm^{-3}) and electrical conductivity (up to 50–1000 S cm^{-1}) in single crystals can be observed [84]. In addition to doping and codoping with several lanthanides, the influences of Sr vacancies have been investigated and were reported to have a positive effect on thermoelectric properties [85,86]. Similarly to $SrTiO_3$, $CaMnO_3$ exhibits a high Seebeck coefficient but an electrically insulating character before doping. Here, rare-earth metals as dopants for the Ca sites as well as transition metals for the Ti sites have been investigated. $CaMnO_3$ and $SrTiO_3$ have perovskite structures with octahedral coordination of Mn and Ti, respectively. The symmetry of the MnO_6 and TiO_6 octahedrons also influences the resulting parameters. A distortion of the octahedron, e.g., that due to a Jahn–Teller distortion as a result of a partial reduction of Mn^{4+} to Mn^{3+} or due to doping with smaller or larger elements, influences the electrical and thermal conductivity of the material [9].

Additionally, *n*-type In_2O_3 was investigated as a promising oxide-based thermoelectric material [20,87]. Undoped In_2O_3 is a semiconductor with a band gap of 1.2 eV that can be strongly influenced via doping. The crystal structure can be described as a cubic bixbyite structure with two nonequivalent cation sites that can be substituted with different dopants [88]. The electron effective mass as well as the carrier concentration of this material strongly depend on the amount of doping within the structure. As a result, a very high carrier mobility can be achieved, making tuning the thermoelectric properties very promising [89]. Bittner et al. [20] presented Sn,Al-doped *n*-type In_2O_3, which reached a comparatively high power factor of 7.1 µW cm^{-1} K^{-2} at 1200 K. However, doped In_2O_3 suffers from its high thermal conductivity and thus shows a noteworthy *zT* only above 1000 K at this time. Nevertheless, doped In_2O_3 represents an interesting *n*-type thermoelectric material for high-temperature applications due to the high power factor resulting from high electrical conductivity.

Table 2 shows the figure of merit *zT* and the power factor $\sigma\alpha^2$ of several doped ZnO, $SrTiO_3$, $CaMnO_3$, and In_2O_3 bulk compounds. As described before, the thermoelectric properties also strongly depend on the synthesis method and the sintering parameters. Here, $SrTiO_3$ compounds exhibit the highest power factor, while the other materials reach *zT* values of approximately 0.3–0.4, except for doped In_2O_3, which only reaches a *zT* value of 0.15.

Table 2. Figure of merit *zT* and power factor $\sigma\alpha^2$ of *n*-type ZnO, $SrTiO_3$, $CaMnO_3$, and In_2O_3 with different dopants.

Material	Dopant	*T*/K	*zT*	$\sigma\alpha^2$/µW cm^{-1} K^{-2}
ZnO	Al [79–81]	1073	0.3–0.45	5–8
	Ni [90]	1073	0.09	5.8
	Al,Ni codopants [91]	773	0.06	5.6
	Ga [92]	973	0.25	12
$SrTiO_3$	La,Nb,Sm,Gd,Dy [93]	1073	0.2–0.28	5.5–9
	La [94]	973	0.365	11.6
	Gd [95]	1023	0.37	10.9
	Nb [96]	1023	0.39	11.3
	Nb,Nd codopants [97]	1073	0.315	8.8
$CaMnO_3$	Nb [98]	1073	0.325	1.9
	Dy,Ho,Er,Yb [99]	1000	0.15–0.2	2–3.5
	W [100]	1073	0.16	3.2
	Y,Dy codopants [101]	800	0.18	3.1
	Pr,Yb codopants [102]	973	0.24	3.3
In_2O_3	Sn,Al [20]	1200	0.08	7.1
	Ge,Mn,Zn [20]	1200	0.15	3.6

2.2. BiCuSeO

Doped BiCuSeO is one of the newest and most promising thermoelectric materials. The first works presenting the thermoelectric properties of this compound were published from 2010 to 2012 [103–105]. BiCuSeO is one of several isostructural RMChO (R = Bi, Ce to Dy; M = Cu or Ag; Ch = S, Se or Te) compounds and exhibits a two-dimensional layered structure with Bi_2O_2 and Cu_2Se_2 layers, as shown in Figure 4a–d [50]. Due to this layered structure, BiCuSeO also shows anisotropic thermoelectric properties, which strongly depend on the synthesis method and the sintering parameters, analogous to the layered cobaltite compounds [50,106,107]. Due to the similar behavior between BiCuSeO and the oxide-based cobaltites, the former material is discussed here, although it is an oxyselenide and not an oxide material. BiCuSeO can be synthesized via hydrothermal methods, solid state reactions, sol-gel methods, or mechanical alloying. The bulk materials are again prepared via cold-pressing, hot-pressing, or SPS [50,51,108–110]. The electrical conductivity of undoped BiCuSeO is relatively low because of a low carrier concentration and carrier mobility, while the material exhibits an exceptionally high Seebeck coefficient of approximately 450 µV K^{-1} and a very low thermal conductivity of approximately

0.4 W m^{-1} K^{-1} [50,111]. Based on this, BiCuSeO can be described as a high-zT material but offers a relatively low power factor $\sigma\alpha^2$ comparable to those of the layered cobaltites. Although a very high $zT > 1$ can be reached. Additionally, BiCuSeO struggles with thermal stability in an air atmosphere showing surface oxidation at 573 K and complete decomposition at 773 K [112].
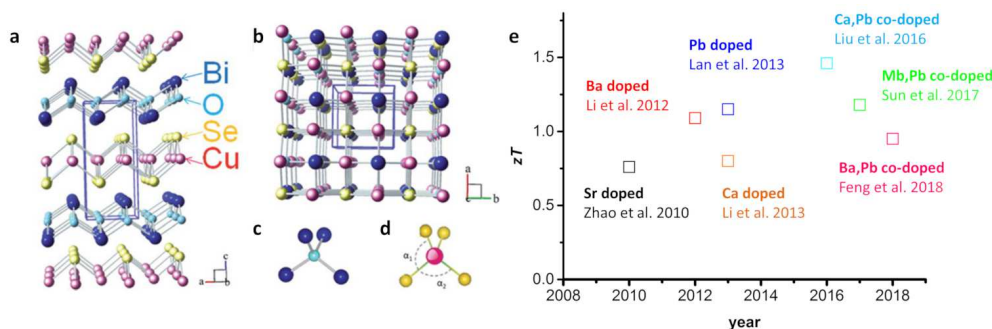

Figure 4. Crystal structure of BiCuSeO (**a**) along the b-axis and (**b**) along the c-axis; (**c**) Bi$_4$O coordination tetrahedra, and (**d**) CuSe$_4$ coordination tetrahedra. Reproduced from [50] with permission from The Royal Society of Chemistry; (**e**) zT values of various doped bulk BiCuSeO materials under an inert gas atmosphere [11,103,105,113–116].

To improve the thermoelectric properties of BiCuSeO, adjusting the electrical conductivity by enhancing the carrier concentration via doping has been extensively studied. For this purpose, element doping with divalent cations at Bi sites to enhance the *p*-type electron conduction is very promising. Here, doping and codoping with various elements have been investigated. Figure 4e shows the reported peak zT of various doped BiCuSeO materials in recent years.

BiCuSeO is an intrinsic *p*-type semiconductor due to Bi and Cu vacancies. Recently, Pan et al. realized *n*-type BiCuSeO by iron incorporation [117] and Zhang et al. [118] presented the realization of *n*-type BiCuSeO by filling these vacancies with additional Bi and Cu and simultaneously introducing Br and I at the Se site for electron doping; the above resulted with Seebeck coefficients of up to −550 µV K^{-1}.

2.3. Comparison of Oxides and Oxyselenides

Overall, the discussed oxide-based thermoelectric materials exhibit good zT values of approximately 0.2–0.8 with the oxyselenide compound BiCuSeO reaching zT values >1, while generally showing a medium power factor of 1–11 µW cm^{-1} K^{-2}. Preparation parameters, doping, defect engineering, and nanostructuring can be utilized to tune the material behavior, thus enhancing the power factor or decreasing the thermal conductivity to reach higher zT values. Figure 5 shows the type-I and type-II Ioffe plots and zT plots for several of the doped *p*- and *n*-type oxide-based bulk materials and oxyselenides. Here, it can be easily seen that doped BiCuSeO and doped SrTiO$_3$ exhibit the highest power factor in relation to electrical conductivity and are therefore the closest to the desired area. In comparison, Figure 5b displays the related zT values of the materials, where the BiCuSeO and Ca$_3$Co$_4$O$_9$ reach the highest zT values. However, the BiCuSeO is not stable in an air atmosphere, as mentioned before. As oxide-based materials are of special interest for high-temperature applications, enhancement of the power factor and thus increasing the resulting power output must be further investigated.
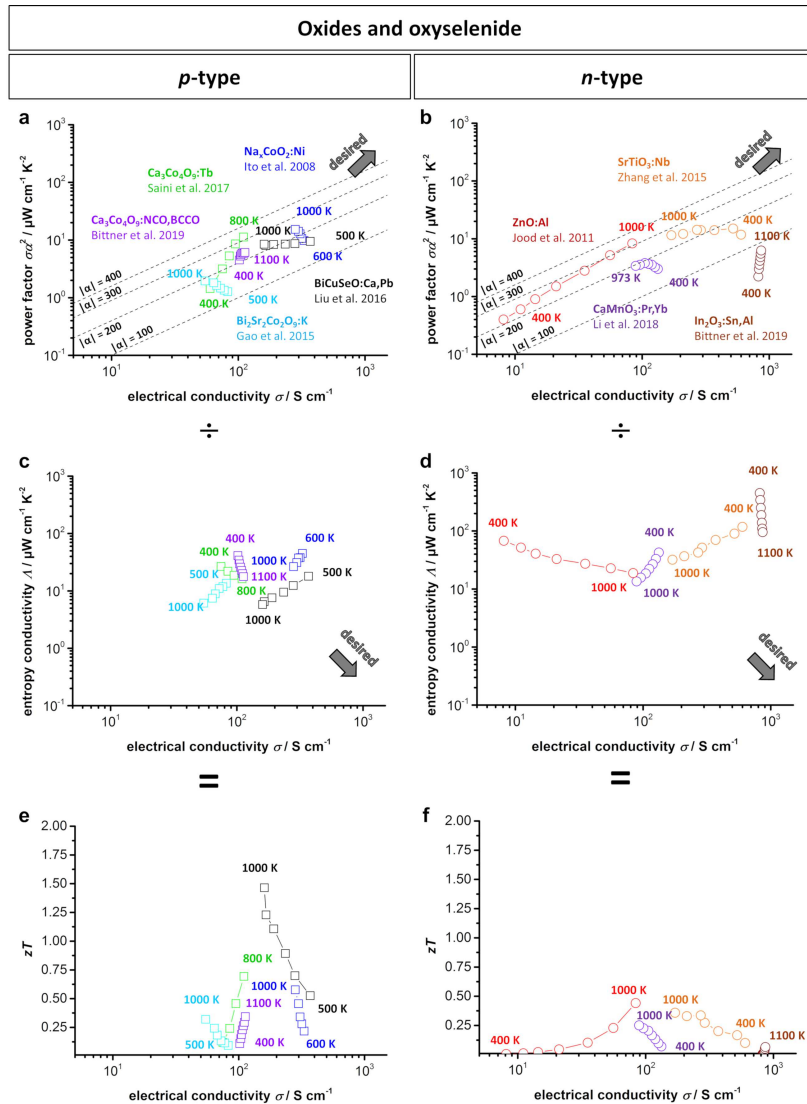
Figure 5. (**a**) *p*-Type; (**b**) *n*-type type-I Ioffe plots; (**c**) *p*-type; (**d**) *n*-type type-II Ioffe plots and (**e**) *p*-type and (**f**) *n*-type *zT*-electrical conductivity plots for several doped oxidic thermoelectric materials and BiCuSeO [10,11,39,69,74,80,96,102]. Dashed lines show the corresponding absolute values of the Seebeck coefficient α given in µV K^{-1}. In the type-I Ioffe plot, a desired material would be located at a high power factor and simultaneously high electrical conductivity in the top right. In the type-II Ioffe plot, a desired material would be located at a low entropy conductivity and simultaneously high electrical conductivity in the bottom right. Note that the data in Ioffe plots of type-I and type-II can be divided by each other according to Equation (2) to give the dimensionless figure of merit *zT* as a function of the electrical conductivity.

3. Metals and Intermetallics

3.1. Zintl Phases

Zintl phases are high-melting intermetallic compounds that are characterized by an ionic structure containing covalently bonded polyanions that build an 'electron crystal', while the cation layers act as a 'phonon glass'. Although this form of intermetallics was discovered in the 1930s and has been highly

investigated since, the first reports about their good thermoelectric properties were not published until 2005 [119]. The thermoelectric properties of many different Zintl families and structures have been investigated. The general composition of a Zintl phase can be described as A_aBX_x with A = active, electropositive metal (mostly alkaline and earth alkaline metals); X = noble, electronegative metal from group 13, 14 and 15, and B = ternary transition metal (Zn, Cd, Mn). Based on this, different groups of Zintl phases can be named after their stoichiometry, e.g., 14-1-11 compounds such as $Yb_{14}MnSb_{11}$. In Figure 6 the *T*-dependent *zT* values of several *p*- and *n*-type Zintl groups can be seen. The investigated Zintl compounds exhibit varying *zT* values between 0.5 and 1.5. Due to their complex structure, Zintl phases are usually characterized by a very low glass-like thermal conductivity. The electronic structure strongly depends on the respective material, varying between extremely low carrier mobility and high carrier concentration in 0D 14-1-11 compounds, and very high carrier mobility and low carrier concentration in 2D 1-2-2 compounds [8]. In this section, several *p*-type (14-1-11, 5-2-6, 9-4.5-9, and 1-2-2) and the most recently investigated *n*-type 1-2-2 Zintl compounds will be discussed. Again, the reader is referred to other review articles for more details on the respective physical properties of Zintl phases [8,49,120].
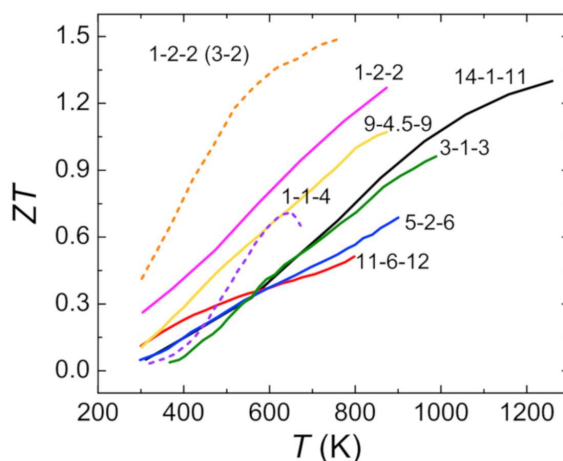

Figure 6. Temperature-dependent *zT*-values of Zintl phases with different stoichiometries. Solid lines represent *p*-type Zintl phases and dashed lines represent *n*-type Zintl phases. Different Zintl families are named after their respective stoichiometry (see also Table 3). Reused from [8] with permission from Elsevier.

3.1.1. *p*-Type Zintl Phases

Currently, the best *p*-type Zintl family are the 14-1-11 compounds, reaching a *zT* > 1 at an operating temperature of up to 1200 K. These 14-1-11 compounds with the general formula $A_{14}MPn_{11}$ (A = alkaline-earth or rare earth element, M = Al, Mn, Zn, Ga, Nb, In or Cd and Pn = group 15 element) exhibit covalently bonded $[MPn_4]^{9-}$ tetrahedra and $[Pn_3]^{7-}$ linear components with Pn^{3-} and A^{2+} ions [121]. Due to their large unit cell and semiconductor nature with low electrical resistivity and low thermal conductivity, these compounds are very promising candidates for achieving good thermoelectric properties via doping. Within this family, $Yb_{14}MnSb_{11}$ showed the highest *zT* values of up to 1.3 [122]. Compared to its isostructural analog $Yb_{14}AlSb_{11}$, which was the first reported 14-1-11 Zintl compound, $Yb_{14}MnSb_{11}$ has the Al^{3+} replaced by Mn^{2+} resulting in *p*-type conduction. To optimize the extremely high carrier concentration of approximately 10^{21} cm^{-3}, several different dopants at various sites have been investigated, e.g., La, Ca, Sc and Y at the Yb site [41,123,124] or Al and Mg at the Mn site [122]. Several doped 14-1-11 Zintl compounds are shown in Table 3. The resulting power factor is approximately 5–10 µW cm^{-1} K^{-2} and therefore, slightly higher than

that of oxide-based materials. $Yb_{14}MnSb_{11}$ is usually prepared by a Sn-flux method or ball milling and densification via hot pressing or SPS sintering.

The 11-6-12 compounds are somewhat newly investigated thermoelectric materials. In 2014, the first work on the thermoelectric properties of *p*-type $Eu_{11}Cd_6Sb_{12}$ was published [125]. The 11-6-12 compounds exhibiting a $Sr_{11}Cd_6Sb_{12}$ structure type consist of $[Cd_6Sb_{12}]^{22-}$ ribbons forming a 1D structure filled with Sr^{2+} cations [126] and are mostly prepared by the Sn-flux method. Due to the infinite 1D structure of polyanions, these compounds feature comparatively high thermal conductivity. For Zn-doped $Sr_{11}Cd_6Sb_{12}$ a *zT* of 0.5 with a power factor of 5.6 µW cm^{-1} K^{-2} could be achieved [127]. The rather low power factor in 11-6-12 compounds is mainly due to the low carrier mobility of approximately 20–30 cm^2 V^{-1} s^{-1} [127]. However, investigations of thermoelectric 11-6-12 have only started, and further optimization and tuning are still the focus of research. Similarly, the thermoelectric properties of 5-2-6 Zintl compounds were also recently reported. It can be described by the general formula $A_5M_2Pn_6$ with A = alkaline earth or rare earth metal, M = trivalent metal and Pn = As, Sb or Bi. The 5-2-6 compounds are mainly produced via ball milling and hot pressing. Within this family, the two basic structure types are $Ca_5Ga_2As_6$ and $Ca_5Al_2Bi_6$, which both consist of infinite $[M_2Pn_6]^{10-}$ chains and A^{2+} cations [128]. A peak *zT* of 0.7 with a power factor of 6.5 µW cm^{-1} K^{-2} can be reached in Zn-doped $Ga_5In_2Sb_6$ [129]. Several other doped materials of the 11-6-12 and 5-2-6 families are shown in Table 3.

The 9-4+x-9 Zintl compounds with a general formula of $A_9M_{4+x}Pn_9$ where A = Ca, Sr, Eu, or Yb, M = transition metal and Pn = Bi or Sb also consist of infinite ribbons of $[M_4Pn_9]^{19-}$ components and exhibit partially filled interstitial sites filled with transition metal [130]. Therefore, the thermoelectric properties can be influenced by occupancy of the interstitial sites and by the exact stoichiometry [131]. To date, several doped and undoped compounds in this family have been investigated, including $Yb_9Mn_{4+x}Sb_9$ [132], $Eu_9Cd_{4+x}Sb_9$ [133], and $Ca_9Zn_{4+x}Sb_9$ [131], reaching *zT* values of approximately 0.7 and a power factor of 5–7 µW cm^{-1} K^{-2} (compare Table 3). Here, again the Sn-flux technique as well as a combination of ball milling and hot pressing or SPS were utilized for preparation.

Table 3. Dimensionless figure of merit *zT* and power factor $\sigma\alpha^2$ of several *p*-type Zintl phases with different dopants.

Composition	Materials	Dopant	*T*/K	*zT*	$\sigma\alpha^2$/µW cm^{-1} K^{-2}
	$Yb_{14}MnSb_{11}$ [121]	-	1200 K	1.02	6.1
		Al [122]	1200 K	1.28	8.82
14-1-11		Sc [41]	1200 K	1.02	8.38
		Y [41]	1200 K	1.01	6.85
	$Yb_{14}MgSb_{11}$ [134]	-	1200 K	1.03	6.5
	$Sr_{14}MgBi_{11}$ [135]	-	1200 K	0.71	9.5
11-6-12	$Eu_{11}Cd_6Sb_{12}$	Zn [127]	800 K	0.51	5.55
		As [125]	800 K	0.185	1.69
	$Ca_5Al_2Sb_6$	Na [136]	1050 K	0.605	4.44
		Zn [137]	800 K	0.4	3.75
		Mn [138]	850 K	0.42	4.12
5-2-6	$Ga_5In_2Sb_6$	Zn [129]	950 K	0.72	6.56
	$Eu_5In_2Sb_6$	Zn [139]	800 K	0.28	4.08
		Cd [140]	850 K	0.46	5.2
	$Sr_5In_2Sb_6$	Zn [141]	800 K	0.36	4.13
9-4+x-9	$Yb_9Mn_{4.2}Sb_9$ [132]	-	1000 K	0.74	4.53
	$Ca_9Zn_{4+x}Sb_9$	Cu [131]	850 K	0.71	6.72
	$CaZn_2Sb_2$	Na,Mg [142]	800 K	0.85	9.24
	$EuZn_2Sb_2$	Cd [143]	650 K	1.05	22.5
	$YbCd_2Sb_2$	Mn [144]	650 K	1.13	10
		Zn [145]	700 K	1.22	19.2
1-2-2		Mg [146]	650 K	1.06	16.8
	$CaMg_2Bi_2$	Na [147]	850 K	0.88	12.3
		Yb [148]	850 K	0.96	12.2
	$Eu_{0.5-x}Yb_{0.5-x}Mg_2Bi_2$	Ca [149]	850 K	1.26	13.5
	Mg_3Sb_2	Na [150]	750 K	0.58	4.2

Next, to the 14-1-11 compounds, the family of 1-2-2 Zintl phases show very good thermoelectric properties, reaching a $zT > 1$. This group can be described as AB_2X_2 with A = Ca, Ba, Sr, Yb or Eu, B = Mn, Zn, Cd or Mg and X = As, Sb or Bi. The $CaAl_2Si_2$-type structure contains two-dimensional $[B_2X_2]^{2-}$ sheets separated by A^{2+} cations [151]. Most *p*-type 1-2-2 Zintl phases are characterized by an extremely high *p*-type carrier concentration due to the vacancies on the A cation sites. Thus, substitution and doping at this site proves to be promising for tuning the thermoelectric properties. Subsequently, doped $EuZn_2Sb_2$ [143] and doped $YbCd_2Sb_2$ [144–146] reached zT values above $zT = 1$. Shuai et al. reported a zT value of 1.3 and a power factor of 13.5 µW cm^{-1} K^{-2} for $Eu_{0.5-x}Yb_{0.5-x}Mg_2Bi_2$ [149]. Additionally, binary *p*-type 1-2-2 compounds with A=B, e.g., Mg_3Sb_2, have been widely investigated [150,152]. However, due to their high resistivity, only a moderate zT at high temperatures can be reached. The thermoelectric properties of several ternary and binary 1-2-2 Zintl compounds are shown in Table 3. Similar to that of the other families, the 1-2-2 Zintl compounds are mostly prepared by melting or ball milling and densification via hot pressing or SPS.

3.1.2. *n*-Type Zintl Phases

As described above, several *p*-type 1-2-2 compounds have been investigated resulting in zT values of up to 1.3. In this group, the stoichiometric Mg_3Sb_2 has taken a special role in research, due to its characteristically low carrier concentration, which opens a pathway to thermoelectric *n*-type Zintl phases [8]. Since the first report, in 2014, of *n*-type conduction in Mn-doped Mg_3Sb_2 [153], many different dopants have been investigated. Doping with Te as an electron donor and Bi to reduce the lattice thermal conductivity proved to be an effective way to realize high zT values in *n*-type Zintl phases. Most recently, Chen et al. [154] reached a zT value of 1.7 at a power factor of 20 µW cm^{-1} K^{-2} by combining Mn doping at the Mg site and Te and Bi doping at the Sb site. Table 4 gives an overview of several doped *n*-type Zintl phases based on Mg_3Sb_2. To date, zT values of approximately 1.5–1.7 and a power factor of up to 20 µW cm^{-1} K^{-2} have been reached.

Table 4. Dimensionless figure of merit zT and power factor $\sigma\alpha^2$ of several *n*-type Zintl phases with different dopants.

Basis	Material	T/K	zT	$\sigma\alpha^2$/µW cm^{-1} K^{-2}
	$Mg_{3+\delta}Sb_{1.99}Te_{0.01}$ [155]	700 K	0.61	9.16
	$Mg_{3+\delta}Sb_{1.48}Bi_{0.48}Te_{0.04}$ [156]	700 K	1.59	12.56
Mg_3Sb_2	$Mg_{3+\delta}Sb_{1.48}Bi_{0.49}Te_{0.01}$ [157]	700 K	1.45	15.14
	$Mg_{3+\delta}Nb_{0.15}Sb_{1.5}Bi_{0.49}Te_{0.01}$ [158]	700 K	1.52	18.5
	$Mg_{3+\delta}Mn_{0.025}Sb_{1.5}Bi_{0.49}Te_{0.01}$ [154]	700 K	1.71	20.02

3.1.3. Comparison of Zintl phases

Figure 7 shows the type-I and type-II Ioffe plots and zT plots from several of the doped *p*-type and *n*-type bulk Zintl materials. As described above, within the *p*-type Zintl phases, the 14-1-11 compounds show the best temperature stability up to 1200 K and reach the highest zT values. However, the Ioffe plots show that ternary 1-2-2 compounds and the 9-4+x-9 compounds feature a comparable or even higher power factor than 14-1-11 compounds at lower temperatures. Improvement of temperature stability could therefore lead to even higher power outputs at high operating temperatures. Within the *n*-type 1-2-2 Zintl phases, heavily doped $Mg_{3+\delta}Sb_2$ exhibits the highest zT reported for Zintl phases thus far and a high power factor of approximately 20 µW cm^{-1} K^{-2}. However, the operating temperature is limited to approximately 700 K for the heavily doped $Mg_{3+\delta}Sb_2$ and up to 1000 K for previously reported compounds. Additionally, the Ioffe plots show a maximum power factor and electrical conductivity at approximately 700 K with decreasing values afterward. Enhancing the temperature stability and improving the thermoelectric properties at temperatures above 700 K may lead to a very promising *n*-type Zintl phase for application at high temperatures.
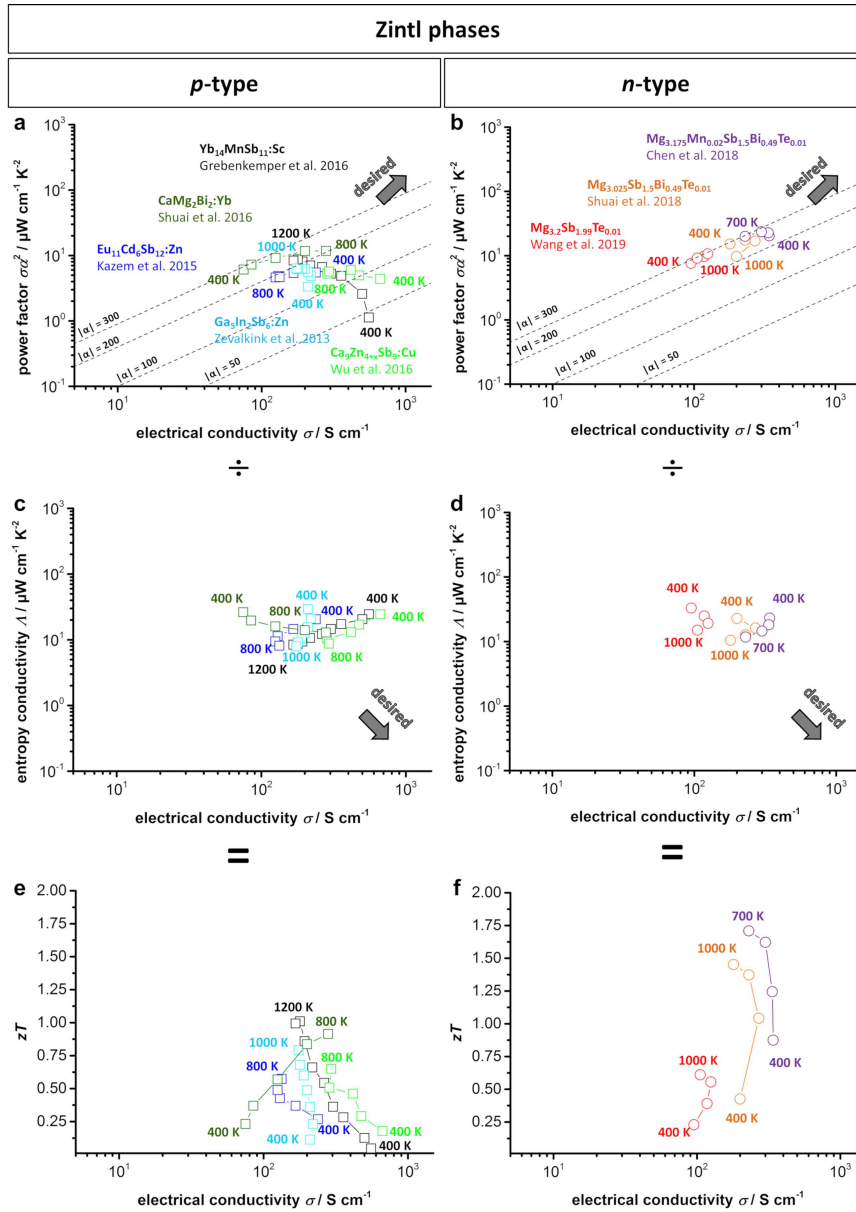
Figure 7. (**a**) *p*-Type; (**b**) *n*-type type-I Ioffe plots; (**c**) *p*-type; (**d**) *n*-type type-II Ioffe plots as well as (**e**) *p*-type and (**f**) *n*-type *zT*-electrical conductivity plots of several doped Zintl materials [41,127,129,131,148,154,155,157]. Dashed lines show the corresponding absolute values of the Seebeck coefficient α given in $\mu V\,K^{-1}$.

3.2. Heusler and Half-Heusler Compounds

Heusler compounds are intermetallics with the formula X_2YZ and are characterized by their cubic structure with the space group $Fm\bar{3}m$ [159]. The X and Y within this formula represent transition metals, while Z is a main group element. The half-Heusler compounds are derived from this and have the formula XYZ with the $F\bar{4}3m$ space group [7,159]. The structures for both compounds are displayed in Figure 8. The full-Heusler structure (Figure 8a) can be described by four interpenetrating face-centered-cubic sublattices, where two of them are equally occupied by the X. In contrast, one

of the equally occupied sublattices is vacant for the half-Heusler compounds (Figure 8b) [7]. The difference in the structures greatly affects the valence electrons and thereby the band structures of both compounds, typically leading to increased effective mass carrier concentrations and a high power factor for half-Heusler compounds, which is the reason for our focus on them within this review [159]. Half-Heusler materials are generally stable if 18 valence electrons are present, because only bonding states are occupied in this case [159]. Notably, this restricts the choice of elements for stable phases. The resulting phases usually show semiconducting behavior, e.g., with band gaps of 0.5 eV for XNiSn compounds or semimetallic behavior for (Zr,Hf)CoSb compounds [159–161]. This narrow electronic band structure results in a characteristically high power factor for half-Heusler compounds in comparison to other thermoelectric material classes [159]. Since the states near the Fermi level are mainly based on *d-d* orbital bonding, the density of states results in large Seebeck coefficients and high electrical conductivities [162]. A more detailed discussion of the physical properties of different half-Heusler compounds can be found in the respective review articles [35,37,49,159,163].
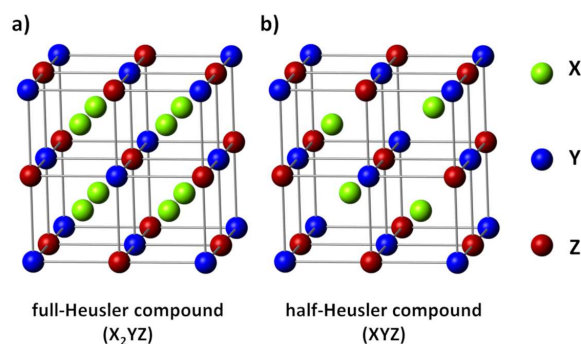

Figure 8. (**a**) Crystal structure of (**a**) full-Heusler- (X_2YZ) and (**b**) half-Heusler-compounds (XYZ). The half-Heusler compounds exhibit an unoccupied sublattice of X resulting in promising thermoelectric characteristics.

The first studies on half-Heusler compounds started in the early 1990s, but intensified with respect to thermoelectrics in the 2000s [164]. Recently, Poon presented an approach for dividing the advances of half-Heusler development for thermoelectrics into three different generations [163]. The first generation in the 2000s was characterized by alloying and doping as main modification factors providing *zT* values below 1, while in the second generation around 2010, more advanced synthesis techniques were introduced, namely, SPS for densification and nanostructuring, which led to *zT* values of approximately 1. In the current third generation, band engineering and structure ordering are becoming increasingly famous in addition to the previous techniques, which results in *zT* values of approximately 1.5 [163]. Advantages of half-Heusler compounds are their nontoxicity and stability to mechanical stress as well as high temperatures [7]. The optimum working temperature with regard to the thermoelectric performance is typically within 700–1000 K when in a vacuum or inert gas. The materials exhibit remarkable oxygen stability, but recent research has shown a sensitivity to oxygen at working temperatures for TiNiSn and ZrNiSn, resulting in the formation of oxides at the surface. Thus, the oxygen influence on the thermoelectric properties still needs to be investigated [165,166].

The elements of the half-Heusler compounds usually maintain very high melting points above 1773 K, which means high-temperature alloying, such as arc melting in a chamber with inert gas, is necessary for synthesis [162]. The usage of rather costly elements such as Hf further increases the production costs, which are major disadvantages of half-Heusler compounds despite their excellent thermoelectric properties.

3.2.1. *p*-Type Half-Heusler Compounds

State-of-the-art *p*-type half-Heusler compounds are mainly based on FeNbSb, where Nb is substituted by Ti or Hf as shown in Table 5. By comparing the power factors of the compounds in Table 5, the high *zT* values were mainly reached by reducing the thermal conductivity with heavy dopants at relatively high doping amounts. The best properties were achieved for $FeNb_{0.88}Hf_{0.12}Sb$ by Fu et al. [22] and reached a power factor of 51 µW cm^{-1} K^{-2} and a *zT* value of 1.45. However, a ZrCoBi-based compound recently reached *zT* values of up to 1.42, opening the way for research at a competing level. A similar half-Heusler system is based on XCoSb (X=Zr or Hf), which shows a decreased power factor at approximately 28 µW cm^{-1} K^{-2} but simultaneously a lower thermal conductivity compared to that of the FeNbSb-based compounds. The XCoSb compounds play a special role in thermoelectric research due to their possible *p*- and *n*-type doping, both leading to *zT* values of up to 1. [167,168] Therefore, these compounds can be found in both Tables 5 and 6 depending on their respective dopants.

Table 5. Dimensionless figure of merit *zT* and power factor $\sigma\alpha^2$ of several *p*-type half-Heusler phases.

Material	*T*/K	*zT*	$\sigma\alpha^2/\mu W\ cm^{-1}\ K^{-2}$
$FeNb_{0.88}Hf_{0.12}Sb$ [22]	1200 K	1.45	51
$FeNb_{0.86}Zr_{0.14}Sb$ [22]	1050 K	0.80	46
$FeNb_{0.95}Ti_{0.05}Sb$ [169]	973 K	0.70	50
$FeNb_{0.8}Ti_{0.2}Sb$ [169]	973 K	1.10	53
$ZrCoBi_{0.65}Sb_{0.15}Sn_{0.20}$ [170]	973 K	1.42	38
$Hf_{0.44}Zr_{0.44}Ti_{0.12}CoSb_{0.8}Sn_{0.2}$ [167]	973 K	1	28

3.2.2. *n*-Type Half-Heusler Compounds

Research on *n*-type half-Heusler compounds mainly focuses on MNiSn (M=Ti, Zr or Hf) compounds as parent materials. These compounds inherit quite remarkable *zT* values in the range of 0.4–0.55 as pure bulk materials, as shown in Table 6, but these values begin to rise to 1–1.5 when the materials are engineered properly toward improved thermoelectric performances. Reduction of grain size, alloying, and carrier doping are suitable tools to significantly improve the *zT* value [162]. Another parent material is XCoSb (X=Ti or Nb), which shows rather poor thermoelectric performance as a pure material due to high thermal conductivity, but drastically improves when doped [171,172]. The record *zT* value of 1.5 was reached with $Ti_{0.5}Zr_{0.25}Hf_{0.25}NiSn_{0.998}Sb_{0.002}$ by Shutoh et al. [173]. Unfortunately, this value cannot be reproduced independently at this time; however, slightly lower values were achieved by similar chemical compositions [37]. As described for *p*-type half-Heusler materials, the XCoSb (X=Zr or Hf) compounds can also show *n*-type behavior when doped accordingly. Here, $(Zr_{0.4}Hf_{0.6})_{0.88}Nb_{0.12}CoSb$ shows a power factor of 27 µW cm^{-1} K^{-2} and a *zT* value of 0.99, as demonstrated by Liu et al. [168] in 2018.

Table 6. Dimensionless figure of merit *zT* and power factor $\sigma\alpha^2$ of several *n*-type half-Heusler phases.

Material	*T*/K	*zT*	$\sigma\alpha^2/\mu W\ cm^{-1}\ K^{-2}$
TiNiSn [174]	775 K	0.4	24
ZrNiSn [175]	1000 K	0.55	33
HfNiSn [175]	1000 K	0.48	35
$Ti_{0.5}Zr_{0.25}Hf_{0.25}NiSn_{0.998}Sb_{0.002}$ [173]	700 K	1.50	62
$Hf_{0.6}Zr_{0.4}Hf_{0.25}NiSn_{0.995}Sb_{0.005}$ [176]	900 K	1.20	47
$NbCoSb_{0.8}Sn_{0.2}$ [172]	973 K	0.56	21
$TiFe_{0.15}Co_{0.85}Sb$ [177]	850 K	0.45	22
$(Zr_{0.4}Hf_{0.6})_{0.88}Nb_{0.12}CoSb$ [168]	1173 K	0.99	27

3.2.3. Comparison of Half-Heusler Compounds

Figure 9 shows type-I and type-II Ioffe plots as well as *zT* plots from several of the doped *p*-type and *n*-type bulk half-Heusler materials. The comparatively high power factor that can be easily seen in the type-I Ioffe plots is attributed to the narrow electronic band structure and *d-d* orbital bonding, as already discussed. The half-Heusler compounds are therefore especially interesting for thermoelectric generators when a high power output is desired. A comparison of *p*- and *n*-type compounds shows similar results for the maximum values of the power factor of approximately 50 μW cm^{-1} K^{-2} and the *zT* up to 1.5, which results in no clear advantage of one specific type. However, the *p*-type compounds exhibit slightly higher thermal stability up to 1200 K for FeNbSb-based materials. The high power factor also means a rather high impact of thermal conductivity on the efficiency of a half-Heusler compound. Thus, further engineering is mainly targeted at reducing thermal conductivity.
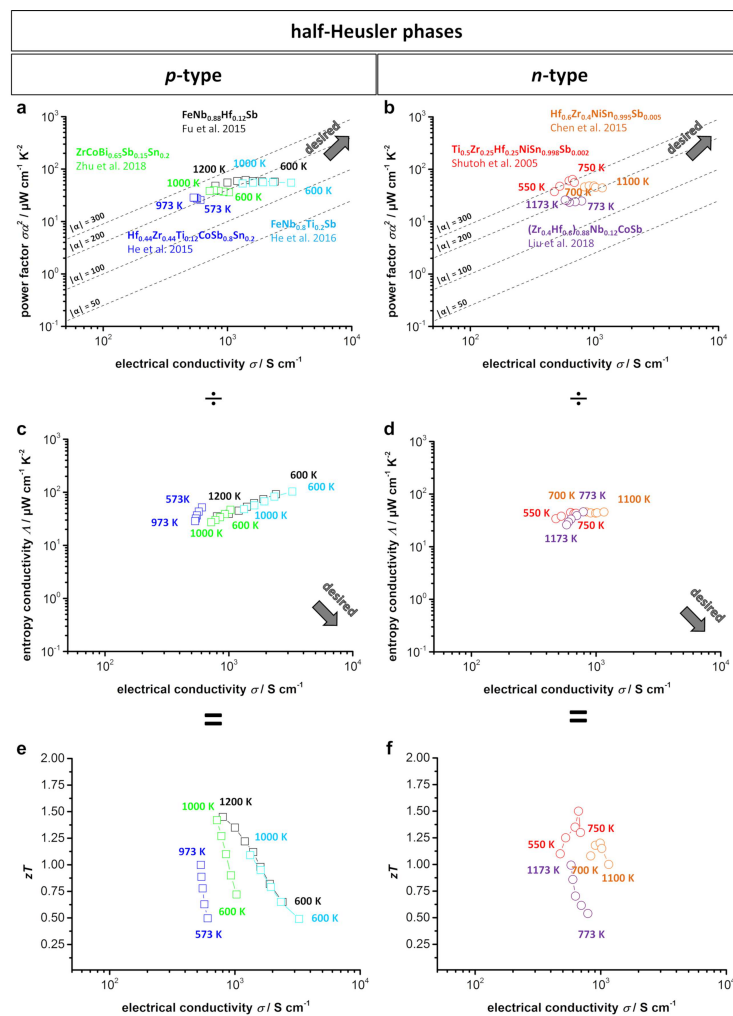

Figure 9. (**a**) *p*-Type; (**b**) *n*-type type-I Ioffe plots; (**c**) *p*-type; (**d**) *n*-type type-II Ioffe plots; (**e**) *p*-type; (**f**) *n*-type *zT*-electrical conductivity plots of several doped half-Heusler compounds [22,167–170,173,176]. Dashed lines show the corresponding absolute values of the Seebeck coefficient α given in μV K^{-1}.

3.3. SiGe Alloys

Eletrical supply of deep-space missions was one of the first application fields of thermoelectric power conversion. Here, mostly *n*- and *p*-type silicon–germanium alloys have been used [178]. This intermetallic material with a diamond crystal structure is characterized by a high thermal stability of up to 1200–1300 K when tested in vacuum. While Si exhibits a very high thermal conductivity of 148 W m^{-1} K^{-1}, the introduction of Ge atoms in the Si matrix strongly enhances the phonon scattering, resulting in a thermal conductivity of approximately 2-5 W m^{-1} K^{-1} and a *zT* > 1 in nanostructured SiGe alloys [120]. Achieving *p*- and *n*-type conduction is realized via doping with B [40] or Ga [179] (*p*-type) and P [180] or Sb [181] (*n*-type). The thermoelectric properties can be strongly influenced by the exact stoichiometry of the SiGe alloy. Materials with an ideal ratio of Si$_{80}$Ge$_{20}$ have been found and widely studied. In SiGe alloys, the large difference in the mean free path between electron (approximately 5 nm) and phonon (approximately 200–300 nm) contributions leads to a strong influence of nanostructuring in a range of 10–100 nm, which reduces the thermal conductivity without significantly reducing the electrical conductivity [182]. Therefore, nanostructuring [183–185] and the use of nanoinclusions [184,186–189] are common strategies to further improve the thermoelectric properties of SiGe alloys. For preparation of SiGe alloys, solid-state ball milling [180,183,186,187,190–194] or melt spinning (MS) [182,189] in combination with subsequent SPS are commonly used. Bathula et al. [192] reported a peak *zT* of 1.72 with a power factor of 28.7 µW cm^{-1} K^{-2} for *n*-doped Si$_{80}$Ge$_{20}$ with SiC nanoinclusions. In 2016, Ahmad et al. [191] presented a strong increase in *p*-type Si$_{80}$Ge$_{20}$ performance up to a *zT* of 1.81 and a power factor of 39.05 µW cm^{-1} K^{-2} via Y$_2$O$_3$ nanoinclusions. Table 7 shows the *zT* value and power factor of several *n*- and *p*-type doped Si$_{80}$Ge$_{20}$ materials.

Table 7. Dimensionless figure of merit *zT* and power factor $\sigma\alpha^2$ of several doped *p*- and *n*-type SiGe alloys.

Composition	Dopant	Inclusion	*T*/K	*zT*	$\sigma\alpha^2$/µW cm^{-1} K^{-2}
n-type Si$_{80}$Ge$_{20}$	P [190]	-	1073	1.78	30.3
	P [185]	-	1173	1.3	30.61
	Sb [181]	-	1073	0.61	18.5
	P	SiC [192]	1173	1.72	28.74
	P	Mg$_2$Si [193]	1173	1.27	29.84
	P	FeSi$_2$ [194]	1173	1.18	27.8
	P	WSi$_2$ [187]	1173	1.16	35.27
p-type Si$_{80}$Ge$_{20}$	B [40]	-	1173	1.22	20.5
	B [180]	-	1073	0.96	22
	Ga [179]	-	1073	0.52	15.5
	B	Y$_2$O$_3$ [191]	1073	1.81	39.05
	B	CrSi$_2$ [186]	1073	0.65	21.25
	B	YSi$_2$ [189]	1073	0.53	16.57
	B	WSi$_2$ [187]	1173	0.66	17.63

Figure 10 shows the type-I and type-II Ioffe plots and *zT* plots from several doped Si$_{80}$Ge$_{20}$ alloys. In general, Si-Ge alloys are characterized by a relatively high power factor of approximately 15–40 µW cm^{-1} K^{-2} due to their high electrical conductivity, which is why they are located at the top right of the type-I Ioffe plot. The drawback of a simultaneously high thermal conductivity can be mitigated via nanostructuring and nanoinclusions without significantly reducing the electrical conductivity, resulting in *zT* values of up to 1.7 for *n*-type and 1.8 for *p*-type materials. Combined with a high thermal stability of up to 1200–1300 K in vacuum, Si-Ge alloys are perfect candidates as thermoelectric materials for deep-space missions. Further adjustment of the thermal conductivity of such alloys is especially interesting if a high conversion efficiency is desired.
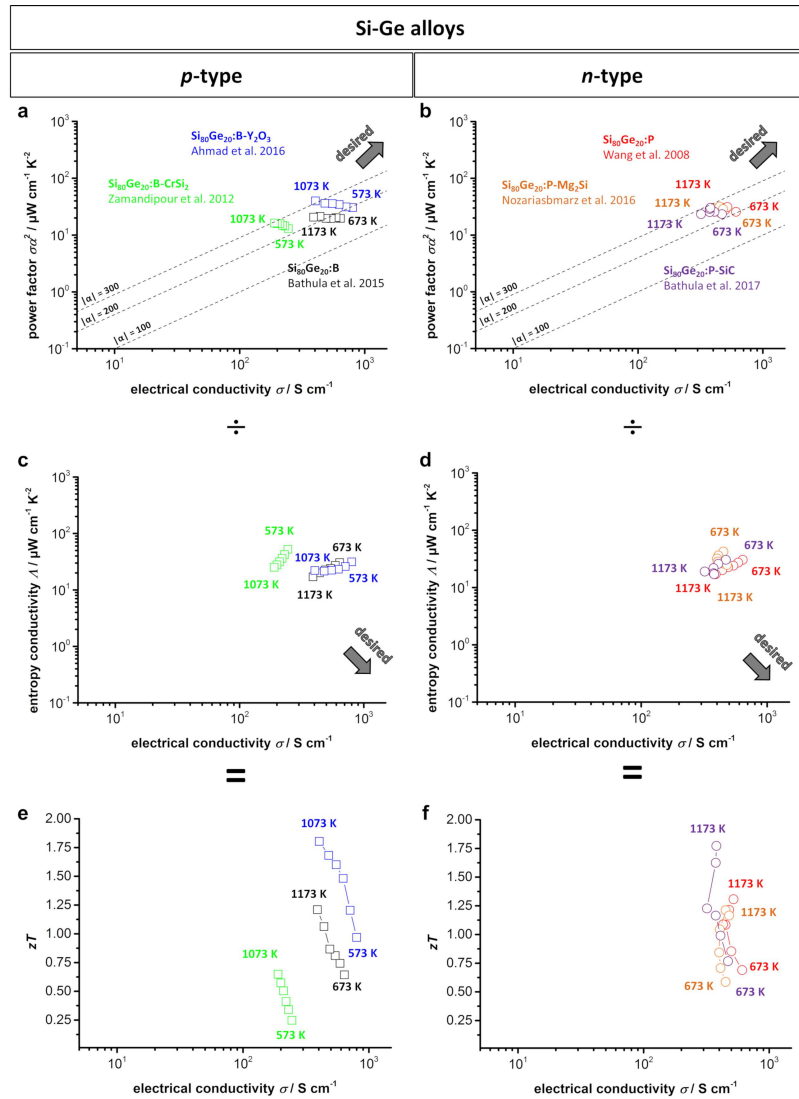
Figure 10. (**a**) *p*-Type; (**b**) *n*-type type-I Ioffe plots; (**c**) *p*-type; (**d**) *n*-type type-II Ioffe plots; (**e**) *p*-type; (**f**) *n*-type *zT*-electrical conductivity plots of several doped Si-Ge alloys [40,185,186,191–193]. Dashed lines show the corresponding absolute values of the Seebeck coefficient α given in $\mu V\ K^{-1}$.

4. Comparison of High-Temperature Thermoelectric Materials

Figure 11 shows the type-I and type-II Ioffe plots and *zT* plots from several of the doped *p*- and *n*-type materials for possible high temperature applications and their comparison to those of the commercially used Bi_2Te_3. Here, the half-Heusler compounds exhibit the highest power factor values with a simultaneously high electrical conductivity as a result of their electronic band structure, described above. Therefore, the half-Heusler compounds are the closest to the desired area for both *p*- and *n*-type materials. The conventional Bi_2Te_3 and the SiGe alloys also show a comparably high power factor at a slightly lower electrical conductivity. Of the compared thermoelectric materials, the oxide-based materials have the lowest power factor and electrical conductivity. This trend corresponds to the type-II Ioffe plots, where the half-Heusler compounds and Bi_2Te_3 exhibit the highest entropy conductivity, while the oxide materials show a significantly lower entropy conductivity, especially at high temperatures. Furthermore, the Zintl phases are also characterized by a low thermal

conductivity, which culminates in the *n*-type Zintl phase of $Mg_{3.175}Mn_{0.025}Sb_{1.5}Bi_{0.49}Te_{0.01}$ having the lowest entropy conductivity of all compared *n*-type materials. As a result, the half-Heusler compounds as well as BiCuSeO show the highest *zT* values within the *p*-type materials, and the Zintl compounds have the highest *zT* value within the *n*-type materials. As described before, the power factor corresponds to the maximum power output of the material, making the half-Heusler compounds the most interesting bulk materials for high-temperature application from this point of view. Yet, the Zintl compounds and oxyselenides provide a high efficiency in power conversion due to their significantly lower entropy conductivity. The oxide-based thermoelectric materials show comparatively low thermoelectric properties, but are characterized by high chemical and thermal stability, especially in air. As mentioned within the introduction, extension to a functional device always comes alongside additional tasks. In particular, contact resistivity is crucial to reach full potential, when applying highly electrical conducting materials such as half-Heusler compounds in a device.
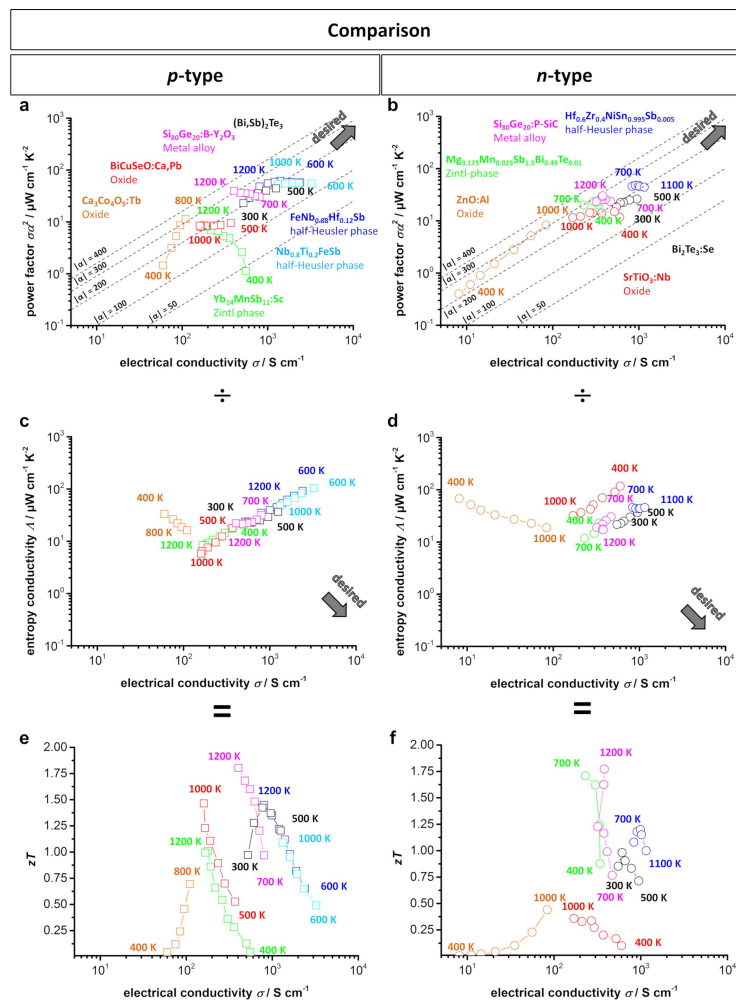

Figure 11. (**a**) *p*-Type; (**b**) *n*-type type-I Ioffe plots; (**c**) *p*-type; (**d**) *n*-type type-II Ioffe plots; (**e**) *p*-type; (**f**) *n*-type *zT*-electrical conductivity plots of several doped oxide materials [11,39,80,96], Zintl phases [41,154], half-Heusler compounds [169,173,176], and Si-Ge alloys [191,192] as compared to doped Bi_2Te_3 [21,195]. Dashed lines show the corresponding absolute values of the Seebeck coefficient α given in $\mu V\ K^{-1}$.

A similar comparison of the material properties can be performed by displaying the power factor as a function of the entropy conductivity, shown in Figure 12. Note that the dashed lines within the plot represent the dimensionless zT value. It can be easily observed that within the p-type thermoelectric materials, several compounds from different classes, such as BiCuSeO, SiGe alloys, and half-Heusler alloys, all reach a zT value of up to 1.5, whereas the power factor shows a strong deviation between 10 and 65 $\mu W\,cm^{-1}\,K^{-2}$. Within the compared n-type materials, the same behavior can be observed, although the materials show overall slightly lower zT values. Therefore, this power factor vs. entropy conductivity plot presents the respective advantages of each kind of thermoelectric material discussed in terms of a high power factor or high zT value.
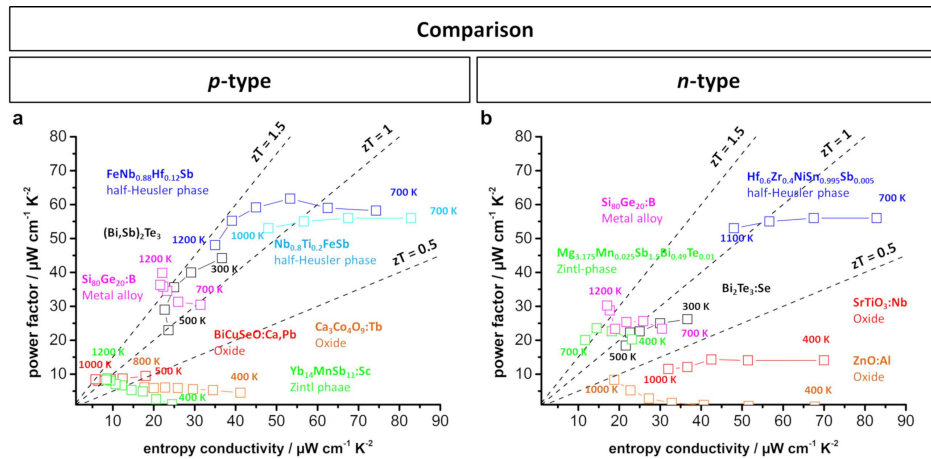

Figure 12. (**a**) p-Type; (**b**) n-type power factor vs. entropy conductivity plots of several doped oxide materials [11,39,80,96], Zintl phases [41,154], half-Heusler compounds [169,176,196] and Si-Ge alloys [191,192] as compared to doped Bi_2Te_3 [21,195]. Dashed lines show the corresponding zT values.

In addition to the thermoelectric materials discussed above, there are a few material classes with noteworthy thermal stability of up to 800–900 K, which should also be mentioned here. Cage compounds such as clathrates [197] and skutterudites [198] are both characterized by good electronic transport properties while reducing thermal conductivity by filling the cages with guest atoms [49]. In this way, high zT values of up to 1.3 and 1.7 at 800 K can be reached in multiple filled clathrates [199] and skutterudites [200,201], respectively. However, despite the similarity of these cage compounds, the respective power factor shows a strong variation with approximately 10 $\mu W\,cm^{-1}\,K^{-2}$ for clathrates [199] and approximately 50 $\mu W\,cm^{-1}\,K^{-2}$ for skutterudites [201] at 800 K. This also results in a possible tuning for either a high power output or a high conversion efficiency. Last, solid solutions of Mg_2Si intermetallic silicides are also a focus of interest as mid-temperature thermoelectric materials of up to 800 K [49]. Solid solutions of $Mg_2Si_{1-x}Ge_x$ and $Mg_2Si_{1-x}Sn_x$, with an optimized carrier concentration via doping, reached a power factor of approximately 30 $\mu W\,cm^{-1}\,K^{-2}$ and a zT value > 1 at 800 K [202,203]. For respective applications at mid-temperatures, a similar comparison to this work could be performed for evaluation and comparison of these materials and their respective parameters.

5. Conclusions

Different kinds of bulk thermoelectric materials have been compared with respect to their high-temperature performance and stability. Within the respective thermoelectric material classes, much research has been conducted within recent decades, however, very few works have compared these classes. Here, the concept of using Ioffe plots to compare and evaluate the power factor and the zT value as two different parameters that can be useful for optimization was successfully presented. Hereby, the strengths and weaknesses of each material class were revealed, which could be useful

for prospective research and associated applications. Out of all of the compared materials, the class of half-Heusler compounds exhibited the highest power factor and electrical conductivity, which is applicable for reaching a high power output at high operating temperatures. Si-Ge alloys reached the highest zT values but had a significantly lower power factor than the half-Heusler compounds. Other materials, such as oxide-based materials, oxyselenides, and Zintl compounds, also reached reasonable zT values, which made these promising materials for reaching high conversion efficiencies.

Author Contributions: M.W., R.H. and A.F. worked on the conceptualization. M.W. and R.H. wrote the original draft. M.W., R.H. and A.F. critically revised and edited the manuscript draft. A.F. is responsible for the acquisition of funding.

Conflicts of Interest: The authors declare no conflict of interest.

References

1. He, J.; Tritt, T.M. Advances in Thermoelectric Materials Research: Looking Back and Moving Forward. *Science* **2017**, *357*, eaak9997. [CrossRef] [PubMed]

2. *Energy Flow Chart U.S. 2017*; Technical Report; Lawrence Livermore National Laboratory (LLNL) and the Departement of Energy: Livermore, CA, USA, 2018.

3. Kishore, R.A.; Marin, A.; Wu, C.; Kumar, A.; Priya, S. *Energy Harvesting—Materials, Physics, and System Design with Practical Examples*; DEStech Publications: Lancaster, PA, USA, 2019.

4. Goldsmid, H.J. *Introduction to Thermoelectricity*; Springer: Berlin/Heidelberg, Germany, 2010.

5. Ioffe, A.F. *Semiconductor Thermoelements, and Thermoelectric Cooling*, 1st ed.; Info-search Ltd.: London, UK, 1957.

6. Snyder, G.J.; Toberer, E. Complex Thermoelectric Materials. *Nat. Mater.* **2008**, *7*, 105–114. [CrossRef] [PubMed]

7. Chen, S.; Ren, Z. Recent Progress of half-Heusler for Moderate Temperature Thermoelectric Applications. *Mater. Today* **2013**, *16*, 387–395. [CrossRef]

8. Shuai, J.; Mao, J.; Song, S.; Zhang, Q.; Chen, G.; Ren, Z. Recent Progress and Future Challenges on Thermoelectric Zintl Materials. *Mater. Today Phys.* **2017**, *1*, 74–95. [CrossRef]

9. Yin, Y.; Tudu, B.; Tiwari, A. Recent Advances in Oxide Thermoelectric Materials and Modules. *Vacuum* **2017**, *146*, 356–374. [CrossRef]

10. Bittner, M.; Kanas, N.; Hinterding, R.; Steinbach, F.; Groeneveld, D.; Wemhoff, P.; Wiik, K.; Einarsrud, M.A.; Feldhoff, A. Triple-phase Ceramic 2D Nanocomposite with Enhanced Thermoelectric Properties. *J. Eur. Ceram. Soc.* **2019**, *39*, 1237–1244. [CrossRef]

11. Liu, Y.; Zhao, L.D.; Zhu, Y.; Liu, Y.; Li, F.; Yu, M.; Liu, D.B.; Xu, W.; Lin, Y.H.; Nan, C.-W. Synergistically Optimizing Electrical and Thermal Transport Properties of BiCuSeO via a Dual-Doping Approach. *Adv. Energy Mater.* **2016**, *6*, 1–9. [CrossRef]

12. Zhao, L.D.; Lo, S.H.; Zhang, Y.; Sun, H.; Tan, G.; Uher, C.; Wolverton, C.; Dravid, V.P.; Kanatzidis, M.G. Ultralow Thermal Conductivity and High Thermoelectric Figure of Merit in SnSe Crystals. *Nature* **2014**, *508*, 373–377. [CrossRef]

13. Toshima, N. Recent Progress of Organic and Hybrid Thermoelectric Materials. *Synth. Met.* **2017**, *225*, 3–21. [CrossRef]

14. Wolf, M.; Menekse, K.; Mundstock, A.; Hinterding, R.; Nietschke, F.; Oeckler, O.; Feldhoff, A. Low Thermal Conductivity in Thermoelectric Oxide-Based Multiphase Composites. *J. Electron. Mater.* **2019**, *48*, 7551–7561. [CrossRef]

15. Feldhoff, A. Thermoelectric Material Tensor Derived from the Onsager–de Groot–Callen Model. *Energy Harvest. Syst.* **2015**, *2*, 5–13. [CrossRef]

16. Fuchs, H.U. A Direct Entropic Approach to Uniform and Spatially Continuous Dynamical Models of Thermoelectric Devices. *Energy Harvest. Syst.* **2014**, *1*, 1–18. [CrossRef]

17. Job, G.; Rüffler, R. *Physical Chemistry from a Different Angle*, 1st ed.; Springer: Berlin/Heidelberg, Germany, 2014. [CrossRef]

18. Goupil, C.; Seifert, W.; Zabrocki, K.; Müller, E.; Snyder, G.J. Thermodynamics of Thermoelectric Phenomena and Applications. *Entropy* **2011**, *13*, 1481–1517. [CrossRef]

19. Fuchs, H. *The Dynamics of Heat—A Unified Approach to Thermodynamics and Heat Transfer*, 2nd ed.; Springer: New York, NY, USA, 2010. [CrossRef]

20. Bittner, M.; Kanas, N.; Hinterding, R.; Steinbach, F.; Räthel, J.; Schrade, M.; Wiik, K.; Einarsrud, M.A.; Feldhoff, A. A Comprehensive Study on Improved Power Materials for High-Temperature Thermoelectric Generators. *J. Power Sources* **2019**, *410-411*, 143–151. [CrossRef]

21. Poudel, B.; Hao, Q.; Ma, Y.; Lan, Y.; Minnich, A.; Yu, B.; Yan, X.; Wang, D.; Muto, A.; Vashaee, D.; et al. High-Thermoelectric Performance of Nanostructured Bismuth Antimony Telluride Bulk Allys. *Science* **2008**, *320*, 634–638. [CrossRef] [PubMed]

22. Fu, C.; Bai, S.; Liu, Y.; Tang, Y.; Chen, L.; Zhao, X.; Zhu, T. Realizing High Figure of Merit in Heavy-Band p-Type half-Heusler Thermoelectric Materials. *Nat. Commun.* **2015**, *6*, 1–7. [CrossRef] [PubMed]

23. Narducci, D. Do we Really need High Thermoelectric Figures of Merit? A Critical Appraisal to the Power Conversion Efficiency of Thermoelectric Materials. *Appl. Phys. Lett.* **2011**, *99*, 102104. [CrossRef]

24. Pei, Y.; Shi, X.; Lalonde, A.; Wang, H.; Chen, L.; Snyder, G.J. Convergence of Electronic Bands for High Performance Bulk Thermoelectrics. *Nature* **2011**, *473*, 66–69. [CrossRef]

25. Pei, Y.; Wang, H.; Snyder, G.J. Band Engineering of Thermoelectric Materials. *Adv. Mater.* **2012**, *24*, 6125–6135. [CrossRef]

26. Hu, L.; Zhu, T.; Liu, X.; Zhao, X. Point Defect Engineering of High-Performance Bismuth-Telluride-Based Thermoelectric Materials. *Adv. Funct. Mater.* **2014**, *24*, 5211–5218. [CrossRef]

27. Kanatzidis, M.G. Nanostructured Thermoelectrics: The New Paradigm? *Chem. Mater.* **2010**, *22*, 648–659. [CrossRef]

28. Cook, B.A.; Kramer, M.J.; Harringa, J.L.; Han, M.K.; Chung, D.Y.; Kanatzidis, M.G. Analysis of Nanostructuring in High Figure-of-Merit $Ag_{1-x}Pb_mSbTe_{2+m}$ Thermoelectric Materials. *Adv. Funct. Mater.* **2009**, *19*, 1254–1259. [CrossRef]

29. Li, J.; Tan, Q.; Li, J.F.; Liu, D.W.; Li, F.; Li, Z.Y.; Zou, M.; Wang, K. BiSbTe-based Nanocomposites with High zT: The Effect of SiC Nanodispersion on Thermoelectric Properties. *Adv. Funct. Mater.* **2013**, *23*, 4317–4323. [CrossRef]

30. Lan, Y.; M., A.J.; Chen, G.; Ren, Z. Enhancement of Thermoelectric Figure-of-Merit by a Bulk Nanostructuring Approach. *Adv. Funct. Mater.* **2010**, *20*, 357–376. [CrossRef]

31. Miyazaki, K.; Kuriyama, K.; Yabuki, T. Printable Thermoelectric Device. In Proceedings of the PowerMEMS 2018 Conference, Daytona Beach, FL, USA, 4–7 December 2018.

32. Biswas, K.; He, J.; Blum, I.D.; Wu, C.I.; Hogan, T.P.; Seidman, D.N.; Dravid, V.P.; Kanatzidis, M.G. High-Performance Bulk Thermoelectrics with All-Scale Hierarchical Architectures. *Nature* **2012**, *489*, 414–418. [CrossRef] [PubMed]

33. Zheng, Y.; Zhang, Q.; Su, X.; Xie, H.; Shu, S.; Chen, T.; Tan, G.; Yan, Y.; Tang, X.; Uher, C.; et al. Mechanically Robust BiSbTe Alloys with Superior Thermoelectric Performance: A Case Study of Stable Hierarchical Nanostructured Thermoelectric Materials. *Adv. Energy Mater.* **2015**, *5*, 1401391. [CrossRef]

34. Tritt, T.M. *Thermal Conductivity—Theory, Properties and Applications*; Kluwer Academic/Plenum Publishers: New York, NY, USA, 2004.

35. Tan, G.; Zhao, L.D.; Kanatzidis, M.G. Rationally Designing High-Performance Bulk Thermoelectric Materials. *Chem. Rev.* **2016**, *116*, 12123–12149. [CrossRef]

36. Fergus, J.W. Oxide Materials for High Temperature Thermoelectric Energy Conversion. *J. Eur. Ceram. Soc.* **2012**, *32*, 525–540. [CrossRef]

37. Poon, S. Recent Advances in Thermoelectric Performance of half-Heusler Compounds. *Metals* **2018**, *8*, 989. [CrossRef]

38. Cowen, L.M.; Atoyo, J.; Carnie, M.J.; Baran, D.; Schroeder, B.C. Review—Organic Materials for Thermoelectric Energy Generation. *ECS J. Solid State Sci. Technol.* **2017**, *6*, N3080–N3088. [CrossRef]

39. Saini, S.; Yaddanapudi, H.S.; Tian, K.; Yin, Y.; Magginetti, D.; Tiwari, A. Terbium Ion Doping in $Ca_3Co_4O_9$: A Step Towards High-Performance Thermoelectric Materials. *Sci. Rep.* **2017**, *7*, 1–9. [CrossRef] [PubMed]

40. Bathula, S.; Jayasimhadri, M.; Gahtori, B.; Singh, N.K.; Tyagi, K.; Srivastava, A.K.; Dhar, A. The Role of Nanoscale Defect Features in Enhancing the Thermoelectric Performance of p-Type Nanostructured SiGe Alloys. *Nanoscale* **2015**, *7*, 12474–12483. [CrossRef] [PubMed]

41. Grebenkemper, J.H.; Klemenz, S.; Albert, B.; Bux, S.K.; Kauzlarich, S.M. Effects of Sc and Y Substitution on the Structure and Thermoelectric Properties of $Yb_{14}MnSb_{11}$. *J. Solid State Chem.* **2016**, *242*, 55–61. [CrossRef]

42. Bell, L.E. Cooling, Heating, Generating Power, and Recovering Waste Heat with Thermoelectric Systems. *Science* **2008**, *321*, 1457–1461. [CrossRef]

43. Kim, H.S.; Liu, W.; Ren, Z. The Bridge Between the Materials and Devices of Thermoelectric Power Generators. *Energy Environ. Sci.* **2017**, *10*, 69–85. [CrossRef]

44. Snyder, G.J.; Snyder, A.H. Figure of Merit zT of a Thermoelectric Device Defined from Materials Properties. *Energy Environ. Sci.* **2017**, *10*, 2280–2283. [CrossRef]

45. Tan, G.; Ohta, M.; Kanatzidis, M.G. Thermoelectric Power Generation: From New Materials to Devices. *Philos. Trans. R. Soc. A Math. Phys. Eng. Sci.* **2019**, *377*. [CrossRef]

46. He, J.; Liu, Y.; Funahashi, R. Oxide Thermoelectrics: The Challenges, Progress, and Outlook. *J. Mater. Res.* **2011**, *26*, 1762–1772. [CrossRef]

47. Hicks, L.D.; Dresselhaus, M.S. Effect of Quantum-Well Structures on the Thermoelectric Figure of Merit. *Phys. Rev. B* **1993**, *47*. [CrossRef]

48. Terasaki, I.; Sasago, Y.; Uchinokura, K. Large Thermoelectric Power in $NaCo_2O_4$ Single Crystals. *Phys. Rev.* **1997**, *56*, 12685–12687. [CrossRef]

49. Shi, X.; Chen, L.; Uher, C. Recent Advances in High-Performance Bulk Thermoelectric Materials. *Int. Mater. Rev.* **2016**, *61*, 379–415. [CrossRef]

50. Zhao, L.D.; He, J.; Berardan, D.; Lin, Y.; Li, J.F.; Nan, C.W.; Dragoe, N. BiCuSeO Oxyselenides: New Promising Thermoelectric Materials. *Energy Environ. Sci.* **2014**, *7*, 2900–2924. [CrossRef]

51. Zhang, X.; Chang, C.; Zhou, Y.; Zhao, L.D. BiCuSeO Thermoelectrics: An Update on Recent Progress and Perspective. *Materials* **2017**, *10*, 198. [CrossRef] [PubMed]

52. Liu, P.; Chen, G.; Cui, Y.; Zhang, H.; Xiao, F.; Wang, L.; Nakano, H. High Temperature Electrical Conductivity and Thermoelectric Power of Na_xCoO_2. *Solid State Ionics* **2008**, *179*, 2308–2312. [CrossRef]

53. Krasutskaya, N.S.; Klyndyuk, A.I.; Evseeva, L.E.; Tanaeva, S.A. Synthesis and Properties of Na_xCoO_2 (x = 0.55, 0.89) Oxide Thermoelectrics. *Inorg. Mater.* **2016**, *52*, 393–399. [CrossRef]

54. Klyndyuk, A.I.; Krasutskaya, N.S.; Chizhova, E.A. Synthesis and Thermoelectric Properties of Ceramics based on $Bi_2Ca_2Co_{1.7}O_y$ Oxide. *Glass Phys. Chem.* **2018**, *44*, 100–107. [CrossRef]

55. Sun, N.; Dong, S.T.; Zhang, B.B.; Chen, Y.B.; Zhou, J.; Zhang, S.T.; Gu, Z.B.; Yao, S.H.; Chen, Y.F. Intrinsically Modified Thermoelectric Performance of Alkaline-Earth Isovalently Substituted $[Bi_2AE_2O_4][CoO_2]_y$ Single Crystals. *J. Appl. Phys.* **2013**, *114*, 1–7. [CrossRef]

56. Chen, Y.; Chen, C.; Li, X. Effect on the Properties of Different Preparation Processes in $Ca_3Co_4O_9$ Thermoelectric Material. *Int. Conf. Electr. Control. Eng.* **2010**, 4672–4676. [CrossRef]

57. Królicka, A.K.; Piersa, M.; Mirowska, A.; Michalska, M. Effect of Sol-Gel and Solid-State Synthesis Techniques on Structural, Morphological and Thermoelectric Performance of $Ca_3Co_4O_9$. *Ceram. Int.* **2018**. [CrossRef]

58. Noudem, J.G.; Kenfaui, D.; Chateigner, D.; Gomina, M. Toward the Enhancement of Thermoelectric Properties of Lamellar $Ca_3Co_4O_9$ by Edge-Free Spark Plasma Texturing. *Scr. Mater.* **2012**, *66*, 258–260. [CrossRef]

59. Schulz, T.; Töpfer, J. Thermoelectric Properties of $Ca_3Co_4O_9$ Ceramics Prepared by an Alternative Pressure-Less Sintering/Annealing Method. *J. Alloy. Compd.* **2016**, *659*, 122–126. [CrossRef]

60. Huang, Y.; Zhao, B.; Fang, J.; Ang, R.; Sun, Y. Tunning of Microstructure and Thermoelectric Properties of $Ca_3Co_4O_9$ Ceramics by High-Magnetic-Field Sintering. *J. Appl. Phys.* **2011**, *110*. [CrossRef]

61. Bittner, M.; Helmich, L.; Nietschke, F.; Geppert, B.; Oeckler, O.; Feldhoff, A. Porous $Ca_3Co_4O_9$ with Enhanced Thermoelectric Properties Derived from Sol–Gel Synthesis. *J. Eur. Ceram. Soc.* **2017**, *37*, 3909–3915. [CrossRef]

62. Prasoetsopha, N.; Pinitsoontorn, S.; Kamwanna, T.; Amornkitbamrung, V.; Kurosaki, K.; Ohishi, Y.; Muta, H.; Yamanaka, S. The Effect of Cr Substitution on the Structure and Properties of Misfit-Layered $Ca_3Co_{4-x}Cr_xO_{9+\delta}$ Thermoelectric Oxides. *J. Alloy. Compd.* **2014**, *588*, 199–205. [CrossRef]

63. Cha, J.S.; Choi, S.; Kim, G.H.; Kim, S.; Park, K. High-Temperature Thermoelectric Properties of Sm^{3+}-Doped $Ca_3Co_4O_{9+delta}$ Fabricated by Spark Plasma Sintering. *Ceram. Int.* **2018**, *44*, 6376–6383. [CrossRef]

64. Wang, K.X.; Wang, J.; Wu, H.; Shaheen, N.; Zha, X.Y.; Gao, L.J.; Bai, H.C. Thermoelectric Properties of Lower Concentration K-Doped $Ca_3Co_4O_9$ Ceramics. *Chin. Phys. B* **2018**, *27*. [CrossRef]

65. Butt, S.; Xu, W.; He, W.Q.; Tan, Q.; Ren, G.K.; Lin, Y.; Nan, C.W. Enhancement of Thermoelectric Performance in Cd-Doped Ca$_3$Co$_4$O$_9$ via Spin Entropy, Defect Chemistry and Phonon Scattering. *J. Mater. Chem. A* **2014**, *2*, 19479–19487. [CrossRef]

66. Delorme, F.; Martin, C.F.; Marudhachalam, P.; Ovono Ovono, D.; Guzman, G. Effect of Ca Substitution by Sr on the Thermoelectric Properties of Ca$_3$Co$_4$O$_9$ Ceramics. *J. Alloy. Compd.* **2011**, *509*, 2311–2315. [CrossRef]

67. Hira, U.; Han, L.; Norrman, K.; Christensen, D.V.; Pryds, N.; Sher, F. High-Temperature Thermoelectric Properties of Na- and W-Doped Ca$_3$Co$_4$O$_9$ System. *RSC Adv.* **2018**, *8*, 12211–12221. [CrossRef]

68. Butt, S.; Liu, Y.C.; Lan, J.L.; Shehzad, K.; Zhan, B.; Lin, Y.; Nan, C.W. High-Temperature Thermoelectric Properties of La and Fe co-Doped Ca-Co-O Misfit-Layered Cobaltites Consolidated by Spark Plasma Sintering. *J. Alloy. Compd.* **2014**, *588*, 277–283. [CrossRef]

69. Ito, M.; Furumoto, D. Effects of Noble Metal Addition on Microstructure and Thermoelectric Properties of Na$_x$Co$_2$O$_4$. *J. Alloy. Compd.* **2008**, *450*, 494–498. [CrossRef]

70. Park, K.; Choi, J.W. High-Temperature Thermoelectric Properties of Na(Co$_{0.91}$Ni$_{0.09}$)$_2$O$_4$ Fabricated by Solution Combustion Method for Power Generation. *J. Nanosci. Nanotechnol.* **2012**, *12*, 3624–3628. [CrossRef] [PubMed]

71. Park, K.; Jang, K.U.; Kwon, H.C.; Kim, J.G.; Cho, W.S. Influence of Partial Substitution of Cu for Co on the Thermoelectric Properties of NaCo$_2$O$_4$. *J. Alloy. Compd.* **2006**, *419*, 213–219. [CrossRef]

72. Nagira, T.; Ito, M.; Katsuyama, S.; Majima, K.; Nagai, H. Thermoelectric Properties of (Na$_{1-y}$M$_y$)$_x$Co$_2$O$_4$(M = K, Sr, Y, Nd, Sm and Yb; Y = 0.01 − 0.35). *J. Alloy. Compd.* **2003**, *348*, 263–269. [CrossRef]

73. Karakaya, G.Ç.; Özçelik, B.; Nane, O.; Sotelo, A. Improvement of Bi$_2$Sr$_2$Co$_2$O$_y$ Thermoelectric Performances by Na Doping. *J. Electroceramics* **2018**, *2*, 11–15. [CrossRef]

74. Gao, F.; He, Q.; Cao, R.; Wu, F.; Hu, X.; Song, H. Enhanced Thermoelectric Properties of the Hole-Doped Bi$_{2-x}$K$_x$Sr$_2$Co$_2$O$_y$ Ceramics. *Int. J. Mod. Phys. B* **2015**, *29*, 1–7. [CrossRef]

75. Hao, H.S.; Ye, J.Q.; Liu, Y.T.; Hu, X. High-Temperature Thermoelectric Properties of Pb- and La-Substituted Bi$_2$Sr$_2$Co$_2$O$_y$ Misfit Compounds. *Adv. Mater. Res.* **2010**, *105-106*, 336–338. [CrossRef]

76. Janotti, A.; Van De Walle, C.G. Fundamentals of Zinc Oxide as a Semiconductor. *Rep. Prog. Phys.* **2009**, *72*. [CrossRef]

77. Van Benthem, K.; Elsässer, C.; French, R.H. Bulk Electronic Structure of SrTiO$_3$: Experiment and Theory. *J. Appl. Phys.* **2001**, *90*, 6156–6164. [CrossRef]

78. Zhang, F.P.; Lu, Q.M.; Zhang, X.; Zhang, J.X. First Principle Investigation of Electronic Structure of CaMnO$_3$ Thermoelectric Compound Oxide. *J. Alloy. Compd.* **2011**, *509*, 542–545. [CrossRef]

79. Tsubota, T.; Ohtaki, M.; Eguchi, K.; Arai, H. Thermoelectric Properties of Al-Doped ZnO as a Promising Oxide Material for High-Temperature Thermoelectric Conversion. *J. Mater. Chem.* **1997**, *7*, 85–90. [CrossRef]

80. Jood, P.; Mehta, R.J.; Zhang, Y.; Peleckis, G.; Wang, X.; Siegel, R.W.; Borca-Tasciuc, T.; Dou, S.X.; Ramanath, G. Al-Doped Zinc Oxide Nanocomposites with Enhanced Thermoelectric Properties. *Nano Lett.* **2011**, *11*, 4337–4342. [CrossRef] [PubMed]

81. Nam, W.H.; Lim, Y.S.; Choi, S.M.; Seo, W.S.; Lee, J.Y. High-Temperature Charge Transport and Thermoelectric Properties of a Degenerately Al-Doped ZnO Nanocomposite. *J. Mater. Chem.* **2012**, *22*, 14633–14638. [CrossRef]

82. Han, L.; Van Nong, N.; Zhang, W.; Hung, L.T.; Holgate, T.; Tashiro, K.; Ohtaki, M.; Pryds, N.; Linderoth, S. Effects of Morphology on the Thermoelectric Properties of Al-Doped ZnO. *RSC Adv.* **2014**, *4*, 12353–12361. [CrossRef]

83. Tian, T.; Cheng, L.; Zheng, L.; Xing, J.; Gu, H.; Bernik, S.; Zeng, H.; Ruan, W.; Zhao, K.; Li, G. Defect Engineering for a Markedly Increased Electrical Conductivity and Power Factor in Doped ZnO Ceramic. *Acta Mater.* **2016**, *119*, 136–144. [CrossRef]

84. Ohta, S.; Nomura, T.; Ohta, H.; Koumoto, K. High-Temperature Carrier Transport and Thermoelectric Properties of Heavily La- Or Nb-Doped SrTiO$_3$ Single Crystals. *J. Appl. Phys.* **2005**, *97*. [CrossRef]

85. Han, J.; Sun, Q.; Song, Y. Enhanced Thermoelectric Properties of La and Dy co-Doped, Sr-deficient SrTiO$_3$ Ceramics. *J. Alloy. Compd.* **2017**, *705*, 22–27. [CrossRef]

86. Chen, Y.; Liu, J.; Li, Y.; Zhang, X.; Wang, X.; Su, W.; Li, J.; Wang, C. Enhancement of Thermoelectric Performance of Sr$_{1-x}$Ti$_{0.8}$Nb$_{0.2}$O$_3$ Ceramics by Introducing Sr Vacancies. *J. Electron. Mater.* **2019**, *48*, 1147–1152. [CrossRef]

87. Bittner, M.; Geppert, B.; Kanas, N.; Singh, S.P.; Wiik, K.; Feldhoff, A. Oxide-Based Thermoelectric Henerator for High-Temperature Application using p-Type $Ca_3Co_4O_9$ and n-Type $In_{1.95}Sn_{0.05}O_3$ Legs. *Energy Harvest. Syst.* **2016**, *3*, 213–222. [CrossRef]

88. Yan, Y.L.; Wang, Y.X. Electronic Structure and Low Temperature Thermoelectric Properties of $In_{24}M_8O_{48}$ (M = Ge^{4+}, Sn^{4+}, Ti^{4+}, and Zr^{4+}). *J. Comput. Chem.* **2012**, *33*, 88–92. [CrossRef]

89. Guilmeau, E.; Brardan, D.; Simon, C.; Maignan, A.; Raveau, B.; Ovono Ovono, D.; Delorme, F. Tuning the Transport and Thermoelectric Properties of In_2O_3 Bulk Ceramics through Doping at In-Site. *J. Appl. Phys.* **2009**, *106*. [CrossRef]

90. Colder, H.; Guilmeau, E.; Harnois, C.; Marinel, S.; Retoux, R.; Savary, E. Preparation of Ni-Doped ZnO Ceramics for Thermoelectric Applications. *J. Eur. Ceram. Soc.* **2011**, *31*, 2957–2963. [CrossRef]

91. Zhang, D.B.; Zhang, B.P.; Ye, D.S.; Liu, Y.C.; Li, S. Enhanced Al/Ni Co-Doping and Power Factor in Textured ZnO Thermoelectric Ceramics Prepared by Hydrothermal Synthesis and Spark Plasma Sintering. *J. Alloy. Compd.* **2016**, *656*, 784–792. [CrossRef]

92. Jung, K.H.; Hyoung Lee, K.; Seo, W.S.; Choi, S.M. An Enhancement of a Thermoelectric Power Factor in a Ga-Doped ZnO System: A Chemical Compression by Enlarged Ga Solubility. *Appl. Phys. Lett.* **2012**, *100*, 3–7. [CrossRef]

93. Liu, J.; Wang, C.L.; Li, Y.; Su, W.B.; Zhu, Y.H.; Li, J.C.; Mei, L.M. Influence of Rare Earth Doping on Thermoelectric Properties of $SrTiO_3$ Ceramics. *J. Appl. Phys.* **2013**, *114*. [CrossRef]

94. Park, K.; Son, J.S.; Woo, S.I.; Shin, K.; Oh, M.W.; Park, S.D.; Hyeon, T. Colloidal Synthesis and Thermoelectric Properties of La-Doped $SrTiO_3$ Nanoparticles. *J. Mater. Chem. A* **2014**, *2*, 4217. [CrossRef]

95. Li, L.; Liu, Y.; Qin, X.; Li, D.; Zhang, J.; Song, C.; Wang, L. Enhanced Thermoelectric Performance of Highly Dense and Fine-Grained $(Sr_{1-x}Gd_x)TiO_{3-\delta}$ Ceramics Synthesized by Sol-Gel Process and Spark Plasma Sintering. *J. Alloy. Compd.* **2014**, *588*, 562–567. [CrossRef]

96. Zhang, B.; Wang, J.; Zou, T.; Zhang, S.; Yaer, X.; Ding, N.; Liu, C.; Miao, L.; Li, Y.; Wu, Y. High Thermoelectric Performance of Nb-Doped $SrTiO_3$ Bulk Materials with Different Doping Levels. *J. Mater. Chem. C* **2015**, *3*, 11406–11411. [CrossRef]

97. Chen, Y.; Liu, J.; Li, X.; Li, Y.; Su, W.; Li, J.; Zhao, L.; Wang, C.; Lu, M. Enhancement of Thermoelectric Performance of $Sr_{0.9-x}Nd_{0.1}Ti_{0.9}Nb_{0.1}O_3$ Ceramics by Introducing Sr Vacancies. *Phys. Status Solidi A* **2018**, *215*. [CrossRef]

98. Bocher, L.; Aguirre, M.H.; Logvinovich, D.; Shkabko, A.; Robert, R.; Trottmann, M.; Weidenkaff, A. $CaMn_{1-x}Nb_xO_3$ (x < 0.08) Perovskite-Type Phases As Promising New High-Temperature n-Type Thermoelectric Materials. *Inorg. Chem.* **2008**, *47*, 8077–8085.

99. Wang, Y.; Sui, Y.; Su, W. High Temperature Thermoelectric Characteristics of $Ca_{0.9}R_{0.1}MnO_3$ (R=La,Pr,Yb). *J. Appl. Phys.* **2008**, *104*. [CrossRef]

100. Thiel, P.; Eilertsen, J.; Populoh, S.; Saucke, G.; Döbeli, M.; Shkabko, A.; Sagarna, L.; Karvonen, L.; Weidenkaff, A. Influence of Tungsten Substitution and Oxygen Deficiency on the Thermoelectric Properties of $CaMnO_{3-\delta}$. *J. Appl. Phys.* **2013**, *114*. [CrossRef]

101. Seo, J.W.; Cha, J.; Won, S.O.; Park, K. Electrical Transport and Thermoelectric Properties of $Ca_{0.8}Y_{0.2-x}Dy_xMnO_{3-\delta}$ (0 < x < 0.2). *J. Am. Ceram. Soc.* **2017**, *100*, 3608–3617. [CrossRef]

102. Li, C.; Chen, Q.; Yan, Y. Effects of Pr and Yb Dual Doping on the Thermoelectric Properties of $CaMnO_3$. *Materials* **2018**, *11*, 1–13. [CrossRef] [PubMed]

103. Zhao, L.D.; Berardan, D.; Pei, Y.L.; Byl, C.; Pinsard-Gaudart, L.; Dragoe, N. $Bi_{1-x}Sr_xCuSeO$ Oxyselenides as Promising Thermoelectric Materials. *Appl. Phys. Lett.* **2010**, *97*, 10–13. [CrossRef]

104. Li, F.; Li, J. F.; Zhao, L.D.; Xiang, K.; Liu, Y.; Zhang, B.P.; Lin, Y.H.; Nan, C.W.; Zhu, H.M. Polycrystalline BiCuSeO Oxide as a Potential Thermoelectric Material. *Energy Environ. Sci.* **2012**, *5*, 7188–7195. [CrossRef]

105. Li, J.; Sui, J.; Pei, Y.; Barreteau, C.; Berardan, D.; Dragoe, N.; Cai, W.; He, J.; Zhao, L.D. A High Thermoelectric Figure of Merit zT > 1 in Ba Heavily Doped BiCuSeO Oxyselenides. *Energy Environ. Sci.* **2012**, *5*, 8543–8547. [CrossRef]

106. Feng, B.; Li, G.; Pan, Z.; Xiaoming, H.; Peihai, L.; Zhu, H.; Yawei, L.; Fan, X. Effect of Synthesis Processes on the Thermoelectric Properties of BiCuSeO Oxyselenides. *J. Alloy. Compd.* **2018**, *754*, 131–138. [CrossRef]

107. Sui, J.; Li, J.; He, J.; Pei, Y.L.; Berardan, D.; Wu, H.; Dragoe, N.; Cai, W.; Zhao, L.D. Texturation Boosts the Thermoelectric Performance of BiCuSeO Oxyselenides. *Energy Environ. Sci.* **2013**, *6*, 2916–2920. [CrossRef]

108. Bhaskar, A.; Lai, R.T.; Chang, K.C.; Liu, C.J. High Thermoelectric Performance of BiCuSeO Prepared by Solid State Reaction and Sol-Gel Process. *Scr. Mater.* **2017**, *134*, 100–104. [CrossRef]

109. Pele, V.; Barreteau, C.; Berardan, D.; Zhao, L.; Dragoe, N. Direct Synthesis of BiCuChO-Type Oxychalcogenides by Mechanical Alloying. *J. Solid State Chem.* **2013**, *203*, 187–191. [CrossRef]

110. Stampler, E.S.; Sheets, W.C.; Bertoni, M.I.; Prellier, W.; Mason, T.O.; Poeppelmeier, K.R. Temperature Driven Reactant Solubilization Synthesis of BiCuOSe. *Inorg. Chem.* **2008**, *47*, 10009–10016. [CrossRef] [PubMed]

111. Pei, Y.L.; He, J.; Li, J.F.; Li, F.; Liu, Q.; Pan, W.; Barreteau, C.; Berardan, D.; Dragoe, N.; Zhao, L.D. High Thermoelectric Performance of Oxyselenides: Intrinsically Low Thermal Conductivity of Ca-Doped BiCuSeO. *NPG Asia Mater.* **2013**, *5*. [CrossRef]

112. Li, F.; Wei, T.R.; Kang, F.; Li, J.F. Thermal Stability and Oxidation Resistance of BiCuSeO Based Thermoelectric Ceramics. *J. Alloy. Compd.* **2014**, *614*, 394–400. [CrossRef]

113. Lan, J.L.; Liu, Y.C.; Zhan, B.; Lin, Y.H.; Zhang, B.; Yuan, X.; Zhang, W.; Xu, W.; Nan, C.W. Enhanced Thermoelectric Properties of Pb-Doped BiCuSeO Ceramics. *Adv. Mater.* **2013**, *25*, 5086–5090. [CrossRef]

114. Li, F.; Wei, T.R.; Kang, F.; Li, J.F. Enhanced Thermoelectric Performance of Ca-Doped BiCuSeO in a Wide Temperature Range. *J. Mater. Chem. A* **2013**, *1*, 11942–11949. [CrossRef]

115. Sun, Y.; Zhang, C.; Cao, C.; Fu, J.; Peng, L. Co-Doping for Significantly Improved Thermoelectric Figure of Merit in p-Type $Bi_{1-2x}Mg_xPb_xCuSeO$ Oxyselenides. *Ceram. Int.* **2017**, *43*, 17186–17193. [CrossRef]

116. Feng, B.; Li, G.; Pan, Z.; Hou, Y.; Zhang, C.; Jiang, C.; Hu, J.; Xiang, Q.; Li, Y.; He, Z.; Fan, X. Effect of Ba and Pb Dual Doping on the Thermoelectric Properties of BiCuSeO Ceramics. *Mater. Lett.* **2018**, *217*, 189–193. [CrossRef]

117. Pan, L.; Lang, Y.; Zhao, L.; Berardan, D.; Amzallag, E.; Xu, C.; Gu, Y.; Chen, C.; Zhao, L.D.; Shen, X.; et al. Realization of n-Type and Enhanced Thermoelectric Performance of p-Type BiCuSeO by Controlled Iron Incorporation. *J. Mater. Chem. A* **2018**, *6*, 13340–13349. [CrossRef]

118. Zhang, X.; Feng, D.; He, J.; Zhao, L.D. Attempting to Realize n-Type BiCuSeO. *J. Solid State Chem.* **2018**, *258*, 510–516. [CrossRef]

119. Gascoin, F.; Ottensmann, S.; Stark, D.; Haïle, S.M.; Snyder, G.J. Zintl phases as thermoelectric materials: Tuned transport properties of the compounds CaxYb1-xZn2Sb2. *Adv. Funct. Mater.* **2005**, *15*, 1860–1864. [CrossRef]

120. Gayner, C.; Kar, K.K. Recent Advances in Thermoelectric Materials. *Prog. Mater. Sci.* **2016**, *83*, 330–382. [CrossRef]

121. Brown, S.R.; Kauzlarich, S.M.; Gascoin, F.; Snyder, G.J. $Yb_{14}MnSb_{11}$: New High Efficiency Thermoelectric Material for Power Generation. *Chem. Mater.* **2006**, *18*, 1873–1877. [CrossRef]

122. Toberer, E.S.; Cox, C.A.; Brown, S.R.; Ikeda, T.; May, A.F.; Kauzlarich, S.M.; Snyder, G.J. Traversing the Metal-Insulator Transition in a Zintl phase: Rational Enhancement of Thermoelectric Efficiency in $Yb_{14}Mn_{1-x}Al_xSb_{11}$. *Adv. Funct. Mater.* **2008**, *18*, 2795–2800. [CrossRef]

123. Toberer, E.S.; Brown, S.R.; Ikeda, T.; Kauzlarich, S.M.; Snyder, G.J. High Thermoelectric Efficiency in Lanthanum Doped $Yb_{14}MnSb_{11}$. *Appl. Phys. Lett.* **2008**, *93*, 11–14. [CrossRef]

124. Cox, C.A.; Brown, S.R.; Snyder, G.J.; Kauzlarich, S.M. Effect of Ca Doping on the Thermoelectric Performance of $Yb_{14}MnSb_{11}$. *J. Electron. Mater.* **2010**, *39*, 1373–1375. [CrossRef]

125. Kazem, N.; Xie, W.; Ohno, S.; Zevalkink, A.; Miller, G.J.; Snyder, G.J.; Kauzlarich, S.M. High-Temperature Thermoelectric Properties of the Solid–Solution Zintl Phase $Eu_{11}Cd_6Sb_{12-x}As_x$ (x < 3). *Chem. Mater.* **2014**, *26*, 1393–1403. [CrossRef]

126. Park, S.M.; Kim, S.J. $Sr_{11}Cd_6Sb_{12}$: A New Zintl Compound with Infinite Chains of Pentagonal Tubes. *J. Solid State Chem.* **2004**, *177*, 3418–3422. [CrossRef]

127. Kazem, N.; Hurtado, A.; Sui, F.; Ohno, S.; Zevalkink, A.; Snyder, J.G.; Kauzlarich, S.M. High Temperature Thermoelectric Properties of the Solid-Solution Zintl Phase $Eu_{11}Cd_{6-x}Zn_xSb_{12}$. *Chem. Mater.* **2015**, *27*, 4413–4421. [CrossRef]

128. Aydemir, U.; Zevalkink, A.; Ormeci, A.; Wang, H.; Ohno, S.; Bux, S.; Snyder, G.J. Thermoelectric Properties of the Zintl Phases $Yb_5M_2Sb_6$ (M = Al, Ga, In). *Dalton Trans.* **2015**, *44*, 6767–6774. [CrossRef]

129. Zevalkink, A.; Swallow, J.; Snyder, G.J. Thermoelectric Properties of Zn-Doped $Ca_5In_2Sb_6$. *Dalton Trans.* **2013**, *42*, 9713. [CrossRef] [PubMed]

130. Bobev, S.; Thompson, J.D.; Sarrao, J.L.; Olmstead, M.M.; Hope, H.; Kauzlarich, S.M. Probing the Limits of the Zintl Concept: Structure and Bonding in Rare-Earth and Alkaline-Earth Zinc-Antimonides $Yb_9Zn_{4+x}Sb_9$ and $Ca_9Zn_{4.5}Sb_9$. *Inorg. Chem.* **2004**, *43*, 5044–5052. [CrossRef] [PubMed]

131. Wu, Z.; Li, J.; Li, X.; Zhu, M.; Wu, K.C.; Tao, X.T.; Huang, B.B.; Xia, S.Q. Tuning the Thermoelectric Properties of $Ca_9Zn_{4+x}Sb_9$ by Controlled Doping on the Interstitial Structure. *Chem. Mater.* **2016**, *28*, 6917–6924. [CrossRef]

132. Bux, S.K.; Zevalkink, A.; Janka, O.; Uhl, D.; Kauzlarich, S.; Snyder, J.G.; Fleurial, J.P. Glass-Like Lattice Thermal Conductivity and High Thermoelectric Efficiency in $Yb_9Mn_{4.2}Sb_9$. *J. Mater. Chem. A* **2014**, *2*, 215–220. [CrossRef]

133. Kazem, N.; Zaikina, J.V.; Ohno, S.; Snyder, G.J.; Kauzlarich, S.M. Coinage-Metal-Stuffed $Eu_9Cd_4Sb_9$: Metallic Compounds with Anomalous Low Thermal Conductivities. *Chem. Mater.* **2015**, *27*, 7508–7519. [CrossRef]

134. Hu, Y.; Wang, J.; Kawamura, A.; Kovnir, K.; Kauzlarich, S.M. $Yb_{14}MgSb_{11}$ and $Ca_{14}MgSb_{11}$-New Mg-Containing Zintl Compounds and their Structures, Bonding, and Thermoelectric Properties. *Chem. Mater.* **2015**, *27*, 343–351. [CrossRef]

135. Tan, W.; Wu, Z.; Zhu, M.; Shen, J.; Zhu, T.; Zhao, X.; Huang, B.; Tao, X.T.; Xia, S.Q. $A_{14}MgBi_{11}$ (A = Ca, Sr, Eu): Magnesium Bismuth Based Zintl Phases as Potential Thermoelectric Materials. *Inorg. Chem.* **2017**, *56*, 10576–10583. [CrossRef]

136. Toberer, E.S.; Zevalkink, A.; Crisosto, N.; Snyder, G.J. The Zintl Compound $Ca_5Al_2Sb_6$ for Low-Cost Thermoelectric Power Generation. *Adv. Funct. Mater.* **2010**, *20*, 4375–4380. [CrossRef]

137. Zevalkink, A.; Toberer, E.S.; Bleith, T.; Flage-Larsen, E.; Snyder, G.J. Improved Carrier Concentration Control in Zn-Doped $Ca_5Al_2Sb_6$. *J. Appl. Phys.* **2011**, *110*. [CrossRef]

138. Zevalkink, A.; Swallow, J.; Snyder, G.J. Thermoelectric Properties of Mn-Doped $Ca_5Al_2Sb_6$. *J. Electron. Mater.* **2012**, *41*, 813–818. [CrossRef]

139. Chanakian, S.; Aydemir, U.; Zevalkink, A.; Gibbs, Z.M.; Fleurial, J.P.; Bux, S.; Snyder, G.J. High Temperature Thermoelectric Properties of Zn-Doped $Eu_5In_2Sb_6$. *J. Mater. Chem. C* **2015**, *3*, 10518–10524. [CrossRef]

140. Lv, W.; Yang, C.; Lin, J.; Hu, X.; Guo, K.; Yang, X.; Luo, J.; Zhao, J.T. Cd Substitution in Zintl Phase $Eu_5In_2Sb_6$ Enhancing the Thermoelectric Performance. *J. Alloy. Compd.* **2017**, *726*, 618–622. [CrossRef]

141. Chanakian, S.; Zevalkink, A.; Aydemir, U.; Gibbs, Z.M.; Pomrehn, G.; Fleurial, J.P.; Bux, S.; Snyder, G.J. Enhanced Thermoelectric Properties of $Sr_5In_2Sb_6$ via Zn-Doping. *J. Mater. Chem. A* **2015**, *3*, 10289–10295. [CrossRef]

142. Wood, M.; Aydemir, U.; Ohno, S.; Snyder, G.J. Observation of Valence Band Crossing: The Thermoelectric Properties of $CaZn_2Sb_2$-$CaMg_2Sb_2$ Solid Solution. *J. Mater. Chem. A* **2018**, *6*, 9437–9444. [CrossRef]

143. Zhang, H.; Baitinger, M.; Tang, M.B.; Man, Z.Y.; Chen, H.H.; Yang, X.X.; Liu, Y.; Chen, L.; Grin, Y.; Zhao, J.T. Thermoelectric Properties of $Eu(Zn_{1-x}Cd_x)_2Sb_2$. *Dalton Trans.* **2010**, *39*, 1101–1104. [CrossRef] [PubMed]

144. Guo, K.; Cao, Q.G.; Feng, X.J.; Tang, M.B.; Chen, H.H.; Guo, X.; Chen, L.; Grin, Y.; Zhao, J.T. Enhanced Thermoelectric Figure of Merit of Zintl Phase $YbCd_{2-x}Mn_xSb_2$ by Chemical Substitution. *Eur. J. Inorg. Chem.* **2011**, *2011*, 4043–4048. [CrossRef]

145. Wang, X.J.; Tang, M.B.; Chen, H.H.; Yang, X.X.; Zhao, J.T.; Burkhardt, U.; Grin, Y. Synthesis and High Thermoelectric Efficiency of Zintl Phase $YbCd_{2-x}Zn_xSb_2$. *Appl. Phys. Lett.* **2009**, *94*, 2007–2010. [CrossRef]

146. Cao, Q.; Zheng, J.; Zhang, K.; Ma, G. Thermoelectric Properties of $YbCd_2Sb_2$ Doped by Mg. *J. Alloy. Compd.* **2016**, *680*, 278–282. [CrossRef]

147. Shuai, J.; Kim, H.S.; Liu, Z.; He, R.; Sui, J.; Ren, Z. Thermoelectric Properties of Zintl Compound $Ca_{1-x}Na_xMg_2Bi_{1.98}$. *Appl. Phys. Lett.* **2016**, *108*. [CrossRef]

148. Shuai, J.; Liu, Z.; Kim, H.S.; Wang, Y.; Mao, J.; He, R.; Sui, J.; Ren, Z. Thermoelectric Properties of Bi-Based Zintl Compounds $Ca_{1-x}Yb_xMg_2Bi_2$. *J. Mater. Chem. A* **2016**, *4*, 4312–4320. [CrossRef]

149. Shuai, J.; Geng, H.; Lan, Y.; Zhu, Z.; Wang, C.; Liu, Z.; Bao, J.; Chu, C.W.; Sui, J.; Ren, Z. Higher Thermoelectric Performance of Zintl Phases $(Eu_{0.5}Yb_{0.5})_{1-x}Ca_xMg_2Bi_2$ by Band Engineering and Strain Fluctuation . *Proc. Natl. Acad. Sci. USA* **2016**, *113*, E4125–E4132. [CrossRef] [PubMed]

150. Bhardwaj, A.; Rajput, A.; Shukla, A.K.; Pulikkotil, J.J.; Srivastava, A.K.; Dhar, A.; Gupta, G.; Auluck, S.; Misra, D.K.; Budhani, R.C. Mg_3Sb_2-Based Zintl Compound: A Non-Toxic, Inexpensive and Abundant Thermoelectric Material for Power Generation. *RSC Adv.* **2013**, *3*, 8504–8516. [CrossRef]

151. Zheng, C.; Hoffmann, R.; Nesper, R.; von Schnering, H.G. Site Preferences and Bond Length Differences in $CaAl_2Si_2$-Type Zintl Compounds. *J. Am. Chem. Soc.* **1986**, *108*, 1876–1884. [CrossRef]

152. Shuai, J.; Wang, Y.; Kim, H.S.; Liu, Z.; Sun, J.; Chen, S.; Sui, J.; Ren, Z. Thermoelectric Properties of Na-Doped Zintl Compound: $Mg_{3-x}Na_xSb_2$. *Acta Mater.* **2015**, *93*, 187–193. [CrossRef]

153. Kim, S.; Kim, C.; Hong, Y.K.; Onimaru, T.; Suekuni, K.; Takabatake, T.; Jung, M.H. Thermoelectric Properties of Mn-Doped Mg-Sb Single Crystals. *J. Mater. Chem. A* **2014**, *2*, 12311–12316. [CrossRef]

154. Chen, X.; Wu, H.; Cui, J.; Xiao, Y.; Zhang, Y.; He, J.; Chen, Y.; Cao, J.; Cai, W.; Pennycook, S.J.; et al. Extraordinary Thermoelectric Performance in n-Type Manganese Doped Mg_3Sb_2 Zintl: High Band Degeneracy, Tuned Carrier Scattering Mechanism and Hierarchical Microstructure. *Nano Energy* **2018**, *52*, 246–255. [CrossRef]

155. Wang, Y.; Zhang, X.; Wang, Y.; Liu, H.; Zhang, J. Enhanced Thermoelectric Properties of n-Type Mg_3Sb_2 by Excess Magnesium and Tellurium Doping. *Appl. Mater. Sci.* **2019**, *1800811*, 1–6.

156. Zhang, J.; Song, L.; Pedersen, S.H.; Yin, H.; Hung, L.T.; Brummerstedt Iversen, B. Discovery of High-Performance Low-Cost n-Type Mg_3Sb_2-Based Thermoelectric Materials with Multi-Valley Conduction Bands. *Nat. Commun.* **2017**, *8*, 1–8. [CrossRef]

157. Shuai, J.; Ge, B.; Mao, J.; Song, S.; Wang, Y.; Ren, Z. Significant Role of Mg Stoichiometry in Designing High Thermoelectric Performance for $Mg_3(Sb,Bi)_2$-based n-Type Zintls. *J. Am. Chem. Soc.* **2018**, *140*, 1910–1915. [CrossRef]

158. Shuai, J.; Mao, J.; Song, S.; Zhu, Q.; Sun, J.; Wang, Y.; He, R.; Zhou, J.; Chen, G.; Singh, D.J.; Ren, Z. Tuning the Carrier Scattering Mechanism to Effectively Improve the Thermoelectric Properties. *Energy Environ. Sci.* **2017**, *10*, 799–807. [CrossRef]

159. Graf, T.; Felser, C.; Parkin, S. Simple Rules for The Understanding of Heusler Compounds. *Prog. Solid State Chem.* **2011**, *39*, 1–50. [CrossRef]

160. Larson, P.; Mahanti, S.D.; Sportouch, S.; Kanatzidis, M.G. Electronic Structure of Rare-Earth Nickel Pnictides: Narrow-Gap Thermoelectric Materials. *Phys. Rev. B Condens. Matter Mater. Phys.* **1999**, *59*, 15660–15668. [CrossRef]

161. Xia, Y.; Bhattacharya, S.; Ponnambalam, V.; Pope, A.L.; Poon, S.J.; Tritt, T.M. Thermoelectric Properties of Semimetallic (Zr, Hf)CoSb half-Heusler Phases. *J. Appl. Phys.* **2000**, *88*, 1952–1955. [CrossRef]

162. Bos, J.W.G.; Downie, R.A. Half-Heusler Thermoelectrics: A Complex Class of Materials. *J. Phys. Condens. Matter* **2014**, *26*. [CrossRef]

163. Poon, S.J. Half-Heusler Compounds: Promising Materials For Mid-To-High Temperature Thermoelectric Conversion. *J. Phys. D Appl. Phys.* **2019**, *52*, 493001. [CrossRef]

164. Aliev, F.G.; Kozyrkov, V.V.; Moshchalkov, V.V.; Scolozdra, R.V.; Durczewski, K. Narrow Band in the Intermetallic Compounds MNiSn (M=Ti, Zr, Hf). *Z. Für Phys. B Condens. Matter* **1990**, *80*, 353–357. [CrossRef]

165. Appel, O.; Cohen, S.; Beeri, O.; Shamir, N.; Gelbstein, Y.; Zalkind, S. Surface Oxidation of TiNiSn (half-Heusler) Alloy by Oxygen and Water Vapor. *Materials* **2018**, *11*, 1–16. [CrossRef]

166. Appel, O.; Breuer, G.; Cohen, S.; Beeri, O.; Kyratsi, T.; Gelbstein, Y.; Zalkind, S. The Initial Stage in Oxidation of ZrNiSn (half Heusler) Alloy by Oxygen. *Materials* **2019**, *12*, 1–14. [CrossRef]

167. He, R.; Kim, H.S.; Lan, Y.; Wang, D.; Chen, S.; Ren, Z. Investigating the Thermoelectric Properties of p-Type half-Heusler $Hf_x(ZrTi)_{1-x}CoSb_{0.8}Sn_{0.2}$ by reducing Hf concentration for power generation. *RSC Adv.* **2015**, *4*, 64711–64716. [CrossRef]

168. Liu, Y.; Fu, C.; Xia, K.; Yu, J.; Zhao, X.; Pan, H.; Felser, C.; Zhu, T. Lanthanide Contraction as a Design Factor for High-Performance Half-Heusler Thermoelectric Materials. *Adv. Mater.* **2018**, *30*, 1–7. [CrossRef]

169. He, R.; Kraemer, D.; Mao, J.; Zeng, L.; Jie, Q.; Lan, Y.; Li, C.; Shuai, J.; Kim, H.S.; Liu, Y.; et al. Achieving High Power Factor and Output Power Density in p-Type half-Heuslers $Nb_{1-x}Ti_xFeSb$. *Proc. Natl. Acad. Sci. USA* **2016**, *113*, 13576–13581. [CrossRef] [PubMed]

170. Zhu, H.; He, R.; Mao, J.; Zhu, Q.; Li, C.; Sun, J.; Ren, W.; Wang, Y.; Liu, Z.; Tang, Z.; et al. Discovery of ZrCoBi Based half-Heuslers with High Thermoelectric Conversion Efficiency. *Nat. Commun.* **2018**, *9*, 1–9. [CrossRef] [PubMed]

171. Barth, J.; Balke, B.; Fecher, G.H.; Stryhanyuk, H.; Gloskovskii, A.; Naghavi, S.; Felser, C. Thermoelectric Properties of CoTiSb Based Compounds. *J. Phys. D Appl. Phys.* **2009**, *42*. [CrossRef]

172. Huang, L.; Zhang, Q.; Wang, Y.; He, R.; Shuai, J.; Zhang, J.; Wang, C.; Ren, Z. The Effect of Sn Doping on Thermoelectric Performance of n-Type half-Heusler NbCoSb. *Phys. Chem. Chem. Phys.* **2017**, *19*, 25683–25690. [CrossRef]

173. Shutoh, N.; Sakurada, S. Thermoelectric Properties of the $Ti_x(Zr_{0.5}Hf_{0.5})_{1-x}NiSn$ half-Heusler Compounds. *J. Alloy. Compd.* **2005**, *389*, 204–208. [CrossRef]

174. Muta, H.; Kanemitsu, T.; Kurosaki, K.; Yamanaka, S. High-Temperature Thermoelectric Properties of Nb-Doped MNiSn (M = Ti, Zr) half-Heusler Compound. *J. Alloy. Compd.* **2009**, *469*, 50–55. [CrossRef]

175. Kimura, Y.; Ueno, H.; Mishima, Y. Thermoelectric Properties of Directionally Solidified half-Heusler $(M_{0.5}{}^a,M_{0.5}{}^b)NiSn$ (M^a, M^b = Hf, Zr, Ti) Alloys. *J. Electron. Mater.* **2009**, *38*, 934–939. [CrossRef]

176. Chen, L.; Gao, S.; Zeng, X.; Mehdizadeh Dehkordi, A.; Tritt, T.M.; Poon, S.J. Uncovering High Thermoelectric Figure of Merit in (Hf,Zr)NiSn half-Heusler Alloys. *Appl. Phys. Lett.* **2015**, *107*. [CrossRef]

177. Wu, T.; Jiang, W.; Li, X.; Zhou, Y.; Chen, L. Thermoelectric Properties of p-Type Fe-Doped TiCoSb half-Heusler Compounds. *J. Appl. Phys.* **2007**, *102*, 1–6. [CrossRef]

178. Rowe, D. *CRC Handbook of Thermoelectrics*; CRC Press: Boca Raton, FL, USA, 1995.

179. Lin, S.; Wang, C.; Chen, H.; Huo, D.; Savvides, N.; Chen, X. Microstructure and Thermoelectric Properties of Ga-Doped SiGe Alloys Prepared by Mechanical Alloying and Induction Hot Pressing. *Funct. Mater. Lett.* **2013**, *07*, 1450008. [CrossRef]

180. Joshi, G.; Lee, H.; Lan, Y.; Wang, X.; Zhu, G.; Wang, D.; Gould, R.; Cuff, D.; Tang, M.; Dresselhaus, M.; et al. Enhanced Thermoelectric Figure-of-Merit in Nanostructured p-type Silicon Germanium Bulk Alloys. *Nano Lett.* **2008**, *8*, 4670–4674. [CrossRef] [PubMed]

181. Wang, C.; Lin, S.; Chen, H.; Zhao, Y.; Zhao, L.; Wang, H.; Huo, D.; Chen, X. Thermoelectric Performance of $Si_{80}Ge_{20-x}Sb_x$ Based Multiphase Alloys with Inhomogeneous Dopant Distribution. *Energy Convers. Manag.* **2015**, *94*, 331–336. [CrossRef]

182. Wongprakarn, S.; Pinitsoontorn, S.; at Tanusilp, S.; Kurosaki, K. Enhancing Thermoelectric Properties of p-Type SiGe Alloy through Optimization of Carrier Concentration and Processing Parameters. *Mater. Sci. Semicond. Process.* **2018**, *88*, 239–249. [CrossRef]

183. Bathula, S.; Jayasimhadri, M.; Singh, N.; Srivastava, A.K.; Pulikkotil, J.; Dhar, A.; Budhani, R.C. Enhanced Thermoelectric Figure-of-Merit in Spark Plasma Sintered Nanostructured n-Type SiGe Alloys. *Appl. Phys. Lett.* **2012**, *101*. [CrossRef]

184. Nozariasbmarz, A.; Agarwal, A.; Coutant, Z.A.; Hall, M.J.; Liu, J.; Liu, R.; Malhotra, A.; Norouzzadeh, P.; Öztürk, M.C.; Ramesh, V.P.; et al. Thermoelectric Silicides: A Review. *Jpn. J. Appl. Phys.* **2017**, *56*, 27. [CrossRef]

185. Wang, X.; Lee, H.; Lan, Y.; Zhu, G.; Joshi, G.; Wang, D.; Yang, J.; Muto, A.; Tang, M.; Klatsky, J.; et al. Enhanced Thermoelectric Figure-of-Merit in Nanostructured n-Type Silicon Germanium Bulk Alloys. *Appl. Phys. Lett.* **2008**, *93*, 193121. [CrossRef]

186. Zamanipour, Z.; Vashaee, D. Comparison of Thermoelectric Properties of p-Type Nanostructured Bulk $Si_{0.8}Ge_{0.2}$ Alloy with $Si_{0.8}Ge_{0.2}$ Composites Embedded with $CrSi_2$ Nano-Inclusisons. *J. Appl. Phys.* **2012**, *112*, 0–9. [CrossRef]

187. Mackey, J.; Dynys, F.; Sehirlioglu, A. Si/Ge–WSi_2 Composites: Processing and Thermoelectric Properties. *Acta Mater.* **2015**, *98*, 263–274. [CrossRef]

188. Usenko, A.; Moskovskikh, D.; Korotitskiy, A.; Gorshenkov, M.; Voronin, A.; Arkhipov, D.; Lyange, M.; Isachenko, G.; Khovaylo, V. Thermoelectric Properties of n-Type $Si_{0.8}Ge_{0.2}$-$FeSi_2$ Multiphase Nanostructures. *J. Electron. Mater.* **2016**, *45*, 3427–3432. [CrossRef]

189. Wongprakarn, S.; Pinitsoontorn, S.; Tanusilp, S.A.; Kurosaki, K. The Effect of YSi_2 Nanoinclusion on the Thermoelectric Properties of p-Type SiGe Alloy. *Phys. Status Solidi (A) Appl. Mater. Sci.* **2017**, *214*, 1–5. [CrossRef]

190. Basu, R.; Bhattacharya, S.; Bhatt, R.; Roy, M.; Ahmad, S.; Singh, A.; Navaneethan, M.; Hayakawa, Y.; Aswal, D.K.; Gupta, S.K. Improved Thermoelectric Performance of Hot Pressed Nanostructured n-Type SiGe Bulk Alloys. *J. Mater. Chem. A* **2014**, *2*, 6922–6930. [CrossRef]

191. Ahmad, S.; Singh, A.; Bohra, A.; Basu, R.; Bhattacharya, S.; Bhatt, R.; Meshram, K.N.; Roy, M.; Sarkar, S.K.; Hayakawa, Y.; et al. Boosting Thermoelectric Performance of p-Type SiGe Alloys through in-situ Metallic YSi_2 Nanoinclusions. *Nano Energy* **2016**, *27*, 282–297. [CrossRef]

192. Bathula, S.; Jayasimhadri, M.; Gahtori, B.; Kumar, A.; Srivastava, A.K.; Dhar, A. Enhancement in Thermoelectric Performance of SiGe Nanoalloys Dispersed with SiC Nanoparticles. *Phys. Chem. Chem. Phys.* **2017**, *19*, 25180–25185. [CrossRef] [PubMed]

193. Nozariasbmarz, A.; Roy, P.; Zamanipour, Z.; Dycus, J.H.; Cabral, M.J.; LeBeau, J.M.; Krasinski, J.S.; Vashaee, D. Comparison of Thermoelectric Properties of Nanostructured Mg_2Si, $FeSi_2$, SiGe, and Nanocomposites of SiGe-Mg_2Si, SiGe-$FeSi_2$. *APL Mater.* **2016**, *4*. [CrossRef]

194. Nozariasbmarz, A.; Zamanipour, Z.; Norouzzadeh, P.; Krasinski, J.S.; Vashaee, D. Enhanced Thermoelectric Performance in a Metal/Semiconductor Nanocomposite of Iron Silicide/Silicon Germanium. *RSC Adv.* **2016**, *6*, 49643–49650. [CrossRef]

195. Zheng, G.; Su, X.; Liang, T.; Lu, Q.; Yan, Y.; Uher, C.; Tang, X. High Thermoelectric Performance of Mechanically Robust n-Type $Bi_2Te_{3-x}Se_x$ Prepared by Combustion Synthesis. *J. Mater. Chem. A* **2015**, *3*, 6603–6613. [CrossRef]

196. Fu, C.; Zhu, T.; Liu, Y.; Xie, H.; Zhao, X. Band Engineering of High Performance p-Type FeNbSb Based half-Heusler Thermoelectric Materials for Figure of Merit $zT > 1$. *Energy Environ. Sci.* **2015**, *8*, 216–220. [CrossRef]

197. Kleinke, H. New Bulk Materials for Thermoelectric Power Generation: Clathrates and Complex Antimonides. *Chem. Mater.* **2010**, *22*, 604–611. [CrossRef]

198. Nolas, G.S.; Morelli, D.T.; Tritt, T.M. Skutterudites: A Phonon-Glass-Electron Crystal Approach to Advanced Thermoelectric Energy Conversion Applications. *Annu. Rev. Mater. Sci.* **1999**, *29*, 89–116. [CrossRef]

199. Shi, X.; Yang, J.; Bai, S.; Yang, J.; Wang, H.; Chi, M.; Salvador, J.R.; Zhang, W.; Chen, L.; Wong-Ng, W. On the Design of High-Efficiency Thermoelectric Clathrates Through a Systematic Cross-Substitution of Framework Elements. *Adv. Funct. Mater.* **2010**, *20*, 755–763. [CrossRef]

200. Zhang, L.; Grytsiv, A.; Rogl, P.; Bauer, E.; Zehetbauer, M. High Thermoelectric Performance of Riple-Filled n-Type Skutterudites $(Sr,Ba,Yb)_yCo_4Sb_{12}$. *J. Phys. D Appl. Phys.* **2009**, *42*. [CrossRef]

201. Shi, X.; Yang, J.; Salvador, J.R.; Chi, M.; Cho, J.; Wang, H.; Bai, S.; Yang, J.; Zhang, W.; Chen, L. Multiple-Filled Skutterudites: High Thermoelectric Figure of Merit Through Separately Optimizing Electrical and Thermal Transports. *J. Am. Chem. Soc.* **2011**, *133*, 7837–7846. [CrossRef] [PubMed]

202. Zaitsev, V.K.; Fedorov, M.I.; Gurieva, E.A.; Eremin, I.S.; Konstantinov, P.P.; Samunin, A.Y.; Vedernikov, M.V. Highly Effective $Mg_2Si_{1-x}Sn_x$ Thermoelectrics. *Phys. Rev. B Condens. Matter Mater. Phys.* **2006**, *74*, 2–6. [CrossRef]

203. Khan, A.U.; Vlachos, N.V.; Hatzikraniotis, E.; Polymeris, G.S.; Lioutas, C.B.; Stefanaki, E.C.; Paraskevopoulos, K.M.; Giapintzakis, I.; Kyratsi, T. Thermoelectric Properties of Highly Efficient Bi-Doped $Mg_2Si_{1-x-y}Sn_xGe_y$ Materials. *Acta Mater.* **2014**, *77*, 43–53. [CrossRef]

1.3 From material to device - Thermoelectric generators

Additionally to the research on improving thermoelectric materials itself, the path from a designed material to a functional TEG raises several new issues. Within this chapter, the working principle of a TEG is introduced and several additional tasks on the way from a material to a device are pointed out. Here, especially the manufacturing process has gained increasing attention in recent years, which is also in the focus of this work. Until now, main application fields for supply of electrical energy via TEGs (generator mode) have been established in space exploration in satellites and space rovers, converting the heat radiated by radio nuclid batteries, energy recycling in power plants and some niche applications like converting body heat for electronic supply of small gadgets [48, 82, 83]. Furthermore, applications in the automotive sector and big industrial processes, where large amounts of waste heat are generated, are promising but require further improvement in power output and efficiency and reduction of production costs of TEGs. Consequently, the manufacturing technology of TEGs is a second large research field besides the previously discussed improvement of the materials itself.

1.3.1 Working principle of TEGs

In Figure 1.13, the schematic working principle of a conventional TEG with two thermocouples of n- and p-type thermoelectric materials is shown [84]. The conventional design is based on an alternating order of n- and p-type bulk thermoelectric materials (legs), connected via metallic connectors. On the left, the currents of entropy (red arrows) and charge (blue arrows) through the device are displayed. Entropy flows from the hot side (top) to the cold side (bottom) through the respective n- and p-type legs. Within the materials, charge carriers (electrons for n- and defect electrons for p-type materials) gain a higher energy at the hot side of the materials, inducing a flow of charge carriers within the thermolegs. The flow of entropy is thus coupled with the flow of charge, either in the same or in the opposite direction. Due to the alternating order of the thermoelectric materials, this results in an electrical ring circuit which is capable of performing electrical work. The occurring energy conversion is displayed on the right side. Thermal energy (red arrows) enters the device at the top side and is partly converted into electrical energy (blue arrows) within the thermoelectric materials. As a result, the amount of thermal energy decreases along the thermoleg (indicated by the decreasing width of the red arrows), while the electrical energy increases (indicated by the increasing width of the blue arrows). In total, at the top side of the device, the thermal energy is higher compared to the bottom side, while the electrical energy is lower on the electrical input of the device compared to the electrical output. As a result of the serial connection of the thermoelectric materials and the requirement to avoid short circuit between the thermolegs, a free space in between the materials is required. As this free space does not contribute in the energy conversion, it is aimed to reduce this free volume as much as possible.

The total power output and power density of a TEG can be analysed via a voltage-electrical current curve and the resulting electrical power curve, exemplarily shown in Figure 1.14. The voltage U and electrical current I_q are measured at different
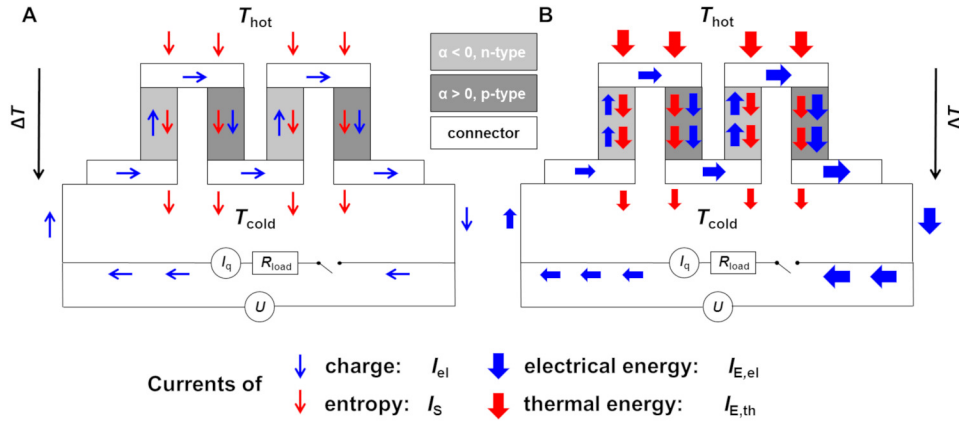
Fig. 1.13: Schematic working principle of a TEG with two thermocouples. A) When a temperature difference between the top and the bottom side is applied, an entropy current (red) is induced, which is coupled to an electrical current (blue) within the n- and p-type materials. As a result, an electrical ring circuit occurs. The energy conversion due to the coupling is shown in B). The thermal energy (red arrows) enters the device at the top and is partly converted into electrical energy within the thermo-electric materials. The electrical energy (blue arrows) is low on the electrical input and high at the electrical output. Reproduced from [84].

external load resistances, which results in the linear U-I_q curve (black). Here, the open-circuited voltage U_{OC} (for electrical open-circuit $I_q = 0$) and the short-circuited current $I_{q,SC}$ (for electrical short-circuit $U = 0$) are characteristic points. The electrical power P_{el} can be determined as the product of voltage U and electrical current I_q (red curve). The maximum electrical power output of a TEG $P_{el,max,TEG}$ is a characteristic point located at half the open-circuit voltage U_{OC} and half the short-circuit current $I_{q,SC}$. Usually, the maximum power output $P_{el,max,TEG}$ is normalized to the effective area of a TEG, resulting in the maximum electrical power density $\omega_{el,max,TEG}$, which is used for comparison in most literature.

The maximum electrical power output of a TEG $P_{el,max,TEG}$ obviously depends on the respective thermoelectric materials and can also be mathematically determined as a function of the material properties according to Equation 1.16.

$$P_{el,max,TEG} = \frac{1}{4} \cdot \frac{A}{l} \cdot \frac{(\sum \alpha_p - \sum \alpha_n)^2}{\sum \frac{1}{\sigma_p} + \sum \frac{1}{\sigma_n}} \cdot (\Delta T)^2 = \frac{U_{OC}^2}{4 \cdot R_{TEG}} \tag{1.16}$$

However, within Equation 1.16, contact resistances between the legs and the connectors are neglected, which can be misleading, as the contacting of the materials is an important task. To achieve maximum electrical power output, the total electrical resistance of the TEG R_{TEG} should be as low as possible, including the resistances of the legs as well as the contacts. The influence of the respective contact resistances is a complex question, which is not fully understood yet.

The maximum conversion efficiency of a TEG can also be calculated via

$$\eta_{TEG,max} = \frac{T_{hot} - T_{cold}}{T_{hot}} \cdot \frac{\sqrt{1 + z\bar{T}} - 1}{\sqrt{1 + z\bar{T}} + 1} \tag{1.17}$$

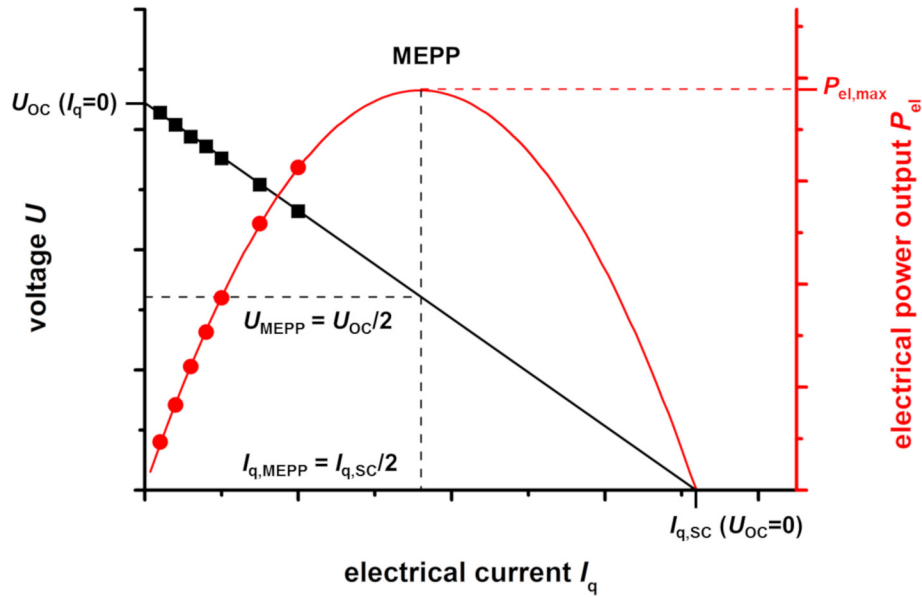with the average figure of merit $z\bar{T}$, which is directly connected to the material

Fig. 1.14: Characterization of a TEG via U-I_q curve (black) and P_{el}-I_q curve (red). The electrical power P_{el} is determined as the product of the voltage U and the electrical current I_q. The maximum electrical power output $P_{el,max}$ is achieved at half the open-circuit voltage U_{OC} and half the short-circuit current $I_{q,SC}$.

properties. Analogously to the deviation of maximum power output and maximum conversion efficiency discussed for materials, the respective properties of a TEG can also deviate for some material combinations according to finite-element (FEM) simulations included in section 1.3.4. Therefore, materials choice for a TEG may also strongly depend on the desired application. This results in a plethora of possibilities to design a device for various situations and applications.

1.3.2   Manufacturing of TEGs

The conventional manufacturing route of TEGs consists of multiple steps including synthesis of materials, pressing, shaping and electrical contacting [85]. Next to the materials itself, this process accounts for a non-negligible share in the overall costs for a desired commercial application [86]. Thus, improving the manufacturing by investigating fast and easy processing, e.g., via printing processes, is an important research field. Over the years, quite different designs of TEGs have been reported: (1) The most common conventional design ('chessboard' design) consisting of a rigid design of alternating p-type and n-type thermoelectric materials with metallic connectors and Al_2O_3 plates and (2) the flexible design, where films are usually used and attached to a flexible polymeric substrates. Both designs can be used in the commercial design of alternating p-type and n-type legs as well as in the uni-leg design, consisting of only a p-type or a n-type thermoelectric active material. Generally, the manufacturing of a TEG strongly depends on the application field, especially in respect to the thermal stability of the respective parts within the certain atmosphere.

1.3.3 Printing processes

In recent years, investigation of fast and easy manufacturing routes for TEGs has drawn more and more attention. Especially the rising concept of additive manufacturing (AM), which describes 'the process of joining materials to make parts or object from 3D model data, usually layer upon layer, as opposed to subtractive manufacturing methods' (ISO/ASTM 52900:2015 [87]), is an interesting concept for the production of TEGs. In Figure 1.15, various additive printing technologies are displayed. All of the displayed methods require inks or pastes of the materials with varying requirements, making the production of these a topic of itself. Inkjet printing (Figure 1.15A) is a well-known solution-based, highly controllable and mask free additive process, where ink droplets are printed onto the substrate. This can be done either in a continuous mode, where selective droplets are charged and deflected onto the substrate, or in drop-on-demand mode, where a thermal or piezoelectric signal triggers the drop. For inkjet printing, the fluid density, viscosity and surface tension are very important, thus additives are often used to reach suitable properties of the respective inks. Additionally, as the ink is printed through a nozzle, a dispersion of particles in a solution can lead to problems like particles agglomerating and blocking the nozzle. In a similar way, dispenser printing (Figure 1.15B) describes a continuous filament extrusion out of a nozzle onto a computer controlled movable substrate. Again, the ink is printed through a nozzle, leading to similar requirement as for inkjet printing. In screen printing (Figure 1.15C), the respective ink is pressed through a porous mesh, which defines the resulting structure. Although the ink requirements for screen printing are less strict compared to nozzle-based techniques in regards to the particle size and agglomeration, it's still necessary to reach a specific viscosity range. Additionally, the design of the resulting structure is given by the printing mesh and changing the structure always requires a new design. Alongside long drying times, this leads to comparably high production costs for this method. All three methods have specific requirements for the ink and the contained particles, thus organic additives are often used to control the resulting viscosity and surface tension. This usually requires organic additives and it has been proven that these additives can have a negative effect on the resulting thermoelectric properties, especially the electrical conductivity [88]. Via stereolithography (Figure 1.15D) self-supporting thermoelectric structures can be produced. Here, the material is suspended in a photosensitive resin, which can be solidified by a computer-controlled ultraviolet laser. This way, self-supporting structures of the materials and the resin can be produced and the resin can be removed in a subsequent thermal sintering step. The main advantage here is the total absence of a printing substrate, but the resulting structures are highly porous, strongly decreasing the resulting electrical conductivity. Furthermore, the production of a functional TEG with many thermocouples would be much slower with this method.

All of these printing technologies have been used for the preparation of thermoelectric structures or functional TEGs before. Table 1.2 displays some reported processed TEG prototypes and the respective maximum power density achieved. Here, prototypes based on the common Bi_2Te_3 systems reached maximum power output values in the range of several $\mu W\ cm^{-2}$ [89] up to a few $mW\ cm^{-2}$ [83] while metallic or polymeric based TEG prototypes reach a somewhat lower maximum power output in the range of several $nW\ cm^{-2}$ [90,91] up to a few $\mu W\ cm^{-2}$ [92]. Additionally, some basic coating methods like dip-coating or spray-coating, where far less requirements for the used ink
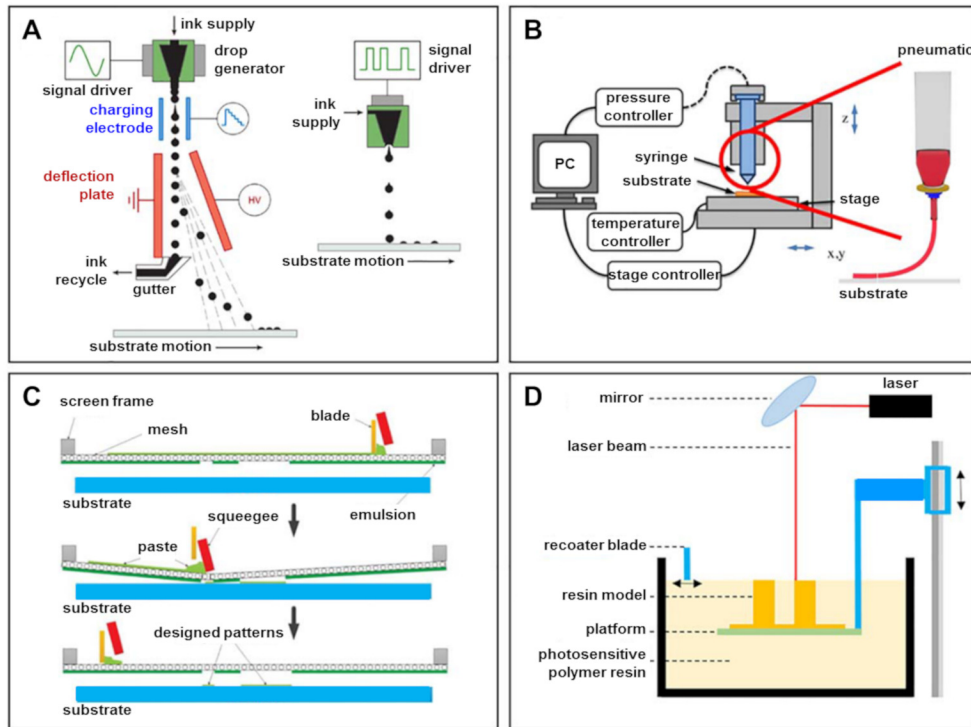
Fig. 1.15: Various printing methods utilized for TEG processing: A) Inkjet printing in continuous mode (left) or in drop-on-demand mode (right), B) dispenser printing, C) screen printing and D) stereolithography process. Reproduced from [85].

are present, could also be interesting for the preparation of thermoelectric layers, however, they do not provide a structuring method to gain the leg-based design of a TEG. Another important factor to utilize printing technology for the production of TEGs is the substrate required for most printing technology. A flexible substrate brings the advantage of being adaptable to the surface of the application, e.g., a curved surface on a mechanical component like in the automotive sector. However, the polymers used as a substrate limit the resulting maximum application temperature of the TEG to the thermal stability of the polymer. Therefore, for applications at elevated temperatures, ceramic-based substrates are usually used, which do not bring the flexibility but can withstand the high temperatures. In the case of oxide-based materials such as CCO, the material requires a sintering step to achieve its promising thermoelectric properties which has to be integrated into a possible manufacturing route and also sets the requirement of thermal stability for the substrate.

1.3.4 Laser-induced processes for manufacturing

For the processing of electronic structures and as generally interesting tool for additive manufacturing, utilization of a laser treatment has arisen in recent years [96, 97]. Via the very high energy input that a laser can provide into a substrate or surface, these can be cut, structured or even partly sintered in a very fast way. Thus, laser-based additive manufacturing has been established as a production technology to produce solid structures via laser sintering of powder components. For this, almost any powder material that can be thermally sintered, can be used. With respect to the used laser source, the material sintered and a variety of other parameters, the

Table 1.2: Literature data for reported processed TEG prototypes with their achieved power output and energy conversion efficiency $\eta_{\text{TEG,max}}$.

| Process	p-type material	n-type material	ΔT / K	$P_{\text{el,max}}$ or $\omega_{\text{el,max}}$	Reference
Electrochemical	Cu	Ni	32	25 nW cm^{-2}	[90]
Dispenser	Sb$_2$Te$_3$	Bi$_2$Te$_3$	20	75 μW cm^{-2}	[89]
Dispenser	-	Bi$_2$Te$_3$	20	1.6 μW	[93]
Screen printing	Sb$_2$Te$_3$	Bi$_2$Te$_3$	50	3.8 mW cm^{-2}	[83]
Inkjet	Ag	PEDOT:PSS	100	11.1 nW	[91]
Screen printing	-	Bi$_2$Te$_3$	60	4.1 μW cm^{-2}	[94]
Screen printing	Sb$_2$Te$_3$	Bi$_2$Te$_3$	20	420 nW	[95]
Screen printing	PEDOT:PSS	TiS$_2$	30	55 μW	[92]
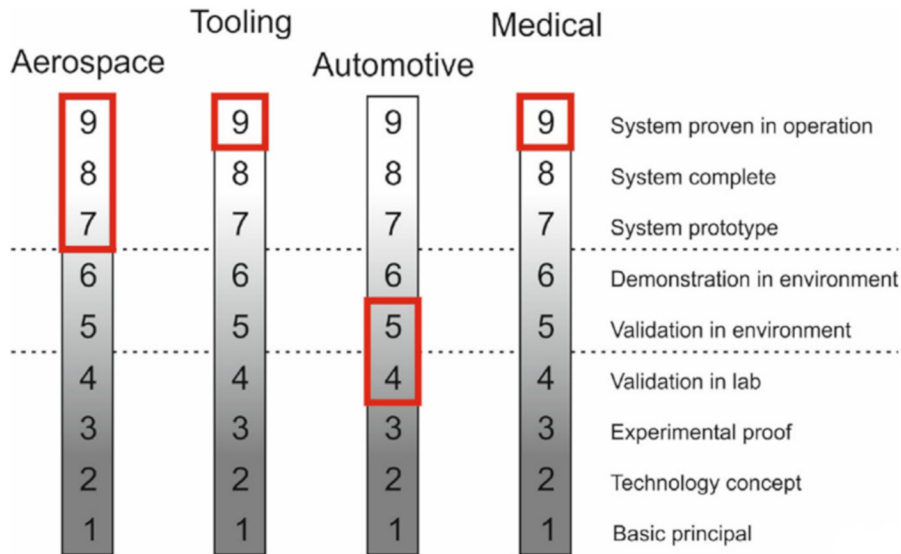
Fig. 1.16: Technology readiness level (TRL) of laser-based additive manufacturing technology for various application fields. Reproduced from [97].

related methods are subdivided into individual processes, e.g., laser beam melting of metals (LBM-M) or of polymers (LBM-P) and many more [97]. The above introduced stereolithography also counts to the category of laser-based additive manufacturing. As laser sources, CO$_2$-lasers, fiber lasers or Nd:YAG lasers are the most common. Usually these lasers can be operated as continuous wave (CW) lasers or pulsed lasers. For metals and polymers, melting and sintering via laser treatment is an established method [97–101]. Figure 1.16 shows the technology readiness levels (TLR) for laser-induced AM processes [97]. In various application fields, LBM products are already established and used frequently. In the categories aerospace, tooling and medical applications a TLR rating of 9 is reached, meaning the according system is proven and established for an operational system. Within the automotive sector, validation of this technology is in work (TRL rating up to 5). Here, mostly metallic and polymeric materials are used for LBM processes.

For thermoelectric materials, however, only a few studies are available investigating a laser treatment of the material to improve the resulting properties, e.g., for the Bi-Sb system, Mn-Si system and SrTiO$_3$ [102]. Additionally, some basic research has been done on laser treatment of materials for other energy harvesting processes like

TiO$_2$ [103], which is commonly used for photocatalysis and for electrolytes for fuel cells [104]. Due to being a very fast process, laser treatment, melting and sintering are interesting tools to be utilized for large-scale TEG production. This can be especially advantageous when a thermal sintering step of the thermoelectric materials or connection can be replaced by a much faster laser-based technique.

1.3.5 Geometry optimization of thermoelectric modules: Deviation of optimum power output and conversion efficiency

Mario Wolf, Alexey Rybakov, Richard Hinterding and Armin Feldhoff

Article

Geometry Optimization of Thermoelectric Modules: Deviation of Optimum Power Output and Conversion Efficiency

Mario Wolf *[ID]**, Alexey Rybakov, Richard Hinterding and Armin Feldhoff ***[ID]

Institute of Physical Chemistry and Electrochemistry, Leibniz University Hannover, Callinstraße 3A,
D-30167 Hannover, Germany; alexey.rybakov@pci.uni-hannover.de (A.R.);
richard.hinterding@pci.uni-hannover.de (R.H.)

***** Correspondence: mario.wolf@pci.uni-hannover.de (M.W.); armin.feldhoff@pci.uni-hannover.de (A.F.)

check for updates

Abstract: Besides the material research in the field of thermoelectrics, the way from a material to a functional thermoelectric (TE) module comes alongside additional challenges. Thus, comprehension and optimization of the properties and the design of a TE module are important tasks. In this work, different geometry optimization strategies to reach maximum power output or maximum conversion efficiency are applied and the resulting performances of various modules and respective materials are analyzed. A Bi_2Te_3-based module, a half-Heusler-based module, and an oxide-based module are characterized via FEM simulations. By this, a deviation of optimum power output and optimum conversion efficiency in dependence of the diversity of thermoelectric materials is found. Additionally, for all modules, the respective fluxes of entropy and charge as well as the corresponding fluxes of thermal and electrical energy within the thermolegs are shown. The full understanding and enhancement of the performance of a TE module may be further improved.

1. Introduction

The direct energy conversion from wasted thermal energy into usable electrical energy via thermoelectric (TE) modules has been extensively studied and improved in recent years. Such devices benefit from long-term stability without the need of maintenance and they are quietly operating without moving parts that may get damaged over time [1]. The main parts of research on thermoelectric energy conversion are investigating and improving thermoelectric materials in order to reach high power output and high conversion efficiency on the one hand [2,3] and the scalable and effective manufacturing of devices on the other hand [4,5]. However, up to now, TE modules have not achieved characteristics that justify the investment for a wide commercial usage. Especially, the design of the device, the optimization of the cross-sectional area ratio, and thermal and electrical contact resistivity are crucial factors on the way from a promising material to a functional device with high power output and conversion efficiency [6], even if suitable thermoelectric materials are provided. The aim of the work is to improve the understanding and the optimization of the working principle of TE modules based on finite element method (FEM) simulations of several material combinations with the software ANSYS for various geometry optimization strategies.

1.1. Thermoelectric Materials

The thermoelectric energy conversion can be described by the coupling of the flux density of electric charge j_q and the flux density of entropy j_s. These fluxes are transmitted by the thermoelectric

material tensor, which represents the characteristics of the included thermoelectric materials with a cross-sectional area A and length l, when simultaneously placed in a gradient of electrical potential $\nabla \varphi$ and a gradient of temperature ∇T, as shown in Equation (1) [7,8].

$$\begin{pmatrix} j_q \\ j_s \end{pmatrix} = \frac{A}{l} \cdot \begin{pmatrix} \sigma & \sigma \cdot \alpha \\ \sigma \cdot \alpha & \sigma \cdot \alpha^2 + \Lambda_{OC} \end{pmatrix} \cdot \begin{pmatrix} -\nabla \varphi \\ -\nabla T \end{pmatrix} \tag{1}$$

The energy conversion is therefore mainly based on three material parameters: the isothermal electrical conductivity σ, the Seebeck coefficient α and the entropy conductivity at electrical open-circuit Λ_{OC}. In principle, all three quantities are tensors themselves, but, for homogeneous materials, they are often treated as scalars [8,9]. The figure of merit $f = zT$ [10,11] shown in Equation (2), which displays the conversion efficiency of a thermoelectric material, is a function of the three material parameters.

$$f = \frac{\sigma \cdot \alpha^2}{\Lambda_{OC}} = \frac{\sigma \cdot \alpha^2}{\lambda_{OC}} \cdot T = zT \tag{2}$$

Consequently, thermoelectric materials are usually desired to have a high power factor $\sigma \alpha^2$ and a simultaneously low open-circuited entropy conductivity Λ_{OC}. Note that, due to the use of entropy conductivity Λ_{OC} instead of the heat conductivity λ_{OC}, the absolute temperature T does not occur explicitly within the short form of Equation (2), but implicitly within the three material parameter $\sigma(T)$, $\alpha(T)$ and $\Lambda_{OC}(T)$ [11].

Within the thermoelectric materials, the respective flux density of thermal energy $j_{E,th}(x)$ and flux density of electrical energy $j_{E,el}(x)$ at a certain point x across the length of the materials are given as the product of the respective flux density of entropy $j_S(x)$ and flux density of electrical charge $j_q(x)$ and the temperature $T(x)$ and voltage $U(x) = \Delta \varphi(x)$ at this point (Equations (3) and (4)) [8]. Note that this description is analyzed as a function of x, along a central line through the respective thermoleg (compare Figure A1), so these values as a function of x are used as scalars.

$$j_{E,th}(x) = j_S(x) \cdot T(x) \tag{3}$$

$$j_{E,el}(x) = j_q(x) \cdot U(x) \tag{4}$$

These descriptions of electrical and thermal phenomena are used as a basis to analyze and improve the understanding of thermoelectric modules within this work. Here, the explicit description of the flux densities of charge and entropy and the resulting flux densities of thermal and electrical energy can be useful in order to further understand and improve the thermoelectric energy conversion.

As thermoelectric materials, various classes of materials have been studied intensively including bismuth telluride [12,13], which is commonly used for thermoelectric modules, other tellurides [14], and selenides [15,16], intermetallic phases, such as as Zintl phases [17–19] and half-Heusler phases [20,21], oxides and oxyselenides [22,23], and conductive polymers [24,25]. Each material class provides a different thermoelectric characteristic, requires special treatments or fabrication and it is suitable in a certain application temperature range [2]. In order to influence and improve the thermoelectric properties, band structure modelling via doping and nanostructuring [26–28], segmentation of thermolegs [29–31] and the utilization of hybrid materials [32–34] are widely investigated.

The resulting thermoelectric performance of a material is usually described by the U-I_q-characteristic (voltage-electrical current curve) and the resulting electrical power curve P_{el}-I_q. Here, two important material working points can be identified: the maximum electrical power point (MEPP) of a respective material (the point where $P_{el} = U \cdot I_q$ reaches its maximum), which is given at half the open-circuited voltage U_{OC}, and half the short-circuited current $I_{q,SC}$ and the maximum conversion efficiency point (MCEP) of a respective material, which is a function of the figure of merit zT of the material. The MCEP and MEPP drift apart with increasing figure of merit zT of the respective material, As shown in a previous work [11] (Figure 1). Therefore, optimizing different parameters to influence the materials MEPP and MCEP are important to effectively improve the performance of

a resulting TE module. Furthermore, this implies that not only the resulting conversion efficiency based on the figure of merit zT, but also the resulting electrical power output, which is a function of the power factor $\sigma\alpha^2$, is a key parameter. In fact, the power factor should have at least the same significance as the figure of merit zT, as has been reported before [2,35].
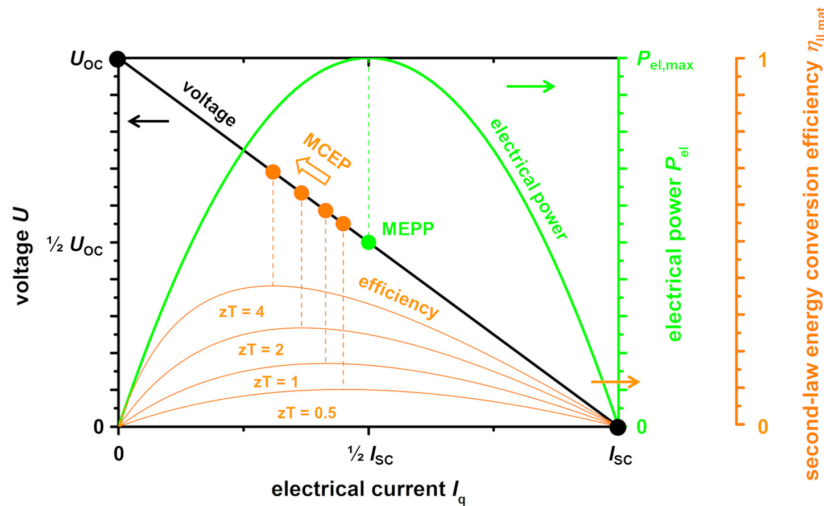

Figure 1. Normalized U-I_q and P_{el}-I_q characteristics of some hypothetic thermoelectric materials with a zT of 0.5, 1, 2, and 4. The second-law energy conversion efficiency $\eta_{II,mat}$ increases with increasing figure of merit zT. The maximum conversion efficiency point (MCEP) is a function of the figure of merit zT and, therefore, drifts apart from the maximum electrical power point (MEPP). Working points of short-circuit (SC) with the short-circuit current $I_{q,SC}$ and open-circuit (OC) with the open-circuit voltage U_{OC} are marked. Reworked from [11].

1.2. From Material to Device

In this work, the concept of the material working points MEPP and MCEP and the resulting significance of figure of merit zT and power factor $\sigma\alpha^2$ are transferred to a TE module. As described before, the concept and design of a TE module also strongly influence the resulting performance. This is based on several factors:

- The respective thermoelectric materials properties.
- The design of the respective device, the flexibility and the free volume.
- The aimed application temperature range, limiting the options for thermoelectric materials.
- Optimization factors, such as thermal- and electrical-contact resistivity, as well as the cross-sectional area ratio between n- and p-type materials

Especially, the respective geometry of the p- and n-type materials strongly influence the certain MEPP and MCEPs of the materials and therefore the resulting performance of the TE module [6]. Often, the geometry is optimized to a maximum figure of merit zT and the resulting A_n/A_p ratio is used for simulations for example by Ouyang and Li [30]. For certain materials, this optimization, in fact, leads to overlapping MCEP and MEPPs of the respective materials in a resulting module due to matching values of the thermal conductivity $\lambda_n = \lambda_p$ [36], which, however, is not always the case. Recently, Xing et al. [36] also described that an optimization of TE modules for a high power output and an according materials choice can strongly enhance the resulting properties when compared to an optimization for maximum energy conversion efficiency. This corresponds to the assertion of the significance of the power factor. Therefore, in this work, an analysis of different material combinations in a TE module is provided, based on the analogous description of $j_{E,th}(x)$ and

$j_{E,el}(x)$ shown above for three different optimization strategies: for maximum zT, for matching $I_{q,SC}$ (and, therefore, overlapping material working points), and for maximum electrical power output. For this purpose, FEM simulations of various modules are provided both based on materials with similar (Bi_2Te_3-based TE module and half-Heusler-based TE module), as well as with very different thermoelectric properties (oxide-based TE module) of the *n*- and *p*-type materials.

2. Methods and Simulation

2.1. Materials and Modules for FEM Simulations

Table 1 shows the used materials. For all thermoelectric materials, literature data have been used. The exact input values are shown in Tables A1–A3 in Appendix A. As a connector, a metal conductor made of copper with 0.5 mm height, an electrical conductivity of 4.85×10^8 S m^{-1} and a thermal conductivity of 400 W m^{-1} K^{-1} was used. Figure 2 shows the resulting TE modules used for FEM simulations.

Table 1. Material combinations for the simulated modules with according literature for the thermoelectric properties. The exact input values are shown in Tables A1–A3 in Appendix A. For all modules, a stable temperature difference of 50 K has been assumed. For the calculation of the A_n/A_p ratios, a linear behavior has been assumed and the calculation was done with the medium values of the respective temperature range.

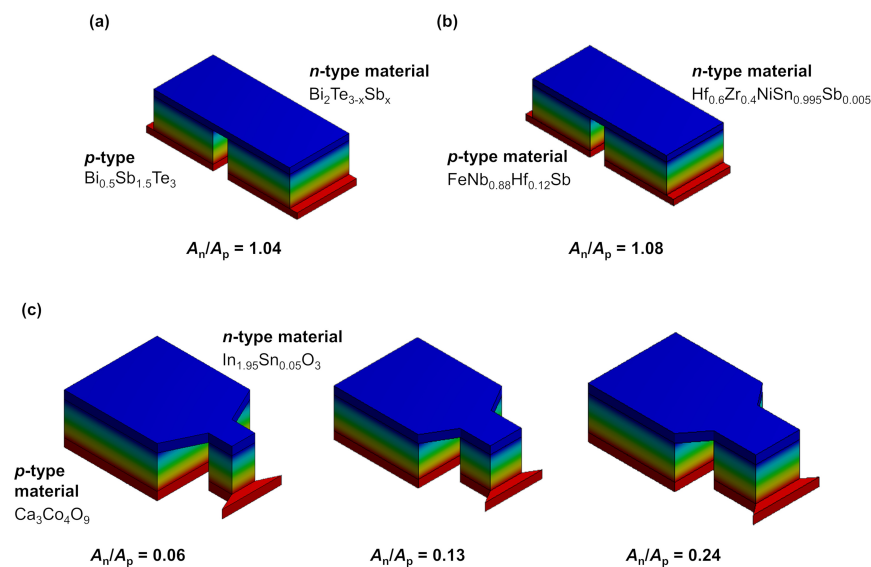| Module	*p*-Type	*n*-Type	T_{hot}/K	T_{cold}/K
Module 1	$Bi_{0.5}Sb_{1.5}Te_3$ [37]	$Bi_2Te_{3-x}Sb_x$ [38]	348	298
Module 2	$FeNb_{0.88}Hf_{0.12}Sb$ [39]	$Hf_{0.6}Zr_{0.4}NiSn_{0.995}Sb_{0.005}$ [40]	1000	950
Module 3	$Ca_3Co_4O_9$ [41]	$In_{1.95}Sn_{0.05}O_3$ [41]	1075	1025

Figure 2. Resulting modules characterized via finite elemente simulations (FEM)-simulations. (**a**) Bi_2Te_3-based TE module 1, (**b**) half-Heusler-based TE module 2, and (**c**) oxide-based TE module 3 with three different A_n/A_p ratios. The colors refer to the respective temperatures (red: hot side, blue: cold side). Note that the effective area $A_n + A_p$ is constant for all modules and A_n/A_p ratios. As connector, the characteristics of copper has been used in the simulation.

2.2. Optimization of Geometry

The A_n/A_p ratios for the simulated modules have been calculated for three different optimizations: First, according to a zT optimization for maximum energy conversion efficiency that has been derived and used before (Equation (5)) [30]. Here, ρ_n and ρ_p are the specific electrical resistivity and λ_n and λ_p the heat conductivity of the *n*- and *p*-type materials, respectively:

$$[\frac{A_n}{A_p}]_{zT} = \sqrt{\frac{\rho_n}{\rho_p} \cdot \frac{\lambda_p}{\lambda_n}} \qquad (5)$$

Second, the $[\frac{A_n}{A_p}]_{\text{matching } I_{q,SC}}$ ratio for overlapping material working points was calculated according to Equation (6) (compare Equations (A1)–(A7) in Appendix B). Here, α_n and α_p are the Seebeck coefficient of the *n*-type and *p*-type materials, respectively:

$$[\frac{A_n}{A_p}]_{\text{matching } I_{q,SC}} = \frac{\alpha_p}{|\alpha_n|} \cdot \frac{\rho_n}{\rho_p} \qquad (6)$$

Third, an optimization for maximum power output was conducted according to Xing et al. [36] via Equation (7) (compare Equations (A8)–(A14) in Appendix C):

$$[\frac{A_n}{A_p}]_{\text{power}} = \sqrt{\frac{\rho_n}{\rho_p}} \qquad (7)$$

Additionally, the areas of the *n*- and *p*-type materials have been chosen for the same effective area $A_n + A_p$ for all modules. The maximum first-law energy conversion efficiency $\eta_{I,TEG,max}$ for all optimized geometries have been calculated from the thermoelectric properties of the materials [9,11,30] (compare Equations (A15)–(A19) in Appendix D). The length of all thermolegs was chosen to be $l = 2$ mm, as otherwise there would have been too many varying parameters and a fixed and matching length for *n*- and *p*-type is reasonable for a functional TE module.

2.3. Simulation Parameters

The software ANSYS Mechanical (Version 2020 R1), which is based on the finite element method, is used in order to simulate the TE modules. Here, a steady-state thermal-electrical conduction analysis that allows for a simultaneous solution of thermal and electrical fields was chosen. After setting the material parameters for the *n*- and *p*-type thermolegs, the following boundary conditions for the simulation were set: the temperature of the cold junction, the ambient temperature that is equal to the temperature of the cold junction, the side at zero potential, and the side that determines the value of the electric current; all of the remaining faces were set for free convection in air with the heat transfer coefficient with a typical value of 20 W m^{-2} K^{-1} [42].

The simulation process was divided into two stages. First, a U-I_q curve was taken in order to evaluate the general characteristics of the TE module. By changing the value of the electrical current that can flow through the TE module, the effect of the external load on the voltage is simulated. Using the U-I_q curve, the electrical power P_{el} was calculated and a P_{el}-I_q curve was constructed to determine the MEPP. Then, to study the specific characteristics of the TE module at the MEPP, the following four distributions were simulated: temperature, flux density of thermal energy, electrical voltage, and flux density of charge. From each distribution, the values alongside the center of the thermoleg have been calculated. For these positions inside the leg, the local entropy flux density was calculated from the local temperature and local flux density of thermal energy according to Equation (3). The values of the electrical voltage and the local flux density of electrical charge were used in order to calculate the flux density of the electrical energy according to Equation (4). As a result, a description of all parameters as a function of the position x, along a central line through the respective thermoleg, is received. The corresponding images of the distribution of the temperature $T(x)$, the voltage $U(x)$,

flux density of thermal energy $j_{E,th}(x)$, and flux density of electrical charge $j_q(x)$ within the thermolegs are shown in Figures A2–A6 in the Appendix E.

2.4. Notes on Limitations

For all material parameters, a linear behavior within the applied temperature range has been assumed and the average value has been used for the calculation of the A_n/A_p ratio. Over a relatively small temperature difference of 50 K, the assumption of linear behavior of the thermoelectric parameters can be made, but, for exact simulations, the respective behavior has to be analyzed in detail for each specific case. Because the maximum temperature difference in the simulation was only 50 K and the maximum application temperature was about 1000 K, the dominant mechanism of heat transfer is convection, so the influence of thermal radiation was not considered. Note that, for temperatures above 1000 K and if ceramic substrates are used on top and at the bottom, the thermal radiation becomes increasingly important and has to be considered if an application at higher temperatures is aimed. For all of the simulated modules, an active cooling with a stable temperature difference of 50 K was assumed. Although a matching length l for both thermolegs is reasonable, this may also be optimized, since the length strongly influences the U–I_q-curve as well as the temperature difference, if no active cooling with a stable temperature difference is applied. Additionally, as mentioned before, the electric and thermal contact resistivity between each individual thermoleg and the connector is an important parameter, which has to be investigated and optimized for each individual case. To allow for comparison, ideal contacts are assumed in this work. The results in this work are specifically shown for a thermoelectric module in generator mode, which, however, may also apply for the entropy pump mode in thermoelectric coolers. For the thermoelectric materials, the respective material working points are also correlated to the material properties [11], but, for the thermoelectric modules in entropy pump mode, this is yet to be proven.

3. Results and Discussion

As material combinations, a Bi_2Te_3-based TE module (module 1), a half-Heusler-based TE module (module 2) and an oxide-based TE module (module 3) were chosen. The respective optimized geometries A_n/A_p for maximum zT, matching $I_{q,SC}$ and for maximum electrical power are shown in Table 2. For module 1 and 2, all of the optimizations led to very similar A_n/A_p ratios. Therefore, only the zT-optimized modules have been simulated. For module 3, the resulting A_n/A_p ratios vary widely, so simulations of this module were done for all the calculated optimized geometries.

Table 2. Resulting optimized geometries according to the zT optimization, matching $I_{q,SC}$ and power optimization. For the values in brackets, no simulations were carried out, due to insignificant deviation from the zT optimization.

Module	$[\frac{A_n}{A_p}]_{zT}$	$[\frac{A_n}{A_p}]_{\text{matching } I_{q,SC}}$	$[\frac{A_n}{A_p}]_{\text{power}}$
Module 1	1.0345	(1.0745)	(1.0459)
Module 2	1.0831	(1.0969)	(1.0308)
Module 3	0.0596	0.1306	0.2433

3.1. Similar Material Properties

For the materials that were chosen for module 1 and 2, the optimizations of the A_n/A_p ratios for maximum zT, matching material working points and for maximum power output all result in ratios near 1, with only a slight variation. This is a result of the fairly similar thermoelectric properties of the respective *n*- and *p*-types. Therefore, a fixed A_n/A_p ratio of 1.04 and 1.08 are used for the simulations of module 1 and module 2, respectively. Note that, although the calculated optimum A_n/A_p ratios for module 1 and 2 all are close together, they are not the same, meaning that an optimization for maximum power output may still result in a slightly higher power output of the respective module

compared to a *zT* optimization. However, the effect is much stronger for the oxide-based module 3, which is the reason why this module is analyzed in depth for all three optimized geometries.

3.1.1. Bi$_2$Te$_3$-Based TE Module

For module 1, Bi$_2$Te$_{3-x}$Sb$_x$ [38] and Bi$_{0.5}$Sb$_{1.5}$Te$_3$ [37] were chosen as *n*- and *p*-type materials, respectively. As A_n/A_p ratio, the *zT*-optimized ratio of 1.04 was used in the simulation. Figure 3 shows the simulated U-I_q characteristics and the electrical power output of the Bi$_2$Te$_3$-based TE module and the respective thermoelectric parameters across the length of the respective legs. The working points of the *p*- and *n*-type material with a *zT*-optimized A_n/A_p ratio show a good overlap. This results in a high electrical power output of the TE module with a maximum power density $\omega_{el,max,TEG}$ of approximately 124.5 mW cm^{-2} at the applied temperature difference of 50 K. The individual fluxes that are within in the *p*-type and *n*-type thermolegs are shown in Figure 3c–h. The temperature is set to be 348 K at the hot side and 298 K at the cold side. The entropy flux density $j_S(x)$ and therefore also the thermal energy flux density $j_{E,th}(x)$ are very similar in the respective legs, due to the similar thermal conductivity of the chosen materials. At the applied temperature difference of 50 K, a voltage $U(x)$ of 11 mV is achieved in one thermocouple. Analogous to the entropy flux density, the electrical flux density $j_q(x)$ is also similar in the *p*-type and *n*-type thermolegs. In one thermocouple, this results in an electrical energy flux density $j_{E,el}(x)$ of 2.4 × 10^{-3} W m^{-2}. Note that the dashed lines presented in Figure 3c–h represent the metallic connector between the *p*-type and *n*-type materials, so both materials are not in direct contact. Thus the different fluxes do not necessarily have the same value at the dashed line.
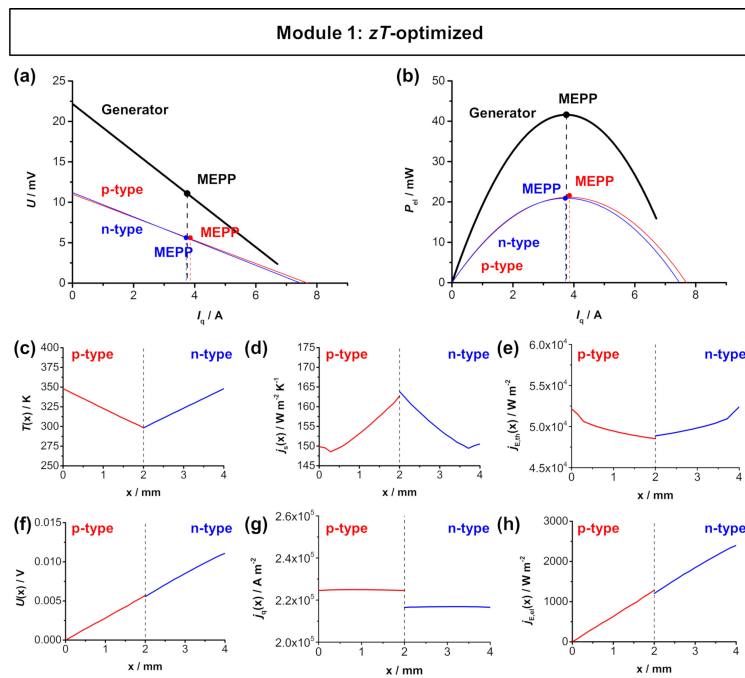

Figure 3. FEM simulations of module 1 (*p*-type Bi$_{0.5}$Sb$_{1.5}$Te$_3$ and *n*-type Bi$_2$Te$_{3-x}$Sb$_x$) with a hot side temperature of 348 K and cold side temperature of 298 K. (**a**) U-I_q characteristics and (**b**) electrical power output P_{el}–I_q of the module. The respective MEPPs of the materials overlap and result in a high power output of the TE module. Thermoelectric characteristics of the respective materials as a function of the length of the respective legs: (**c**) temperature $T(x)$, (**d**) entropy flux density $j_S(x)$, (**e**) thermal energy flux density $j_{E,th}(x)$, (**f**) voltage $U(x)$, (**g**) electrical flux density $j_q(x)$, and (**h**) electrical energy flux density $j_{E,el}(x)$ trend throughout one thermocouple. Note that the dashed line in (**c**–**h**) represents the metallic connector between the *p*-type and *n*-type materials. The simulated distributions are shown in Figure A2 in Appendix E.

3.1.2. Half-Heusler-Based TE Module

Figure 4 shows the simulated U-I_q characteristics and the electrical power output of the half-Heusler-based TE module and the respective thermoelectric parameters across the length of the respective legs. For n- and p-type materials, $Hf_{0.6}Zr_{0.4}NiSn_{0.995}Sb_{0.005}$ [40] and $FeNb_{0.88}Hf_{0.12}Sb$ [39] were chosen.
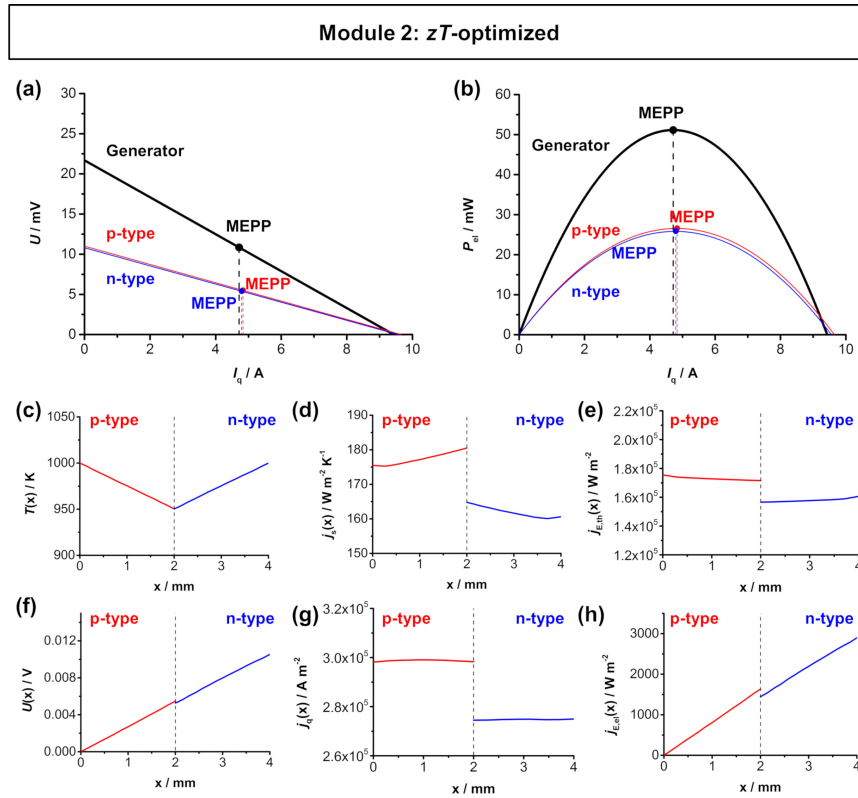
Figure 4. FEM simulations of module 2 (p-type $FeNb_{0.88}Hf_{0.12}Sb$ and n-type $Hf_{0.6}Zr_{0.4}NiSn_{0.995}Sb_{0.005}$) with a hot side temperature of 1000 K and cold side temperature of 950 K. (**a**) U-I_q characteristics and (**b**) electrical power output P_{el}–I_q of the module. The respective MEPPs of the materials overlap and result in a high power output of the module. Thermoelectric characteristics of the respective materials as a function of the length of the respective legs: (**c**) temperature $T(x)$, (**d**) entropy flux density $j_S(x)$, (**e**) thermal energy flux density $j_{E,th}(x)$, (**f**) voltage $U(x)$, (**g**) electrical flux density $j_q(x)$, and (**h**) electrical energy flux density $j_{E,el}(x)$ trend throughout one thermocouple. Note that the dashed line in (**c**–**h**) represent the metallic connector between the p-type and n-type materials. The simulated distributions are shown in Figure A3 in Appendix E.

Analogous to the Bi_2Te_3-based module, the materials exhibit similar thermoelectric properties and the resulting A_n/A_p ratio is still near 1. For the simulations, the zT-optimized A_n/A_p ratio of 1.08 was used. The material working points also show a good overlap as a result of the zT optimization. Therefore, the module's MEPP and MCEP are also close together. The TE module reaches a high electrical power output of approximately 51.1 mW. With an effective area of 0.334 cm^2, this corresponds to a similarly high maximum power density $\omega_{el,max,TEG}$ of 153.14 mW cm^{-2}, which is slightly higher compared to the Bi_2Te_3-based module 1. The individual fluxes within in the p-type and n-type thermolegs are shown in Figure 4c–h. The temperature is set to be 1000 K at the hot side and 950 K at the cold side. At the applied 50 K temperature difference, a voltage $U(x)$ of 10.54 mV can be reached, which is slightly lower compared to the Bi_2Te_3-based module, as a result of the slightly lower Seebeck

coefficient of the *n*-type material. The entropy flux density $j_S(x)$ of the *p*-type is slightly higher when compared to the *n*-type thermoleg, due to the higher thermal conductivity of the *p*-type material. Analogously, the electrical flux density $j_q(x)$ is also slightly higher in the *p*-type material, due to the higher electrical conductivity of the *p*-type material. In one thermocouple, a thermal energy flux density $j_{E,th}(x)$ of 16×10^3 W m^{-2} and an electrical energy flux density $j_{E,el}(x)$ of 2.9×10^3 W m^{-2} are reached, both being higher when compared to the Bi$_2$Te$_3$-based module, due to the higher values of electrical and thermal conductivity of the respective materials.

Table 3 summarizes the simulated characteristics of the Bi$_2$Te$_3$-based and half-Heusler-based TE modules. The respective material working points are close together, which results in a high electrical power output and conversion efficiency of both modules. However, the Bi$_2$Te$_3$-based module 1 reaches a higher conversion efficiency of 2.5%, while the half-Heusler based module 2 reaches a higher power output of up to 153 mW cm^{-2}. This is the expected behavior, due to the higher power factor, but simultaneously higher thermal conductivity of the half-Heusler materials. This also displays the aforementioned importance of the power factor (for power output), which, for certain applications, may be equally important as the figure of merit zT (for efficiency).

Table 3. Resulting maximum electrical power output $P_{el,max,TEG}$, electrical power density $\omega_{el,max,TEG}$ and maximum first-law energy conversion efficiency $\eta_{I,TEG,max}$ of module 1 (Bi$_2$Te$_3$) and module 2 (half-Heusler materials) for zT-optimized geometry.

Module	Module MEPP/A	$P_{el,max,TEG}$/mW	$\omega_{el,max,TEG}$/mW cm^{-2}	$\eta_{I,TEG,max}$
Module 1	3.75	41.60	124.50	2.50
Module 2	4.72	51.10	153.14	0.97

3.2. Dissimilar Material Properties

For *n*- and *p*-type materials of module 3, In$_{1.995}$Sn$_{0.05}$O$_3$ and Ca$_3$Co$_4$O$_9$ [41] were chosen. For these materials, the optimizations of the A_n/A_p ratios for maximum zT, matching $I_{q,SC}$ and for maximum power output result in dissimilar ratios of 0.06, 0.13, and 0.24, respectively. Therefore, modules with all calculated A_n/A_p ratios were simulated.

Oxide-Based TE Module

Figure 5 shows the simulated U-I_q characteristics and the electrical power output of the Ca$_3$Co$_4$O$_9$-In$_{1.95}$Sn$_{0.05}$O$_2$ TE module and the thermoelectric parameters across the length of the respective legs. Here, the zT optimization of the A_n/A_p ratio does not result in an overlap of the respective material working points. The short-circuited electrical current $I_{q,SC}$ of the *p*-type Ca$_3$Co$_4$O$_9$ is approximately twice the short-circuited current $I_{q,SC}$ of the *n*-type In$_{1.95}$Sn$_{0.05}$O$_2$. Therefore, the resulting MEPP of the TE module is located between the respective material working points, and the power output of the module is only slightly higher when compared to the power output of the *p*-type Ca$_3$Co$_4$O$_9$ leg. With an effective area of 0.3332 cm^2 the simulated TE module reaches a maximum electrical power density $\omega_{el,max,TEG}$ of approximately 4.5 mW cm^{-2}. The individual fluxes within in the *p*-type and *n*-type thermolegs are shown in Figure 4c–h. The temperature difference was again set to 50 K, with a hot side temperature of 1075 K and a cold side temperature of 1025 K. The strong difference of the Seebeck coefficient of *n*- and *p*-type materials is displayed in the distribution of the voltage $U(x)$. In the *p*-type material, a voltage of 6.6 mV is reached, while, in the *n*-type material, the voltage only increases by 1 mV to 7.6 mV. The strong difference of thermoelectric properties of *p*- and *n*-type materials is also displayed in the flux density of charge and flux density of entropy, both being higher in the *n*-type In$_{1.995}$Sn$_{0.05}$O$_3$ due to the higher electrical and thermal conductivity. Therefore, the same behavior is noticeable in the flux densities of thermal energy and electrical energy.
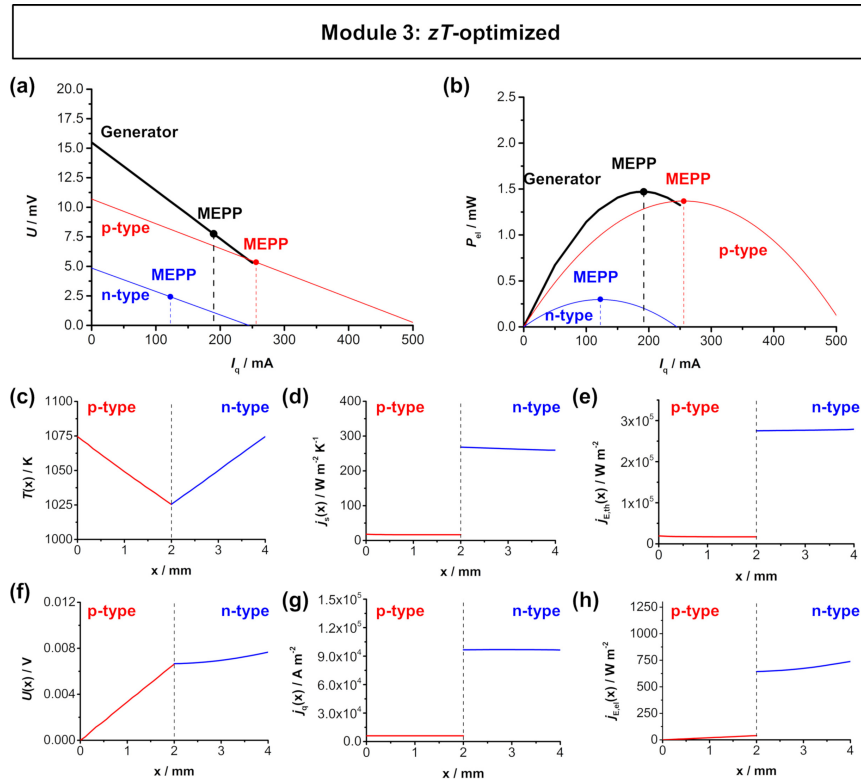
Figure 5. FEM simulations of the *zT*-optimized module 3 (*p*-type $Ca_3Co_4O_9$ and *n*-type $In_{1.95}Sn_{0.05}O_3$) with a hot side temperature of 1050 K and cold side temperature of 1000 K. (**a**) U-I_q characteristics and (**b**) electrical power output P_{el}-I_q of the module. Thermoelectric characteristics of the respective materials as a function of the length of the respective legs: (**c**) temperature $T(x)$, (**d**) entropy flux density $j_S(x)$, (**e**) thermal energy flux density $j_{E,th}(x)$, (**f**) voltage $U(x)$, (**g**) electrical flux density $j_q(x)$, and (**h**) electrical energy flux density $j_{E,el}(x)$ trend throughout one thermocouple. Note, that the dashed line in (**c**–**h**) represent the metallic connector between the *p*-type and *n*-type materials. The simulated distributions are shown in Figure A4 in Appendix E.

Figure 6 shows the simulated U-I_q characteristics and the electrical power output of the $Ca_3Co_4O_9$–$In_{1.95}Sn_{0.05}O_2$ TE module and the respective thermoelectric parameters across the length of the respective legs for an optimized A_n/A_p ratio for matching $I_{q,SC}$. As a result of this optimization, the module MEPP is also similar to the both materials' working points and the power output of the module is already significantly higher than of the respective materials. With an effective area of 0.333 cm^2 a maximum electrical power density $\omega_{el,max,TEG}$ of approximately 5.64 mW cm^{-2} can be reached. The individual fluxes within in the *p*-type and *n*-type thermolegs for the module optimized for matching $I_{q,SC}$ are shown in Figure 6c–h. When compared to the *zT* optimization, the larger area of the *n*-type $In_{1.995}Sn_{0.05}O_3$ results in a bigger impact of the material, displayed in a higher value of voltage reached in the *n*-type material. Additionally, both the entropy flux density (slightly) as well as the electrical flux density (significantly) of the *n*-type material are lower, due to the larger area, which results in the same trend for the flux densities of thermal energy and electrical energy.
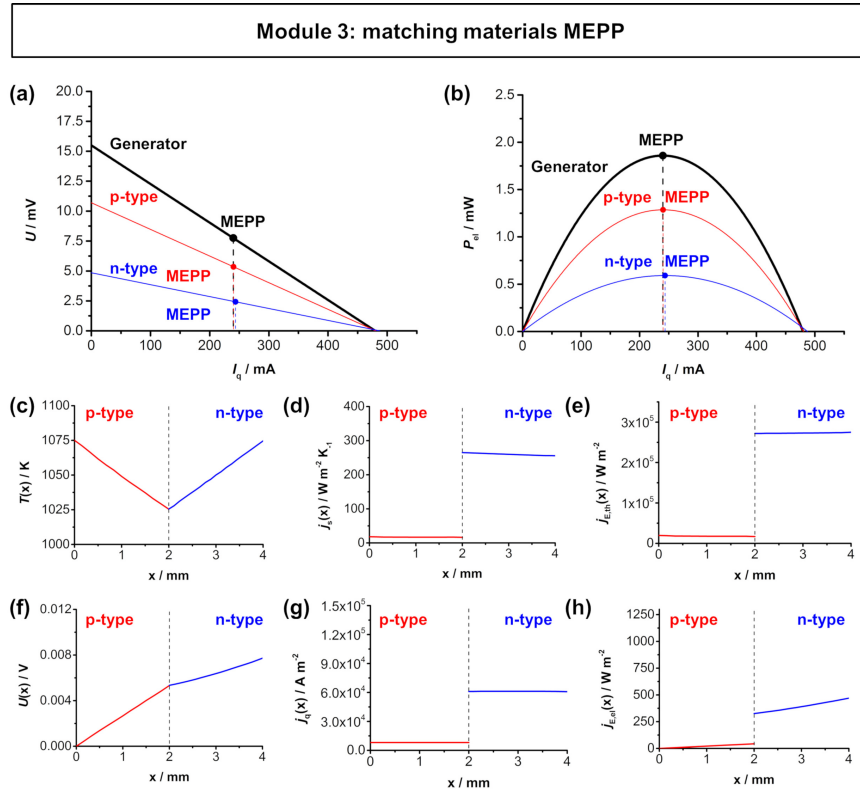
Figure 6. FEM simulations of the module 3 (*p*-type $Ca_3Co_4O_9$ and *n*-type $In_{1.95}Sn_{0.05}O_3$) with matching $I_{q,SC}$ with a hot side temperature of 1050 K and cold side temperature of 1000 K. (**a**) U–I_q characteristics and (**b**) electrical power output P_{el}-I_q of the module. Thermoelectric characteristics of the respective materials as a function of the length of the respective legs: (**c**) temperature $T(x)$, (**d**) entropy flux density $j_S(x)$, (**e**) thermal energy flux density $j_{E,th}(x)$, (**f**) voltage $U(x)$, (**g**) electrical flux density $j_q(x)$, and (**h**) electrical energy flux density $j_{E,el}(x)$ trend throughout one thermocouple. Note, that the dashed line in (**c**–**h**) represent the metallic connector between the *p*-type and *n*-type materials. The simulated distributions are shown in Figure A5 in Appendix E.

Finally, in Figure 7, the power optimization of the A_n/A_p ratio according to Equation (7) is shown. Again, the material working points do not overlap, but as a result of the increasing cross-sectional area of the *n*-type $In_{1.95}Sn_{0.05}O_2$, the electrical power output of the the *n*-type material is significantly higher compared to the other two optimization strategies. In fact, both materials reach a similar electrical power output $P_{el,max}$ of about 1 mW, resulting in a maximum electrical power output $P_{el,max,TEG}$ of about 2 mW for the module. This corresponds to a maximum electrical power density $\omega_{el,max,TEG}$ of 5.89 mW cm^{-2}. The individual fluxes within in the *p*-type and *n*-type thermolegs for the power-optimized module are shown in Figure 7c–h. Here, the trend from the module optimized for matching $I_{q,SC}$ continues. The larger area of the *n*-type material results in a higher voltage $U(x)$ and as well as decreasing flux densities of entropy $j_S(x)$ (slightly lower) and charge $j_q(x)$ (significantly lower).
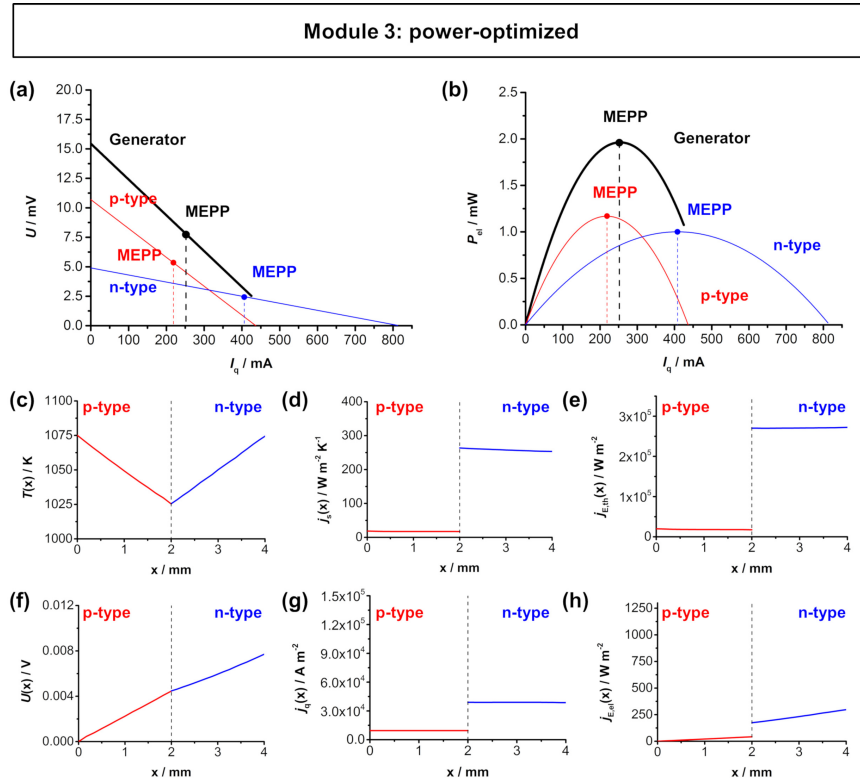
Figure 7. FEM simulations of the power-optimized module 3 (*p*-type $Ca_3Co_4O_9$ and *n*-type $In_{1.95}Sn_{0.05}O_3$) with a hot side temperature of 1050 K and cold side temperature of 1000 K. (**a**) U-I_q characteristics and (**b**) electrical power output P_{el}-I_q of the module. Thermoelectric characteristics of the respective materials as a function of the length of the respective legs: (**c**) temperature $T(x)$, (**d**) entropy flux density $j_S(x)$, (**e**) thermal energy flux density $j_{E,th}(x)$, (**f**) voltage $U(x)$, (**g**) electrical flux density $j_q(x)$, and (**h**) electrical energy flux density $j_{E,el}(x)$ trend throughout one thermocouple. Note, that the dashed line in (**c**–**h**) represent the metallic connector between the *p*-type and *n*-type materials. The simulated distributions are shown in Figure A6 in Appendix E.

Table 4 summarizes the simulated characteristics of the *zT*-optimized $Ca_3Co_4O_9$-$In_{1.95}Sn_{0.05}O_2$ TE module, the optimized module for matching $I_{q,SC}$, as well as for the power-optimized geometry. The module with power-optimized A_n/A_p ratio reaches a maximum power density of 5.89 mW cm^{-2}, which is slightly higher compared to the module with overlapping material working points and about 30% higher when compared to the module with *zT*-optimized geometry. Additionally, the maximum first-law energy conversion efficiency $\eta_{I,TEG,max}$ for all three optimized geometries have been calculated. As expected, the *zT*-optimized module reaches the highest $\eta_{I,TEG,max}$ with 0.13%, while the module optimized for matching $I_{q,SC}$ and the power-optimized module show slightly lower efficiencies of 0.11% and 0.09%, respectively. This shows the contrary trend of a higher efficiency (for the *zT*-optimized module) and of higher power density (for the power-optimized module).

Table 4. Resulting maximum electrical power output $P_{el,max,TEG}$, electrical power density $\omega_{el,max,TEG}$, and maximum first-law energy conversion efficiency $\eta_{I,TEG,max}$ of module 3 with optimized geometry for maximum zT, matching $I_{q,SC}$ and maximum power output. The resulting power density increases due to the overlapping material working points.

Module	Module MEPP/mA	$P_{el,max,TEG}$/mW	$\omega_{el,max,TEG}$/mW cm^{-2}	$\eta_{I,TEG,max}$
zT-optimized	189.90	1.50	4.51	0.13%
same $I_{q,SC}$	239.89	1.86	5.64	0.11%
power-optimized	252.00	1.96	5.89	0.09%

As a result, module 3 is build based on the same materials with identical thermoelectric properties, but it is either optimized for maximum zT, matching $I_{q,SC}$ or maximum power output. Figure 8 summarizes the results of all three optimization strategies. The zT optimization leads to a module with the highest conversion efficiency, but the lowest electrical power output. Contrary, the power optimization leads to a module with the the highest electrical power output, but the lowest conversion efficiency. The module with optimized geometry for matching $I_{q,SC}$ is in between, but closer to the maximum electrical power output. This also corresponds to the results of Xing et al. [36], who observed a similar increase in the maximum electrical power output with a respective geometry optimization when compared to an optimization for maximum zT. Note that this correlation between the deviation of optimum power output and optimum conversion efficiency is here shown on the example of module 3, but also applies for the other TE modules. As shown in Table 2, the optimum A_n/A_p ratio for the Bi$_2$Te$_3$-based module 1 and the half-Heusler-based module 2 also varies slightly for the different optimization strategies. Therefore, also for quite similar thermoelectric materials, a slight deviation between optimum power output and energy conversion efficiency can be expected.
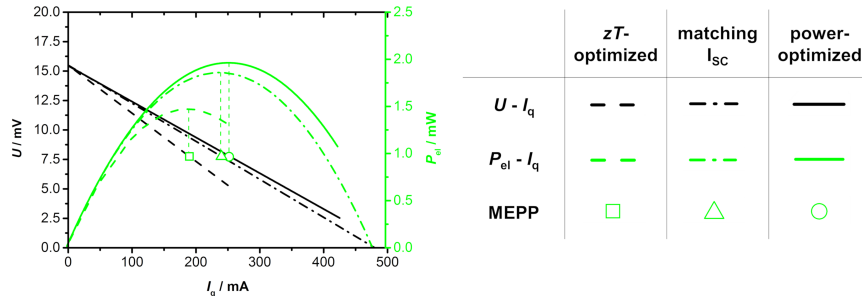

Figure 8. Comparison of all three optimization strategies for module 3 (dash: zT-optimized, dash-dot: matching $I_{q,SC}$, line: power-optimized). The power-optimized module shows a significantly higher power output when compared to zT-optimized module. The module with overlapping material working points is in between, but closer to the maximum power output.

4. Conclusions

Three different optimization strategies for the A_n/A_p ratio were applied, whereas, for certain modules, they all resulted in different geometries. For module 3, based on strongly dissimilar thermoelectric properties of the p-type Ca$_3$Co$_4$O$_9$ and the n-type In$_{1.95}$Sn$_{0.05}$O$_3$, the geometry optimizations show strongly dissimilar A_n/A_p ratios. Here, a strong deviation between high conversion efficiency (with zT-optimized geometry) and high power output (with power-optimized geometry) was found. The power optimization resulted in a 30% higher power output compared to the zT-optimized counterpart. For modules with more similar thermoelectric properties of the n- and p-type, which, in this work, are the Bi$_2$Te$_3$-based module 1 and the half-Heusler-based module 2, the respective optimum geometries only differ slightly, but also show this deviation in the geometry optimization. This emphasizes that, for TE module concepts, various optimization strategies may be

applied, either to target high conversion efficiency or high power output. This phenomena correlates to the diversity of the thermoelectric materials that were used for the TE module. Additionally, this also underlines the similar importance of the power factor of thermoelectric materials, to target a high power output, when compared to the figure of merit *zT*.

Author Contributions: M.W., R.H. and A.F. worked on the conceptualization. A.R. developed the methods and carried out the simulations. M.W. wrote the original draft. All authors critically revised and edited the manuscript draft. A.F. is responsible for the acquisition of funding. All authors have read and agreed to the published version of the manuscript.

Conflicts of Interest: The authors declare no conflict of interest.

Abbreviations

The following abbreviations are used in this manuscript:

TE module	thermoelectric module
TEG	thermoelectric generator
MCEP	maximum conversion efficiency point
MEPP	maximum electrical power point
OC	(electrical) open-circuit
SC	(electrical) short-circuit

Symbols

The following symbols are used in this manuscript:

Geometry

A	cross-sectional area of thermoelectric material
A_n	cross-sectional area of *n*-type material
A_p	cross-sectional area of *p*-type material
l	length of thermoelectric material
l_n	length of *n*-type material
l_p	length of *p*-type material
$\frac{A_n}{A_p}$	ratio of the cross-sectional areas of the *n*-type and *p*-type materials
$\left[\frac{A_n}{A_p}\right]_{zT}$	ratio of the cross-sectional areas of the *n*-type and *p*-type materials for maximum *zT*
$\left[\frac{A_n}{A_p}\right]_{\text{matching } I_{q,SC}}$	ratio of the cross-sectional areas of the *n*-type and *p*-type materials for matching $I_{q,SC}$
$\left[\frac{A_n}{A_p}\right]_{\text{power}}$	ratio of the cross-sectional areas of the *n*-type and *p*-type materials for maximum power

Material properties

α	Seebeck coefficient
α_n	Seebeck coefficient of *n*-type material
α_p	Seebeck coefficient of *p*-type material
λ_n	heat conductivity of *n*-type material
λ_p	heat conductivity of *p*-type material
λ_{OC}	heat conductivity under electrically open-circuited (OC) conditions
Λ_{OC}	entropy conductivity under electrically open-circuited (OC) conditions
ρ	specific electrical resistivity
ρ_n	specific electrical resistivity of *n*-type material
ρ_p	specific electrical resistivity of *p*-type material
R_n	resistance of *n*-type material
R_p	resistance of *p*-type material
σ	isothermal electrical conductivity
f	figure of merit (as introduced by Zener [43]
zT	figure of merit (as introduced by Ioffe [10])

Thermodynamic potentials

φ	electric potential
T	absolute temperature
T_{cold}	temperature of the thermoelectric material at its cold side
T_{hot}	temperature of the thermoelectric material at its hot side
∇T	gradient of the temperature
ΔT	difference of temperature (along the thermoelectric material)
U	voltage
U_{OC}	voltage at electrically open-circuited (OC) conditions

Fluxes

i	normalized electrical current
I_{q}	electrical current
$I_{\text{q,SC}}$	electrical current at electrically short-circuited (SC) conditions
$\mathbf{j}_{\text{q}}$	electrical flux density
$\mathbf{j}_{\text{s}}$	entropy flux density
$\mathbf{j}_{\text{E,el}}$	electrical energy flux density
$\mathbf{j}_{\text{E,th}}$	thermal energy flux density
q	electric charge
S	entropy

Performance

$P_{\text{el,max}}$	maximum electrical power output of the thermoelectric material (at MEPP)
$P_{\text{el,max,TEG}}$	maximum electrical power output of the module (at MEPP)
$\omega_{\text{el,max,TEG}}$	maximum electrical power density of the module (at MEPP)
$I_{\text{q,MEPP}}$	current I_{q} at the MEPP
$I_{\text{q,MEPP,n}}$	current I_{q} at the MEPP of the *n*-type material
$I_{\text{q,MEPP,p}}$	current I_{q} at the MEPP of the *p*-type material
$U_{\text{MEPP,TEG}}$	voltage U at the MEPP of the TE module
$I_{\text{q,MEPP,TEG}}$	current I_{q} at the MEPP of the TE module
R_{TEG}	internal resistance of the TE module
$\eta_{\text{II,mat}}$	second-law energy conversion efficiency of a thermoelectric material
$\eta_{\text{I,TEG,max}}$	maximum first-law energy conversion efficiency of the TE module
η_{Carnot}	Carnot efficiency of the TE module
$\eta_{\text{II,TEG,max}}$	maximum second-law energy conversion efficiency of the TE module

Appendix A. Input Data for FEM-Simulation

Table A1. Thermoelectric parameters of module 1 (*p*-type $Bi_{0.5}Sb_{1.5}Te_3$ [37], *n*-type $Bi_2Te_{3-x}Sb_x$ [38]) used for FEM simulations. For all material parameters a linear behavior within the applied temperature range has been assumed and the average value has been used for the calculation of the $A_{\text{n}}/A_{\text{p}}$ ratio.

	p-Type		*n*-Type	
T/K	348	298	348	298
σ/S cm^{-1}	760	990	711	875
α/μV K^{-1}	227	213	-228	-220
λ_{OC}/W m^{-1} K^{-1}	1.31	1.39	1.40	1.35
Λ_{OC}/W m^{-1} K^{-2}	3.76×10^{-3}	4.66×10^{-3}	4.02×10^{-3}	4.53×10^{-3}

Table A2. Thermoelectric parameters of module 2 (p-type FeNb$_{0.88}$Hf$_{0.12}$Sb [39], n-type Hf$_{0.6}$Zr$_{0.4}$NiSn$_{0.995}$Sb$_{0.005}$ [40]) used for FEM simulations. For all material parameters a linear behavior within the applied temperature range has been assumed and the average value has been used for the calculation of the A_n/A_p ratio.

	p-Type		**n-Type**	
T/K	1000	950	1000	950
σ/S cm^{-1}	1053	1158	960	1000
α/μV K^{-1}	223	217	-212	-219
λ_{OC}/W m^{-1} K^{-1}	4.33	4.44	4.16	3.90
Λ_{OC}/W m^{-1} K^{-2}	4.33×10^{-3}	4.76×10^{-3}	4.16×10^{-3}	4.11×10^{-3}

Table A3. Thermoelectric parameters of module 3 (p-type Ca$_3$Co$_4$O$_9$ [41], n-type In$_{1.95}$Sn$_{0.05}$O$_3$ [41]) used for FEM simulations. For all material parameters a linear behavior within the applied temperature range has been assumed and the average value has been used for the calculation of the A_n/A_p ratio.

	p-Type		**n-Type**	
T/K	1075	1025	1075	1025
σ/S cm^{-1}	29.63	31.48	609.26	448.15
α/μV K^{-1}	202.83	225.74	-100.94	-92.45
λ_{OC}/W m^{-1} K^{-1}	0.63	0.66	10.70	10.94
Λ_{OC}/W m^{-1} K^{-2}	0.59×10^{-3}	0.64×10^{-3}	9.95×10^{-3}	10.67×10^{-3}

Appendix B. A$_n$/A$_p$ Optimization for Matching Short-Circuit Current

Here, the optimized A_n/A_p ratio for matching $I_{q,SC}$ is derived. The idea of this optimization is as follows: the working points of the respective thermoelectric materials overlap, if the flux of charge in both materials is the same. Then, the working points of the materials overlap, so

$$I_{q,\text{MEPP,n}} = I_{q,\text{MEPP,p}} \tag{A1}$$

By including

$$I_{q,\text{MEPP,n}} = \frac{|\alpha_n|(\Delta T)^2}{2R_n} \tag{A2}$$

and

$$I_{q,\text{MEPP,p}} = \frac{\alpha_p(\Delta T)^2}{2R_p} \tag{A3}$$

with the electrical resistance of the materials

$$R_n = \rho_n \cdot \frac{l_n}{A_n} \tag{A4}$$

and

$$R_p = \rho_p \cdot \frac{l_p}{A_p} \tag{A5}$$

the following relation is received:

$$\frac{|\alpha_n| \cdot (\Delta T)^2}{2\rho_n \frac{l_n}{A_n}} = \frac{\alpha_p \cdot (\Delta T)^2}{2\rho_p \frac{l_p}{A_p}} \tag{A6}$$

After rearrangement and with the assumed same length of the thermolegs $l_n = l_p$ the result for a A_n/A_p ratio for matching $I_{q,SC}$ is:

$$\frac{A_\mathrm{n}}{A_\mathrm{p}} = \frac{\alpha_\mathrm{p}}{|\alpha_\mathrm{n}|} \cdot \frac{\rho_\mathrm{n}}{\rho_\mathrm{p}} \tag{A7}$$

Appendix C. $A_\mathrm{n}/A_\mathrm{p}$ Optimization for Maximum Power

The maximum power output of a TE module is a function of the electrical current I_q of the module at the MEPP $I_\mathrm{q,MEPP,TEG}$ and the voltage U of the module at the MEPP $U_\mathrm{MEPP,TEG}$, which are calculated according to Equations (A8) and (A9):

$$I_\mathrm{q,MEPP,TEG} = \frac{(\alpha_\mathrm{p} - \alpha_\mathrm{n}) \cdot \Delta T}{2R} \tag{A8}$$

$$U_\mathrm{MEPP,TEG} = \frac{(\alpha_\mathrm{p} - \alpha_\mathrm{n}) \cdot \Delta T}{2} \tag{A9}$$

From this, the maximum electrical power output of a module at the MEPP can be derived as

$$P_\mathrm{el,max,TEG} = \frac{(\alpha_\mathrm{p} - \alpha_\mathrm{n})^2 \cdot (\Delta T)^2}{4R_\mathrm{TEG}} \tag{A10}$$

with the internal electrical resistance of the module R_TEG

$$R_\mathrm{TEG} = \rho_\mathrm{p} \frac{l_\mathrm{p}}{A_\mathrm{p}} + \rho_\mathrm{n} \frac{l_\mathrm{n}}{A_\mathrm{n}} \tag{A11}$$

Considering, that the effecive area A is a sum of the cross-sectional areas A_n and A_p, Equation (A11) can be differentiated and has to be equal 0 for its maximum. So

$$-(\alpha_\mathrm{p} - \alpha_\mathrm{n})^2 (\Delta T)^2 \cdot \frac{\frac{\rho_\mathrm{p} l_\mathrm{p}}{(A + A_\mathrm{p})^2} - \frac{\rho_\mathrm{n} l_\mathrm{n}}{A_\mathrm{p}{}^2}}{\left(\frac{\rho_\mathrm{p} l_\mathrm{p}}{A_\mathrm{p}} + \frac{\rho_\mathrm{n} l_\mathrm{n}}{A - A_\mathrm{p}}\right)^2} = 0 \tag{A12}$$

This Equation (A12) is zero, if the numerator of the fraction is zero, so

$$\frac{\rho_\mathrm{p} l_\mathrm{p}}{(A + A_\mathrm{p})^2} - \frac{\rho_\mathrm{n} l_\mathrm{n}}{A_\mathrm{p}{}^2} = 0 \tag{A13}$$

After rearrangement, the optimum $A_\mathrm{n}/A_\mathrm{p}$ ratio for maximum power output is received as

$$\frac{A_\mathrm{n}}{A_\mathrm{p}} = \sqrt{\frac{\rho_\mathrm{n}}{\rho_\mathrm{p}}} \tag{A14}$$

The final Equation (A14) derived corresponds to the reported ratio for maximum power output of Xing et al. [36] .

Appendix D. Efficiency of the Module

The maximum first-law efficiency $\eta_\mathrm{I,TEG,max}$ of a module is the product of the Carnot efficiency η_Carnot and the second-law efficiency $\eta_\mathrm{II,TEG,max}$ [9,11] and can be determined as

$$\eta_\mathrm{I,TEG,max} = \eta_\mathrm{Carnot} \cdot \eta_\mathrm{II,TEG,max} = \frac{T_\mathrm{hot} - T_\mathrm{cold}}{T_\mathrm{hot}} \cdot \frac{\sqrt{1 + Z\bar{T}} - 1}{\sqrt{1 + Z\bar{T}} + 1} \tag{A15}$$

Here, $\bar{T}$ is the average temperature and Z is a function of the materials thermoelectric parameters:

$$Z = \frac{\alpha^2}{R \cdot K} \tag{A16}$$

with

$$\alpha = (\alpha_p - \alpha_n) \tag{A17}$$

$$R = \frac{1}{\sigma_p} \cdot \frac{l_p}{A_p} + \frac{1}{\sigma_n} \cdot \frac{l_n}{A_n} \tag{A18}$$

and

$$K = \lambda_p \cdot \frac{A_p}{l_p} + \lambda_n \cdot \frac{A_n}{l_n} \tag{A19}$$

So, the maximum first-law efficiency $\eta_{I,TEG,max}$ of a module can be determined as a function of the materials thermoelectric parameter and the respective cross-sectional areas A_n and A_p [30].
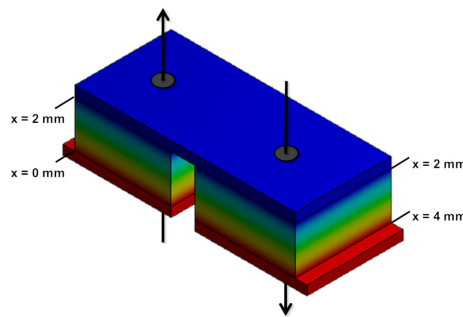
Appendix E. Simulated Module Fluxes

Figure A1. Analyzed path x along a central line through the respective thermoleg on the example of module 1.
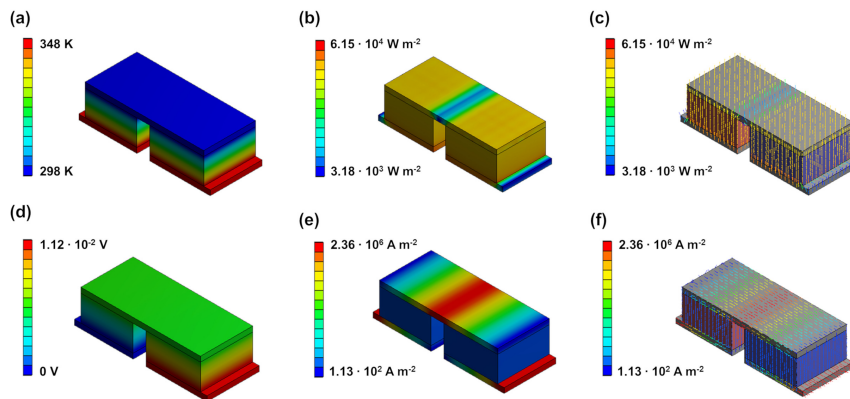
Figure A2. Distribution of (**a**) temperature $T(x)$, (**b**,**c**) flux density of thermal energy $j_{E,th}(x)$, (**d**) voltage $U(x)$ and (**e**,**f**) flux density of electrical charge $j_q(x)$ in module 1.
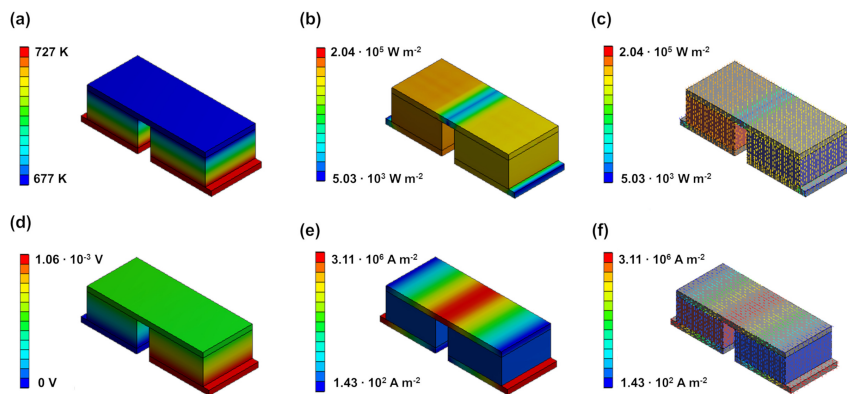
Figure A3. Distribution of (**a**) temperature $T(x)$, (**b**,**c**) flux density of thermal energy $j_{E,th}(x)$, (**d**) voltage $U(x)$ and (**e**,**f**) flux density of electrical charge $j_q(x)$ in module 2.
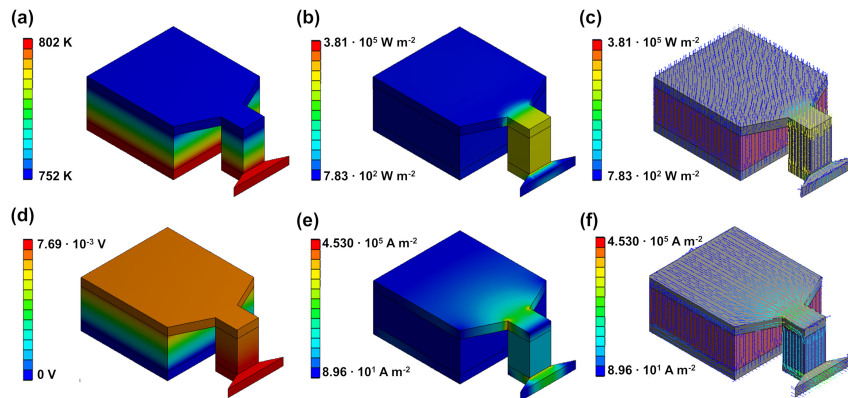
Figure A4. Distribution of (**a**) temperature $T(x)$, (**b**,**c**) flux density of thermal energy $j_{E,th}(x)$, (**d**) voltage $U(x)$ and (**e**,**f**) flux density of electrical charge $j_q(x)$ in module 3 with zT-optimized geometry.
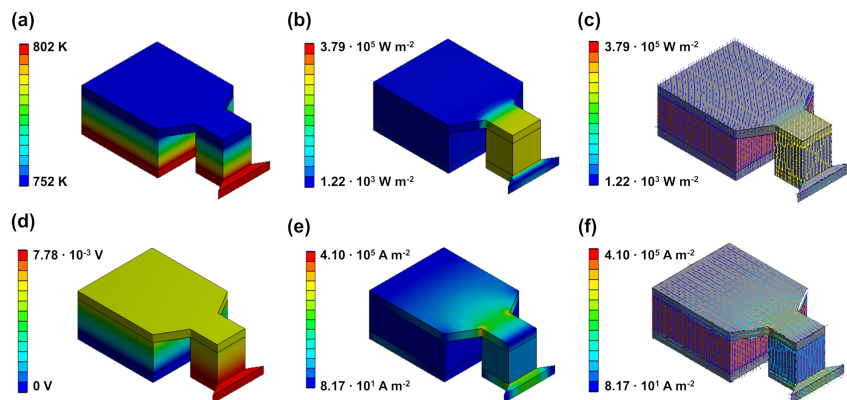
Figure A5. Distribution of (**a**) temperature $T(x)$, (**b**,**c**) flux density of thermal energy $j_{E,th}(x)$, (**d**) voltage $U(x)$ and (**e**,**f**) flux density of electrical charge $j_q(x)$ in module 3 with geometry for matching $I_{q,SC}$.
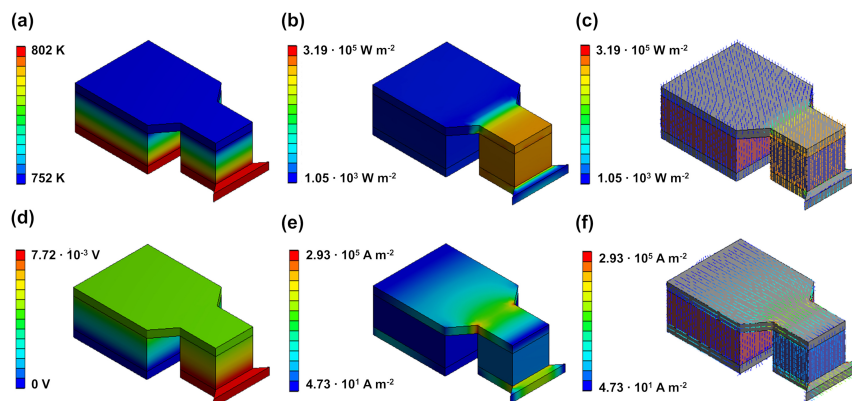
Figure A6. Distribution of (**a**) temperature $T(x)$, (**b**,**c**) flux density of thermal energy $j_{E,th}(x)$, (**d**) voltage $U(x)$ and (**e**,**f**) flux density of electrical charge $j_q(x)$ in module 3 with power-optimized geometry.

References

1. Kishore, R.A.; Marin, A.; Wu, C.; Kumar, A.; Priya, S. *Energy Harvesting—Materials, Physics, and System Design with Practical Examples*; DEStech Publications: Boston, MA, USA; Berlin, Germany, 2019.
2. Wolf, M.; Hinterding, R.; Feldhoff, A. High Power Factor vs. High zT—A Review of Thermoelectric Materials for High-Temperature Application. *Entropy* **2019**, *21*, 1058. [CrossRef]
3. Gayner, C.; Kar, K.K. Recent Advances in Thermoelectric Materials. *Prog. Mater. Sci.* **2016**, *83*, 330–382. [CrossRef]
4. He, R.; Schierning, G.; Nielsch, K. Thermoelectric Devices: A Review of Devices, Architectures, and Contact Optimization. *Adv. Mater. Technol.* **2018**, *3*. [CrossRef]
5. Liu, X.; Wang, Z. Printable Thermoelectric Materials and Applications. *Front. Mater.* **2019**, *6*, 1–5. [CrossRef]
6. He, W.; Zhang, G.; Zhang, X.; Ji, J.; Li, G.; Zhao, X. Recent Development and Application of Thermoelectric Generator and Cooler. *Appl. Energy* **2015**, *143*, 1–25. [CrossRef]
7. Fuchs, H.U. A Direct Entropic Approach to Uniform and Spatially Continuous Dynamical Models of Thermoelectric Devices. *Energy Harvest. Syst.* **2014**, *1*, 1–18. [CrossRef]
8. Feldhoff, A. Thermoelectric Material Tensor Derived from the Onsager-de Groot-Callen Model. *Energy Harvest. Syst.* **2015**, *2*, 5–13. [CrossRef]
9. Fuchs, H. *The Dynamics of Heat—A Unified Approach to Thermodynamics and Heat Transfer*, 2nd ed.; Springer: New York, NY, USA, 2010. [CrossRef]
10. Ioffe, A.F. *Semiconductor Thermoelements, and Thermoelectric Cooling*, 1st ed.; Info-search Ltd.: London, UK, 1957. [CrossRef]
11. Feldhoff, A. Power Conversion and its Efficiency in Thermoelectric Materials. *Entropy* **2020**, *22*, 803. [CrossRef]
12. Mamur, H.; Bhuiyan, M.R.; Korkmaz, F.; Nil, M. A Review on Bismuth Telluride (Bi_2Te_3) Nanostructure for Thermoelectric Applications. *Renew. Sustain. Energy Rev.* **2018**, *82*, 4159–4169. [CrossRef]
13. Guo, W.; Ma, J.; Zheng, W. Bi_2Te_3 Nanoflowers Assembled of Defective Nanosheets with Enhanced Thermoelectric Performance. *J. Alloy. Compd.* **2016**, *659*, 170–177. [CrossRef]
14. Zhang, J.; Wu, D.; He, D.; Feng, D.; Yin, M.; Qin, X.; He, J. Extraordinary Thermoelectric Performance Realized in n-Type PbTe through Multiphase Nanostructure Engineering. *Adv. Mater.* **2017**, *29*, 1–7. [CrossRef] [PubMed]
15. Zhao, L.D.; Lo, S.H.; Zhang, Y.; Sun, H.; Tan, G.; Uher, C.; Wolverton, C.; Dravid, V.P.; Kanatzidis, M.G. Ultralow Thermal Conductivity and High Thermoelectric Figure of Merit in SnSe Crystals. *Nature* **2014**, *508*, 373–377. [CrossRef] [PubMed]
16. Peng, K.; Lu, X.; Zhan, H.; Hui, S.; Tang, X.; Wang, G.; Dai, J.; Uher, C.; Wang, G.; Zhou, X. Broad Temperature Plateau for High zTs in Heavily Doped p-Type SnSe Single Crystals. *Energy Environ. Sci.* **2016**, *9*, 454–460. [CrossRef]

17. Shuai, J.; Mao, J.; Song, S.; Zhang, Q.; Chen, G.; Ren, Z. Recent Progress and Future Challenges on Thermoelectric Zintl Materials. *Mater. Today Phys.* **2017**, *1*, 74–95. [CrossRef]

18. Sun, J.; Singh, D.J. Thermoelectric Properties of AMg_2X_2, AZn_2Sb_2 (A = Ca, Sr, Ba; X = Sb, Bi), and Ba_2ZnX_2 (X = Sb, Bi) Zintl Compounds. *J. Mater. Chem. A* **2017**, *5*, 8499–8509. [CrossRef]

19. Chen, X.; Wu, H.; Cui, J.; Xiao, Y.; Zhang, Y.; He, J.; Chen, Y.; Cao, J.; Cai, W.; Pennycook, S.J.; et al. Extraordinary Thermoelectric Performance in n-Type Manganese Doped Mg_3Sb_2 Zintl: High Band Degeneracy, Tuned Carrier Scattering Mechanism and Hierarchical Microstructure. *Nano Energy* **2018**, *52*, 246–255. [CrossRef]

20. Zhu, H.; He, R.; Mao, J.; Zhu, Q.; Li, C.; Sun, J.; Ren, W.; Wang, Y.; Liu, Z.; Tang, Z.; et al. Discovery of ZrCoBi Based Half Heuslers with High Thermoelectric Conversion Efficiency. *Nat. Commun.* **2018**, *9*, 1–9. [CrossRef]

21. Poon, S.J. Half-Heusler Compounds: Promising Materials For Mid-To-High Temperature Thermoelectric Conversion. *J. Phys. D Appl. Phys.* **2019**, *52*, 493001. [CrossRef]

22. Yin, Y.; Tudu, B.; Tiwari, A. Recent Advances in Oxide Thermoelectric Materials and Modules. *Vacuum* **2017**, *146*, 356–374. [CrossRef]

23. Zhang, X.; Chang, C.; Zhou, Y.; Zhao, L.D. BiCuSeO Thermoelectrics: An Update on Recent Progress and Perspective. *Materials* **2017**, *10*, 198. [CrossRef]

24. Cowen, L.M.; Atoyo, J.; Carnie, M.J.; Baran, D.; Schroeder, B.C. Review—Organic Materials for Thermoelectric Energy Generation. *ECS J. Solid State Sci. Technol.* **2017**, *6*, N3080–N3088. [CrossRef]

25. Boudouris, B.W.; Yee, S. Structure, Properties and Applications of Thermoelectric Polymers. *J. Appl. Polym. Sci.* **2017**, *134*. [CrossRef]

26. Ashalley, E.; Chen, H.; Tong, X.; Li, H.; Wang, Z.M. Bismuth Telluride Nanostructures: Preparation, Thermoelectric Properties and Topological Insulating Effect. *Front. Mater. Sci.* **2015**, *9*, 103–125. [CrossRef]

27. Gharsallah, M.; Serrano-Sánchez, F.; Bermúdez, J.; Nemes, N.M.; Martínez, J.L.; Elhalouani, F.; Alonso, J.A. Nanostructured Bi_2Te_3 Prepared by a Straightforward Arc-Melting Method. *Nanoscale Res. Lett.* **2016**, *11*, 4–10. [CrossRef]

28. Kim, K.; Kim, G.; Lee, H.; Lee, K.H.; Lee, W. Band Engineering and Tuning Thermoelectric Transport Properties of p-type $Bi_{0.52}Sb_{1.48}Te_3$ by Pb Doping for Low-Temperature Power Generation. *Scr. Mater.* **2018**, *145*, 41–44. [CrossRef]

29. Ming, T.; Wu, Y.; Peng, C.; Tao, Y. Thermal Analysis on a Segmented Thermoelectric Generator. *Energy* **2015**, *80*, 388–399. [CrossRef]

30. Ouyang, Z.; Li, D. Modelling of Segmented High-Performance Thermoelectric Generators with Effects of Thermal Radiation, Electrical and Thermal Contact Resistances. *Sci. Rep.* **2016**, *6*, 1–12. [CrossRef]

31. Korotkov, A.S.; Loboda, V.V.; Makarov, S.B.; Feldhoff, A. Modeling Thermoelectric Generators Using the ANSYS Software Platform: Methodology, Practical Applications, and Prospects. *Russ. Microelectron.* **2017**, *46*, 131–138. [CrossRef]

32. Oshima, K.; Inoue, J.; Sadakata, S.; Shiraishi, Y.; Toshima, N. Hybrid-Type Organic Thermoelectric Materials Containing Nanoparticles as a Carrier Transport Promoter. *J. Electron. Mater.* **2017**, *46*, 3207–3214. [CrossRef]

33. Culebras, M.; Igual-Muñoz, A.M.; Rodríguez-Fernández, C.; Gómez-Gómez, M.I.; Gómez, C.; Cantarero, A. Manufacturing Te/PEDOT Films for Thermoelectric Applications. *ACS Appl. Mater. Interfaces* **2017**, *9*, 20826–20832. [CrossRef]

34. Wolf, M.; Menekse, K.; Mundstock, A.; Hinterding, R.; Nietschke, F.; Oeckler, O.; Feldhoff, A. Low Thermal Conductivity in Thermoelectric Oxide-Based Multiphase Composites. *J. Electron. Mater.* **2019**, *48*, 7551–7561. [CrossRef]

35. Narducci, D. Do we Really Need High Thermoelectric Figures of Merit? A Critical Appraisal to the Power Conversion Efficiency of Thermoelectric Materials. *Appl. Phys. Lett.* **2011**, *99*. [CrossRef]

36. Xing, Z.; Liu, R.; Liao, J.; Wang, C.; Zhang, Q.; Song, Q.; Xia, X.; Zhu, T.; Bai, S.; Chen, L. A-Device-To-Material Strategy Guiding the "Double-High" Thermoelectric Module. *Joule* **2020**. [CrossRef]

37. Poudel, B.; Hao, Q.; Ma, Y.; Lan, Y.; Minnich, A.; Yu, B.; Yan, X.; Wang, D.; Muto, A.; Vashaee, D.; et al. High-Thermoelectric Performance of Nanostructured Bismuth Antimony Telluride Bulk Allys. *Science* **2008**, *320*, 634–638. [CrossRef]

38. Kim, H.S.; Kikuchi, K.; Itoh, T.; Iida, T.; Taya, M. Design of Segmented Thermoelectric Generator Based on Cost-Effective and Light-Weight Thermoelectric Alloys. *Mater. Sci. Eng. B Solid State Mater. Adv. Technol.* **2014**, *185*, 45–52. [CrossRef]

39. Fu, C.; Bai, S.; Liu, Y.; Tang, Y.; Chen, L.; Zhao, X.; Zhu, T. Realizing High Figure of Merit in Heavy-Band p-Type half-Heusler Thermoelectric Materials. *Nat. Commun.* **2015**, *6*, 1–7. [CrossRef] [PubMed]

40. Chen, L.; Gao, S.; Zeng, X.; Mehdizadeh Dehkordi, A.; Tritt, T.M.; Poon, S.J. Uncovering High Thermoelectric Figure of Merit in (Hf,Zr)NiSn half-Heusler Alloys. *Appl. Phys. Lett.* **2015**, *107*, 041902. [CrossRef]

41. Bittner, M.; Geppert, B.; Kanas, N.; Singh, S.P.; Wiik, K.; Feldhoff, A. Oxide-Based Thermoelectric Generator for High-Temperature Application Using p-Type $Ca_3Co_4O_9$ and n-Type $In_{1.95}Sn_{0.05}O_3$ Legs. *Energy Harvest. Syst.* **2016**, *3*, 213–222. [CrossRef]

42. Bergman, T.L.; Lavine, A.S.; Incropera, F.P.; DeWitt, D.P. *Fundamentals of Heat and Mass Transfer*, 7th ed.; John Wiley & Sons: Hoboken, NJ, USA, 2011; p. 8.

43. Zener, C. Putting Electrons to Work. *Trans. ASM* **1961**, *53*, 1052–1068.

List of Figures

Bibliography

[1] IEA, IEA Data and Statistics (2020).
URL `https://www.iea.org/data-and-statistics?country=WORLD&fuel=Energy` `supply&indicator=ElecGenByFuel, visited 2020-11-10.`

[2] T. Takaishi, R. Nakano, A. Numata, K. Sakaguchi, Approach to High Efficiency Diesel and Gas Engines, Mitsubishi Heavy Industries, Ltd.; Technical Review 45 (1) (2008).

[3] Energy Flowchart (2020).
URL `https://electrek.co/2020/04/09/us-energy-chart-2019/, visited` `2020-11-10.`

[4] R. Kishore, A. Marin, C. Wu, A. Kumar, S. Priya, Energy Harvesting - Materials, Physics, and System Design with Practical Examples, DEStech Publications, 2019.

[5] M. Shirvanimoghaddam, K. Shirvanimoghaddam, M. M. Abolhasani, M. Farhangi, V. Zahiri Barsari, H. Liu, M. Dohler, M. Naebe, Towards a Green and Self-Powered Internet of Things Using Piezoelectric Energy Harvesting, IEEE Access 7 (December) (2019) 94533–94556. doi:10.1109/ACCESS.2019.2928523.

[6] A. Feldhoff, Power Conversion and Its Efficiency in Thermoelectric Materials, Entropy 22 (8) (2020) 803. doi:10.3390/e22080803.

[7] A. Feldhoff, Thermoelectric Material Tensor Derived from the Onsager-de Groot-Callen Model, Energy Harvesting and Systems 2 (1-2) (2015) 5–13. doi:10.1515/ehs-2014-0040.

[8] H. U. Fuchs, A Direct Entropic Approach to Uniform and Spatially Continuous Dynamical Models of Thermoelectric Devices, Energy Harvesting and Systems 1 (3-4) (2014) 1–18. doi:10.1515/ehs-2014-0011.

[9] C. Goupil, W. Seifert, K. Zabrocki, E. Müller, G. J. Snyder, Thermodynamics of Thermoelectric Phenomena and Applications, Entropy 13 (8) (2011) 1481–1517. doi:10.3390/e13081481.

[10] A. Feldhoff, B. Geppert, A High-Temperature Thermoelectric Generator Based on Oxides, Energy Harvesting and Systems 1 (1-2) (2014) 69–78. doi:10.1515/ehs-2014-0003.

[11] A. F. Ioffe, Semiconductor Thermoelements, and Thermoelectric Cooling., 1st Edition, Info-search Ltd., London, 1957. doi:10.1080/01650521.2017.1414983.

[12] C. Kittel, Einführung in die Festkörperphysik, 12th Edition, R. Oldenbourg Verlag, München, Wien, Dresden, 1999.

[13] H. Ibach, H. Lüth, Festkörperphyisk - Einführung in die Grundlagen, 7th Edition, Springer, Berlin, Heidelberg, 2008.

[14] H. Goldsmid, Introduction to Thermoelectricity, Springer-Verlag, Berlin, Heidelberg, 2010.

[15] E. H. Hwang, E. Rossi, S. Das Sarma, Theory of Thermopower in Two-Dimensional Graphene, Physical Review B - Condensed Matter and Materials Physics 80 (23) (2009) 1–5. doi:10.1103/PhysRevB.80.235415.

[16] K. Seeger, Semiconductor Physics, 9th Edition, Springer-Verlag, Berlin, Heidelberg, 1991. doi:10.1007/978-3-662-09855-4.

[17] M. Bittner, B. Geppert, N. Kanas, S. P. Singh, K. Wiik, A. Feldhoff, Oxide-Based Thermoelectric Generator for High-Temperature Application Using p-Type $Ca_3Co_4O_9$ and n-Type $In_{1.95}Sn_{0.05}O_3$ Legs, Energy Harvesting and Systems 3 (3) (2016) 213–222. doi:10.1515/ehs-2016-0002.

[18] E. Guilmeau, D. Bardan, C. Simon, A. Maignan, B. Raveau, D. Ovono, F. Delorme, Tuning the Transport and Thermoelectric Properties of In_2O_3 Bulk Ceramics through Doping at In-Site, Journal of Applied Physics 106 (5) (2009). doi:10.1063/1.3197064.

[19] G. Job, R. Rüffler, Physikalische Chemie - Eine Einführung nach neuem Konzept mit zahlreichen Experimenten, 1st Edition, Vieweg + Teubner Verlag, Wiebaden, 2011.

[20] M. Wolf, K. Menekse, A. Mundstock, R. Hinterding, F. Nietschke, O. Oeckler, A. Feldhoff, Low Thermal Conductivity in Thermoelectric Oxide-Based Multiphase Composites, Journal of Electronic Materials 48 (11) (2019) 7551–7561. doi:10.1007/s11664-019-07555-2.

[21] M. Bittner, N. Kanas, R. Hinterding, F. Steinbach, D. Groeneveld, P. Wemhoff, K. Wiik, M. A. Einarsrud, A. Feldhoff, Triple-Phase Ceramic 2D Nanocomposite with Enhanced Thermoelectric Properties, Journal of the European Ceramic Society 39 (4) (2019) 1237–1244. doi:10.1016/j.jeurceramsoc.2018.10.023.

[22] M. Wolf, R. Hinterding, A. Feldhoff, High Power Factor vs. High zT - A Review of Thermoelectric Materials for High-Temperature Application, Entropy 21 (2019) 1058. doi:10.3390/e21111058.

[23] D. Narducci, Do we Really Need High Thermoelectric Figures of Merit? A Critical Appraisal to the Power Conversion Efficiency of Thermoelectric Materials, Applied Physics Letters 99 (10) (2011). doi:10.1063/1.3634018.

[24] G. Tan, L. D. Zhao, M. G. Kanatzidis, Rationally Designing High-Performance Bulk Thermoelectric Materials, Chemical Reviews 116 (19) (2016) 12123–12149. doi:10.1021/acs.chemrev.6b00255.

[25] J. He, T. M. Tritt, Advances in Thermoelectric Materials Research: Looking Back and Moving Forward, Science 357 (2017) eaak9997. doi:10.1126/SCIENCE.AAK9997.

[26] J. P. Heremans, B. Wiendlocha, A. M. Chamoire, Resonant Levels in Bulk Thermoelectric Semiconductors, Energy and Environmental Science 5 (2) (2012) 5510–5530. doi:10.1039/c1ee02612g.

[27] X. Shi, L. Chen, C. Uher, Recent Advances in High-Performance Bulk Thermoelectric Materials, International Materials Reviews 61 (6) (2016) 379–415. doi:10.1080/09506608.2016.1183075.

[28] M. G. Kanatzidis, Nanostructured Thermoelectrics: The New Paradigm?, Chemistry of Materials 22 (3) (2010) 648–659. doi:10.1021/cm902195j.

[29] W. Liu, X. Yan, G. Chen, Z. Ren, Recent Advances in Thermoelectric Nanocomposites, Nano Energy 1 (1) (2012) 42–56. doi:10.1016/j.nanoen.2011.10.001.

[30] B. C. Sales, Electron Crystals and Phonon Glasses: A New Path to Improved Thermoelectric Materials, MRS Bulletin 23 (1) (1998) 15–21. doi:10.1557/S0883769400031419.

[31] N. Toshima, Recent Progress of Organic and Hybrid Thermoelectric Materials, Synthetic Metals 225 (2017) 3–21. doi:10.1016/j.synthmet.2016.12.017.

[32] Y. Wang, Y. Sui, J. Cheng, X. Wang, W. Su, Comparison of the High Temperature Thermoelectric Properties for Ag-Doped and Ag-Added $Ca_3Co_4O_9$, Journal of Alloys and Compounds 477 (1-2) (2009) 817–821. doi:10.1016/j.jallcom.2008.10.162.

[33] D. J. Bergman, O. Levy, Thermoelectric Properties of a Composite Medium, Journal of Applied Physics 70 (11) (1991) 6821–6833. doi:10.1063/1.349830.

[34] R. Hinterding, Z. Zhao, M. Wolf, M. Jakob, O. Oeckler, A. Feldhoff, Ceramic Composites Based on $Ca_3Co_4O_9$ and $La_2NiO_{4+\delta}$ with Enhanced Thermoelectric Properties, Open Ceramics 6 (2021) 100103. doi:10.1016/j.oceram.2021.100103.

[35] H. Mamur, M. R. Bhuiyan, F. Korkmaz, M. Nil, A Review on Bismuth Telluride (Bi_2Te_3) Nanostructure for Thermoelectric Applications, Renewable and Sustainable Energy Reviews 82 (2018) 4159–4169. doi:10.1016/j.rser.2017.10.112.

[36] C. Gayner, K. Kar, Recent Advances in Thermoelectric Materials, Progress in Materials Science 83 (2016) 330–382. doi:10.1016/j.pmatsci.2016.07.002.

[37] V. Q. Nguyen, J. Kim, S. Cho, A Review of SnSe: Growth and Thermoelectric Properties, Journal of the Korean Physical Society 72 (8) (2018) 841–857. doi:10.3938/jkps.72.841.

[38] X. L. Shi, X. Tao, J. Zou, Z. G. Chen, High-Performance Thermoelectric SnSe: Aqueous Synthesis, Innovations, and Challenges, Advanced Science 7 (7) (2020). doi:10.1002/advs.201902923.

[39] J. W. Fergus, Oxide Materials for High Temperature Thermoelectric Energy Conversion, Journal of the European Ceramic Society 32 (3) (2012) 525–540. doi:10.1016/j.jeurceramsoc.2011.10.007.

[40] Y. Yin, B. Tudu, A. Tiwari, Recent Advances in Oxide Thermoelectric Materials and Modules, Vacuum 146 (2017) 356–374. doi:10.1016/j.vacuum.2017.04.015.

[41] J. Shuai, J. Mao, S. Song, Q. Zhang, G. Chen, Z. Ren, Recent Progress and Future Challenges on Thermoelectric Zintl Materials, Materials Today Physics 1 (2017) 74–95. doi:10.1016/j.mtphys.2017.06.003.

[42] S. Chen, Z. Ren, Recent Progress of half-Heusler for Moderate Temperature Thermoelectric Applications, Materials Today 16 (10) (2013) 387–395. doi:10.1016/j.mattod.2013.09.015.

[43] J. S. Poon, Recent Advances in Thermoelectric Performance of half-Heusler Compounds, Metals 8 (12) (2018) 989. doi:10.3390/met8120989.

[44] J. S. Poon, Half-Heusler Compounds: Promising Materials for Mid-to-High Temperature Thermoelectric Conversion, J. Phys. D: Appl. Phys. 52 (2019) 493001.

[45] G. Schierning, Silicon Nanostructures for Thermoelectric Devices: A Review of the Current State of the Art, Physica Status Solidi (A) Applications and Materials Science 211 (6) (2014) 1235–1249. doi:10.1002/pssa.201300408.

[46] L. M. Cowen, J. Atoyo, M. J. Carnie, D. Baran, B. C. Schroeder, Review - Organic Materials for Thermoelectric Energy Generation, ECS Journal of Solid State Science and Technology 6 (3) (2017) N3080–N3088. doi:10.1149/2.0121703jss.

[47] M. Kishi, H. Nemoto, T. Hamao, M. Yamamoto, S. Sudou, M. Mandai, S. Yamamoto, Micro Thermoelectric Modules and their Application to Wristwatches as an Energy Source, Eighteenth International Conference on Thermoelectrics. Proceedings, ICT'99 (Cat. No.99TH8407) (1999) 301–307doi:10.1109/ICT.1999.843389.

[48] L. E. Bell, Cooling, Heating, Generating Power, and Recovering Waste Heat with Thermoelectric Systems, Science 321 (5895) (2008) 1457–1461. doi:10.1126/science.1158899.

[49] E. Ashalley, H. Chen, X. Tong, H. Li, Z. M. Wang, Bismuth Telluride Nanostructures: Preparation, Thermoelectric Properties and Topological Insulating Effect, Frontiers of Materials Science 9 (2) (2015) 103–125. doi:10.1007/s11706-015-0285-9.

[50] B. Poudel, Q. Hao, Y. Ma, Y. Lan, A. Minnich, B. Yu, X. Yan, D. Wang, A. Muto, D. Vashaee, X. Chen, J. Liu, Dresselaus, G. Chen, Z. Ren, High-Thermoelectric Performance of Nanostructured Bismuth Antimony Telluride Bulk Alloys, Science 320 (5876) (2008) 634–638. doi:10.1126/science.1155140.

[51] S. I. Kim, K. H. Lee, H. A. Mun, H. S. Kim, S. W. Hwang, J. W. Roh, D. J. Yang, W. H. Shin, X. S. Li, Y. H. Lee, G. J. Snyder, S. W. Kim, Dense Dislocation Arrays Embedded in Grain Boundaries for High-Performance Bulk Thermoelectrics, Science 348 (6230) (2015) 109–114. doi:10.1126/science.aaa4166.

[52] A. Feldhoff, M. Arnold, J. Martynczuk, T. M. Gesing, H. Wang, The Sol-Gel Synthesis of Perovskites by an EDTA/Citrate Complexing Method Involves Nanoscale Solid State Reactions, Solid State Sciences 10 (6) (2008) 689–701. doi:10.1016/j.solidstatesciences.2007.11.030.

[53] Z. Shi, J. Xu, J. Zhu, Y. Zhang, T. Gao, M. Qin, H. Sun, Effect of Platelet Template Seeds on Microstructure and Thermoelectric Properties of $Ca_3Co_4O_9$ Ceramics, Ceramics International (October) (2018) 1–7. doi:10.1016/j.ceramint.2018.10.092.

[54] T. Schulz, J. Töpfer, Thermoelectric Properties of $Ca_3Co_4O_9$ Ceramics Prepared by an Alternative Pressure-Less Sintering/Annealing Method, Journal of Alloys and Compounds 659 (2016) 122–126. doi:10.1016/j.jallcom.2015.11.001.

[55] S. Bresch, B. Mieller, C. Selleng, T. Stöcker, R. Moos, T. Rabe, Influence of the Calcination Procedure on the Thermoelectric Properties of Calcium Cobaltite $Ca_3Co_4O_9$, Journal of Electroceramics 40 (3) (2018) 225–234. doi:10.1007/s10832-018-0124-3.

[56] M. Bittner, L. Helmich, F. Nietschke, B. Geppert, O. Oeckler, A. Feldhoff, Porous $Ca_3Co_4O_9$ with Enhanced Thermoelectric Properties Derived from Sol-Gel Synthesis, Journal of the European Ceramic Society 37 (13) (2017) 3909–3915. doi:10.1016/j.jeurceramsoc.2017.04.059.

[57] K. X. Wang, J. Wang, H. Wu, N. Shaheen, X.-Y. Zha, L.-J. Gao, H.-C. Bai, Thermoelectric Properties of Lower Concentration K-Doped $Ca_3Co_4O_9$ Ceramics, Chinese Physics B 27 (5) (2018). doi:10.1088/1674-1056/27/5/057201.

[58] G. Constantinescu, S. H. Rasekh, M. A. Torres, C. Chocarro, J. C. Díez, M. A. Madre, A. Sotelo, Influence of Ca Substitution by Mg on the $Ca_3Co_4O_9$ Performances, Boletin de la Sociedad Espanola de Ceramica y Vidrio 53 (1) (2014) 41–47. doi:10.3989/cyv.62014.

[59] J. S. Cha, S. Choi, G. H. Kim, S. Kim, K. Park, High-Temperature Thermoelectric Properties of Sm^{3+}-Doped $Ca_3Co_4O_{9+\delta}$ Fabricated by Spark Plasma Sintering, Ceramics International 44 (6) (2018) 6376–6383. doi:10.1016/j.ceramint.2018.01.030.

[60] S. Saini, H. S. Yaddanapudi, K. Tian, Y. Yin, D. Magginetti, A. Tiwari, Terbium Ion Doping in $Ca_3Co_4O_9$: A Step Towards High-Performance Thermoelectric Materials, Scientific Reports 7 (November 2016) (2017) 1–9. doi:10.1038/srep44621.

[61] N. Prasoetsopha, S. Pinitsoontorn, T. Kamwanna, V. Amornkitbamrung, K. Kurosaki, Y. Ohishi, H. Muta, S. Yamanaka, The Effect of Cr Substitution on the Structure and Properties of Misfit-Layered $Ca_3Co_{4-x}Cr_xO_{9+\delta}$ Thermoelectric Oxides, Journal of Alloys and Compounds 588 (2014) 199–205. doi:10.1016/j.jallcom.2013.11.034.

[62] S. Butt, W. Xu, W. Q. He, Q. Tan, G. K. Ren, Y. Lin, C. W. Nan, Enhancement of Thermoelectric Performance in Cd-Doped $Ca_3Co_4O_9$ via Spin Entropy, Defect Chemistry and Phonon Scattering, Journal of Materials Chemistry A 2 (45) (2014) 19479–19487. doi:10.1039/c4ta03891f.

[63] U. Hira, L. Han, K. Norrman, D. Christensen, N. Pryds, F. Sher, High-Temperature Thermoelectric Properties of Na- and W-Doped $Ca_3Co_4O_9$ System, RSC Adv. 8 (2018) 12211–12221. doi:10.1039/c8ra01691g.

[64] C. Liu, F. Jiang, M. Huang, B. Lu, R. Yue, J. Xu, Free-Standing PEDOT-PSS/$Ca_3Co_4O_9$ Composite Films as Novel Thermoelectric Materials, Journal of Electronic Materials 40 (5) (2011) 948–952. doi:10.1007/s11664-010-1465-0.

[65] F. Kahraman, M. A. Madre, S. Rasekh, C. Salvador, P. Bosque, M. A. Torres, J. C. Diez, A. Sotelo, Enhancement of Mechanical and Thermoelectric Properties of $Ca_3Co_4O_9$ by Ag Addition, Journal of the European Ceramic Society 35 (14) (2015) 3835–3841. doi:10.1016/j.jeurceramsoc.2015.05.029.

[66] L. Han, N. Van Nong, W. Zhang, L. T. Hung, T. Holgate, K. Tashiro, M. Ohtaki, N. Pryds, S. Linderoth, Effects of Morphology on the Thermoelectric Properties of Al-Doped ZnO, RSC Advances 4 (24) (2014) 12353–12361. doi:10.1039/c3ra47617k.

[67] N. H. Tran Nguyen, T. H. Nguyen, Y.-r. Liu, M. Aminzare, A. T. T. Pham, S. Cho, D. P. Wong, K.-H. Chen, T. Seetawan, N. K. Pham, H. K. T. Ta, V. C. Tran, T. B. Phan, Thermoelectric Properties of Indium and Gallium Dually Doped ZnO Thin Films, ACS Applied Materials & Interfaces 8 (49) (2016) 33916–33923. doi:10.1021/acsami.6b10591.

[68] A. Graff, Y. Amouyal, Effects of Lattice Defects and Niobium Doping on Thermoelectric Properties of Calcium Manganate Compounds for Energy Harvesting Applications, Journal of Electronic Materials 45 (3) (2016) 1508–1516. doi:10.1007/s11664-015-4089-6.

[69] S. Paengson, P. Pilasuta, K. Singsoog, W. Namhongsa, W. Impho, T. Seetawan, Improvement in Thermoelectric Properties of $CaMnO_3$ by Bi Doping and Hot Pressing, Materials Today: Proceedings 4 (5) (2017) 6289–6295. doi:10.1016/j.matpr.2017.06.129.

[70] J. W. Seo, G. H. Kim, S. M. Choi, K. Park, High-Temperature Thermoelectric Properties of Polycrystalline $CaMn_{1-x}Nb_xO_{3-\delta}$, Ceramics International 44 (8) (2018) 9204–9214. doi:10.1016/j.ceramint.2018.02.130.

[71] M. Qin, F. Gao, M. Wang, C. Zhang, Q. Zhang, L. Wang, Fabrication and High-Temperature Thermoelectric Properties of Ti-Doped $Sr_{0.9}La_{0.1}TiO_3$ Ceramics, Ceramics International 42 (15) (2016) 16644–16649. doi:10.1016/j.ceramint.2016.07.091.

[72] A. C. Iyasara, W. L. Schmidt, R. Boston, D. C. Sinclair, I. M. Reaney, La and Sm Co-Doped $SrTiO_{3-\delta}$ Thermoelectric Ceramics, Materials Today: Proceedings 4 (12) (2017) 12360–12367. doi:10.1016/j.matpr.2017.10.004.

[73] Y. Chen, J. Liu, Y. Li, X. Zhang, X. Wang, W. Su, J. Li, C. Wang, Enhancement of Thermoelectric Performance of $Sr_{1-x}Ti_{0.8}Nb_{0.2}O_3$ Ceramics by Introducing Sr Vacancies, Journal of Electronic Materials 48 (2) (2019) 1147–1152. doi:10.1007/s11664-018-6831-3.

[74] J. Mao, Y. Wang, H. S. Kim, Z. Liu, U. Saparamadu, F. Tian, K. Dahal, J. Sun, S. Chen, W. Liu, Z. Ren, High Thermoelectric Power Factor in Cu-Ni Alloy Originate from Potential Barrier Scattering of Twin Boundaries, Nano Energy 17 (2015) 279–289. doi:10.1016/j.nanoen.2015.09.003.

[75] H. Muta, K. Kurosaki, M. Uno, S. Yamanaka, Thermoelectric Properties of Constantan/Spherical SiO_2 and Al_2O_3 Particles Composite, Journal of Alloys and Compounds 359 (2003) 326–329. doi:10.1016/S0925-8388(03)00295-0.

[76] M. Yuan, L. Sun, X. W. Lu, P. Jiang, X. H. Bao, Enhancing the Thermoelectric Performance of Cu-Ni Alloys by Introducing Carbon Nanotubes, Materials Today Physics 16 (2021). doi:10.1016/j.mtphys.2020.100311.

[77] C. A. Wu, K. C. Chang, F. H. Lin, Z. R. Yang, A. Gharleghi, T. Z. Wei, C. J. Liu, Low Thermal Conductivity and Enhanced zT Values of Porous and Nanostructured $Cu_{1-x}Ni_x$ alloys, Chemical Engineering Journal 368 (February) (2019) 409–416. doi:10.1016/j.cej.2019.02.198.

[78] H. Kang, Z. Yang, X. Yang, J. Li, W. He, Z. Chen, E. Guo, L. D. Zhao, T. Wang, Preparing Bulk Cu-Ni-Mn Based Thermoelectric Alloys and Synergistically Improving their Thermoelectric and Mechanical Properties using Nanotwins and Nanoprecipitates, Materials Today Physics 17 (2021). doi:10.1016/j.mtphys.2020.100332.

[79] J. Shuai, B. Ge, J. Mao, S. Song, Y. Wang, Z. Ren, Significant Role of Mg Stoichiometry in Designing High Thermoelectric Performance for $Mg_3(Sb,Bi)_2$-Based n-Type Zintls, Journal of the American Chemical Society 140 (5) (2018) 1910–1915. doi:10.1021/jacs.7b12767.

[80] C. Fu, S. Bai, Y. Liu, Y. Tang, L. Chen, X. Zhao, T. Zhu, Realizing High Figure of Merit in Heavy-Band p-Type half-Heusler Thermoelectric Materials, Nature Communications 6 (2015) 1–7. doi:10.1038/ncomms9144.

[81] X. Wang, H. Lee, Y. Lan, G. Zhu, G. Joshi, D. Wang, J. Yang, A. Muto, M. Tang, J. Klatsky, S. Song, M. Dresselhaus, G. Chen, Z. Ren, Enhanced Thermoelectric Figure-of-Merit in Nanostructured n-Type Silicon Germanium Bulk Alloys, Applied Physics Letters 93 (2008) 193121. doi:10.1021/nl8026795.

[82] S. B. Riffat, X. Ma, Thermoelectrics: A Review of Present and Potential Applications, Applied Thermal Engineering 23 (8) (2003) 913–935. doi:10.1016/S1359-4311(03)00012-7.

[83] S. J. Kim, J. H. We, B. J. Cho, A Wearable Thermoelectric Generator Fabricated on a Glass Fabric, Energy and Environmental Science 7 (6) (2014) 1959–1965. doi:10.1039/c4ee00242c.

[84] M. Wolf, M. Abt, G. Hoffmann, L. Overmeyer, A. Feldhoff, Ceramic-Based Thermoelectric Generator Processed via Spray-Coating and Laser Structuring, Open Ceramics 1 (2020) 100002. doi:10.1016/j.oceram.2020.100002.

[85] M. Orrill, S. LeBlanc, Printed Thermoelectric Materials and Devices: Fabrication Techniques, Advantages, and Challenges, Journal of Applied Polymer Science 134 (3) (2017) 44256. doi:10.1002/app.44256.

[86] S. Leblanc, S. K. Yee, M. L. Scullin, C. Dames, K. E. Goodson, Material and Manufacturing Cost Considerations for Thermoelectrics, Renewable and Sustainable Energy Reviews 32 (2014) 313–327. doi:10.1016/j.rser.2013.12.030.

[87] International Organization for Standartization: ISO/ASTM 52900, Tech. rep. (2015).

[88] X. Huang, T. Leng, X. Zhang, J. C. Chen, K. H. Chang, A. K. Geim, K. S. Novoselov, Z. Hu, Binder-Free Highly Conductive Graphene Laminate for Low Cost Printed Radio Frequency Applications, Applied Physics Letters 106 (20) (2015) 203105. doi:10.1063/1.4919935.

[89] A. Chen, D. Madan, P. K. Wright, J. W. Evans, Dispenser-Printed Planar Thick-Film Thermoelectric Energy Generators, Journal of Micromechanics and Microengineering 21 (10) (2011) 104006. doi:10.1088/0960-1317/21/10/104006.

[90] W. Glatz, S. Muntwyler, C. Hierold, Optimization and Fabrication of Thick Flexible Polymer Based Micro Thermoelectric Generator, Sensors and Actuators, A: Physical 132 (1 SPEC. ISS.) (2006) 337–345. doi:10.1016/j.sna.2006.04.024.

[91] A. Besganz, V. Zöllmer, R. Kun, E. Pál, L. Walder, M. Busse, Inkjet Printing as a Flexible Technology for the Deposition of Thermoelectric Composite Structures, Procedia Technology 15 (2014) 99–106. doi:10.1016/j.protcy.2014.09.043.

[92] A. G. Rösch, A. Gall, S. Aslan, M. Hecht, L. Franke, M. M. Mallick, L. Penth, D. Bahro, D. Friderich, U. Lemmer, Fully Printed Origami Thermoelectric Generators for Energy-Harvesting, npj Flexible Electronics 5 (1) (2021) 1–8. doi:10.1038/s41528-020-00098-1.

[93] D. Madan, A. Chen, P. K. Wright, J. W. Evans, Printed Se-doped MA n-Type Bi_2Te_3 Thick-Film Thermoelectric Generators, Journal of Electronic Materials 41 (6) (2012) 1481–1486. doi:10.1007/s11664-011-1885-5.

[94] T. Varghese, C. Hollar, J. Richardson, N. Kempf, C. Han, P. Gamarachchi, D. Estrada, R. J. Mehta, Y. Zhang, High-Performance and Flexible Thermoelectric Films by Screen Printing Solution-Processed Nanoplate Crystals, Scientific reports 6 (September) (2016) 33135. doi:10.1038/srep33135.

[95] Z. Cao, E. Koukharenko, M. J. Tudor, R. N. Torah, S. P. Beeby, Flexible Screen Printed Thermoelectric Generator with Enhanced Processes and Materials, Sensors and Actuators, A: Physical 238 (2016) 196–206. doi:10.1016/j.sna.2015.12.016.

[96] S. Nolte, F. Schrempel, F. Dausinger, Ultrashort Pulse Laser Technology, Springer International Publishing, Heidelberg, New York, Dordrecht, London, 2016.

[97] M. Schmidt, M. Merklein, D. Bourell, D. Dimitrov, T. Hausotte, K. Wegener, L. Overmeyer, F. Vollertsen, G. N. Levy, Laser Based Additive Manufacturing in Industry and Academia, CIRP Annals 66 (2) (2017) 561–583. doi:10.1016/j.cirp.2017.05.011.

[98] M. Agarwala, D. Bourell, J. Beaman, H. Marcus, J. Barlow, Direct Selective Laser Sintering of Metals, Rapid Prototyping Journal 1 (1) (1995) 26–36.

[99] J. Kruth, X. Wang, T. Laoui, L. Froyen, Laser and Materials in Selective Laser Sintering, Assembly Automation 23 (4) (2003) 357–371.

[100] J. P. Kruth, P. Mercelis, J. Van Vaerenbergh, L. Froyen, M. Rombouts, Binding Mechanisms in Selective Laser Sintering and Selective Laser Melting, Rapid Prototyping Journal 11 (1) (2005) 26–36. doi:10.1108/13552540510573365.

[101] R. D. Goodridge, C. J. Tuck, R. J. Hague, Laser Sintering of Polyamides and Other Polymers, Progress in Materials Science 57 (2) (2012) 229–267. doi:10.1016/j.pmatsci.2011.04.001.

[102] Y. Kinemuchi, M. Mikami, I. Terasaki, W. Shin, Rapid Synthesis of Thermoelectric Compounds by Laser Melting, Materials and Design 106 (2016) 30–36. doi:10.1016/j.matdes.2016.05.093.

[103] M. Radović, G. Dubourg, S. Kojić, Z. Dohčević-Mitrović, B. Stojadinović, M. Bokorov, V. Crnojević-Bengin, Laser Sintering of Screen-Printed TiO_2 Nanoparticles for Improvement of Mechanical and Electrical Properties, Ceramics International 44 (9) (2018) 10975–10983. doi:10.1016/j.ceramint.2018.03.181.

[104] S. Mu, H. Huang, A. Ishii, Z. Zhao, M. Zou, P. Kuzbary, F. Peng, K. S. Brinkman, H. Xiao, J. Tong, Rapid Laser Reactive Sintering of $BaCe_{0.7}Zr_{0.1}Y_{0.1}Yb_{0.1}O_{3-\delta}$ Electrolyte for Protonic Ceramic Fuel Cells, Journal of Power Sources Advances 4 (February) (2020) 100017. doi:10.1016/j.powera.2020.100017.

2. Improvement of thermoelectric materials

2.1 Summary

In this chapter, material research for improving the properties of thermoelectric materials is presented. As described before, the deviation of maximum conversion efficiency and maximum power output is an increasing and important topic within the thermoelectric community. The deviation can strongly influence the viability of some materials, as they may be either designed for high conversion efficiency or high power output. This is shown here via two examples:

In section 2.2, the concept of multiphase hybrid materials is presented. Here, the idea is the combination of different materials into one hybrid material in the hope to combine the favorable attributes of every component. The most promising oxide-based thermoelectric material, $Ca_3Co_4O_9$ (CCO), was combined with metallic Ag particles in order to increase the electrical properties, as well as with a polymeric phase to adjust the thermal conductivity. Via the introduction of heteromaterial interfaces and due to the utilization of a polymer, the resulting hybrid materials showed an exceptionally low thermal conductivity. This, however, also resulted in a decrease of the electrical conductivity. Although the inclusion of an increasing amount of Ag leads to an improvement, the resulting power factor is still lower than that of pure, sintered, bulk CCO. This concept of hybrid materials nevertheless proved to be able to strongly decrease the thermal conductivity and is therefore promising to adjust the figure of merit zT.

In section 2.3, the thermoelectric properties of Cu-Ni alloys are investigated. As introduced, the utilization of metallic materials in order to achieve high power output is interesting, even if the conversion efficiency is lower compared to established semiconductors. Here, Cu-Ni alloys with added Sn or W are presented. This is based on the well-known isotan, which has seen wide use in the form of thermoelements. Tin and tungsten have been chosen as much heavier elements in order to alter the structure and reduce the still comparably high thermal conductivity of the material, its major drawback. In the displayed work, the results of the nanoparticles-based arc melted samples are presented, showing an increase in both the power factor as well as the figure of merit zT for low doping levels of 1 - 2 %, resulting in a maximum power factor of 52 μW cm^{-1} K^{-2} and a maximum zT of 0.15 for the 1 % Sn alloyed sample. This work shows the promising properties of basic metal alloys such as Cu-Ni to achieve a high power factor via noncritical and nontoxic materials that are suitable for large scale metallurgic processes.

2.2 Low thermal conductivity in thermoelectric oxide-based multiphase composites

Mario Wolf, Kaan Menekse, Alexander Mundstock, Richard Hinterding, Frederik Nietschke, Oliver Oeckler and Armin Feldhoff

Low Thermal Conductivity in Thermoelectric Oxide-Based Multiphase Composites

MARIO WOLF [ID],[1,3] KAAN MENEKSE,[1] ALEXANDER MUNDSTOCK,[1]
RICHARD HINTERDING [ID],[1] FREDERIK NIETSCHKE,[2]
OLIVER OECKLER [ID],[2] and ARMIN FELDHOFF [ID][1,4]

1.—Institute of Physical Chemistry and Electrochemistry, Leibniz University Hannover, Hannover, Germany. 2.—Institute of Mineralogy, Crystallography and Materials Science, Leipzig University, Leipzig, Germany. 3.—e-mail: mario.wolf@pci.uni-hannover.de. 4.—e-mail: armin.feldhoff@pci.uni-hannover.de

Thermoelectric oxide-based multiphase systems gain synergistic properties from different materials. Therefore, multiphase systems based on a thermoelectric oxide, combined with both a polymeric phase (Matrimid) and a highly electrically conducting phase (Ag, carbon black) have been investigated. Compared to single-phase porous $Ca_3Co_4O_9$, the resulting composite materials showed a decreased electrical conductivity while reaching a high Seebeck coefficient of up to 200 μV/K as well as a 4 times lower thermal conductivity. The strongly enhanced phonon scattering in the multiphase system resulting in low thermal conductivity is an especially interesting concept to design thermoelectric multiphase materials. Additionally, Ioffe plots are revitalized to compare the resulting power factor and thermal properties of the composite materials. The significantly low thermal conductivity due to the heteromaterial interfaces in the composite materials especially underlines the potential of multiphase systems as thermoelectric materials.

Key words: Energy harvesting, thermoelectric materials, energy materials, composite materials

INTRODUCTION

In recent years, the utilization of waste energy has become an important topic in energy research. Since wasted energy is dissipated as heat, thermoelectric materials are of special interest for the direct conversion of heat to electrical energy.[1,2] However, due to low overall conversion efficiency, low energy density and high material costs,[3] thermoelectric materials still need to be improved. In general, thermoelectric power generation from a temperature gradient is based on the diffusion of charge carriers from the hot side to the cold side of the material. The applied temperature gradient ∇T is coupled with the electrical potential gradient $\nabla \varphi$, resulting in flux densities of entropy j_S and charge j_q. The relation between the potential gradients and the related flux densities is mediated by a thermoelectric material tensor (Eq. 1).[4,5]

$$\begin{pmatrix} j_q \\ j_S \end{pmatrix} = \begin{pmatrix} \sigma & \sigma \cdot \alpha \\ \sigma \cdot \alpha & \sigma \cdot \alpha^2 + \Lambda \end{pmatrix} \cdot \begin{pmatrix} -\nabla \varphi \\ -\nabla T \end{pmatrix} \quad (1)$$

The thermoelectric material tensor is composed of the isothermal electrical conductivity σ, the Seebeck coefficient α and the electrically open-circuited entropy conductivity Λ. The efficiency of power conversion can be derived from this material tensor resulting in the dimensionless figure of merit zT (Eq. 2), as first described by Ioffe[6]:

$$zT = \frac{\sigma \cdot \alpha^2}{\Lambda} = \frac{\sigma \cdot \alpha^2}{\lambda} \cdot T \quad (2)$$

Wolf, Menekse, Mundstock, Hinterding, Nietschke, Oeckler, and Feldhoff

Based on Eq. 2, promising thermoelectric materials exhibit a high power factor $\sigma\alpha^2$ and a low electrically open-circuited entropy conductivity Λ. The thermal conductivity can be either expressed by the entropy conductivity Λ or the heat conductivity λ, which are related by the absolute temperature T (Eq. 3). In the following, both entropy conductivity Λ and heat conductivity λ refer to electrically open-circuited conditions.

$$\lambda = \Lambda \cdot T \qquad (3)$$

Expressing the thermal conductivity by the entropy conductivity Λ enables concise forms of the basic transport equation (Eq. 1) as well as of the figure of merit zT (Eq. 2).[5,7,8] In the authors' opinion, use of the more fundamental entropy conductivity is straightforward and advantageous. However, to allow comparison with reported values, the traditional heat conductivity is used as well.

Commercial thermoelectric generators mostly consist of Bi_2Te_3-based compounds, which offer good thermoelectric properties with $zT > 1$,[9] but feature disadvantages in costs, toxicity, elaborate production needs and scale-up difficulty.[10] Therefore, different groups of materials including metal-based materials and intermetallics [half-Heusler compounds MCoSb (M = Ti, Zr, Hf),[11,12] Zintl-phases,[13,14] etc.], oxide-based materials ($Ca_3Co_4O_9$,[15,16] ZnO[17,18] etc.) or other metal-chalcogenide compounds ($SnSe$,[19] tetrahedrites,[20] etc.) are being researched. Apart from the conventional materials, organic and hybrid materials for thermoelectric applications have aroused high interest in recent years.[21–24] Within the group of thermoelectric metallic oxides, different n-type materials such as ZnO[25,26] or $SrTiO_3$[27] as well as p-type materials such as Na_xCoO_2[28] or $Ca_3Co_4O_9$ (CCO)[16,29] have

already been studied extensively. Thermoelectric oxides are characterized by their non-toxicity, high temperature and mechanical stability, and show good thermoelectric properties at high temperatures, reaching zT values up to 0.75 in a bulk material.[30]

For a better understanding, the interrelation between the thermoelectric properties can be demonstrated by Ioffe plots[6] of these different materials, which present the power factor $\sigma\alpha^2$ as a function of the electrical conductivity σ. Figure 1a shows Ioffe plots of different materials from various groups of thermoelectric materials. Here, metals show the highest power factor despite their low Seebeck coefficient, while polymers feature the lowest power factor of the materials discussed here. Bi_2Te_3 compounds and oxide-based materials offer the highest Seebeck coefficient α. A desired material would be located at a high power factor and high electrical conductivity (top right). Analogous plots can be made for the electrically open-circuited entropy conductivity Λ, which can be displayed with the same unit and scale leading to a directly observable zT value. In Fig. 1b, it can clearly be seen that metals exhibit the highest entropy conductivity, while polymers have the lowest entropy conductivity. Here, a desired material with a high figure of merit zT would be located at a low entropy conductivity and high electrical conductivity (bottom right). Furthermore, the slopes in Fig. 1b show the Lorenz number L, according to the Wiedemann–Franz relation. This empirical relation, which is valid for many metals, alloys and half-metals at $T > 150$ K, describes a proportional behavior between electrical conductivity and thermal conductivity. This proportional behavior generally leads to an inherent conflict, since a high-zT material requires high electrical conductivity but low
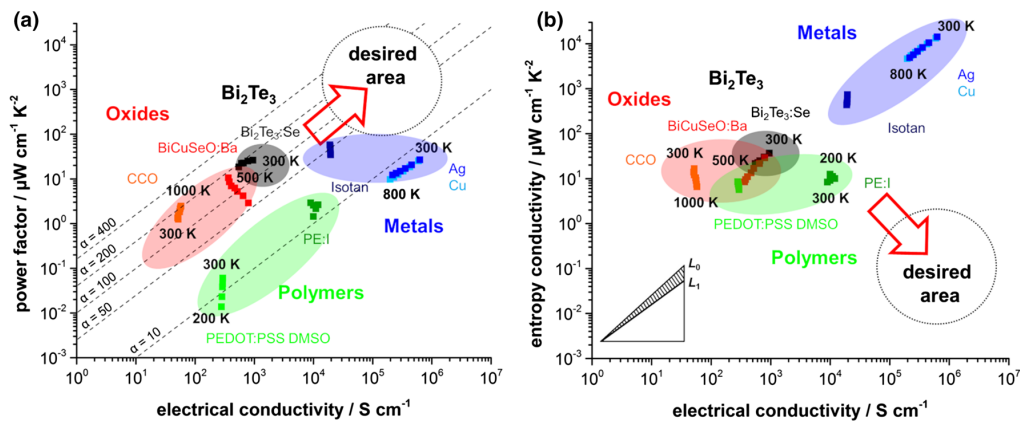

Fig. 1. (a) Ioffe plot and (b) entropy-electrical conductivity plot of different materials (note: Isotan = alloy with 55% Cu, 44% Ni, 1% Mn).[36–40] Dashed lines in (a) show Seebeck coefficient α in μV/K. Slopes in (b) show the empirical Wiedemann–Franz relation with the two classical limiting cases of the Lorenz number for complete degeneracy (L_0) and complete non-degeneracy (L_1). Some complex semiconducting materials like CCO do not follow this slope, making them very promising materials. Note that both plots use an identical unit and scale on horizontal and vertical axes, respectively.

Low Thermal Conductivity in Thermoelectric Oxide-Based Multiphase Composites

thermal conductivity.[31] Classically, the ratio $L = \Lambda/\sigma$ varies between the Sommerfeld value for complete degeneracy of $L_0 = \pi^2 \cdot k_B^2/3 \cdot e^2 = 2.45 \times 10^{-8}$ W $\Omega/$K^2 (Fermi gas) and $L_1 = 1.48 \times 10^{-8}$ W $\Omega/$K^2 for complete non-degeneracy.[6,32] However, especially non-degenerated inorganic semiconductors with low carrier concentration, and thus many modern thermoelectric materials with complex structural and electronic properties, diverge from the classical proportionality.[33,34] Moreover, the respective ratio shows a strong dependency on the specific materials, charge carrier concentrations, effective electron masses and external conditions like pressure and temperature.[33,35] As a result of the inherent conflict mentioned above, investigation of promising new thermoelectric materials focuses on materials with a strong deviation from the empirical relation. Accordingly, the plots in Fig. 1b clearly show that some high-zT semiconducting thermoelectric materials, like CCO, as well as many organic thermoelectric materials and even metal alloys such as Isotan, do not follow the slope of the empirical Wiedemann–Franz relation, thus making these materials very promising candidates for a significantly low ratio of thermal conductivity to electrical conductivity and therefore a high zT value.

Besides common strategies such as the enhancement of concentration, mobility as well as effective mass of charge carriers and the nanostructuring as well as doping, the combination of different materials is a promising way of tuning thermoelectric parameters and especially the thermal conductivity, which is pursued in this work. Resulting composite materials offer an interesting pathway of utilizing beneficial properties of different materials. Besides adjusting thermal properties by nanostructuring, texturing and homomaterial interfaces in a bulk material, a high concentration of heteromaterial interfaces in a multiphase system leads to enhanced phonon scattering at these interfaces, resulting in

an exceptionally low thermal conductivity.[41] As described above, the slope of the well-known thermoelectric material CCO does not show Wiedemann–Franz behavior, thus making it a very interesting material to design a multiphase system. Here, the advantages of composite materials were already shown, for example, by adding metallic phases (e.g. Ag) to oxide-based thermoelectric materials, such as CCO, resulting in composite materials with enhanced thermoelectric properties.[42,43] Recently, composite materials of conducting polymers with small amounts of inorganic compounds have been investigated.[24,44–47] Zheng et al.[48] showed that the Seebeck coefficient of polyaniline can be strongly improved by adding low amounts of CCO. The possibility of increasing the Seebeck coefficient by developing PEDOT:PSS composite materials with low amounts of CCO was also presented.[44,49] Recently, composite materials with Bi_2Te_3[50,51] or carbon nanotubes[52,53] in a polymeric matrix, e.g. polyethylene or PEDOT derivates, were analyzed and also showed enhanced thermoelectric properties, especially a high power factor. In Fig. 2, several of the aforementioned composite materials are classified within an Ioffe plot and an entropy-electrical conductivity plot.

In this paper, the feasibility to synthesize bulk multiphase composites with combined thermoelectric properties of different materials has been investigated. All thermoelectric parameters of a composite material are strongly affected by its composition and microstructure.[54,55] To prepare multiphase composites, non-toxic CCO was combined with low amounts of up to 10% of polymeric and metallic phases. As a polymer, Matrimid 5218, a thermoplastic polyimide, was used because of its good processability and high thermal stability of up to 623 K in air.[56,57] Ag and carbon black were used to reach a tunable electrical conductivity. The thermoelectric properties as well as the
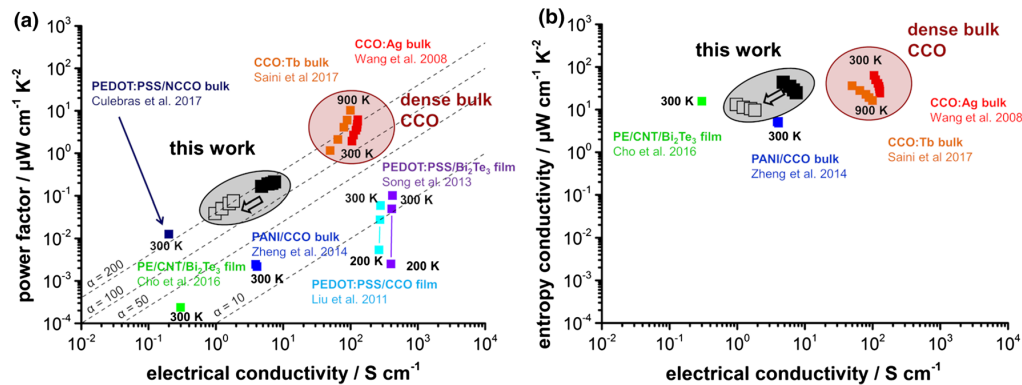

Fig. 2. (a) Ioffe plot and (b) entropy-electrical conductivity plot of different composites and dense bulk CCO materials.[30,44,47–51,58] Dashed lines in (a) show Seebeck coefficient α in μV/K. Note that both plots use an identical unit and scale on horizontal and vertical axes, respectively. Compared to (a), literature values in (b) have been reported only in some cases. From this work, single-phase porous CCO (filled symbols) and one representative composite material (open symbols) are included.

Wolf, Menekse, Mundstock, Hinterding, Nietschke, Oeckler, and Feldhoff
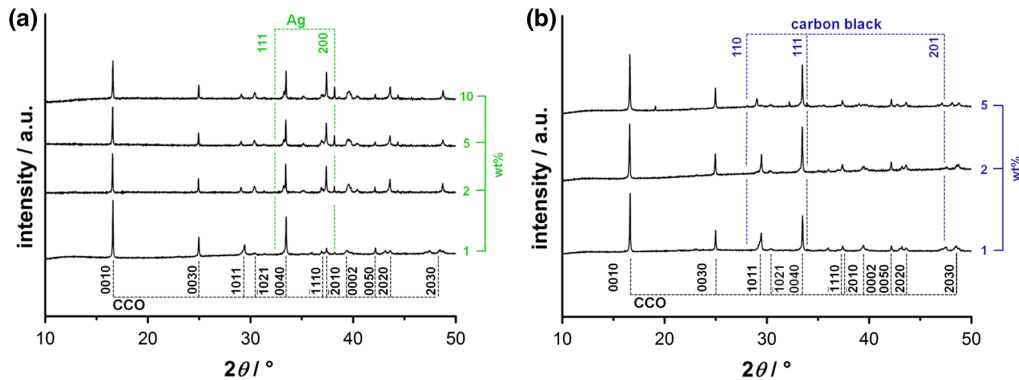

Fig. 3. XRD patterns of (a) multiphase composite materials with 1 wt.%, 2 wt.%, 5 wt.% and 10 wt.% Ag and (b) multiphase composite materials with 1 wt.%, 2 wt.% and 5 wt.% C. Positions of reflections with their Laue indices are given for Ag[59] and carbon black.[60] Reflections of CCO correspond to superspace group Cm (0 1 − p 0).[61] Increasing amounts of Ag and carbon black can be observed by increasing intensities of corresponding reflections.

microstructure of the multiphase composites were analyzed and compared to a single-phase porous CCO sample. One representative sample is also classified within the Ioffe plot and entropy-electrical conductivity plot in Fig. 2.

RESULTS AND DISCUSSION

Microstructural Characterization

Results of x-ray diffraction (XRD) analysis in Fig. 3 reveal successful preparation of CCO and composites. XRD patterns of multiphase systems show reflections of Ag and carbon black next to the CCO matrix, whereas the amorphous polymer exhibits no reflections. With increasing amount of Ag and carbon black, intensities of their corresponding reflections also increase.

Figure 4 shows scanning electron microscopy (SEM) micrographs of CCO and CCO/Ag powder used. The CCO powder exhibits typical platelet-like crystals with a diameter of about 1–2 μm and a thickness of about 40–60 nm. Figure 4d shows a larger Ag particle within the CCO/Ag powder surrounded by the CCO particles.

After pressing of pellets, the samples were stored in a dichloromethane (DCM) atmosphere leading to a dissolving process of included polymer which then fills the pores in the samples and leads to interlaced stripes perpendicular to the pressing direction. For the CCO/Ag/polymer sample (Fig. 5a, b, c, and d), Ag inclusions in the range of 10–20 μm can be observed within the matrix, which are well contacted to surrounding particles and the polymeric matrix. Analogously to the polymer, in the CCO/C/polymer sample (Fig. 5e, f, g, and h), the included carbon black forms stripes perpendicular to the pressing direction, leading to a matrix of polymer and carbon black. In the CCO/Ag/C/polymer composite (Fig. 5i, j, k, and l), both Ag particles and carbon black stripes can be observed, resulting in
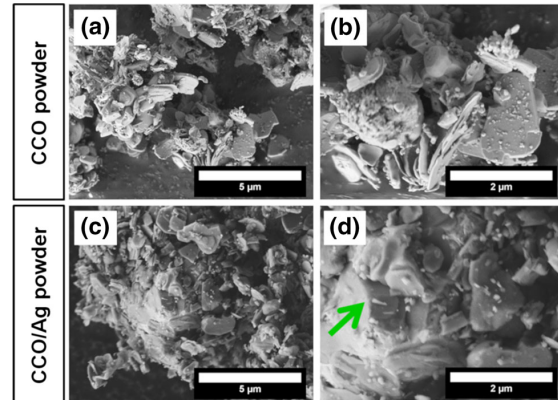

Fig. 4. SEM micrographs of (a, b) CCO and (c, d) CCO/Ag powder samples. CCO particles exhibit a platelet-like shape. Green marker in (d) shows larger Ag inclusion, surrounded by CCO particles (Color figure online).

the same matrix with included particles of CCO and Ag. In the higher magnified images (Fig. 5b, f, and j), the CCO agglomerates exhibit dimensions of about 500 nm–1 μm thickness and a length of 1–3 μm, while in the CCO/C/polymer samples some larger agglomerations of CCO particles can be observed. Furthermore, due to the relatively low sintering temperature, the CCO agglomerates exhibit a high amount of interfaces and do not show any preferred orientation in the composites.

Thermoelectric Properties of Multiphase Composites

In Fig. 6, the electrical conductivity σ and Seebeck coefficient α of prepared multiphase composites are displayed. For all samples, the electrical conductivity increases with the temperature. Compared to single-phase porous CCO, the CCO/

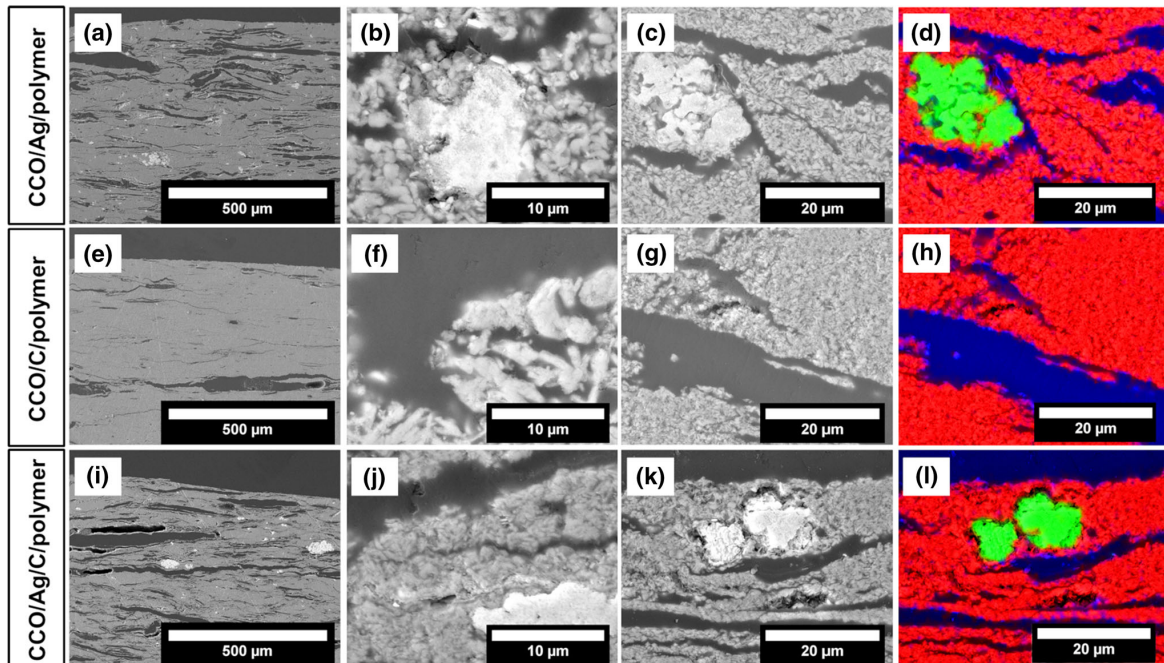Low Thermal Conductivity in Thermoelectric Oxide-Based Multiphase Composites

Fig. 5. Cross-sectional SEM micrographs and energy-dispersive x-ray spectroscopy (EDXS) elemental distributions (red = Co; green = Ag; blue = C): (a–d) CCO/Ag/polymer composite material with 10 wt.% Ag, (e–h) CCO/C/polymer composite material with 5 wt.% carbon black and (i–l) CCO/Ag/C/polymer composite material with 10 wt.% Ag and 5 wt.% carbon black. The Ag inclusions (bright contrast) are in the range of 10–20 μm. Both the carbon black and the polymer form stripes perpendicular to the vertical pressing direction (Color figure online).

polymer composites exhibit a strong decrease in electrical conductivity, which is attributed to the insulating polymer and the relatively low sintering temperature. However, by adding the highly conductive third-phase material, the electrical conductivity can be slightly enhanced depending on the amount of Ag or carbon black. The expected trend of increasing σ with increasing amounts of Ag and carbon black can be clearly seen (Fig. 6a, c, and e). The inclusions of Ag and carbon black stripes lead to additional highly electrically conducting pathways inside the matrix. However, due to the usage of insulating polymer, the electrical conductivity of the multiphase system is around 1 S/cm and therefore still lower than that of single-phase porous CCO (up to 10 S/cm). The Seebeck coefficient α is positive and thus shows p-type conduction for all samples investigated. Analogous to the electrical conductivity, the Seebeck coefficient α slightly decreases in CCO/polymer composites compared to single-phase porous CCO. Here, addition of Ag and carbon black again has a beneficial effect, although these materials normally exhibit a low Seebeck coefficient.[62] In general, the same trend of decreasing α by adding of the polymeric phase and then an increasing α by adding increasing amounts of Ag and carbon black can be seen (Fig. 6d, e, and f). This behavior disagrees with the expected and already reported trend of a

decreasing Seebeck coefficient with increasing amount of Ag inclusions without a polymeric phase.[42] Therefore, this effect has to be explained as an effect of the multiphase system, where the Ag inclusion alongside the polymer leads to an electron-scattering process at the heteromaterial interfaces. Despite this electron scattering, the electrical conductivity increases with the amount of Ag, as described above, which could be explained by the high charge carrier mobility of Ag. Therefore, these oxide-based multiphase systems with a polymeric and a metallic phase exhibit values of electrical conductivity of about 1 S/cm and a high Seebeck coefficient of about 150–200 μV/K, which results in a slightly lower power factor compared to single-phase porous CCO phase.

Figure 7 shows the thermal conductivity, expressed either as entropy conductivity Λ (a, c, e) or heat conductivity λ (b, d, f) for various samples as a function of the temperature T. The entropy conductivity was calculated by normalizing the heat conductivity λ with the absolute temperature T (Eq. 3). Despite not being able to measure the entropy conductivity directly, it is more fundamental than the heat conductivity as it appears in the thermoelectric material tensor in the basic transport equation (Eq. 1). For the evaluation of a material, both expressions of the thermal conductivity can be used, but the entropy conductivity Λ
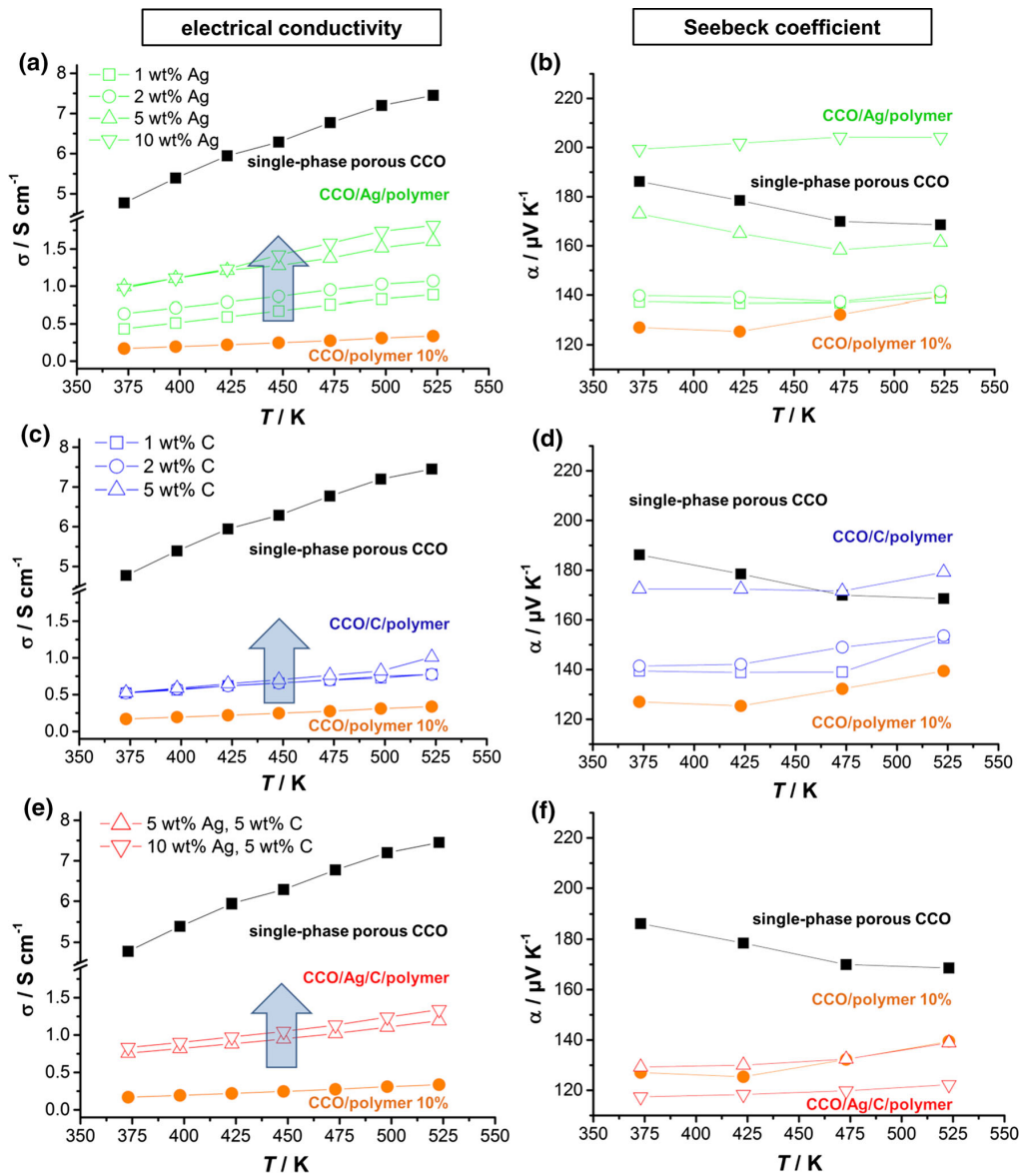
Wolf, Menekse, Mundstock, Hinterding, Nietschke, Oeckler, and Feldhoff

Fig. 6. Electrical conductivity σ and Seebeck coefficient α of (a, b) CCO/Ag/polymer, (c, d) CCO/C/polymer and (e, f) CCO/Ag/C/polymer composites and comparison to single-phase porous CCO sample and CCO/polymer composite, respectively. Both values were measured perpendicular to the pressing direction.

exhibits the same unit as the power factor. Here, both values show the expected decreasing thermal conductivity in the CCO/polymer system, caused by the low thermal conductivity of the polymer and additional inorganic–organic interfaces. Additionally, the thermal conductivity of all composites further decreases with increasing amounts of Ag and carbon black, although the added materials normally are characterized by a high electrical conductivity as well as thermal conductivity and

Wiedemann–Franz behavior.[63] This can be explained by the phonon scattering at the interfaces of the CCO agglomerates as well as at the hetero-material interfaces in the composite material. The scattering is defined by the mean free path of phonon distribution and therefore strongly correlates with the amount and distance of the scattering centers. With increasing amount of Ag or carbon black, the propagation of phonons is therefore

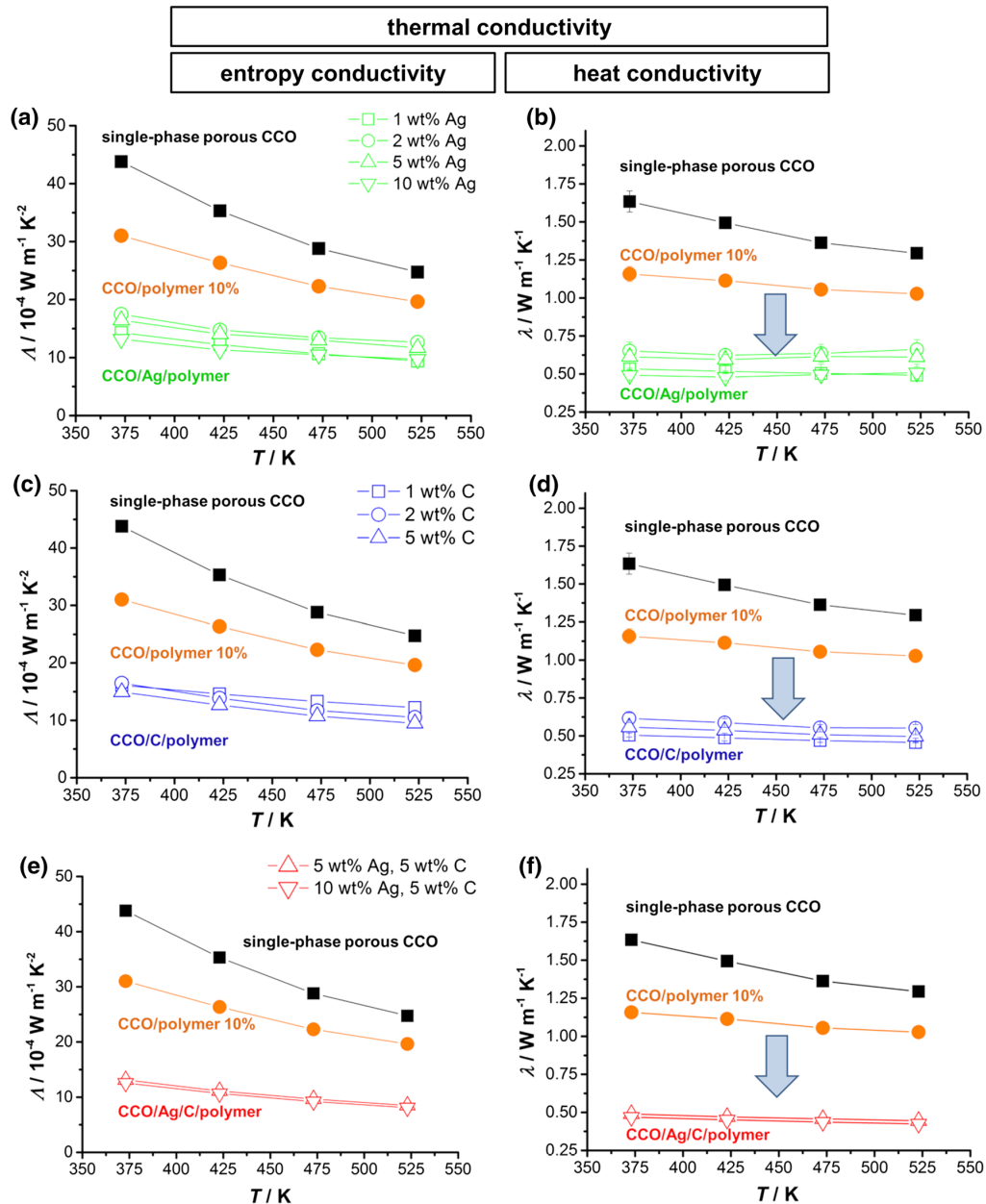Low Thermal Conductivity in Thermoelectric Oxide-Based Multiphase Composites

Fig. 7. Thermal conductivity expressed as entropy conductivity Λ and heat conductivity λ of (a, b) CCO/Ag/polymer, (c, d) CCO/C/polymer and (e, f) CCO/Ag/C/polymer composites and comparison to single-phase porous CCO sample and CCO/polymer composite, respectively. The thermal conductivity was measured parallel to the pressing direction.

disturbed, and the resulting thermal conductivity can be strongly decreased.

Note, that the authors renounce the determination of zT values since the composites may show different behavior parallel and perpendicular to the pressing direction, caused by the anisotropic character of CCO as well as the texturing of the composites. Correct determination of in-plane and out-of-plane properties can only be done for large bulk samples, which, however, require special preparation techniques that are not suitable for the investigated samples.[64]

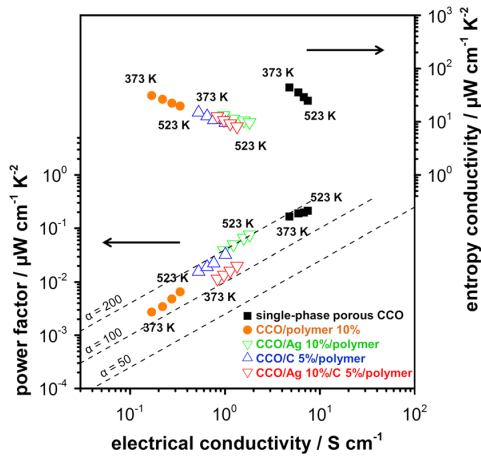Wolf, Menekse, Mundstock, Hinterding, Nietschke, Oeckler, and Feldhoff

Fig. 8. Ioffe plots (bottom, left axis) and entropy-electrical conductivity plots (top, right axis) of CCO/Ag/polymer, CCO/C/polymer and CCO/Ag/C/polymer compared to single-phase porous CCO (black) and CCO/polymer composite (orange), respectively. Dashed lines show Seebeck coefficient α in μV/K. Note that the axes to the left and right use identical physical units (Color figure online).

observed, especially regarding the high Seebeck coefficient of up to 200 μV/K at 523 K, despite increasing amounts of Ag or carbon black, as well as significantly decreased thermal conductivity. Especially, the latter could be reduced by a factor of four even at relatively low temperatures (see Fig. 2b). Additionally, compared to other CCO-based composite materials, designed multiphase systems reach a slightly higher power factor at a comparable thermal conductivity. A combination of other interesting materials (e.g. conductive polymers such as PEDOT) may lead to composite materials with higher electrical conductivity and, consequently, more competitive thermoelectric properties. Compared to known dense bulk materials, this concept may lead to composite materials with a comparable power factor and significantly lower thermal conductivity.

CONCLUSIONS

Overall, multiphase composites with combined properties and up to four times lower thermal conductivity compared to single-phase porous CCO have been presented. Although the materials are characterized by a lower overall performance compared to dense bulk CCO, the concept of multiphase systems is a promising path to combine the properties of different materials and classes. Especially, the thermal conductivity could be significantly lowered, attributed to various material interfaces, even if highly thermally conductive materials such as Ag and carbon black were used. Furthermore, the combination with materials characterized by a high electrical conductivity also showed a beneficial effect on the resulting power factor. Additionally, Ioffe plots were utilized to present and compare the power factors as well as the thermal properties of composites and dense bulk materials. The designed composite systems also show strong deviations from the classical Wiedemann–Franz relation, thus making them an interesting concept towards exceptionally low thermal conductivity. Further investigation of multiphase composite materials, e.g. by using conductive polymers, may lead to a promising thermoelectric multiphase material.

EXPERIMENTAL SECTION

Material Synthesis

If not mentioned separately, all reagents were obtained from commercial vendors at reagent-grade purity or higher and used without further purification. The $Ca_3Co_4O_9$ was prepared via a sol–gel synthesis route.[65] The corresponding metal nitrates [calcium(II) nitrate tetrahydrate and cobalt(II) nitrate hexahydrate] were dissolved in an aqueous ammonia solution (pH = 9) and complexed by adding 1:1 citric acid and ethylenediaminetetraacetic acid (EDTA). The obtained powders were calcined at 973 K for 10 h in air with a heating and cooling

Figure 8 shows the Ioffe plot and entropy-electrical conductivity plot of the studied composite materials combined into a single plot. Note again that the entropy conductivity Λ uses the same physical unit as the power factor $\sigma\alpha^2$. The Ioffe plots (Fig. 8 bottom) of the composites display the expected combined behavior, by showing an increased power factor $\sigma\alpha^2$ and electrical conductivity σ with increasing amounts of Ag, as described above. The Seebeck coefficient α, displayed as dashed lines in the Ioffe plot, also shows an increasing behavior, resulting in a high Seebeck coefficient up to 200 μV/K. However, the prepared composite materials exhibit lower power factor values compared to the single-phase porous CCO. The entropy-electrical conductivity plots (Fig. 8 top) show the significantly decreased thermal conductivity in the composite materials due to strongly enhanced phonon scattering at the CCO interfaces and the heteromaterial interfaces and simultaneously the increased electrical conductivity by use of Ag and carbon black. Note that none of the studied materials follow the Wiedemann–Franz relation, which can be easily seen when comparing the slopes of the entropy-electrical conductivity to Fig. 1b.

Due to the low electrical conductivity, the thermoelectric properties of the prepared composite materials are not yet competitive as compared to dense bulk CCO. Based on this, both values of the power factor as well as the electrical conductivity are about two orders of magnitude lower, as shown in Fig. 2. Nevertheless, promising synergetic properties of different materials in composites could be

Low Thermal Conductivity in Thermoelectric Oxide-Based Multiphase Composites

rate of 3 K/min. The samples containing Ag were prepared by adding the according amount of silver(I) nitrate to the solution of metal nitrates driving the sol–gel synthesis. The hybrid materials containing non-conducting Matrimid, a thermoplastic polyimide based on 5(6)-amino-1-(4′aminophenyl)-1,3-trimethylindane, were prepared by grinding the $Ca_3Co_4O_9$ powder with Matrimid 5218 powder (purchased at HUNTSMAN US) and carbon black (spherical porous particles, average thickness 30 μm) or grinding the Ag-containing $Ca_3Co_4O_9$ with Matrimid 5218. The mixed powders were then pressed in pellet shape (16 mm diameter and about 1 mm thickness) at 60 kN for 15 min, stored in an atmosphere of dichloromethane for 12 h and sintered at 573 K for 10 h with a heating and cooling rate of 3 K/min. The full preparation scheme is also shown in Fig. 9. The pellets were cut into bar-shaped specimens (area = 1 mm $\times$ 2 mm, length = 7 mm for thermoelectric measurements; area = 1 mm $\times$ 4 mm, length = 16 mm for

mechanical stability measurement) using an O'Well model 3242 precision vertical diamond wire saw.

An overview of all prepared samples is shown in Table I. CCO/polymer multiphase systems were prepared with 10 wt.% of Matrimid polymer. Multiphase systems containing Ag and carbon black were developed using fixed 10 wt.% of polymer and different amounts of Ag and carbon black between 1 wt.% and 10 wt.%. Additionally, a single-phase CCO pellet was pressed for comparison. All samples were treated at 573 K (maximum treatment temperature for used polymer) for 10 h to cause consolidating effects within the samples.

Characterization

Powders as well as the sintered composites were characterized by x-ray diffraction (XRD, Bruker D8 Advance with Cu-K$_z$ radiation). For microstructural characterization, a field-emission scanning electron microscope (FE-SEM, JEOL JSM-6700F) equipped with an energy-dispersive x-ray spectrometer (EDXS,
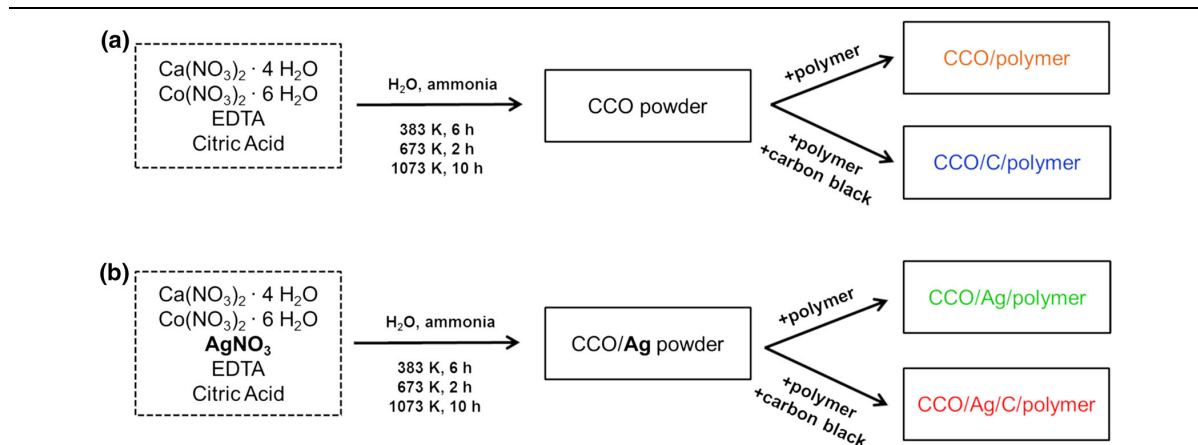

Fig. 9. Preparation scheme of multiphase systems. (a) Sol–gel synthesis of CCO powder and preparation of CCO/polymer and CCO/C/polymer composites and (b) sol–gel synthesis of CCO/Ag powder and preparation of CCO/Ag/polymer and CCO/Ag/C/polymer composites.

Table I. Prepared multiphase composites and corresponding amounts of CCO, polymer (Matrimid) and additional phases (Ag, C)

Composite	wt.% polymer	Treatment	Additional phases
Single-phase porous CCO	–	573 K 10 h	–
CCO/polymer	10	573 K 10 h	–
CCO/Ag/polymer	10	573 K 10 h	1 wt.%, 2 wt.%, 5 wt.%, 10 wt.% Ag
CCO/C/polymer	10	573 K 10 h	1 wt.%, 2 wt.%, 5 wt.% carbon black
CCO/Ag/C/polymer	10	573 K 10 h	5 wt.% Ag + 5 wt.% carbon black and 10 wt.% Ag + 5 wt.% carbon black

Included is single-phase porous CCO, which was treated at the same temperature, thus resulting in a porous single-phase sample.

Oxford Instruments INCA 300) for elemental analysis was used. Thermoelectric properties were measured as a function of temperature from room temperature to 520 K. The electrical conductivity σ and the Seebeck coefficient α were measured with home-made measurement cells with an ELITE thermal system and KEITHLEY 2100 digital multimeters. Heat conductivity λ was calculated from thermal diffusivity, measured with a Linseis LFA 1000 laser flash setup equipped with an InSb detector and carbon-coated samples in air atmosphere. Density measurement was performed by an Archimedes setup, and heat capacity was estimated from the Dulong–Petit model. The power factor $\sigma\alpha^2$ and the entropy conductivity Λ (Eq. 3) were calculated.

ACKNOWLEDGMENTS

REFERENCES

1. J. He and T.M. Tritt, *Science* 357, eaak9997 (2017).
2. R.A. Kishore, A. Marin, C. Wu, A. Kumar, and S. Priya, *Energy Harvesting—Materials, Physics, and System Design with Practical Examples* (Lancaster: DEStech Publications, 2019).
3. W. He, G. Zhang, X. Zhang, J. Ji, G. Li, and X. Zhao, *Appl. Energy* 143, 1 (2015).
4. H.U. Fuchs, *Energy Harvest. Syst.* 1, 1 (2014).
5. A. Feldhoff, *Energy Harvest. Syst.* 2, 5 (2015).
6. A.F. Ioffe, *Semiconductor Thermoelements, and Thermoelectric Cooling*, 1st ed. (London: Info-search Ltd., 1957).
7. H.U. Fuchs, *The Dynamics of Heat—A Unified Approach to Thermodynamics and Heat Transfer*, 2nd ed. (New York: Springer, 2010).
8. G. Job and R. Rüffler, *Physical Chemistry from a Different Angle*, 1st ed. (Berlin: Springer, 2014).
9. H. Mamur, M.R.A. Bhuiyan, F. Korkmaz, and M. Nil, *Renew. Sustain. Energy Rev.* 82, 4159 (2018).
10. G. Tan, L.D. Zhao, and M.G. Kanatzidis, *Chem. Rev.* 116, 12123 (2016).
11. S. Chen and Z. Ren, *Mater. Today* 16, 387 (2013).
12. X. Yan, G. Joshi, W. Liu, Y. Lan, H. Wang, S. Lee, J.W. Simonson, S.J. Poon, T.M. Tritt, G. Chen, and Z.F. Ren, *Nano Lett.* 11, 556 (2011).
13. E.S. Toberer, A.F. May, and G.J. Snyder, *Chem. Mater.* 22, 624 (2010).
14. J. Shuai, J. Mao, S. Song, Q. Zhang, G. Chen, and Z. Ren, *Mater. Today Phys.* 1, 74 (2017).
15. M. Shikano and R. Funahashi, *Appl. Phys. Lett.* 82, 1851 (2003).
16. A.K. Królicka, M. Piersa, A. Mirowska, and M. Michalska, *Ceram. Int.* 44, 13736 (2018).
17. A. Janotti and C.G. Van De Walle, *Rep. Prog. Phys.* 72, 126501 (2009).
18. D.B. Zhang, B.P. Zhang, D.S. Ye, Y.C. Liu, and S. Li, *J. Alloys Compd.* 656, 784 (2016).
19. L.-D. Zhao, S.-H. Lo, Y. Zhang, H. Sun, G. Tan, C. Uher, C. Wolverton, V.P. Dravid, and M.G. Kanatzidis, *Nature* 508, 373 (2014).
20. R. Chetty, A. Bali, and R.C. Mallik, *J. Mater. Chem. C* 3, 12364 (2015).
21. N. Wang, L. Han, H. He, N.H. Park, and K. Koumoto, *Energy Environ. Sci.* 4, 3676 (2011).
22. A.K. Menon, O. Meek, A.J. Eng, and S.K. Yee, *J. Appl. Polym. Sci.* 134, 1 (2017).
23. C. Wan, R. Tian, M. Kondou, R. Yang, P. Zong, and K. Koumoto, *Nat. Commun.* 8, 1024 (2017).
24. N. Toshima, *Synth. Met.* 225, 3 (2017).
25. T. Tsubota, M. Ohtaki, K. Eguchi, and H. Arai, *J. Mater. Chem.* 7, 85 (1997).
26. L. Han, N. Van Nong, W. Zhang, L.T. Hung, T. Holgate, K. Tashiro, M. Ohtaki, N. Pryds, and S. Linderoth, *RSC Adv.* 4, 12353 (2014).
27. A.M. Youssef, H.K. Farag, A. El-Kheshen, and F.F. Hammad, *Silicon* 10, 1225 (2018).
28. N.S. Krasutskaya, A.I. Klyndyuk, L.E. Evseeva, and S.A. Tanaeva, *Inorg. Mater.* 52, 393 (2016).
29. M. Bittner, L. Helmich, F. Nietschke, B. Geppert, O. Oeckler, and A. Feldhoff, *J. Eur. Ceram. Soc.* 37, 3909 (2017).
30. S. Saini, H.S. Yaddanapudi, K. Tian, Y. Yin, D. Magginetti, and A. Tiwari, *Sci. Rep.* 7, 1 (2017).
31. G.J. Snyder and E.S. Toberer, *Nat. Mater.* 7, 105 (2008).
32. S.R. Elliot, *The Physics and Chemistry of Solids* (Chichester: Wiley, 1998).
33. E. Flage-Larsen and O. Prytz, *Appl. Phys. Lett.* 99, 20 (2011).
34. A. Putatunda and D.J. Singh, *Mater. Today Phys.* 8, 49 (2019).
35. G.S. Kumar, G. Prasad, and R.O. Pohl, *J. Mater. Sci.* 28, 4261 (1993).
36. Y. Wang, Y. Sui, J. Cheng, X. Wang, J. Miao, Z. Liu, Z. Qian, and W. Su, *J. Alloys Compd.* 448, 1 (2008).
37. M. Ito, T. Nagira, and S. Hara, *J. Alloys Compd.* 408–412, 1217 (2006).
38. G. Zheng, X. Su, T. Liang, Q. Lu, Y. Yan, C. Uher, and X. Tang, *J. Mater. Chem. A* 3, 6603 (2015).
39. C. Liu, F. Jiang, M. Huang, R. Yue, B. Lu, J. Xu, and G. Liu, *J. Electron. Mater.* 40, 648 (2011).
40. R. Zuzok, A.B. Kaiser, W. Pukacki, and S. Roth, *J. Chem. Phys.* 95, 1270 (1991).
41. K. Kato, K. Kuriyama, T. Yabuki, and K. Miyazaki, *J. Phys. Conf. Ser.* 1052, 012008 (2018).
42. F. Kahraman, M.A. Madre, S. Rasekh, C. Salvador, P. Bosque, M.A. Torres, J.C. Diez, and A. Sotelo, *J. Eur. Ceram. Soc.* 35, 3835 (2015).
43. Y. Wang, Y. Sui, J. Cheng, X. Wang, and W. Su, *J. Alloys Compd.* 477, 817 (2009).
44. M. Culebras, A. Garcia-Barbera, J.F. Serrano-Claumarchirant, C.M. Gomez, and A. Cantarero, *Synth. Met.* 225, 103 (2017).
45. D. Yoo, J. Kim, and J.H. Kim, *Nano Res.* 7, 717 (2014).
46. N. Toshima, K. Oshima, H. Anno, T. Nishinaka, and S. Ichikawa, *Adv. Mater.* 27, 2246 (2015).
47. M. Culebras, A.M. Igual-Muñoz, C. Rodríguez-Fernández, M.I. Gómez-Gómez, C. Gómez, and A. Cantarero, *ACS Appl. Mater. Interfaces* 9, 20826 (2017).
48. B. Zheng, Y. Lin, J. Lan, and X. Yang, *J. Mater. Sci. Technol.* 30, 423 (2014).
49. C. Liu, F. Jiang, M. Huang, B. Lu, R. Yue, and J. Xu, *J. Electron. Mater.* 40, 948 (2011).
50. H. Pang, Y.Y. Piao, Y.Q. Tan, G.Y. Jiang, J.H. Wang, and Z.M. Li, *Mater. Lett.* 107, 150 (2013).
51. H. Song, C. Liu, H. Zhu, F. Kong, B. Lu, J. Xu, J. Wang, and F. Zhao, *J. Electron. Mater.* 42, 1268 (2013).
52. M. Culebras, C. Cho, M. Krecker, R. Smith, Y. Song, C.M. Gómez, A. Cantarero, and J.C. Grunlan, *ACS Appl. Mater. Interfaces* 9, 6306 (2017).
53. C. Cho, K.L. Wallace, P. Tzeng, J.H. Hsu, C. Yu, and J.C. Grunlan, *Adv. Energy Mater.* 6, 1 (2016).
54. J. Wang, J.K. Carson, M.F. North, and D.J. Cleland, *Int. J. Heat Mass Transf.* 51, 2389 (2008).
55. B. Geppert, A. Brittner, L. Helmich, M. Bittner, and A. Feldhoff, *J. Electron. Mater.* 46, 2356 (2017).
56. T. Khosravi, S. Mosleh, O. Bakhtiari, and T. Mohammadi, *Chem. Eng. Res. Des.* 90, 2353 (2012).

Low Thermal Conductivity in Thermoelectric Oxide-Based Multiphase Composites

57. J. Ahmad and M.B. Hägg, *Sep. Purif. Technol.* 115, 190 (2013).
58. Y. Wang, Y. Sui, J. Cheng, X. Wang, and W. Su, *J. Phys. D Appl. Phys.* 41, 045406 (2008).
59. E.R. Jette and F. Foote, *J. Chem. Phys.* 3, 605 (1935).
60. J. Fayos, *J. Solid State Chem.* 148, 278 (1999).
61. Y.M. Iyazaki, M.O. Noda, T.O. Ku, M.K. Ikuchi, and Y.I. Shii, *J. Phys. Soc. Jpn.* 71, 491 (2002).
62. C. Van Baarle, F.W. Gorter, and P. Winsemius, *Physica* 35, 223 (1967).
63. G.W.C. Kaye and T.H. Laby, *Tables of Physics and Chemical Constants*, 13th ed. (London: Longmans, 1966).
64. C.-H. Lim, W.-S. Seo, S. Lee, Y.S. Lim, J.-Y. Kim, H.-H. Park, S.-M. Choi, K.H. Lee, and K. Park, *J. Korean Phys. Soc.* 66, 794 (2015).
65. A. Feldhoff, M. Arnold, J. Martynczuk, T.M. Gesing, and H. Wang, *Solid State Sci.* 10, 689 (2008).

2.3 Cu-Ni-based alloys from nanopowders as potent thermoelectric materials for high power output applications

Mario Wolf, Jan Flormann, Timon Steinhoff, Gregory Gerstein, Florian Nürnberger,
Hans Jürgen Maier and Armin Feldhoff
   submitted to *Alloys*, **2021**

Article

Cu-Ni-Based Alloys from Nanopowders as Potent Thermoelectric Materials for High Power Output Applications

Mario Wolf[1,*], Jan Flormann[1], Timon Steinhoff[2], Gregory Gerstein[2], Florian Nürnberger[2], Hans-Jürgen Maier[2] and Armin Feldhoff[1,*]

[1] Institute of Physical Chemistry and Electrochemistry, Leibniz University Hannover, Callinstraße 3A, D-30167 Hannover

[2] Institut für Werkstoffkunde (Materials Science), Leibniz University Hannover, An der Universität 2, D-30823 Garbsen

[*] Correspondence: M.W. mario.wolf@pci.uni-hannover.de, A.F. armin.feldhoff@pci.uni-hannover.de

Abstract: A new approach for designing thermoelectric materials while focusing on a high power factor instead of a large figure of merit zT has drawn attention in recent years. In this context, the thermoelectric properties of Cu-Ni-based alloys with a very high electrical conductivity, a moderate Seebeck coefficient and therefore a high power factor are presented as promising low-cost alternative materials for applications aiming to have a high electrical power output. The Cu-Ni based alloys are prepared via an arc melting process of metallic nanopowders. The heavy elements tin and tungsten are chosen for alloying, to further improve the power factor while simultaneously reducing the high thermal conductivity of the resulting metal alloy to also beneficially influence the zT value. Overall, the samples prepared with low amounts of Sn and W show an increase in the power factor and the figure of merit zT compared to the pure Cu-Ni alloy. These results demonstrate the potential of these often overlooked metal alloys and the utilization of nanopowders for thermoelectric energy conversion.

1. Introduction

To achieve a sustainable electric power supply, the use of thermoelectric generators is a possible method to increase the energy efficiency in various applications by directly converting heat (waste) to electrical energy [1]. Thermoelectric materials have been intensely studied in recent decades, and promising candidates have been found for different applications [2]. The performance of a thermoelectric material is defined by the three central thermoelectric quantities, namely, the Seebeck coefficient α, the electrical conductivity σ and the open-circuited entropy conductivity Λ, which is related to the heat conductivity $\lambda = T \cdot \Lambda$ via the absolute temperature [3–6]. In the context of this work, thermal conductivity is used as a general term that can be expressed either by the heat conductivity λ or by the more fundamental entropy conductivity Λ. From these thermoelectric quantities, the power factor $\sigma\alpha^2$, which can be used to calculate the maximum achievable power, and the figure of merit $f = zT$, which is used to calculate the maximum energy conversion efficiency, can be determined according to Eq. 1 [3,4,6]. By using the entropy conductivity Λ in Eq. 1, the dimensionless figure of merit appears in a more concise form only containing the material parameters and it is not explicitly a function of the absolute temperature T, but implicitly as all material parameters are temperature-dependent.

$$f = \frac{\sigma\alpha^2}{\Lambda} = \frac{\sigma\alpha^2}{\lambda} \cdot T := zT \tag{1}$$

Thermoelectric materials are conventionally designed to maximize the figure of merit zT, and thus the energy conversion efficiency. For example, these benefits can be achieved by nanostructuring or doping of promising materials [7–9]. For near room-temperature energy conversion, Bi_2Te_3 shows the most advanced properties [10,11], but is characterized by major drawbacks: The toxicity of telluride compounds and the poor thermal stability. Consequently, various alternatives such as oxides [12–14] or intermetallic phases such as Zintl [15,16] or half-Heusler phases [17–19] are widely investigated. In recent years, investigation of promising polymeric thermoelectric materials such as PEDOT:PSS also arose [20–22]. However, the focus on maximizing the figure of merit zT is questionable [2,23], as the electrical power output of the material is determined by the power factor and not the figure of merit zT [24]. As a result, recent considerations have shown that to achieve a high electrical power output for high-temperature applications with a constant heat gradient, a high power factor can be equally or more important than a high efficiency [2,23]. A promising approach for developing thermoelectric materials is to focus on a material with a high electrical conductivity, such as one of the infrequently considered metal alloys, and then try to gradually improve the Seebeck coefficient and lower the thermal conductivity, while retaining a high electrical conductivity, and thus achieving a very high power factor. In **Fig. 1**, Ioffe plots of type I (power factor vs. electrical conductivity) and type II (entropy conductivity vs. electrical conductivity) are displayed for comparison of common thermoelectric materials. Here, all relevant material parameters can be displayed in a concise form giving a direct comparison and including information about the figure of merit due to the utilization of the entropy conductivity Λ instead of the heat conductivity λ. In this plots, the thermoelectric properties are displayed as a function of their material parameters and not the absolute temperature T. This corresponds to the concise form of the figure of merit by utilization of the entropy conductivity. The aforementioned Bi_2Te_3 compounds show a very good power factor of 30 to 50 µW cm^{-1} K^{-2} [10,25]. Additionally, half-Heusler compounds such as $FeNb_{0.88}Hf_{0.12}Sb$ [26] have been shown to reach a very high power factor of approximately 40 to 60 µW cm^{-1} K^{-2} [19,26] and good zT values, and they are among the most advanced materials in the field. However, within the Ioffe plots, another promising material from the group of metal alloys can be identified, when a high power output is the main goal: Cu-Ni alloys. This elemental combination has been widely used in thermoelements as constantan (Cu-Ni-Mn) due to its properties and stability at elevated temperatures. It is characterized simultaneously by a very high power factor up to 100 µW cm^{-1} K^{-2} (see **Fig. 1a**) and a high thermal conductivity, showing potential for high-temperature applications where power output may be more relevant than conversion efficiency [27,28]. Cu-Ni alloys are especially promising candidates due to the resonant levels in their electronic structure, resulting in a remarkably high Seebeck coefficient [29]. Furthermore, Cu-Ni alloys show a strong deviation of the empirical Wiedemann-Franz relation, which is especially promising to be utilized for thermoelectric energy conversion [30]. Another major advantage of such alloys is that they consist of inexpensive and nontoxic elements, are characterized by a good thermal and mechanical stability and they can be produced via large-scale metallurgic processes. The only disadvantage is the high thermal conductivity, which leads to a relatively low conversion efficiency (see **Fig. 1b**). But especially for high-temperature applications with low-cost heat sources, e.g. in the automotive sector or solar heat, and when a constant temperature gradient can be maintained, e.g, by an active cooling, the thermal conductivity plays a subordinate role and a high power factor is highly advantageous [2,23,31].
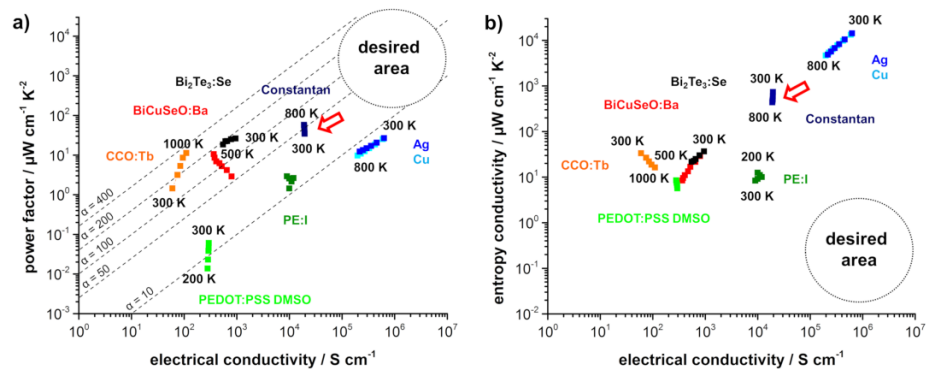
Fig. 1. Ioffe plots of type I (power factor vs. electrical conductivity) and type II (entropy conductivity vs. electrical conductivity) for comparison of promising materials form various classes. Cu-Ni alloys are located at a very high power factor, making them promising materials for applications where a high power output is desired. Reworked from [30] with permission from Springer.

In this study, the above approach was employed, and the thermoelectric properties of Cu-Ni-based alloys were investigated. To date, only a few studies have investigated Cu-Ni alloys for thermoelectric purpose. Some researchers tried to alter the material at the nanoscale by incorporating carbon nanotubes or Al_2O_3 nanoparticles into the alloy [27,32]. In both cases, the thermal conductivity could be significantly lowered, resulting in an increased zT up to 0.35 at 800 K [32]. However, the incorporation also strongly reduced the electrical conductivity and therefore the power factor. Nanostructured and nanotwinned Cu-Ni alloys were also investigated and were found to reach an exceptionally high power factor up to 100 μW cm^{-1} K^{-2} at 900 K and a figure of merit of 0.18 [28,33]. Shimizu et al. presented a Cu/Cu-Ni thin film TEG on a polyimide substrate; this film attained a remarkable power output of 21 μW at a temperature difference of 70 K [34].

The approach of this study was to alter the structure of the metal on the atomic level by alloying Cu-Ni with heavier elements to beneficially influence the power factor and simultaneously reduce the thermal conductivity via long-range phonon scattering. Specifically, Sn and W were chosen as metals; they are both heavier than Ni and Cu but have quite different properties. While Sn has a low melting point of 505 K [35] and mixes well with Cu (bronzen), W has a much higher melting point of 3695 K [35] and is not incorporated in the matrix [36]. The degree to which these different properties influence the resulting microstructure and the thermoelectric properties was studied. All alloys have been prepared from metal nanopowders via arc melting, compared to our previous report [37] that presented the idea of Cu-Ni alloys from larger flakes resulting in more inhomogeneous distribution and inferior thermoelectric properties. By this, the influence of the utilization of nanopowders as well as the results of alloying with Sn and W are investigated.

2. Materials and Methods

If not mentioned otherwise, all metals were obtained from commercial vendors at 99.9 % purity or higher and are used without further purification. Cu, Sn and W nanopowders (average diameter less than 100 nm) were obtained from IoLiTec Nanomaterials, and Ni (average diameter less than 100 nm) was obtained from Sigma-Aldrich. These powders were stored and processed under an intert gas atmosphere in a glove box. Metallic precursor mixtures were prepared by mixing, agitating and shaking under inert gas with the stoichiometric ratios listed in **Tab. 1**. The resulting powders were pressed into discs using a hydraulic press; they were subsequently arc-melted in a copper crucible to form ingots

by means of an EWM TETRIX 521 CLASSIC activArc TIG welding machine that was operated for 30 s with a current of 150 A and an inert gas flow of 5 l min^{-1}.

Tab. 1. Designations and atomic compositions of the prepared samples in atomic percent. All samples have been prepared from nanopowders with an average diameter less than 100 nm.

	x **(Cu)**	x **(Ni)**	x **(Sn)**	x **(W)**
Cu50Ni50	50	50	-	-
Sn1	49.5	49.5	1	-
Sn2	49	49	2	-
Sn5	47.5	47.5	5	-
W1	49.5	49.5	-	1
W5	47.5	47.5	-	5
W10	45	45	-	10

For the measurement of the Seebeck coefficient and the electrical conductivity, rod-shaped samples (3 mm diameter and 10 mm length) were cut with a Sodick AD325L wire electrical discharge machine (EDM) unit. The microstructure and composition were characterized by X-ray diffraction (XRD, Bruker D8 Advance with Cu-Kα radiation) of the polished alloys and by field-emission scanning electron microscope (FE-SEM, ZEISS Supra 55 VP) of polished cross-sections. The electron microscope was additionally equipped with an energy-dispersive X-ray spectrometer (EDXS System Quantax from Bruker). The electrical conductivity σ was determined with a custom-made measurement cell with an ELITE thermal system and KEITHLEY 2100 digital multimeters. The Seebeck coefficient α was measured using a ProbotStat A apparatus from NorECs. The density was then determined at room temperature by using the Archimedes method with isopropanol as solvent. The thermal diffusivity was measured using a light flash analyzer (Netzsch LFA 467 HT) from room temperature to 600 K. The heat capacity was calculated using the Dulong-Petit law.

3. Results and Discussion

XRD patterns of the Cu-Ni-based alloys are shown in **Fig. 2**. For the Cu50Ni50 sample, good agreement with the literature data for Cu-Ni alloys is apparent. Small additional reflections marked with an asterisk correspond to minor NiO impurities, most likely due to the utilization of nanopowders, which are especially susceptible to oxidation due to their high surface area. This impurities can be identified for all Sn-alloyed samples, but cannot be identified for the 5 at.% and the 10 at.% W samples. For the Sn-alloyed samples, the observed 111 and 200 Cu-Ni reflections are shifted towards lower angles as indicated by vertical dashed lines. This can be explained by an incorporation of the Sn atoms into the Cu-Ni matrix, resulting in a larger lattice parameter. With increasing amount of Sn, this shift to lower angles becomes more apparent (**Fig. 2a**). Additionally, no pure Sn inclusion can be identified. In the W-alloyed samples, the Cu-Ni reflections are not shifted, as again indicated by vertical dashed lines, and additional reflections can be observed for the 10 at.% W sample, that match the reflections expected for pure W from literature (**Fig. 2b**). This indicates that W is not incorporated into the matrix, but forms a separate phase, which is in good agreement with the much higher melting point and the previous results of the flake-based samples [37]. As a result, Sn seems to be at least partly incorporated into the matrix, while tungsten primarily forms inclusion. For the alloys, changed ratios of the intensities of the 111 and 200 reflections can be detected, e.g., shown in the Sn2 sample, which is based on a preferred orientation due to directed solidification in the arc-melting process. This has been reported before for arc-melted Cu-Ni alloys [28,33] but

with minor influence on the thermoelectric properties due to the isotropic fcc crystal structure [33].
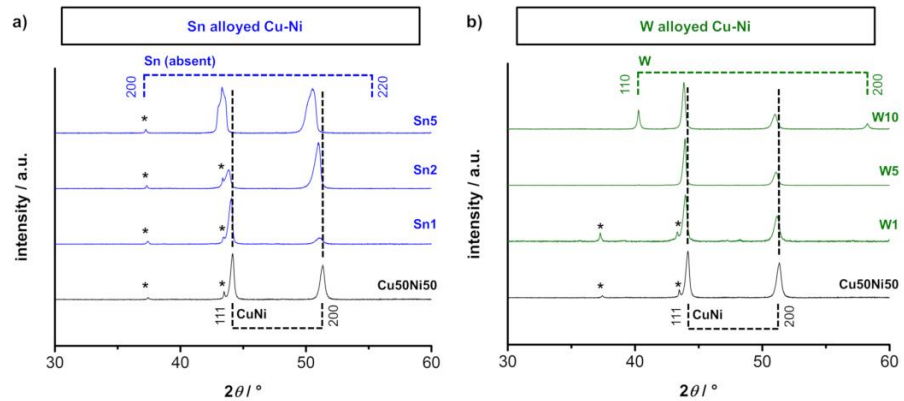

Fig. 2. Normalized XRD patterns of the prepared samples from nanopowders. a) Sn-alloyed and b) W-alloyed Cu-Ni samples. Positions of the expected reflections for Cu-Ni (PDF 01-077-7711, black), Sn (PDF 01-077-3457, blue and W (PDF 01-080-3012, green) are included and marked via vertical dashed lines, which are grouped by horizontal lines. Reflections marked with an asterisk correspond to NiO impurities (PDF 01-089-5881). The black dashed lines show the 111 and 200 Cu-Ni reflections of the undoped Cu-Ni to highlight the occurring shift in the Sn alloyed samples compared to the W alloys samples. For the Sn samples, this shift indicates the incorporation of Sn in the matrix. In the W samples, W can be identified as an additional phase that is not incorporated in the matrix.

Backscattered electron (BSE) micrographs and EDXS elemental mappings for Cu, Ni, Sn and W of the Cu50Ni50 sample and the Sn-alloyed samples are shown in **Fig. 3**. The BSE micrograph of the Cu50Ni50 sample shows a mostly homogeneous distribution and some darker spots indicating lighter elements such as oxygen. Alongside the small impurities found in the XRD pattern, this could be caused by NiO inclusions. Within the EDXS mapping, the mostly purple coloration is assumed to indicate a relatively homogenous distribution of Ni (blue) and Cu (red). This shows a significantly improved elemental distribution due to the utilization of nanopowders, compared to the large flake-based samples [37]. However, some areas with increased Cu or Sn concentrations are still recognizable. On closer inspection, it is noticeable that Sn mixes preferentially with Cu (reddish-turquoise spots), while there is less mixing of Ni and Sn (blueish-magenta spots). This indicates that on a macroscopic scale, Sn is at least partly incorporated into the Cu-Ni matrix. Additionally, small lighter spots are recognizable within the BSE micrographs, which correspond to Sn-rich areas according to the EDXS elemental analysis. Although the XRD patterns show that Sn is incorporated into the structure, some additional small Sn-rich spots are also formed. So, Sn seems to be partly incorporated and partly is apparent as a separate phase. This is most likely the result of two factors: First, the mixture of the nanopowders was prepared by mixing, agitating and shaking under inert gas. This may not result in a homogeneous mixture on the nanoscale and may be improved by dispersing the powders in an organic solvent with a subsequent drying step or via a bottom-up synthesis. Second, the relatively short time within the arc-melting process compared to annealing the alloys over several hours does not leave much time for the melted particles for a better distribution and incorporation. The Sn-alloyed samples also exhibit dark blue, Ni-rich spots. Here, a beginning dendritic growth of this inclusion becomes apparent, which have been reported for NiO before [38–40]. It is assumed, that the formation of NiO is also a result of the utilization of nanopowders, which are susceptible to oxidation due to their high surface area.
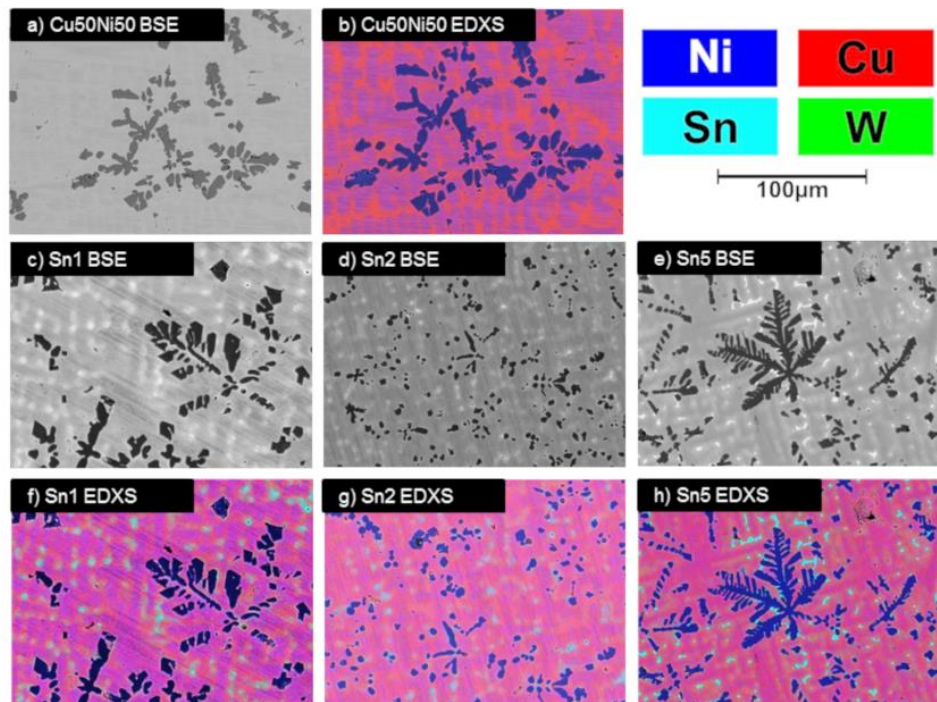
Fig. 3. SEM BSE micrographs and EDXS elemental mappings of prepared Sn-alloyed samples from nanopowders. a) BSE micrograph and b) EDXS elemental mapping of the Cu50Ni50 sample, c-e) BSE micrographs and f-h) EDXS elemental mappings of the Sn-alloyed samples. Cu (red) and Ni (blue) form the matrix, in which Sn (cyan) is incorporated.

The measured temperature-dependent thermoelectric properties of the Sn-alloyed samples are shown in **Fig. 4**. Here, an additional comparison to the constantan alloy ($Cu_{56}Ni_{42}Mn_2$) reported from Mao et al. [28] was chosen (dashed lines), as they also used a top-down approach via ball-milling with subsequent arc-melting, resulting in the best comparability. In the following, this literature sample for comparison is referred to as constantan. The Cu50Ni50 sample shows a similar electrical conductivity compared to constantan around 20,000 S cm^{-1} with weak temperature dependence. After alloying with 1 at.-% Sn (Sn1), an increased electrical conductivity between 23,500 S cm^{-1} and 21,500 S cm^{-1} could be reached (**Fig. 4a**). For 2 at.-% Sn (Sn2), the electrical conductivity is again slightly increased, up to 24,500 S cm^{-1} at 300 K. Afterwards, it decreases with increasing amount of Sn, equaling the Cu50Ni50 sample at 5 at.-% Sn, as further Sn addition forms more and more inclusions. All prepared samples show a more metallic behavior, with a decreasing electrical conductivity with increasing temperature. The higher electrical conductivity of the Sn1 and Sn2 samples is assumed to be a result of the incorporation of the Sn into the matrix which directly influences the charge carrier concentration. The Seebeck coefficient of the Sn1 sample is slightly higher compared to Cu50Ni50 and then also showing a slightly decreasing behavior with increasing amounts of Sn (**Fig. 4b**). The resulting power factor (**Fig. 4c**) of 38 μW cm^{-1} K^{-2} at 573 K for the Sn1 sample is therefore about 12 % higher compared to the Cu50Ni50, surpassing the aforementioned half-Heusler compounds, which usually show a power factor around 20 to 30 μW cm^{-1} K^{-2} in this temperature region [19]. Compared to constantan, however, the resulting power factor is lower due to the lower Seebeck coefficient. The density of the metal alloys (**Fig. 4d**) increase as a result of the Sn inclusion for the Sn1 sample and then also show a decreasing behavior with increasing amounts of Sn. The values for the heat conductivity of the Sn-alloyed samples are shown in **Fig. 4e**. With 1 at.% Sn, the heat conductivity is slightly higher compared to the Cu50Ni50 sample, due to the much higher electrical conductivity. With increasing

amounts of Sn, the heat conductivity decreases as expected, as a result of the decreasing electrical conductivity and long-range phonon scattering at the inclusions. Compared to constantan, the samples are characterized by a significantly lower thermal conductivity, probably also due to the utilization of nanopowders. Finally, the resulting figure of merit is displayed in **Fig. 4f**. As a result of the increased electrical conductivity, the *zT* of the Sn1 sample is slightly higher compared to the Cu50Ni50, but slightly lower compared to constantan, reaching a *zT* up to 0.09 at 573 K. The *zT* value of the Cu50Ni50 is therefore also slightly lower compared to constantan, as it is characterized by a lower Seebeck coefficient, which is not fully compensated by the lower thermal conductivity.
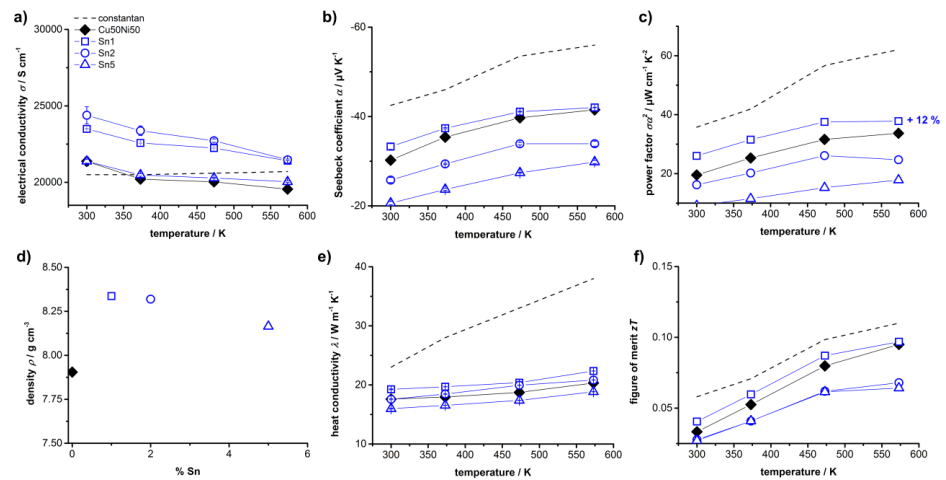
Fig. 4. Measured temperature-dependent thermoelectric properties of the Sn-alloyed samples from nanopowders. a) Isothermal electrical conductivity σ; b) Seebeck coefficient α, note the reversed vertical axis; c) resulting power factor $\sigma\alpha^2$; d) density ρ; e) heat conductivity λ; f) resulting figure of merit *zT*. Especially the Sn1 sample shows an increased electrical conductivity. The power factor is slightly higher compared to the Cu50Ni50 sample, but lower compared to the constantan ($Cu_{56}Ni_{42}Mn_2$) from Mao et al. [28]. The heat conductivity slightly decreases with increasing amount of Sn. The resulting figure of merit *zT* of the Sn1 sample is slightly higher compared to the Cu50Ni50 sample, but slightly lower compared to constantan.

SEM microstructural analyses of the W-alloyed Cu-Ni samples are shown in **Fig. 5**. The distribution of Cu and Ni is analogous to the Sn-alloyed samples and again NiO inclusions can be seen in all samples. In accordance to the discussion of the XRD patterns, the W seems to be not incorporated into the matrix and can be clearly identified as lighter spots in the BSE micrographs. With increasing amount of W, more of these spots can be seen. This is confirmed by the EDXS elemental mappings of the samples, where sharply defined green spots are recognizable; they also show that W forms its own pure phase and is not part of the matrix.
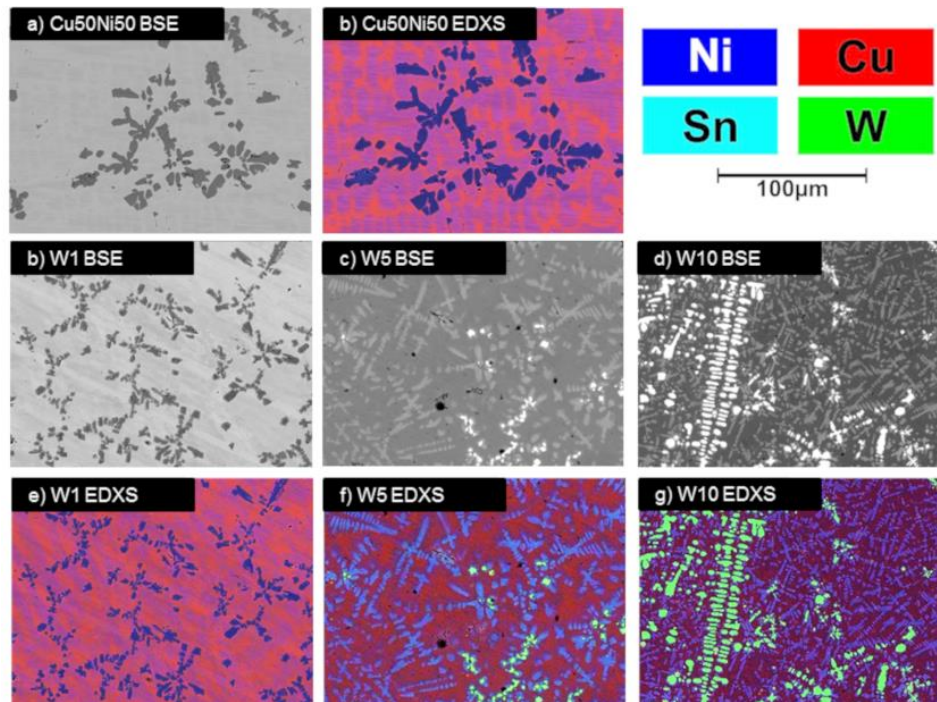
Fig. 5. SEM BSE micrographs and EDXS elemental mappings of prepared W-alloyed samples from nanopowders. a) BSE micrograph and b) EDXS elemental mapping of the Cu50Ni50 sample, c-e) BSE micrographs and f-h) EDXS elemental mappings of the W alloyed samples. Cu (red) and Ni (blue) form the matrix, in which W (green) is not incorporated.

The measured temperature-dependent thermoelectric properties of the W-alloyed samples are shown in **Fig. 6**. A comparison to constantan is again shown via dashed lines. The electrical conductivity slightly decreases as a result of the W inclusions and with increasing amount of W (**Fig. 6a**). The Seebeck coefficient of the W1 sample is slightly higher compared to the Cu50Ni50 sample and similar to constantan (**Fig. 6b**). However, with increasing amount of W, the Seebeck coefficient shows the same decrease as in the Sn samples. Resultantly, the power factor (**Fig. 6c**) of the W1 sample is also higher compared to the Cu50Ni50 sample (about 38 %), due to the higher Seebeck coefficient, but decreases with increasing amount of W. This is analogously to the Sn-alloyed samples, however, here the increased power factor is a result of a higher Seebeck coefficient, while in the Sn-alloyed samples it is based on a higher electrical conductivity. Compared to constantan, the power factor again is slightly lower. The values of the sample density also show a similar behavior as the Sn-alloyed samples; first it shows an increase up to 5 at.-% and then decreases to the value of the Cu50Ni50 sample (**Fig. 6d**). The measured heat conductivity again decreases with increasing amounts of W, as expected, due to the decreasing electrical conductivity and long-range phonon scattering due to the inclusions (**Fig. 6e**). Here, the alloying with 1 at.-% W results in a figure of merit of approximatelay 0.12 at 573 K, corresponding to an increase of about 26 % compared to the Cu50Ni50 sample. (**Fig. 6f**).
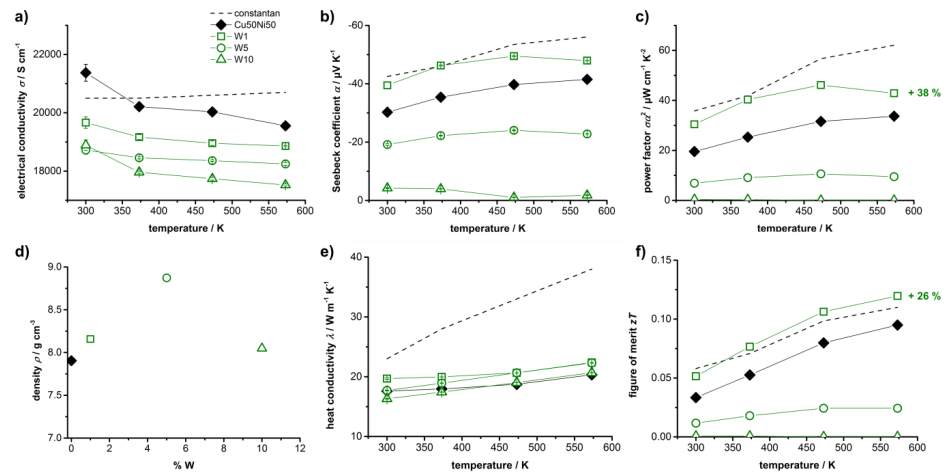
Fig. 6. Measured temperature-dependent thermoelectric properties of the W-alloyed samples from nanopowders. a) Isothermal electrical conductivity σ; b) Seebeck coefficient α, note the reversed vertical axis; c) resulting power factor $\sigma\alpha^2$; d) density ρ; e) heat conductivity λ; f) resulting figure of merit zT. The W1 sample shows the highest power factor, which is slightly higher compared to the Cu50Ni50 sample, but slightly lower compared to constantan. The heat conductivity of all samples is again reduced, resulting in a higher figure of merit zT of the W1 sample compared to the literature reference and the Cu50Ni50 sample.

Fig. 7 summarized the measured thermoelectric properties of the Sn-alloyed and W-alloyed Cu-Ni samples. In the type-I Ioffe plot (**Fig. 7a**) the power factor of the samples is shown as a function of the electrical conductivity. Both, the Sn1 and W1 sample exhibit a higher power factor compared to the Cu50Ni50 sample, but slightly lower compared to the reported values for constantan. The Sn-alloyed samples show a strong increase in the electrical conductivity, most likely due to the incorporation of the Sn into the matrix and the consequent influence on the charge carrier concentration. The W-alloyed samples are characterized by a higher Seebeck coefficient but a decreased electrical conductivity as it is not incorporated and primarily forms inclusions. In the type-II Ioffe plot (**Fig. 7b**), the entropy conductivity is displayed as a function of the electrical conductivity. All prepared samples have a lower thermal conductivity compared to constantan, which is based on the alloying with Sn and W resulting in enhanced phonon scattering, especially at the inclusions, and on the utilization of nanopowders. With increasing amounts of Sn and W, the thermal conductivity further decreases slightly. The resulting figure of merit of all prepared samples is shown in **Fig. 7c**. For W-alloying, the respective sample with 1 at.-% are characterized by an increased zT value of 0.12, while the Sn-alloying resulted in similar zT value of 0.09.
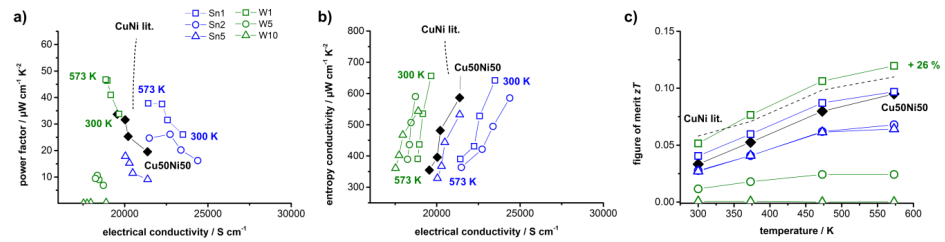
Fig. 7. Summarized thermoelectric properties of the investigated samples. a) Power factor as a function of the electrical conductivity (type-I Ioffe plot). b) Entropy conductivity as a function of the electrical conductivity (type-II Ioffe plot). c) Resulting temperature-dependent figure of merit zT for Sn and W alloying. The power factor could be increased by low amounts of Sn and W compared to the pure Cu-Ni alloy, but is lower compared to constantan. The energy conversion efficiency could be improved in comparison to both, the pure Cu-Ni alloy and constantan with low amounts of Sn and W.

Overall, Cu-Ni alloys containing Sn and W could be prepared. Due to the utilization of nanopowders, the distribution within the alloys could be significantly improved compared to large flake-based samples [37]. However, the distribution and homogeneity of the Sn and W can still be further enhanced, as both can still be identified as inclusions, although especially Sn should be incorporated in the Cu-Ni matrix. To improve this, other or multiple melting steps or additional annealing steps could be applied. Additionally, formation of NiO impurities could be found (see Figures 2, 3 and 5), which also might influence the resulting thermoelectric properties. Generally, these impurities should lead to a reduced electrical conductivity, due to the insulating character of NiO, but simultaneously also to a lower thermal conductivity. Here, the latter has been found for all investigated alloys. For the electrical conductivity, however, the expected decrease can be identified for the W-alloyed sample, while alloying with small amount of Sn show an increase in electrical conductivity, due to the incorporation of Sn into the matrix. If these impurities can be avoided, the thermoelectric properties and especially the power factor may be improved even further. In general, alloying with only small amounts, namely, 1 at.-% Sn or W, shows a beneficial behavior. For these samples, a higher power factor of 38 and 47 μW cm^{-1} K^{-2} and *zT* values of 0.09 and 0.12 were determined, respectively, corresponding to an increase of approximately 12 % and 38 % in the power factor compared to the Cu50Ni50 sample and 26 % increase in the figure of merit for the W-alloyed sample. Here, alloying with Sn resulted mainly in an increase in electrical conductivity, while alloying with W resulted in an increase in the Seebeck coefficient. This proves the potential of utilization of nanopowders, as a preparation from large metal flakes did not result in improved properties [37]. Compared to other works, Kang et al. [33] also prepared constantan with a nominal composition of $Cu_{56}Ni_{42}Mn_2$ doped with 0.25 at.-% Zr via ball milling and induction melting, resulting in similar values to constantan for the undoped samples and increased values for Zr-doped samples with a power factor of 80 μW cm^{-1} K^{-2} and a peak zT of 0.22 at 800 K after aging. Yuan et al. [32] prepared a $Cu_{55}Ni_{45}Se$/carbon nanotube hybrid material via ball milling and annealing, resulting in a *zT* value of 0.35 at 873 K, strongly increased by the inclusion of the carbon nanotubes which leads to a drastically lowered thermal conductivity. Here, the results of this work are slightly lower, but show the beneficial characteristics by alloying with other elements and the utilization of nanopowders, which could be consequently combined with other concepts. These results underline the potential of this mostly overlooked materials; by alloying with other metals, the thermoelectric properties can be further enhanced and may even reach a moderate figure of merit *zT*, under maintaining a high power factor within an inexpensive, nontoxic and easily obtainable material.

4. Conclusions

Cu-Ni-based metals alloyed with tin and tungsten were successfully produced via the arc melting of metal nanopowders. XRD and SEM analyses showed that tin is partly incorporated into the matrix, while tungsten primarily forms a separate phase. The thermal conductivity is slightly reduced by both alloying elements, whereas the power factor could be enhanced by small amounts of tin and tungsten compared to the pure Cu-Ni alloy. The largest improvement were observed for samples with 1 at.-% tin or tungsten, resulting in a peak power factor of 38 $\mu W\ cm^{-1}\ K^{-2}$ and 47 $\mu W\ cm^{-1}\ K^{-2}$ for 1 at.-% Sn and 1 at.-% W at 573 K. Especially the utilization of nanopowders proved to result in better distribution and increased thermoelectric properties. Remarkably, Sn alloying mainly resulted in an increase in electrical conductivity, while W alloying increased the Seebeck coefficient. Within all samples, NiO impurities could be found. If avoided, then these values are expected to be improved even further. These results showed that Cu-Ni alloys are an interesting starting point for the development of a new generation of inexpensive, non-toxic, easily obtainable and processable thermoelectric materials with a very high power factor to be utilized for high power output.

References

1. Kishore, R.A.; Marin, A.; Wu, C.; Kumar, A.; Priya, S. *Energy Harvesting - Materials, Physics, and System Design with Practical Examples*; DEStech Publications, 2019;
2. Wolf, M.; Hinterding, R.; Feldhoff, A. High Power Factor vs . High zT - A Review of Thermoelectric Materials for High-Temperature Application. *Entropy* **2019**, *21*, 1058, doi:10.3390/e21111058.
3. Feldhoff, A. Thermoelectric Material Tensor Derived from the Onsager-de Groot-Callen Model. *Energy Harvest. Syst.* **2015**, *2*, 5–13, doi:10.1515/ehs-2014-0040.
4. Feldhoff, A. Power Conversion and Its Efficiency in Thermoelectric Materials. *Entropy* **2020**, *22*, 803, doi:10.3390/e22080803.
5. Fuchs, H.U. *The Dynamics of Heat - A Unified Approach to Thermodynamics and Heat Transfer*; 2nd ed.; Springer-Verlag: New York, 2010;
6. Ioffe, A.F. *Semiconductor Thermoelements, and Thermoelectric Cooling.*; 1st ed.; Info-search Ltd.: London, 1957;
7. Tan, G.; Zhao, L.D.; Kanatzidis, M.G. Rationally Designing High-Performance Bulk Thermoelectric Materials. *Chem. Rev.* **2016**, *116*, 12123–12149, doi:10.1021/acs.chemrev.6b00255.
8. Shi, X.; Chen, L.; Uher, C. Recent Advances in High-Performance Bulk Thermoelectric Materials. *Int. Mater. Rev.* **2016**, *61*, 379–415, doi:10.1080/09506608.2016.1183075.
9. Kanatzidis, M.G. Nanostructured Thermoelectrics: The New Paradigm? *Chem. Mater.* **2010**, *22*, 648–659, doi:10.1021/cm902195j.
10. Poudel, B.; Hao, Q.; Ma, Y.; Lan, Y.; Minnich, A.; Yu, B.; Yan, X.; Wang, D.; Muto, A.; Vashaee, D.; Chen, X.; Liu, J.; Dresselhaus, M. S.; Chen, G.; Ren, Z. High-Thermoelectric Performance of Nanostructured Bismuth Antimony Telluride Bulk Alloys. *Science (80)* **2008**, *320*, 634–638, doi:10.1126/science.1155140.
11. Ashalley, E.; Chen, H.; Tong, X.; Li, H.; Wang, Z.M. Bismuth Telluride Nanostructures: Preparation, Thermoelectric Properties and Topological Insulating Effect. *Front. Mater. Sci.* **2015**, *9*, 103–125, doi:10.1007/s11706-015-0285-9.
12. Bittner, M.; Helmich, L.; Nietschke, F.; Geppert, B.; Oeckler, O.; Feldhoff, A. Porous $Ca_3Co_4O_9$ with Enhanced Thermoelectric Properties Derived from Sol–Gel Synthesis. *J. Eur. Ceram. Soc.* **2017**, *37*, 3909–3915, doi:10.1016/j.jeurceramsoc.2017.04.059.
13. Delorme, F.; Giovannelli, F. Effect of Ca Substitution by Fe on the Thermoelectric Properties of $Ca_3Co_4O_9$ Ceramics. *J. Electroanal. Chem. Interfacial Electrochem.* **2018**, *40*, 107–114, doi:10.1007/s10832-018-0109-2.
14. He, J.; Liu, Y.; Funahashi, R. Oxide Thermoelectrics: The Challenges, Progress, and Outlook. *J. Mater. Res.* **2011**, *26*, 1762–1772, doi:10.1557/jmr.2011.108.
15. Imasato, K.; Kang, S.D.; Snyder, G.J. Exceptional Thermoelectric Performance in $Mg_3Sb_{0.6}Bi_{1.4}$ for Low-Grade Waste Heat Recovery . *Energy Environ. Sci.* **2019**, *12*, 965–971, doi:10.1039/c8ee03374a.
16. Toberer, E.S.; May, A.F.; Snyder, G.J. Zintl Chemistry for Designing High Efficiency Thermoelectric Materials. *Chem. Mater.* **2010**, *22*, 624–634, doi:10.1021/cm901956r.

17. Poon, J.S. Recent Advances in Thermoelectric Performance of Half-Heusler Compounds. *Metals (Basel).* **2018**, *8*, 989, doi:10.3390/met8120989.
18. Chen, S.; Ren, Z. Recent Progress of Half-Heusler for Moderate Temperature Thermoelectric Applications. *Mater. Today* **2013**, *16*, 387–395, doi:10.1016/j.mattod.2013.09.015.
19. Zhu, H.; He, R.; Mao, J.; Zhu, Q.; Li, C.; Sun, J.; Ren, W.; Wang, Y.; Liu, Z.; Tang, Z.; Sotnikov, A.; Wang, Z.; Broido, D.; Singh, D. J.; Chen, G.; Nielsch, K.; Ren, Z. Discovery of ZrCoBi-Based Half-Heuslers with High Thermoelectric Conversion Efficiency. *Nat. Commun.* **2018**, *9*, 1–9, doi:10.1038/s41467-018-04958-3.
20. Gayner, C.; Kar, K.K. Recent Advances in Thermoelectric Materials. *Prog. Mater. Sci.* **2016**, *83*, 330–382, doi:10.1016/j.pmatsci.2016.07.002.
21. Toshima, N. Conductive Polymers as a New Type of Thermoelectric Material. *Macromol. Symp.* **2002**, *186*, 81–86, doi:10.1002/1521-3900(200208)186:1<81::AID-MASY81>3.0.CO;2-S.
22. Toshima, N. Recent Progress of Organic and Hybrid Thermoelectric Materials. *Synth. Met.* **2017**, *225*, 3–21, doi:10.1016/j.synthmet.2016.12.017.
23. Narducci, D. Do we Really Need High Thermoelectric Figures of Merit? A Critical Appraisal to the Power Conversion Efficiency of Thermoelectric Materials. *Appl. Phys. Lett.* **2011**, *99*, doi:10.1063/1.3634018.
24. Bittner, M.; Kanas, N.; Hinterding, R.; Steinbach, F.; Groeneveld, D.; Wemhoff, P.; Wiik, K.; Einarsrud, M.A.; Feldhoff, A. Triple-Phase Ceramic 2D Nanocomposite with Enhanced Thermoelectric Properties. *J. Eur. Ceram. Soc.* **2019**, *39*, 1237–1244, doi:10.1016/j.jeurceramsoc.2018.10.023.
25. Xu, Z.J.; Hu, L.P.; Ying, P.J.; Zhao, X.B.; Zhu, T.J. Enhanced Thermoelectric and Mechanical Properties of Zone Melted *p*-Type $(Bi,Sb)_2Te_3$ Thermoelectric Materials by Hot Deformation. *Acta Mater.* **2015**, *84*, 385–392, doi:10.1016/j.actamat.2014.10.062.
26. Fu, C.; Bai, S.; Liu, Y.; Tang, Y.; Chen, L.; Zhao, X.; Zhu, T. Realizing High Figure of Merit in Heavy-Band *p*-Type Half-Heusler Thermoelectric Materials. *Nat. Commun.* **2015**, *6*, 1–7, doi:10.1038/ncomms9144.
27. Muta, H.; Kurosaki, K.; Uno, M.; Yamanaka, S. Thermoelectric Properties of Constantan/Spherical SiO_2 and Al_2O_3 Particles Composite. *J. Alloys Compd.* **2003**, *359*, 326–329, doi:10.1016/S0925-8388(03)00295-0.
28. Mao, J.; Wang, Y.; Kim, H.S.; Liu, Z.; Saparamadu, U.; Tian, F.; Dahal, K.; Sun, J.; Chen, S.; Liu, W.; Ren, Z. High Thermoelectric Power Factor in Cu-Ni Alloy Originate from Potential Barrier Scattering of Twin Boundaries. *Nano Energy* **2015**, *17*, 279–289, doi:10.1016/j.nanoen.2015.09.003.
29. Wiendlocha, B. Thermopower of Thermoelectric Materials with Resonant Levels: PbTe:Tl versus PbTe:Na and $Cu_{1-x}Ni_x$. *Phys. Rev. B* **2018**, *97*, 1–15, doi:10.1103/PhysRevB.97.205203.
30. Wolf, M.; Menekse, K.; Mundstock, A.; Hinterding, R.; Nietschke, F.; Oeckler, O.; Feldhoff, A. Low Thermal Conductivity in Thermoelectric Oxide-Based Multiphase Composites. *J. Electron. Mater.* **2019**, *48*, 7551–7561, doi:10.1007/s11664-019-07555-2.
31. Liu, W.; Kim, H.S.; Chen, S.; Jie, Q.; Lv, B.; Yao, M.; Ren, Z.; Opeil, C.P.; Wilson, S.; Chu, C.W.; Ren, Z. n-Type Thermoelectric Material $Mg_2Sn_{0.75}Ge_{0.25}$ for High Power Generation. *Proc. Natl. Acad. Sci. U. S. A.* **2015**, *112*, 3269–3274, doi:10.1073/pnas.1424388112.
32. Yuan, M.; Sun, L.; Lu, X.W.; Jiang, P.; Bao, X.H. Enhancing the Thermoelectric Performance of Cu–Ni Alloys by Introducing Carbon Nanotubes. *Mater. Today Phys.* **2021**, *16*, doi:10.1016/j.mtphys.2020.100311.
33. Kang, H.; Yang, Z.; Yang, X.; Li, J.; He, W.; Chen, Z.; Guo, E.; Zhao, L.D.; Wang, T. Preparing Bulk Cu-Ni-Mn Based Thermoelectric Alloys and Synergistically Improving their Thermoelectric and Mechanical Properties using Nanotwins and Nanoprecipitates. *Mater. Today Phys.* **2021**, *17*, doi:10.1016/j.mtphys.2020.100332.
34. Shimizu, Y.; Mizoshiri, M.; Mikami, M.; Sakurai, J.; Hata, S. Fabrication of Copper/Copper-Nickel Thin-Film Thermoelectric Generators with Energy Storage Devices. *J. Phys. Conf. Ser.* **2018**, *1052*, doi:10.1088/1742-6596/1052/1/012032.
35. Lide, D.R. *CRD Handbook of Chemistry and Physics*; 89th ed.; CRC Press/Taylor and Francis: Boca Raton, FL, 2009;
36. Haubold, T.; Gertsman, V. On the Structure and Properties of Nanostructured Copper-Tungsten Alloys. *Nanostructured Mater.* **1992**, *1*, 303–312, doi:10.1016/0965-9773(92)90037-X.
37. Steinhoff, T.; Wolf, M.; Nürnberger, F.; Gerstein, G.; Feldhoff, A. Evaluation of Cu-Ni-Based Alloys for Thermoelectric Energy Conversion. *Mater. Sci. Forum* **2021**, *1016 MSF*, 107–112, doi:10.4028/www.scientific.net/MSF.1016.107.
38. Wang, J.; Wei, L.; Zhang, L.; Zhang, J.; Wei, H.; Jiang, C.; Zhang, Y. Zinc-Doped Nickel Oxide Dendritic Crystals with Fast Response and Self-Recovery for Ammonia Detection at Room Temperature. *J. Mater. Chem.* **2012**, *22*, 20038–20047, doi:10.1039/c2jm34192a.
39. Zhuo, K.; Jeong, M.G.; Chung, C.H. Dendritic Nanoporous Nickel Oxides for a Supercapacitor Prepared by a Galvanic Displacement Reaction with Chlorine Ions as an Accelerator. *RSC Adv.* **2013**, *3*, 12611–12615, doi:10.1039/c3ra22322a.
40. Wang, F.; Lu, Y.; Zeng, S.; Song, Y.; Zheng, D.; Xu, W.; Lu, X. Nickel@Nickel Oxide Dendritic Architectures with Boosted Electrochemical Reactivity for Aqueous Nickel–Zinc Batteries. *ChemElectroChem* **2020**, *7*, 4572–4577, doi:10.1002/celc.202001112.

3. Processing of thermoelectric generators

3.1 Summary

Within this chapter, a new manufacturing route for functional thermoelectric generators (TEGs) on a large scale is presented. As discussed before, various different additive and subtractive manufacturing methods are in focus of research.

In section 3.1, investigation of a spray-coating process is applied to a thermoelectric calcium cobaltite (CCO) layer. The CCO can be easily dispersed in isopropanol without the need of any additives and subsequently spray-coated on top of various substrates. For this work, a flexible low-temperature co-fired ceramic substrate was utilized, as its sintering conditions overlap with the sintering of CCO around 1100 K to 1200 K. During the spray-coating, the resulting layer thickness can be controlled by the duration of spray-coating. In the subsequent laser structuring step, the geometry of the CCO structures can also be precisely controlled. After sintering, expected values for the Seebeck coefficient of the CCO layers can be achieved, while the electrical conductivity only reaches about 5 % of the electrical conductivity of the conventional sintered bulk material. This is a result of the high porosity of the layer and due to the missing pressing step that is used for the bulk material.

In section 3.2, the combination of a spray-coating process with subsequent laser structuring is expanded to a functional TEG. For proof of concept, commercial Ag paste is used as counterpart to the CCO. With the developed process, the geometry of both the CCO and Ag structures and therefore of the resulting TEG can be precisely controlled within the spray-coating and laser structuring. All steps before the final sintering can be done rapidly and are suitable for large scale production. A prototype of a CCO/Ag TEG is presented, reaching an electrical power density of 1.6 μW cm^{-2} with 9 thermocouples at a hot-side temperature of 673 K and a temperature difference of 100 K. The concept of this manufacturing process may also be adapted for other kinds of thermoelectric materials, e.g., half-Heusler compounds or alloys.

Finally, in section 3.3, the concept of a laser sintering step, either instead of or additionally to the thermal sintering is investigated. As the structuring of the TEG is done by utilization of a laser anyway, an additional sintering of the layer with suitable laser parameters can be favorably. Here, especially the combination of laser treatment and thermal sintering was beneficial for increasing the electrical conductivity of the CCO film compared to an only thermally sintered layer. This concept is therefore proven to be a promising addition to the thermal sintering and to be included in the manufacturing of TEGs.

3.2 Combined spray-coating and laser structuring of thermoelectric ceramics

Marvin Abt, Mario Wolf, Armin Feldhoff and Ludger Overmeyer

Combined spray-coating and laser structuring of thermoelectric ceramics

Marvin Abt[a],[*], Mario Wolf[b],[*], Armin Feldhoff[b], Ludger Overmeyer[a]

[a] *Institute for Integrated Production Hannover, Hollerithallee 6, D-30419 Hanover, Germany*
[b] *Institute of Physical Chemistry and Electrochemistry, Leibniz University of Hanover, Callinstraße 3A, D-30167 Hanover, Germany*

ARTICLE INFO

ABSTRACT

The processing of ceramics is an important technology for various technical applications. In this paper, a highly controllable process consisting of spray-coating and laser structuring to design ceramic layers on a versatile applicable substrate is presented. A thermoelectric oxide, $Ca_3Co_4O_9$, which is a type of thermoelectric material, is used in the process and applied to a flexible ceramic substrate. The resulting structures have highly controllable shapes and good thermoelectric properties, and they can be used to produce a printable thermoelectric generator (TEG). The use of a flexible ceramic substrate and the high feasibility of the process lead to a universally applicable procedure that can be used to process ceramics with unique structures and designs.

1. Introduction

1.1. Thermoelectric energy harvesting

Today, wireless sensor networks and monitoring systems are common components in building infrastructure, e.g., for smart home applications, as shown by Matiko et al. (2014), automotive safety and control applications, as reported by Vullers et al. (2010), medical applications (e.g., portable biomedical systems, as shown by Chen and Wright (2012)) and smart agriculture (e.g., resource optimization and land monitoring, as described by Lachure et al. (2015)). Energy harvesting solutions often secure the power supply for such systems, especially when the installation and maintenance of battery storage and supply networks is too costly. Thermoelectric power conversion is one way to convert energy obtained from the environment into electrical energy to power sensors and measuring and transmitting electronics. The conversion of energy by thermoelectric generators (TEGs) can be described as the thermal induction of an electrical current (see Feldhoff (2015)). The maximum achievable electrical power output of a thermoelectric generator is determined by the power factor *PF* of a thermoelectrically active material.

$$PF = \sigma_T \cdot \alpha^2 \qquad (1)$$

Therefore, the power factor of a material is characterized by the isothermal electrical conductivity σ_T and the Seebeck coefficient α. Bismuth telluride is the state of the art thermoelectric and is the most effective known thermoelectric material at room temperature. However, according to Rowe (2012), the raw materials used to produce bismuth telluride are expensive and toxic.

Therefore, the development of telluride-free alternatives has gained much attention in recent years. In particular, intermetallic compounds, e.g., Zintl phases, as shown by Toberer et al. (2010), and Heusler compounds, as shown by Chen and Ren (2013), as well as oxide-based materials, e.g., layered cobaltites such as $Ca_3Co_4O_9$ (CCO), have become a primary focus of research on thermoelectric materials.

1.2. Processing of thermoelectric generators

In addition to materials research, the production of conventional thermoelectric generators is a complex process that also requires research attention. As described by Orrill and LeBlanc (2017), conventional TEGs are produced by several steps, which include synthesis, pressing, sawing and electrical contacting. LeBlanc et al. (2014) showed that the cost of manufacturing these manually assembled TEGs accounts for a significant portion of the commercial price of conventional thermoelectric generators. Therefore, research has also focused on investigating alternative additive and subtractive manufacturing methods for producing various thermoelectric materials.

In this context, several additive manufacturing processes have already been investigated. In particular, various printing technologies, such as ink jet printing, dispensing or screen-printing, have already been used to process thermoelectric structures. For example, (Besganz et al., 2014) developed PEDOT:PSS/ZnO structures via an inkjet technology and (Madan et al., 2011) prepared Bi_2Te_3 and Sb_2Te_3 thick films via dispensing. (Cao et al., 2016) reported the production of printed flexible TEGs composed of Bi_2Te_3 by a screen-printing method. In particular, the latter approach is suitable because it is an inexpensive and easily scalable method that can be used to produce ceramic

materials and has already been used for thermoelectric applications, as demonstrated by Shin et al. (2017). The investigated printing processes are often carried out on flexible substrates. For this purpose, polymers such as polyethylene terephthalate (PET) or polyamides, are commonly used, as demonstrated by Du et al. (2018). The use of polymers enables the innovative design and manufacture of thermoelectric generators by a technique known as "roll-to-roll". Using this technique, the structures are first printed two-dimensionally on a flexible substrate, and then, the printed substrate is rolled up into a three-dimensional cylinder. As stated by Wu et al. (2016), the main advantages of these printable TEGs over conventional thermoelectric generators are their scalability, improved geometric flexibility and more compact design.

However, due to their reduced thermal stabilities, the use of polymeric substrates limits the availability of suitable thermoelectric materials. Additionally, most of the abovementioned printing technologies are characterized by long production times and require the elaborate development of pastes and dispersions. Specifically, oxide-based materials, which have high thermal stabilities and are nontoxic and relatively inexpensive, can only be manufactured by conventional methods and still require innovative processes, designs and substrates.

1.3. Process design

Here, we present a two-dimensional subtractive manufacturing process to prepare conductive ceramic structures on a flexible substrate, as shown in Fig. 1. Due to the use of a subtractive manufacturing technology, a large area of the substrate can be coated, and the coating can be quickly structured afterwards. During this process, thermoelectric CCO and a flexible low-temperature co-fired ceramic substrate (LTCC), which consists of ceramic particles embedded in a polymeric matrix, are used. First, the CCO particles are dispersed in a solvent, and the resulting dispersion is applied to the LTCC substrate by spray-coating (Fig. 1A). Due to the flexibility of the substrate, the thermoelectric material can be easily processed and adapted to accommodate various application needs. As reported by Bechtold (2009), because the LTCC substrates are highly resilient and have higher thermal conductivities compared to polymer films, laser technology can be used for structuring the LTCC substrates. Thus, the CCO particles can be selectively removed to structure the coated surface (Fig. 1B). Subsequently, the LTCC substrate and the thermoelectric CCO layer can be sintered in a single post-treatment step (Fig. 1C and D). This ensures the electrical conductivity of the CCO layer and turns the substrate into a rigid and robust material. This flexible substrate allows for the use of a roll-to-roll process and can subsequently be transformed into a robust structure. Additionally, the proposed method is also suitable for processing other thermoelectric materials for various applications.
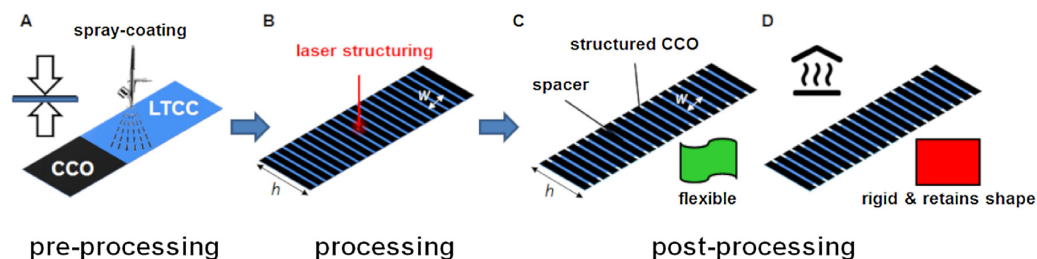
2. Experimental

2.1. Materials synthesis

Unless otherwise mentioned, all reagents obtained from commercial vendors were reagent grade or higher and used without further purification. Calcium cobalt oxide $Ca_3Co_4O_9$ was purchased from CerPoTech (Tiller, Norway). The spray-coating paste was obtained by dispersing 30 wt.% CCO in isopropyl alcohol by stirring and ultrasonication. For the flexible LTCC substrate, a material called 951 PX, which was obtained from DuPont, with a thickness of 220 μm was used. For easier handling, a two-layer substrate with an effective substrate thickness of 440 μm was used in the process. CCO was applied by spray-coating. In one cycle, 16 ml of the dispersion of CCO in isopropyl alcohol was applied to an area of approximately 152.4 mm × 152.4 mm (6″ × 6″). The substrate was heated to approximately 363 K by a heating plate to directly remove the isopropyl alcohol. A 75 W pulsed CO_2 laser with 30% to 40% of the maximum power input (Epilog Fusion 32 M2 Dual, spot diameter = 80 μm) was used to structure the CCO layer. The coated and structured substrates were sintered at 973 K for 10 h in air. The heating rate was 3 K min^{-1}.

2.2. Characterization

The CCO powder and the sintered CCO ceramic layers on the LTCC substrate were characterized by X-ray diffraction (XRD, Bruker D8 Advance with Cu-Kα radiation). The confocal laser scanning microscope images were acquired at a 10x magnification (Nanofocus μsurf custom). For the microstructural characterization, a field-emission scanning electron microscope (FE-SEM, JEOL JSM-6700F) equipped with an energy-dispersive X-ray spectrometer (EDXS, Oxford Instruments INCA 300) for elemental analysis was used. The thermoelectric properties were measured as a function of temperature from room temperature to 673 K. The electrical conductivity σ and the Seebeck coefficient α were measured with a homemade measurement cell, an ELITE thermal system and Keithley 2100 Digital Multimeters. The power *PF* was calculated using Eq. (1).

3. Results and discussion

Fig. 2 presents the process proposed to design sintered ceramic structures via spray-coating and laser structuring. The CCO powder exhibits platelet shaped crystals with width from 0.1 μm to 0.4 μm and thicknesses of approximately 30 nm (Fig. 2 A and B). A black paste containing 30 wt.% CCO was obtained with stirring and ultrasonication and used for spray-coating. The LTCC substrate exhibits good adhesion properties, leading to a stable CCO layer after spray-coating and drying at 373 K. Using a laser structuring process (Fig. 2D), the CCO layer can be selectively detached, leading to a defined structure. Additionally, the laser can be utilized to cut the whole substrate into the desired shape. Therefore, the geometry and shape can be more easily controlled using
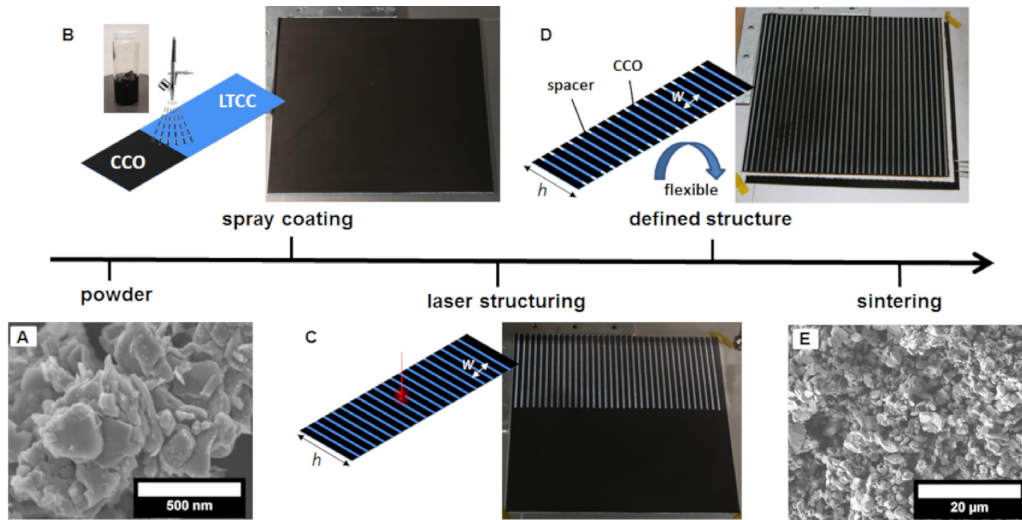

Fig. 1. Proposed concept for processing thermoelectric CCO layers. Commercial CCO powder is dispersed into a paste, and the resulting dispersion is spray-coated and pressed onto a flexible LTCC substrate (preprocessing, A). Laser structuring is utilized to obtain a defined structure on the CCO layer deposited on the flexible substrate (processing, B). During sintering (postprocessing, C and D), the substrate becomes rigid and retains its given shape.

2

Fig. 2. Highly controllable process to obtain a ceramic CCO layer on a flexible LTCC substrate. (A) SEM micrographs of commercially obtained CCO powder platelets; (B) spray-coating of the CCO paste on the LTCC substrate; (C) laser structuring process used to obtained a defined structure; (D) resulting flexible substrate with a structured CCO layer; and (E) SEM micrograph of the CCO layer after sintering.

laser structuring compared to conventional sawing and the manual deposition of bulk materials onto rigid ceramic substrates. Because this process is highly controllable, many different structures and shapes can be obtained. For our purposes, the ceramic CCO structures were designed for potential thermoelectric applications (Fig. 2E). Furthermore, due to the flexibility of the substrate, its shape can be individually modified, e.g., using a roll-up step. Finally, a sintering step is used to harden the substrate and sintering of the CCO layer. The substrate can therefore be adapted to accommodate the various needs of a potential application and retains its given shape after sintering. As opposed to the rigid design of conventional thermoelectric generators, this flexible substrate can be adjusted to have varying surface structures and textures, while still retaining a good mechanical stability after sintering.

In Fig. 3, the designed ceramic structures are shown in detail. The resulting structures exhibit widths of 2 mm and heights of 20 mm. The substrate is highly flexible before sintering (Fig. 3B). The confocal laser scanning microscope images show that CCO partially detaches during the laser structuring. Additionally, short-circuit between the ceramic structures was not detected, proving the successful detachment of the ceramic structures. After sintering, the difference in height between the smooth ceramic structures and the substrate is approximately 250 μm.

Fig. 4 shows the XRD patterns of the pristine LTCC substrate and the spray-coated CCO layer after sintering. The XRD patterns of the coated substrate prove the successful preparation of a CCO layer on the

substrate. After 1 and 2 cycles of spray-coating, peaks of the substrate as well as the CCO layer are visible in the XRD patterns. However, with an increasing number of spray-coating cycles, the peaks corresponding to the substrate become less intense and can no longer be identified. This leads to the assumption that, by increasing the number of spray coating cycles, the resulting CCO layer becomes thicker; therefore, no peaks corresponding to the LTCC substrate can be observed.

Fig. 5 shows the cross-sectional SEM micrographs and the resulting layer thicknesses after varying numbers of spray-coating cycles. The cross-sectional SEM micrographs show porous CCO layers, which have thicknesses between 17 μm and 37 μm, on top of the sintered substrate. As expected, the layer thicknesses increase as the number of spray-coating cycles increases. This agrees with the abovementioned results of the XRD results. The EDXS elemental maps prove that a Co-rich thermoelectric phase exists on top of the Al-rich LTCC substrate. Both the SEM micrographs and the EDXS elemental maps show that the CCO layer is highly porous due to the low pressure and relatively low sintering temperature.

Fig. 6 shows the general trend observed for the layer thickness with increasing numbers of spray-coating cycles before and after the sintering step. Both show the same trend of increasing layer thicknesses. Before sintering, the bar representing thickness on the plot exhibits larger error bars, due to the rougher surface. After sintering, the layers practically did not shrink, thus resulting in a highly porous layer of
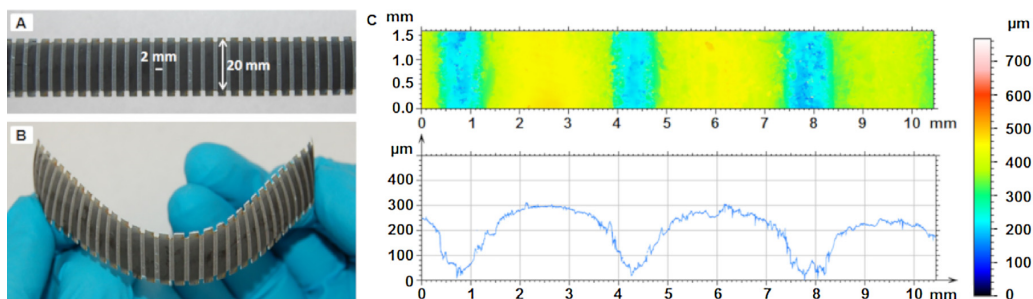

Fig. 3. (A and B) Images of the resulting structured CCO layer on the flexible LTCC after laser structuring and (C) confocal laser scanning microscope images and height profile after laser structuring and sintering. The latter images show the successful partial detachment of CCO, resulting in the thermoelectric CCO structures (width: 2 mm, height: 20 mm) on a flexible substrate.
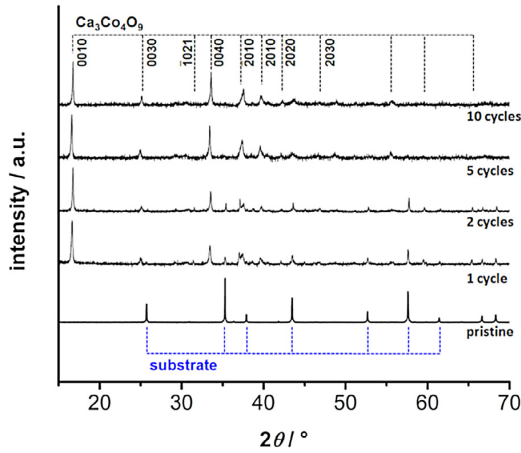
3

Fig. 4. XRD pattern of the pristine LTCC substrate after sintering and after spray-coating the substrate with 1 cycle, 2 cycles, 5 cycles and 10 cycles of CCO and sintering. The peaks obtained for CCO correspond to the Cm (0 1 − p 0) space group, according to Miyazaki et al. (2002). XRD patterns obtained for the spray-coated samples have peaks that correspond to the substrate and the CCO layer. As the number of spray-coating cycles increases, the peaks corresponding to the substrate can no longer be identified.

Fig. 6. Resulting thicknesses, before and after sintering, of the CCO layers after spin-coating with 1 cycle, 2 cycles, 5 cycles and 10 cycles.

sintered CCO particles. Therefore, in the proposed process, a porous layer of CCO can successfully be attached to the flexible LTCC substrate, and the thickness of the CCO porous layer can be controlled by tuning the number of spray-coating cycles. Compared to conventional bulk materials, this leads to a more efficient use of the material. After sintering, a porous and smooth CCO layer with a thickness between 15 μm and 40 μm can be obtained.

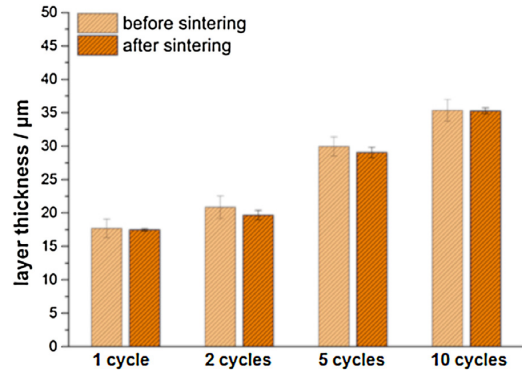The resulting values of the electrical resistance R, electrical conductivity σ and the Seebeck coefficient α, as well as the determined power factor $\sigma\alpha^2$, are shown in Fig. 7. The resistance R of the CCO layer decreases as the number of spray-coating cycles increases and can be explained by the presence of a thicker and denser layer. When between 5 and 10 cycles are performed, on the other hand, only a slight decrease in the resistance can be detected; under these conditions, the CCO layer exhibits a resistance of approximately 200Ω at 673 K. The determination of the electrical conductivity σ by using the layer thicknesses shown in Fig. 6 leads to the observation of a similar trend when increasing the number of spray-coating cycles. The sample obtained after 10 cycles of spray-coating exhibits a slightly lower electrical conductivity, due to an increase in the layer thickness, but it also exhibits a similar resistance compared to the sample obtained after 5 cycles. The sample obtained after 5 cycles of spray-coating has an electrical conductivity of approximately 3 S cm^{-1} at 673 K.

The measured values of the Seebeck coefficient α show a similar
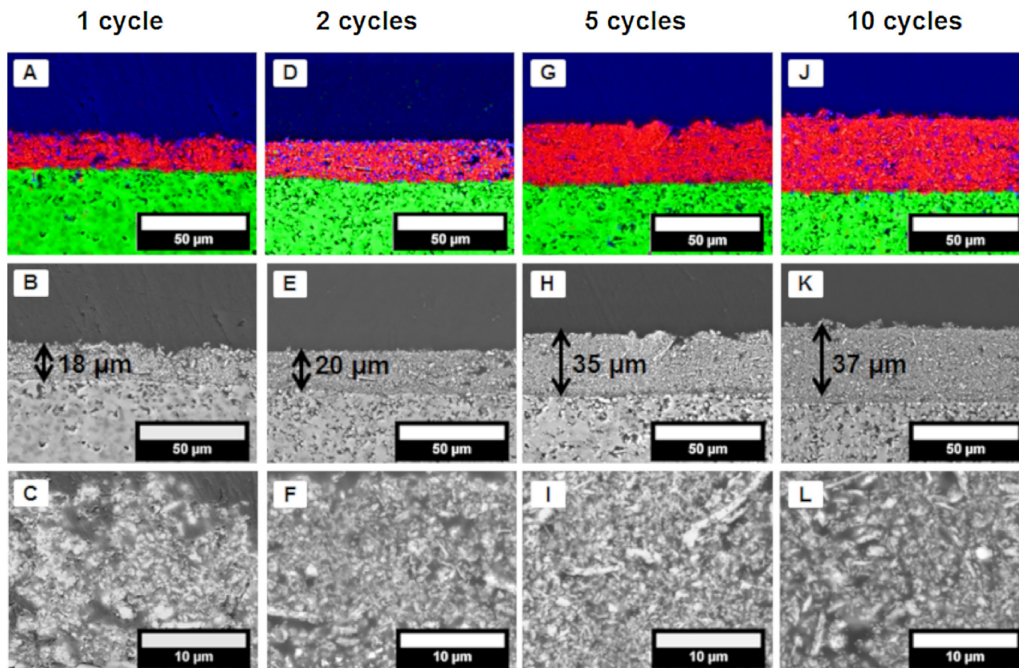

Fig. 5. Cross-sectional SEM micrographs and EDXS maps of the spray-coated CCO layers after sintering and spray-coating with (A–C) 1 cycle, (D–F) 2 cycles, (G–I) 5 cycles and (J–L) 10 cycles. Layer thickness of the CCO layer increases as the number of spray-coating cycles increases. After sintering, a smooth and porous CCO layer with a thickness of 15-40 μm can be identified.
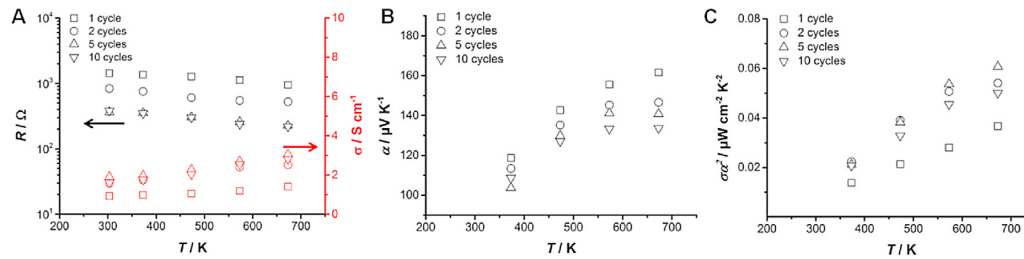
Fig. 7. In-plane measurements of (A) the electrical resistance R and electrical conductivity σ, (B) the Seebeck coefficient α and (C) the power factor *PF* as a function of the temperature T of the spray-coated CCO after sintering. As the number of spray-coating cycles increases, the resistance decreases due to the larger resulting layer thickness, leading to a higher electrical conductivity. Resulting structures exhibit a maximum power factor of approximately $\mu\text{W cm}^{-1}\text{K}^{-2}$.

trend. The Seebeck coefficient is approximately 120 to 160 $\mu\text{V K}^{-1}$ at 673 K, decreasing with the amount of cycles and therefore with increasing electrical conductivity. The opposite relationship between the electrical conductivity σ and the Seebeck coefficient α results in the sample obtained with 5 cycles of spray-coating having a maximum resulting power factor of approximately 0.07 $\mu\text{W cm}^{-1}\text{K}^{-2}$. Compared to bulk CCO, porous CCO exhibits a lower electrical conductivity, as reported by Bittner et al. (2017), which can be explained by the low pressure and low sintering temperature used in the process and leads to porous layers that have higher intergranular contact resistances. The measured values of the Seebeck coefficient α are slightly lower compared to bulk CCO but are slightly higher compared to thin film CCO, as published by Wei et al. (2013); a similar trend is observed for these CCO sample types, so our results agree with these data.

In conclusion, the developed process is an interesting approach that can be used to design printed thermoelectric structures composed of oxide ceramic materials. The developed process can be easily adapted to accommodate various application needs, geometries, structures and materials, which leads to a more efficient material use, and the properties of the resulting materials can be maintained during scale-up processes, e.g., a roll-to-roll process. The thermoelectric properties may be further enhanced, e.g., achieving denser structures, by improving the process and using nanostructuring and doping.

4. Conclusions

A highly controllable process used to obtain thermoelectric ceramic structures via spray-coating and laser structuring was presented. A flexible LTCC substrate with interesting properties was successfully utilized and coated with a CCO-based paste via spray-coating. The thickness was controlled in the process by varying the number of spray-coating cycles. Furthermore, laser structuring produced ceramic coatings that had well defined and highly controllable designed structures. Due to the flexibility of the substrate, it can be easily adapted to accommodate various application needs, e.g., a curved surface. The substrate and the CCO layer could be sintered at temperatures up to 973 K, leading to a rigid substrate and ceramic structures with electrical conductivities of up to 3 S cm^{-1}. Overall, the spray-coated porous CCO layer achieved a power factor of approximately 0.07 $\mu\text{W cm}^{-1}\text{K}^{-2}$. Further improvement and research may lead to a fully printable oxide-based thermoelectric device. In general, this process can be easily applied to different types of materials and application needs.

References

Bechtold, F., 2009. A comprehensive overview on today's ceramic substrate technologies. 2009 European Microelectronics and Packaging Conference 1–12.

Besganz, A., Zollmer, V., Kun, R., Pal, E., Walder, L., Busse, M., 2014. Inkjet printing as a flexible technology for the deposition of thermoelectric composite structures. Proc. Technol. 15, 99–106.

Bittner, M., Helmich, L., Nietschke, F., Geppert, B., Oeckler, O., Feldhoff, A., 2017. Porous $Ca_3Co_4O_9$ with enhanced thermoelectric properties derived from sol–gel synthesis. J. Eur. Ceram. Soc. 37 (13), 3909–3915.

Cao, Z., Koukharenko, E., Tudor, M.J., Torah, R.N., Beeby, S.P., 2016. Flexible screen printed thermoelectric generator with enhanced processes and materials. Sens. Actuators A: Phys. 238, 196–206.

Chen, A., Wright, P.K., 2012. Medical Applications of Thermoelectrics. pp. 26-1.

Chen, S., Ren, Z., 2013. Recent progress of half-Heusler for moderate temperature thermoelectric applications. Mater. Today 16 (10), 387–395.

Du, Y., Xu, J., Paul, B., Eklund, P., 2018. Flexible thermoelectric materials and devices. Appl. Mater. Today 12, 366–388.

Feldhoff, A., 2015. Thermoelectric material tensor derived from the Onsager-de Groot-Callen model. Energy Harvest. Syst. 2 (1–2), 517.

Lachure, S., Bhagat, A., Lachure, J., 2015. Review on Precision Agriculture Using Wireless Sensor Network, vol. 10.

LeBlanc, S., Yee, S.K., Scullin, M.L., Dames, C., Goodson, K.E., 2014. Material and manufacturing cost considerations for thermoelectrics. Renew. Sustain. Energy Rev. 32, 313–327.

Madan, D., Chen, A., Wright, P.K., Evans, J.W., 2011. Dispenser printed composite thermoelectric thick films for thermoelectric generator applications. J. Appl. Phys. 109 (3), 034904.

Matiko, J.W., Grabham, N.J., Beeby, S.P., Tudor, M.J., 2014. Review of the application of energy harvesting in buildings. Meas. Sci. Technol. 25 (1), 012002.

Miyazaki, Y., Onoda, M., Oku, T., Kikuchi, M., Ishii, Y., Ono, Y., Morii, Y., Kajitani, T., 2002. Modulated structure of the thermoelectric compound $[Ca_2CoO3]_{0.62}CoO_2$. J. Phys. Soc. Jpn. 71 (2), 491–497.

Orrill, M., LeBlanc, S., 2017. Printed thermoelectric materials and devices: fabrication techniques, advantages, and challenges. J. Appl. Polym. Sci. 134 (3), 5147.

Rowe, D.M., 2012. Modules, Systems, and Applications in Thermoelectrics. Thermoelectrics and Its Energy Harvesting. CRC Press, Boca Raton, FL.

Shin, S., Kumar, R., Roh, J.W., Ko, D.S., Kim, H.S., Kim, S.I., Yin, L., Schlossberg, S.M., Cui, S., You, J.M., Kwon, S., Zheng, J., Wang, J., Chen, R., 2017. High-performance screen-printed thermoelectric films on fabrics. Sci. Rep. 7 (1), 7317.

Toberer, E.S., May, A.F., Snyder, G.J., 2010. Zintl chemistry for designing high efficiency thermoelectric materials. Chem. Mater. 22 (3), 624–634.

Vullers, R., Schaijk, R., Visser, H., Penders, J., Hoof, C., 2010. Energy harvesting for autonomous wireless sensor networks. IEEE Solid-State Circuits Mag. 2 (2), 29–38.

Wei, R., Jian, H., Tang, X., Yang, J., Hu, L., Chen, L., Dai, J., Zhu, X., Sun, Y., 2013. Enhanced thermoelectric properties in Cu-doped c-axis-oriented $Ca_3Co_4O_9$ thin films. J. Am. Ceram. Soc. 96 (8), 2396–2401.

Wu, H., Huang, Y., Xu, F., Duan, Y., Yin, Z., 2016. Energy harvesters for wearable and stretchable electronics: from flexibility to stretchability. Adv. Mater. (Deerfield Beach, Fla) 28 (45), 9881–9919.

5

3.3 Ceramic-based thermoelectric generator processed via spray-coating and laser structuring

Mario Wolf, Marvin Abt, Gerd Hoffmann, Ludger Overmeyer and Armin Feldhoff

Ceramic-based thermoelectric generator processed via spray-coating and laser structuring

Mario Wolf [a,*], Marvin Abt [b,**], Gerd Hoffmann [c], Ludger Overmeyer [b,c], Armin Feldhoff [a,***]

[a] *Institute of Physical Chemistry and Electrochemistry, Leibniz University Hannover, Callinstraße 3A, D-30167, Hannover, Germany*
[b] *Institute for Integrated Production Hannover, Hollerithallee 6, D-30419, Hannover, Germany*
[c] *Institute of Transport and Automation Technology, An der Universität 2, D-30823, Garbsen, Germany*

ARTICLE INFO

ABSTRACT

Processing technology to improve the manufacturing of thermoelectric generators (TEGs) is a growing field of research. In this paper, an adaptable and scalable process comprising spray-coating and laser structuring for fast and easy TEG manufacturing is presented. The developed process combines additive and subtractive processing technology towards an adaptable ceramic-based TEG, which is applicable at high temperatures and shows a high optimization potential. As a prototype, a TEG based on $Ca_3Co_4O_9$ (CCO) and Ag on a ceramic substrate was prepared. Microstructural and thermoelectric characterization is shown, reaching up to 1.65 μW cm^{-2} at 673 K and a ΔT of 100 K. The high controllability of the developed process also enables adaptation for different kinds of thermoelectric materials.

1. Introduction

Thermoelectric energy conversion has attracted researchers from various fields in recent years due to its potential in direct energy conversion from waste heat to electrical energy [1,2]. Therefore, energy harvesting of wasted thermal energy is the focus of research for several new technologies such as sensor technology and sensor networks or microelectronic devices, as well as multiple high temperature applications [3]. The energy conversion in thermoelectric materials is based on the coupling of electrical current I_{el} and entropy current I_S. When a voltage U and a temperature difference ΔT are applied across the length l of a thermoelectric materials with a cross-sectional area A, the coupled currents can be obtained for steady-state conditions by Eq. (1) [4,5]. Here, the thermoelectric material is represented by a tensor, which contains the isothermal electrical conductivity σ, the Seebeck coefficient α and the electrically open-circuited entropy conductivity Λ_{OC}.

$$\begin{pmatrix} I_{el} \\ I_S \end{pmatrix} = \frac{A}{l} \begin{pmatrix} \sigma & \sigma \cdot \alpha \\ \sigma \cdot \alpha & \sigma \cdot \alpha^2 + \Lambda_{OC} \end{pmatrix} \cdot \begin{pmatrix} U \\ \Delta T \end{pmatrix} \tag{1}$$

Note, that the here used entropy conductivity Λ_{OC} is a more fundamental parameter to describe the thermal conductivity and is connected

to the traditional heat conductivity λ_{OC} via the absolute temperature T [6]. Based on this, the power factor PF of a thermoelectric material can be determined as a function of the isothermal electrical conductivity σ and the Seebeck coefficient α (Eq. (2)):

$$PF = \sigma \cdot \alpha^2 \tag{2}$$

The figure-of-merit zT (Eq. (3)), which is related to the material's power conversion efficiency, is obtained as a function of the power factor PF and the entropy conductivity Λ_{OC}.

$$zT = \frac{PF}{\Lambda_{OC}} = \frac{PF}{\lambda_{OC}} \cdot T \tag{3}$$

The basic working principle of a thermoelectric generator (TEG) via coupled currents is schematically shown in Fig. 1. Driven by the temperature difference ΔT, entropy flows from the hot side (top) to the cold side (bottom) through the device. In the alternating n- ($\alpha < 0$) and p-type ($\alpha > 0$) materials, a current of charge in the opposite or the same direction is induced, respectively. Consequently, a circular electrical current results in the case of an electrical closed circuit. As a result, a transfer from thermal energy (red arrows in Fig. 1b) to electrical energy (blue arrows in Fig. 1b) within the thermoelectric materials occurs, which can

* Corresponding author.
** Corresponding author.
*** Corresponding author.
E-mail addresses: mario.wolf@pci.uni-hannover.de (M. Wolf), abt@iph-hannover.de (M. Abt), armin.feldhoff@pci.uni-hannover.de (A. Feldhoff).
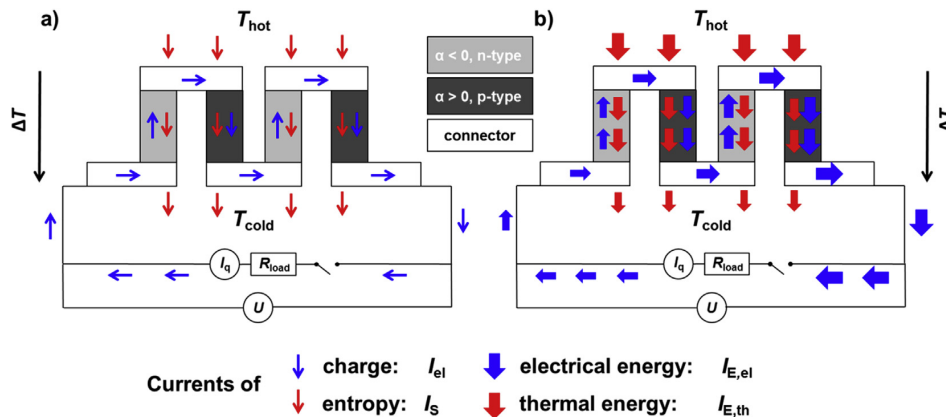
Fig. 1. Working principle schematic of a TEG with two thermocouples of n-type ($\alpha < 0$) and p-type ($\alpha > 0$) materials. a) The currents of charge I_{el} and entropy I_s are coupled in the thermoelectric materials. Entropy enters the device at the hot side (top) and leaves it at the cold side (bottom), as indicated by red arrows. The thermally induced currents of charge in the n-type and p-type materials lead to an external ring circuit, as indicated by blue arrows. Note, that the dissipation of excess entropy has been skipped for clarity. b) Thermal energy, as indicated by red arrows, enters the device at the hot side, and in the thermoelectric materials, it is partly converted into electrical energy. The latter is indicated by blue arrows. Note that the width of the blue arrows indicates that at the electrical input of the device the electrical power is low, whereas at the electrical output, it is high. The difference is the useful electrical power to drive some external load, which is symbolized by an external load resistance. (For interpretation of the references to colour in this figure legend, the reader is referred to the Web version of this article.)

be used in an external load. The electrical power output is determined by the power factor *PF* of the thermoelectric materials and the temperature difference ΔT [7].

Thermoelectric materials are therefore desired to have a high power factor *PF* and a simultaneously low open-circuited entropy conductivity Λ_{OC}. Commercially available TEGs are based on n- and p-type doped Bi_2Te_3, which provides good thermoelectric properties at room temperature [8]. However, Bi_2Te_3 struggles on its poor temperature stability and toxic precursors. Therefore, especially for application at higher temperatures [9], intermetallics such as Zintl phases [10–13] and half-Heusler phases [14–16] as well as oxide-based ceramics [17], such as layered cobaltites [18,19] or oxyselenides [20–22], have been studied extensively in the last decade. Here, the oxide-based materials are characterized by their good temperature stability in air and are less toxic compared to telluride based alternatives [9,23]. Within this group, the layered misfit $Ca_3Co_4O_9$ (CCO) is one of the best known p-type materials [24,25]. To further improve the material properties, many different strategies have been investigated, including doping, nanostructuring, optimization of calcination and sintering and preparation of thin films and hybrid materials [26–28].

In addition to material improvement, research has also focused on the production technology of TEGs [29]. Conventionally, TEGs are processed via manual assembling of thermoelectric materials on rigid substrates such as Al_2O_3. However, this leads to an inflexible design and a rather costly manufacturing with a noteworthy share in the overall price [29, 30]. Consequently, different highly controllable and scalable manufacturing methods are the focus of research [31]. Especially, the concept of flexible thermoelectric devices via printing and additive manufacturing have been investigated recently, including various techniques such as ink jetting [32], dispensing [33,34] and screen printing [35,36]. Here, mostly organic electronics [37,38] or the conventional Bi_2Te_3 [39,40] have been investigated as thermoelectric materials. A desired high-temperature application of TEGs, however, leads to special requirements in the temperature stability and longevity of the used thermoelectric materials as well as the connectors and substrates. The above-mentioned substrate-based scalable production technologies were shown only on glass or polymeric substrates and are mostly based on organic electronics, resulting in a relatively low temperature stability, which limits the application to temperatures below 600 K [41]. For high application temperatures, only free-standing films such as flexible

graphene oxide have been presented [42]. As a result, a universal and scalable preparation technique for TEGs, especially including a flexible substrate, combined with possible application at high temperatures in air is still desired.

In our previous work [43], the processing of ceramic materials such as CCO within a precisely controllable and adaptable process was presented. Here, we extend this process to develop a universal manufacturing route for functional and high-temperature applicable TEGs. To show the functionality of the process, a prototype based on the well-known CCO as thermoelectric materials is prepared. For electrical contact, commercially available Ag paste is used, which is also characterized by a high temperature stability. Spray-coating and laser structuring of the layers on a flexible low-temperature co-fired ceramic (LTCC) substrate are used to design the TEG prototype. The LTCC technology is in the focus of research since it found application in various fields of microelectronic devices and can be easily adapted to the preparation process and the final application [44–46]. It consists of ceramic particles, embedded in a polymeric matrix, thus ensuring the flexibility within the preparation and also allowing a simultaneous sintering process at high temperatures. The universal manufacturing process and adaptable substrates also enable similar processing for different kinds of thermoelectric materials and TEGs Additionally, the design of the TEG can be easily adapted to the desired application field, while the application temperature of the prepared TEG is not restricted by a polymeric substrate.

2. Experimental section

2.1. Generator design

If not mentioned separately, all reagents were obtained from commercial vendors at reagent purity of higher and used without further purification. CCO was purchased at CerPoTech (Tiller, Norway) and used to obtain spray-coating paste by dispersing 30 wt% in isopropyl alcohol via stirring and ultrasonication. As a contact material, a commercial Ag paste (conductive silver varnish spray, purchased at Tifoo) was used, because of the high temperature stability of Ag allowing the post-process sintering at 1033 K. Both pastes were applied on a commercially available two-layer flexible LTCC substrate (951 X, purchased at DuPont) with an effective substrate thickness of 440 μm via spray-coating (Sogolee Airbrush HP-200) of CCO on one side of the substrate and Ag on the other

M. Wolf et al.

Table 1
Details of the spray-coating process step to build CCO and Ag layers on the LTCC substrate and the laser structuring process step for partly ablation.

| Spray-coating Sogolee Airbrush HP-200		Laser structuring Epilog Fusion 32 M2 Dual CO$_2$	
nuzzle diameter	0.2 mm	spot diameter	80 μm
pressure	3.5 bar	max. laser output	40 W
distance to substrate	30 mm	power output used	30–40%
spray-coating angle	30°	number of cycles	1
line distance	25 mm	wave type	continuous wave
number of cycles	5	scan mode	parallel line scan
subsequently dried at	373 K	scan speed	240 mm s^{-1}
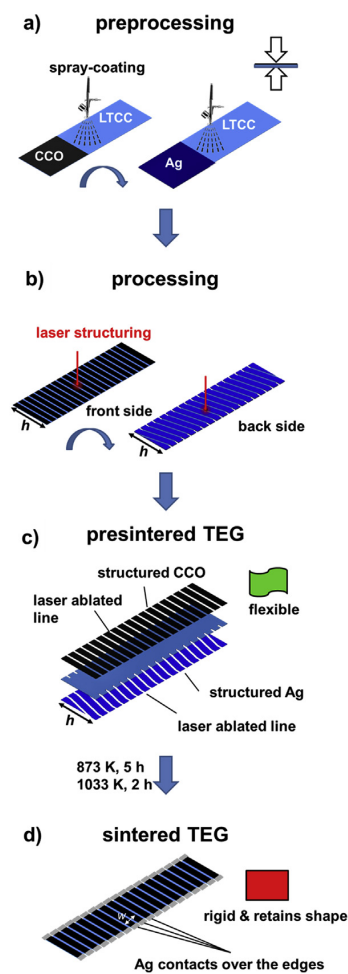
Fig. 2. Schematic manufacturing process of the TEG with CCO and Ag via a) spray-coating (preprocessing) and b) laser structuring (processing) on top of a flexible LTCC substrate. In the postprocessing step (c,d), the flexible and structured substrate is sintered to obtain a robust body. For details of the respective process parameters compare Table 1.

side. Details of the spray-coating step are shown in Table 1. The coated substrate was dried at 373 K on a heating plate after each step. A CO$_2$ laser (Epilog Fusion 32 M2 Dual) was used for subsequent laser structuring of both sides, details for the laser structuring are also shown in Table 1.

Subsequently, the still flexible substrate with CCO and Ag structures on the front and back side, respectively, was sintered at 873 K for 5 h and

1033 K for 2 h under air with a heating and cooling rate of 3 K min^{-1}. The maximum sintering temperature of 1033 K was chosen as a result of the commercial sintering temperature of the LTCC (1033 K) and the temperature stability of CCO, which starts to decompose above 1073 K. Finally, the CCO and Ag layers were contacted via Ag paste and again dried at 973 K for 5 h with a heating and cooling rate of 3 K min^{-1}. The developed preparation process is also shown in Fig. 2.

2.2. Microstructural characterization

Spray-coated structures and the LTCC substrate were characterized by X-ray diffraction (XRD, Bruker D8 Advance with Cu-K$_\alpha$ radiation). Microstructural characterization was performed with a field-emission scanning electron microscope (FE-SEM, JEOL JSM-6700F) and a field-emission transmission electron microscope (FE-TEM, JEOL JEM-2100F-UHR) both equipped with an energy-dispersive X-ray spectrometer (EDXS, Oxford Instruments INCA) for elemental analysis. The TEM was also equipped with a spectrometer for electron energy-loss spectroscopy (EELS, Gatan Imaging Filter GIF 2001). EELS measurements of the sample were carried out in scanning transmission electron microscope (STEM) mode at 0.5 eV/channel or 0.1 eV/channel with the electrostatic drift tube calibrated to the first maximum of the Ni-L$_3$ edge of an NiO standard (853 eV [47]). The background was subtracted with a power-law model. TEM specimen was prepared by cutting (Diamond wire saw, O'Well model 3242), infiltration with epoxy resin, grinding and polishing from both sides on polymer embedded diamond lapping films (Allied High Tech, Multiprep) down to 10 μm thickness. Subsequent Ar ion polishing (Gatan model 691 PIPS, precision ion polishing system) yielded electron transparent regions. However, for SEM analysis, fractured samples were used to prevent the porous layer to be infiltrated by epoxy resin, which would change the sample structure at the top of the porous layer.

2.3. Thermoelectric characterization

The Seebeck coefficient α and generator power output were measured as a function of the temperature with a ProboStat A setup from NorECs with ELITE thermal system and KEITHLEY 2100 Digit Multimeters. The isothermal electrical conductivity σ was measured with a home-made modified measurement cell based on the description of Indris [48] with a horizontal Carbolite tube furnace and KEITHLEY 2100 Digit Multimeters. The power factor *PF* of CCO and Ag was calculated according to Eq. (2). The power output of the generator was measured near room temperature (T_{hot} = 373 K and T_{hot} = 423 K) and at higher temperatures (T_{hot} = 573 K and T_{hot} = 673 K). For the U-I_{el} and power output curves, linear fits and second-degree polynominal fits were used, respectively. The maximum electrical power output of the TEG $P_{el,max,TEG}$ was calculated via Eq. (4) with the open-circuited voltage U_{OC} and the internal generator resistance R_{TEG} [7,38].

$$P_{el,max,TEG} = \frac{U_{OC}^2}{4 \cdot R_{TEG}} \qquad (4)$$

3. Results and discussion

The schematic manufacturing process for a TEG based on CCO and Ag via spray-coating and laser structuring is shown in Fig. 2. First, the prepared CCO paste and the Ag paste are spray-coated on the front and back side of the flexible LTCC substrate, respectively. Compared to other processing technologies such as screen printing, no additives within the pastes, which may influence the resulting properties such as electrical conductivity [49], are used and the layer thickness can be precisely controlled (compare [43]). Furthermore this can be easily transferred to other particle systems and non-planar substrates or surfaces. After a drying step, laser structuring is utilized to give a defined structure of both sides as well as make cuts for later contact. Here, the CCO is ablated from the substrates in the respective lines, resulting in a thermoleg structure.
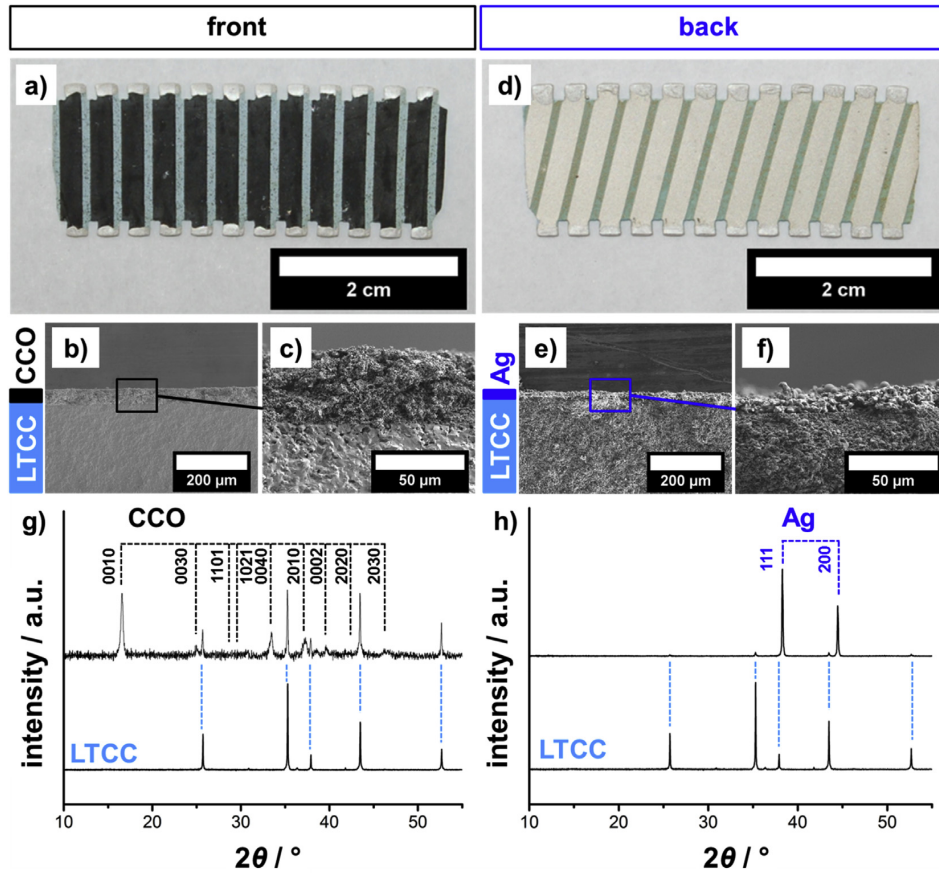
3

Fig. 3. Photos and SEM cross-section micrographs of the processed TEG: a,b,c) front side with CCO and d,e,f) back side with Ag. The corresponding XRD patterns confirm the presence of g) CCO and h) Ag on top of the sintered LTCC substrate. In the XRD patterns, reflections of the blank sintered LTCC substrate are given to indicate reflections from the substrate in coated specimens.

This ablation of the CCO can be done with a rather low laser power, minimizing the risk of graphit formation out of the polymeric matrix of the substrate. Accordingly, no short circuit between the resulting layers could be detected. Utilization of laser structuring enables highly controllable processing, making it possible to obtain many different structures and shapes. Additionally, compared to the established screen printing, the laser structuring does not require printing masks and is capable to reach much finer structures and therefore show a higher optimization potential. With this two-step combination of additive and subtractive processing, easy and fast preparation and structuring of large areas is enabled and the layer formation and structuring are decoupled and can be individually controlled and adapted. This is beneficial for research as well as commercial TEG manufacturing, especially due to the absence of additives and the precise control of the resulting structures. It results in a flexibility to adjust the design for a certain form or application. Subsequently, the flexible substrate and both layers are sintered at
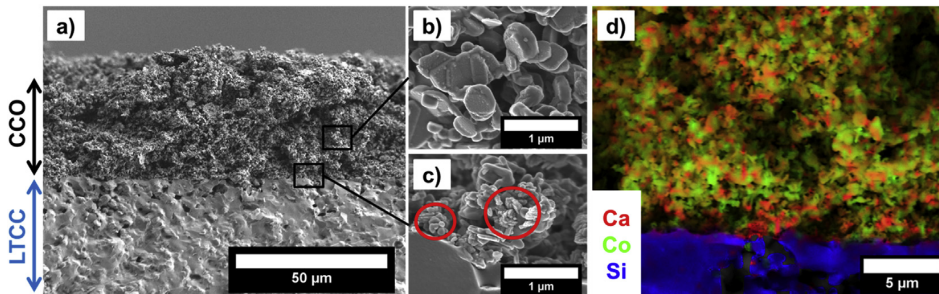

Figure 4. a-c) Cross-sectional SEM micrographs and d) EDXS elemental distribution (red: Ca, green: Co, blue: Si) of the fractured CCO-coated front side. The CCO layer shows typical platelet-like CCO crystals. EDXS elemental distribution shows the Al- and Si-based LTCC substrate and the Ca- and Co-rich phases on top. High-resolution images of the interface between the CCO layer and the LTCC substrate show smaller particles (red entangled areas in c)) attributed to the decomposition of CCO at the interface.
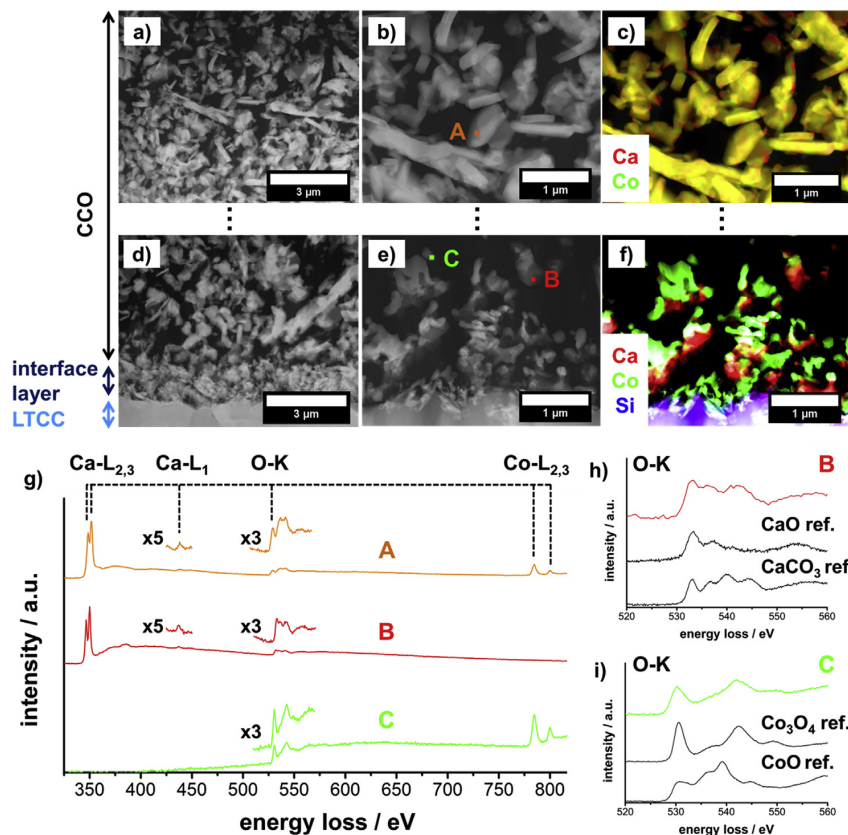
4

Fig. 5. Cross-sectional STEM micrographs and EDXS elemental distribution (red: Ca, green: Co, blue: Si) of the CCO coated front side a-c) in the CCO layer approximately 10 μm from the top of the substrate and d-f) at the interface of the CCO layer and the LTCC substrate. In the first 2 μm of the layer, an interface can be seen, where CCO has decomposed into Ca-rich and Co-rich phases. EELS measurements in g) of the spots marked in b) and e) proves this decomposition in the interface layer, while showing CCO above. The energy-loss near-edge structures (ELNESs) of the O–K edge in h) and i) show CaO and Ca_3O_4 as products of decomposition at the interface with the LTCC substrate. (For interpretation of the references to colour in this figure legend, the reader is referred to the Web version of this article.)

1033 K in one post-processing step resulting in a rigid TEG.

The front and back side are electrically contacted with Ag ink using the edges prepared via laser cutting. Generally, the presented process may also be adapted to various kinds of thermoelectric materials.

Micrographs of the front and back side of the resulting sintered TEG are shown in Fig. 3a and d. For this prototype, CCO structures with a width of 2 mm and a length of 20 mm have been prepared within the laser structuring process. This CCO layers on the front side are contacted via silver ink with the Ag structures on the back side. The contact can be done manually or by dipping the edges into silver ink. In the laser ablated lines, the CCO and Ag have been removed, respectively. SEM micrographs in Fig. 3b and c and Fig. 3e and f shows the corresponding layers on top of the ceramic-based LTCC substrate. The CCO layer has a layer thickness of approximately 36 μm, which can be controlled within the process via the amount of spray-coating cycles [43]. Control of the resulting layer thickness of the ceramic layer is an important parameter to adjust and improve the resulting thermoelectric properties. For this prototype, processing via 5 cycles of spray-coating, resulting in a layer thickness of approximately 36 μm, showed the best results [43]. The sintered Ag layer on the back side of the substrate exhibits a thickness of approximately 7–8 μm. XRD patterns in Fig. 3g and h confirm the presence of the CCO layer on the front side and the Ag layer on the back side of the sintered ceramic substrate, respectively.

Coatings and interfaces on both sides of the LTCC substrate were investigated in detail by SEM and EDXS elemental analysis. Fig. 4 shows the microstructural characterization of the CCO layer and its interface with the ceramic substrate. The sintered substrate mostly contains ceramic Al- and Si-based phases. Within the porous CCO layer with a thickness of approximately 36 μm, typical platelet-like CCO particles are present with diameters varying from 500 nm up to a few μm. However, at the interface of the LTCC substrate and the CCO layer, some smaller particles can be found, thus leading to the assumption of interface reactions occurring between the CCO and substrate during sintering.

Therefore, the CCO layer and especially the interface of the CCO layer and the LTCC substrate were investigated by TEM micrographs and EELS measurements, as shown in Fig. 5. Between the ceramic substrate and the CCO layer, the TEM micrographs reveal an interface layer with a thickness of approximately 2 μm. Within this interface layer, some particles smaller than the typical platelet-like CCO particles can be observed. The EDXS elemental maps (Fig. 5c and f) show that within this interface layer decomposition occurred, resulting in Ca-rich and Co-rich particles next to each other. Above this interface layer, the typical platelet-like CCO particles can be identified, and the EDXS elemental distribution also exhibits only particles containing both Ca and Co.

To further analyze the decomposition within this interface layer and to prove the identity of CCO above this layer, EELS spectra of the Ca-rich and Co-rich phases as well as of the CCO particles above were taken (Fig. 5g). While in the EELS spectra of the CCO particles, the Ca-$L_{2,3}$, O–K as well as the Co-$L_{2,3}$ edge can be observed, the particles in the interface layer exhibit only the Ca-$L_{2,3}$ or the Co-$L_{2,3}$ edge together with the O–K edge. Fine-structure measurements of the O–K edges and comparison with reference materials (Fig. 5h and i) were used to identify Co_3O_4 and CaO as products of decomposition. This corresponds to the typical decomposition products of CCO [50]. Before sintering, the LTCC substrate contains ceramic particles embedded in a polymeric matrix, while in the sintering process, the polymer is burnt out, and the ceramic particles are sintered to a rigid substrate. Here, the burn of the polymer is assumed to lead to a reduced partial oxygen pressure at the interface,
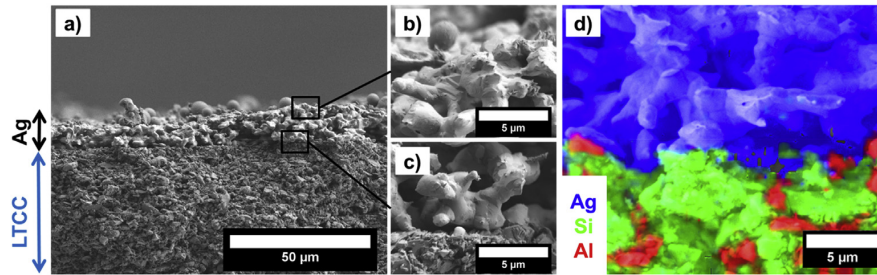
Figure 6. a-c) Cross-sectional SEM micrographs and d) EDXS elemental distribution (red: Al, green: Si, blue: Ag) of the fractured Ag-coated back side. The EDXS elemental distribution shows the Al- and Si-based LTCC substrate and the Ag layer on top.
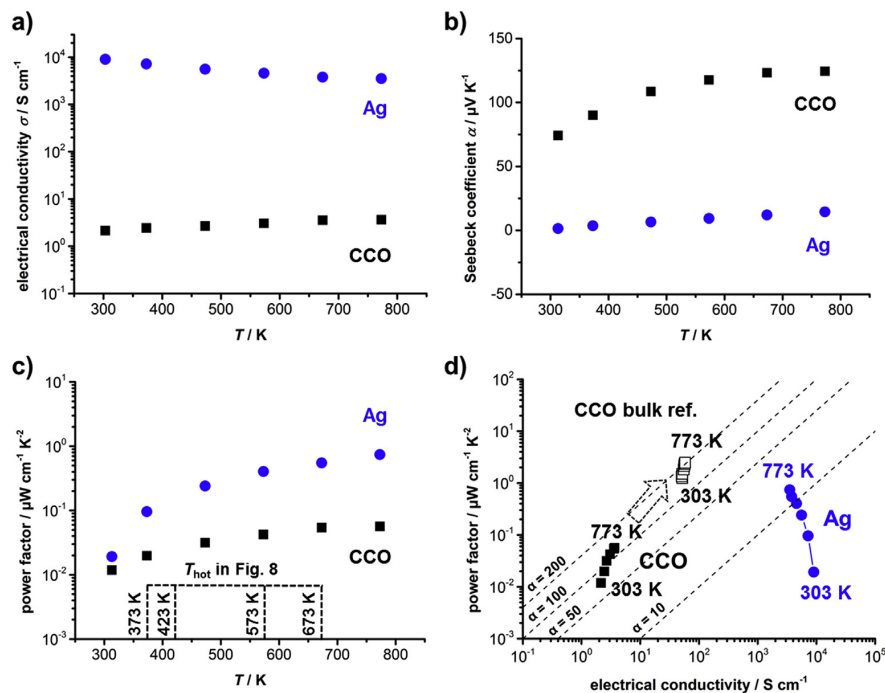

Fig. 7. Measured values of the a) electrical conductivity σ, b) Seebeck coefficient α and c) resulting power factor and d) power factor as a function of electrical conductivity (Ioffe plot) of the Ag and CCO layers. The CCO bulk reference (open symbols) [24] in d) shows an example of an achievable power factor by optimizing the CCO processing. Dashed lines in d) show the Seebeck coefficient α in $\mu V\ K^{-1}$.

resulting in the decomposition of the oxygen-rich CCO near the substrate and therefore the formation of cobalt oxide and calcium oxide. However, above this interface layer with a thickness of about 2 μm and therefore as main part of the layer, no decomposition of CCO has occurred, resulting in a functional thermoelectric layer.

The Ag layer on the back side was also investigated via SEM micrographs and EDXS elemental distribution (Fig. 6). The observed Ag layer exhibits a layer thickness of approximately 7–8 μm with a high porosity, analogous to the CCO layer. Here, no additional phases at the interface of the LTCC substrate and the Ag layer were found. The EDXS elemental distribution shows the Si- and Al-rich LTCC substrate and the overlying pure Ag phase with a sharp distinction.

The thermoelectric properties of both the CCO and the Ag layer are shown in Fig. 7. For the CCO, processing via 5 cycles of spray-coating were chosen, based on the analysis in the previous work [43]. The sintered Ag exhibits a high electrical conductivity of approximately 7000 S cm^{-1} at 373 K and 3000 S cm^{-1} at 773 K and a typical Seebeck coefficient of approximately 3–5 $\mu V\ K^{-1}$. However, the CCO exhibits a rather low

electrical conductivity of approximately 2–3 S cm^{-1} which corresponds to approximately 2.5–5% of the undoped bulk material [24,51,52] and annealed undoped films [53,54]. This is mainly attributed to the high porosity of the CCO layer, which results due to the fact of a missing high pressure densification within the process. Due to the utilization of the flexible LTCC substrate, only a relatively low pressure densification with $4.2 \cdot 10^6$ Pa could be applied.

The measured Seebeck coefficient α of the CCO layer up to 125 $\mu V\ K^{-1}$ at 773 K shows p-type conduction and is comparable to reported undoped thin film CCO [53,54] prepared via chemical solution deposition and is therefore in good agreement with literature data as well as our previous results [43]. However, it is lower than that of undoped bulk CCO [24,51,52] and that of thin film CCO prepared via pulsed-laser deposition [28,55]. The resulting values of the power factor of both layers are as high as 0.06 $\mu V\ cm^{-1}\ K^{-2}$ and as high as 0.75 $\mu W\ cm^{-1}\ K^{-2}$ for the CCO and Ag layers at 773 K, respectively. To allow an easy comparison of measured data with literature, Fig. 7d summarizes the measured thermoelectric properties of both layers in an Ioffe plot,
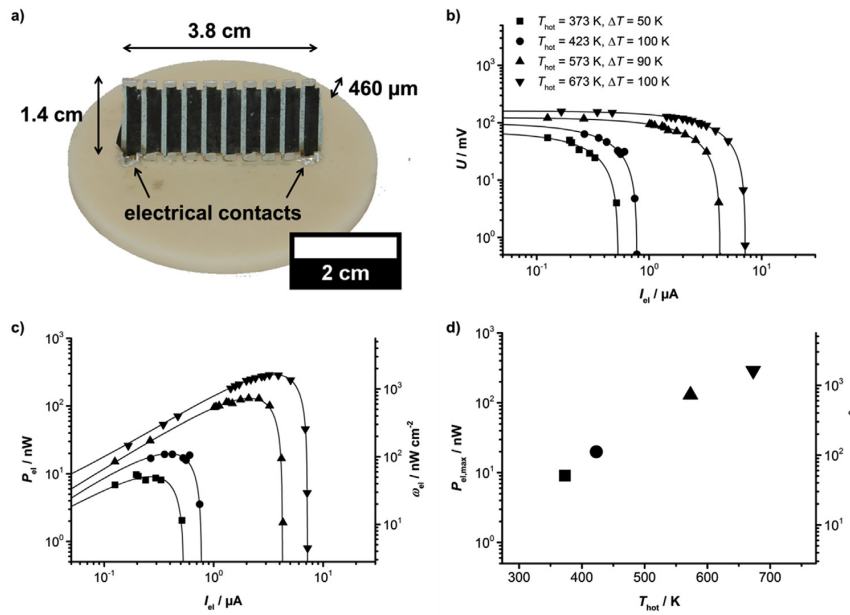
Fig. 8. a) Photograph of the prototype TEG (10 CCO and 9 Ag layers) with a length of 3.8 cm and a thickness of 460 μm. Note that the temperature gradient is applied from the top to the bottom, resulting in an effective area of 0.175 cm^2. b) Voltage and c) electrical power output P_{el} and electrical power density ω_{el} as a function of the electrical current I_{el} measured at $T_{hot} = 373$ K and $\Delta T \approx 50$ K, $T_{hot} = 423$ K and $\Delta T \approx 100$ K, $T_{hot} = 573$ K and $\Delta T \approx 90$ K and $T_{hot} = 673$ K and $\Delta T \approx 100$ K. Data in d) show the correspodning $P_{el,max}$ and $\omega_{el,max}$ as a function of T_{hot}.

Table 2

Measure values of the open-circuited voltage U_{OC} and short-circuited electrical current $I_{el,SC}$ and via Eq. (4) calculated maximum electrical power output $P_{el,max}$ of the TEG at different applied T_{hot}. The electrical power density $\omega_{el,max}$ was obtained by normalizing the maximum electrical power output $P_{el,max}$ with the geometry shown in Fig. 8a.

T_{hot}/K	ΔT/K	U_{OC}/mV	$I_{el,SC}$/mA	$P_{el,max}$/nW	$\omega_{el,max}$/nW cm^{-2}
373	50	70.5	$5.28 \cdot 10^{-4}$	9.31	53.18
423	100	99.7	$7.82 \cdot 10^{-4}$	19.49	111.38
573	90	122.96	$4.14 \cdot 10^{-3}$	127.26	727.20
673	100	161.16	$7.18 \cdot 10^{-3}$	289.28	1653.03

showing the power factor as a function of the electrical conductivity. Displayed reference data for undoped bulk CCO [24] show the potential of optimizing the CCO processing, especially by gaining higher densification and therefore less porosity of the CCO layer to obtain a higher power factor. For this, the process may be transferred to other kinds of thermoelectric materials or performed on alternative substrates, where a high pressure densification step can be done or is not even needed. Note also, that for this prototype, undoped CCO has been used, to prove the functionality of the system. As a result, the thermoelectric properties could also be enhanced by using doped CCO or hybrid materials e.g. Ag-added CCO.

In Fig. 8, the voltage-electrical current curves and the resulting electrical power output of the prepared prototype TEG at different T_{hot} values are given. At relatively low temperatures, the device reaches $P_{el,max} = 10$ and 20 nW at a ΔT of approximately 50 K and 100 K, respectively. With the geometry of 0.175 cm^2, shown in Fig. 8a, this corresponds to an electrical power density $\omega_{el,max}$ of 50–115 nW cm^{-2}. Both the electrical conductivity σ and the Seebeck coefficient α of both sides increase with increasing temperature, resulting in an analogous increase in the electrical power output of the generator. At $T_{hot} = 673$ K and $\Delta T = 100$ K, the processed TEG reaches an electrical power output of $P_{el,max} = 289$ nW and a corresponding electrical power density of $\omega_{el,max}$ of 1.65 μW cm^{-2}.

Table 2 summarizes the measured thermoelectric parameters at different applied temperature conditions. With an electrical power density of 1.65 μW cm^{-2} with 10 CCO and 9 Ag layers, this prototype provide

similar electrical power density compared to printed devices based on thermoelectric polymers, which are usually in the range of approximately 500 nm [56,57] up to several μW with a high amount of thermocouples [58]. However, Bi$_2$Te$_3$-based printed devices have been reported to reach higher electrical power densities, e.g. by Chen et al. [59] up to 75 μW cm^{-2} at a ΔT of 20 K or by Kim et al. [60] reaching 3.8 mW cm^{-2} at a ΔT of 50 K. Compared to this, our prototype provides a rather low electrical power density, which is attributed to the low electrical conductivity of the CCO layer, resulting in a high electrical resistivity of the generator R_{TEG}. Further adjustment of the presented process, especially the sintering of the layers and of course the adaptation to other thermoelectric materials, may strongly increase the electrical power output of the processed generator, making the presented manufacturing process a promising way to prepare and adapt TEGs for a desired application.

4. Conclusions

An adaptable process for TEG manufacturing has been presented on the example of a prototype based on CCO and Ag on a ceramic-based LTCC substrate. The structure and shape of the thermoelectric layers and the resulting TEG are given by the utilization of spray-coating and laser structuring, while no printing masks or additives are required. The prepared prototype consists of porous layers of CCO and Ag and is applicable at higher temperature compared to polymer-based manufactured TEGs. An electrical power density of up to 1.65 μW cm^{-2} at 673 K and a ΔT of 100 K could be achieved, mainly limited by the high porosity of the ceramic CCO layer reaching a low electrical conductivity of only approximately 5% of the bulk material. However, a high potential to optimize the thermoelectric properties and electrical power output is given by adjusting the process to tailor the densification and sintering of the layers and further adjustment of the thermoelectric materials. The presented process may also be adapted to different kinds of thermoelectric materials and TEG design for various applications.

Declaration of competing interest

The authors declare that they have no known competing financial interests or personal relationships that could have appeared to influence

the work reported in this paper.

Acknowledgment

References

[1] G.J. Snyder, E.S. Toberer, Complex thermoelectric materials, Nat. Mater. 7 (2008) 105–114, https://doi.org/10.1038/nmat2090.

[2] J. He, T.M. Tritt, Advances in thermoelectric materials research: Looking back and Moving Forward, Science 80 (2017) 357, https://doi.org/10.1126/SCIENCE.AAK9997, eaak9997.

[3] R.A. Kishore, A. Marin, C. Wu, A. Kumar, S. Priya, Energy Harvesting - Materials, Physics, and System Design with Practical Examples, DEStech Publications, 2019.

[4] H.U. Fuchs, The Dynamics of Heat - A Unified Approach to Thermodynamics and Heat Transfer, 2nd ed., Springer-Verlag, New York, 2010 https://doi.org/10.1007/978-1-4419-7604-8.

[5] A. Feldhoff, Thermoelectric material tensor Derived from the Onsager–de Groot–Callen model, Energy Harvest. Syst. 2 (2015) 5–13, https://doi.org/10.1515/ehs-2014-0040.

[6] M. Wolf, K. Menekse, A. Mundstock, R. Hinterding, F. Nietschke, O. Oeckler, A. Feldhoff, Low thermal conductivity in thermoelectric oxide-based Multiphase Composites, J. Electron. Mater. 48 (2019) 7551–7561, https://doi.org/10.1007/s11664-019-07555-2.

[7] M. Bittner, N. Kanas, R. Hinterding, F. Steinbach, J. Räthel, M. Schrade, K. Wiik, M. Einarsrud, A. Feldhoff, A Comprehensive Study on improved power materials for high-temperature thermoelectric generators, J. Power Sources 410–411 (2019) 143–151, https://doi.org/10.1016/j.jpowsour.2018.10.076.

[8] H. Mamur, M.R.A. Bhuiyan, F. Korkmaz, M. Nil, A Review on Bismuth telluride (Bi₂Te₃) nanostructure for thermoelectric applications, Renew. Sustain. Energy Rev. 82 (2018) 4159–4169, https://doi.org/10.1016/j.rser.2017.10.112.

[9] M. Wolf, R. Hinterding, A. Feldhoff, High power factor vs . High zT — a Review of thermoelectric materials for high-temperature application, Entropy 21 (2019) 1058, https://doi.org/10.3390/e21111058.

[10] J. Shuai, J. Mao, S. Song, Q. Zhang, G. Chen, Z. Ren, Recent Progress and Future Challenges on thermoelectric Zintl materials, Mater. Today Phys. 1 (2017) 74–95, https://doi.org/10.1016/j.mtphys.2017.06.003.

[11] J.H. Grebenkemper, S. Klemenz, B. Albert, S.K. Bux, S.M. Kauzlarich, Effects of Sc and Y Substitution on the structure and thermoelectric properties of Yb₁₄MnSb₁₁, J. Solid State Chem. 242 (2016) 55–61, https://doi.org/10.1016/j.jssc.2016.03.015.

[12] P. Gorai, B.R. Ortiz, E.S. Toberer, V. Stevanović, Investigation of n-type doping strategies for Mg₃Sb₂, J. Mater. Chem. A. 6 (2018) 13806–13815, https://doi.org/10.1039/C8TA03344G.

[13] X. Chen, H. Wu, J. Cui, Y. Xiao, Y. Zhang, J. He, Y. Chen, J. Cao, W. Cai, S.J. Pennycook, Z. Liu, L.D. Zhao, J. Sui, Extraordinary thermoelectric performance in n-type Manganese doped Mg₃Sb₂ Zintl: high Band Degeneracy, Tuned carrier Scattering Mechanism and Hierarchical microstructure, Nano Energy 52 (2018) 246–255, https://doi.org/10.1016/j.nanoen.2018.07.059.

[14] L. Chen, S. Gao, X. Zeng, A. Mehdizadeh Dehkordi, T.M. Tritt, S.J. Poon, Uncovering high thermoelectric figure of merit in (Hf,Zr)NiSn half-Heusler Alloys, Appl. Phys. Lett. 107 (2015), https://doi.org/10.1063/1.4927661.

[15] C. Fu, T. Zhu, Y. Liu, H. Xie, X. Zhao, Band Engineering of high performance p-type FeNbSb based half-Heusler thermoelectric materials for figure of merit zT > 1, Energy Environ. Sci. 8 (2015) 216–220, https://doi.org/10.1039/c4ee03042g.

[16] H. Zhu, R. He, J. Mao, Q. Zhu, C. Li, J. Sun, W. Ren, Y. Wang, Z. Liu, Z. Tang, A. Sotnikov, Z. Wang, D. Broido, D.J. Singh, G. Chen, K. Nielsch, Z. Ren, Discovery of ZrCoBi based half Heuslers with high thermoelectric conversion efficiency, Nat. Commun. 9 (2018) 1–9, https://doi.org/10.1038/s41467-018-04958-3.

[17] Y. Yin, B. Tudu, A. Tiwari, Recent Advances in oxide thermoelectric materials and Modules, Vacuum 146 (2017) 356–374, https://doi.org/10.1016/j.vacuum.2017.04.015.

[18] J.W. Fergus, Oxide materials for high temperature thermoelectric energy conversion, J. Eur. Ceram. Soc. 32 (2012) 525–540, https://doi.org/10.1016/j.jeurceramsoc.2011.10.007.

[19] M. Ohtaki, Recent Aspects of oxide thermoelectric materials for power generation from Mid-to-high temperature heat Source, J. Ceram. Soc. Japan. 119 (2011) 770–775, https://doi.org/10.2109/jcersj2.119.770.

[20] X. Zhang, C. Chang, Y. Zhou, L.D. Zhao, BiCuSeO thermoelectrics: an Update on recent Progress and Perspective, Materials 10 (2017) 1–16, https://doi.org/10.3390/ma10020198.

[21] Y. Liu, L.D. Zhao, Y. Zhu, Y. Liu, F. Li, M. Yu, D.B. Liu, W. Xu, Y.H. Lin, C.W. Nan, Synergistically optimizing electrical and thermal Transport properties of BiCuSeO via a Dual-doping Approach, Adv. Energy Mater. 6 (2016) 1–9, https://doi.org/10.1002/aenm.201502423.

[22] X. Zhang, D. Feng, J. He, L.D. Zhao, Attempting to Realize n-type BiCuSeO, J. Solid State Chem. 258 (2018) 510–516, https://doi.org/10.1016/j.jssc.2017.11.012.

[23] S. Bresch, B. Mieller, D. Schoenauer-Kamin, R. Moos, F. Giovanelli, T. Rabe, Influence of pressure Assisted sintering and reaction sintering on microstructure

[24] and thermoelectric properties of bi-doped and undoped calcium cobaltite, J. Appl. Phys. 126 (2019), https://doi.org/10.1063/1.5107476, 0–11.

[24] M. Bittner, L. Helmich, F. Nietschke, B. Geppert, O. Oeckler, A. Feldhoff, Porous Ca₃Co₄O₉ with enhanced thermoelectric properties Derived from Sol–Gel Synthesis, J. Eur. Ceram. Soc. 37 (2017) 3909–3915, https://doi.org/10.1016/j.jeurceramsoc.2017.04.059.

[25] S. Saini, H.S. Yaddanapudi, K. Tian, Y. Yin, D. Magginetti, A. Tiwari, Terbium ion doping in Ca₃Co₄O₉: a step towards high-Performance thermoelectric materials, Sci. Rep. 7 (2017) 1–9, https://doi.org/10.1038/srep44621.

[26] C. Gayner, K.K. Kar, Recent Advances in thermoelectric materials, Prog. Mater. Sci. 83 (2016) 330–382, https://doi.org/10.1016/j.pmatsci.2016.07.002.

[27] S. Bresch, B. Mieller, C. Selleng, T. Stöcker, R. Moos, T. Rabe, Influence of the calcination Procedure on the thermoelectric properties of calcium cobaltite Ca₃Co₄O₉, J. Electroceramics. 40 (2018) 225–234, https://doi.org/10.1007/s10832-018-0124-3.

[28] V. Rogé, F. Delorme, A. Stolz, A. Talbi, N. Semmar, J. Perrière, F. Giovannelli, E. Millon, Effect of post-deposition thermal Treatment on thermoelectric properties of pulsed-laser deposited Ca₃Co₄O₉ thin films, Mater. Chem. Phys. 221 (2019) 361–366, https://doi.org/10.1016/j.matchemphys.2018.09.069.

[29] R. He, G. Schierning, K. Nielsch, Thermoelectric devices: a Review of devices, Architectures, and contact optimization, Adv. Mater. Technol. 3 (2018), https://doi.org/10.1002/admt.201700256.

[30] S. Leblanc, S.K. Yee, M.L. Scullin, C. Dames, K.E. Goodson, Material and manufacturing Cost Considerations for thermoelectrics, Renew. Sustain. Energy Rev. 32 (2014) 313–327, https://doi.org/10.1016/j.rser.2013.12.030.

[31] M. Orrill, S. LeBlanc, Printed thermoelectric materials and devices: Fabrication techniques, Advantages and Challenges, J. Appl. Polym. Sci. 134 (2017) 44256, https://doi.org/10.1002/app.44256.

[32] C. Ou, A.L. Sangle, T. Chalklen, Q. Jing, V. Narayan, S. Kar-Narayan, Enhanced thermoelectric properties of flexible Aerosol-Jet printed Carbon Nanotube-based Nanocomposites, Apl. Mater. 6 (2018), 096101, https://doi.org/10.1063/1.5043547.

[33] D. Madan, A. Chen, P.K. Wright, J.W. Evans, Dispenser printed Composite thermoelectric Thick films for thermoelectric generator applications, J. Appl. Phys. 109 (2011), 034904, https://doi.org/10.1063/1.3544501.

[34] D. Madan, A. Chen, P.K. Wright, J.W. Evans, Printed Se-doped MA n-type Bi₂Te₃ Thick-film thermoelectric generators, J. Electron. Mater. 41 (2012) 1481–1486, https://doi.org/10.1007/s11664-011-1885-5.

[35] Z. Cao, E. Koukharenko, M.J. Tudor, R.N. Torah, S.P. Beeby, Flexible screen printed thermoelectric generator with enhanced Processes and materials, Sensors Actuators, A Phys. 238 (2016) 196–206, https://doi.org/10.1016/j.sna.2015.12.016.

[36] S.J. Kim, H. Choi, Y. Kim, J.H. We, J.S. Shin, H.E. Lee, M.W. Oh, K.J. Lee, B.J. Cho, Post Ionized Defect Engineering of the screen-printed Bi₂Te₂.₇Se₀.₃ Thick film for high performance flexible thermoelectric generator, Nano Energy 31 (2017) 258–263, https://doi.org/10.1016/j.nanoen.2016.11.034.

[37] Y. Chen, Y. Zhao, Z. Liang, Solution processed organic thermoelectrics: towards flexible thermoelectric Modules, Energy Environ. Sci. 8 (2015) 401–422, https://doi.org/10.1039/c4ee03297g.

[38] R. Kroon, D.A. Mengistie, D. Kiefer, J. Hynynen, J.D. Ryan, L. Yu, C. Müller, Thermoelectric Plastics: from design to Synthesis, processing and structure-Property relationships, Chem. Soc. Rev. 45 (2016) 6147–6164, https://doi.org/10.1039/c6cs00149a.

[39] Z. Cao, M.J. Tudor, R.N. Torah, S.P. Beeby, Screen printable flexible BiTe-SbTe-based Composite thermoelectric materials on Textiles for Wearable applications, IEEE Trans. Electron Devices 63 (2016) 4024–4030, https://doi.org/10.1109/TED.2016.2603071.

[40] T. Zhang, K. Li, C. Li, S. Ma, H.H. Hng, L. Wei, Mechanically durable and flexible thermoelectric films from PEDOT:PSS/PVA/Bi₀.₅Sb₁.₅Te₃ Nanocomposites, Adv. Electron. Mater. 3 (2017) 1–9, https://doi.org/10.1002/aelm.201600554.

[41] X. Liu, Z. Wang, Printable thermoelectric materials and applications, Front. Mater. 6 (2019) 1–5, https://doi.org/10.3389/fmats.2019.00088.

[42] T. Li, A.D. Pickel, Y. Yao, Y. Chen, Y. Zeng, S.D. Lacey, Y. Li, Y. Wang, J. Dai, Y. Wang, B. Yang, M.S. Fuhrer, A. Marconnet, C. Dames, D.H. Drew, L. Hu, Thermoelectric properties and performance of flexible reduced graphene oxide films up to 3,000 K, Nat. Energy. 3 (2018) 148–156, https://doi.org/10.1038/s41560-018-0086-3.

[43] M. Abt, M. Wolf, A. Feldhoff, L. Overmeyer, Combined spray-coating and laser structuring of thermoelectric ceramics, J. Mater. Process. Technol. 275 (2020) 116319, https://doi.org/10.1016/j.jmatprotec.2019.116319.

[44] M.T. Sebastian, R. Ubic, H. Jantunen, Low-loss Dielectric ceramic materials and their properties, Int. Mater. Rev. 60 (2015) 392–412, https://doi.org/10.1179/1743280415Y.0000000007.

[45] J.M. Dominik Jurków, Thomas Maeder, Arkadiusz Dąbrowski, Marina Santo Zarnik, Darko Belavič, Heike Bartsch, Overview on low temperature co-fired ceramic sensors, Sensors Actuators, A Phys. 233 (2015) 125–146, https://doi.org/10.1016/j.sna.2015.05.023.

[46] Z. Sun, W. Li, Y. Liu, H. Zhang, D. Zhu, H. Sun, C. Hu, S. Chen, Design and preparation of a Novel Degradable low-temperature co-fired ceramic (LTCC) Composites, Ceram. Int. 45 (2019) 7001, https://doi.org/10.1016/j.ceramint.2018.12.201, 7010.

[47] P.L. Potapov, D. Schryvers, Measuring the absolute Position of EELS Ionisation edges in a TEM, Ultramicroscopy 99 (2004) 73–85, https://doi.org/10.1016/S0304-3991(03)00185-2.

[48] S. Indris, Perkolation von Grenzflächen in nanokristallinen keramischen Kompositen, 1st ed., Cuvillier Verlag, Göttingen, 2001.

[49] X. Huang, T. Leng, X. Zhang, J.C. Chen, K.H. Chang, A.K. Geim, K.S. Novoselov, Z. Hu, Binder-free highly conductive graphene Laminate for low Cost printed Radio Frequency applications, Appl. Phys. Lett. 106 (2015) 203105, https://doi.org/10.1063/1.4919935.

[50] M. Sopicka-Lizer, P. Smaczyński, K. Kozłowska, E. Bobrowska-Grzesik, J. Plewa, H. Altenburg, Preparation and characterization of calcium cobaltite for thermoelectric application, J. Eur. Ceram. Soc. 25 (2005) 1997–2001, https://doi.org/10.1016/j.jeurceramsoc.2005.03.222.

[51] M.E. Song, H. Lee, M.G. Kang, W. Li, D. Maurya, B. Poudel, J. Wang, M.A. Meeker, G.A. Khodaparast, S.T. Huxtable, S. Priya, Nanoscale Texturing and interfaces in Compositionally modified $Ca_3Co_4O_9$ with enhanced thermoelectric performance, ACS Omega 3 (2018) 10798–10810, https://doi.org/10.1021/acsomega.8b01552.

[52] S. Porokhin, L. Shvanskaya, V. Khovaylo, A. Vasiliev, Effect of NaF doping on the thermoelectric properties of $Ca_3Co_4O_9$, J. Alloys Compd. 695 (2017) 2844–2849, https://doi.org/10.1016/j.jallcom.2016.11.405.

[53] R. Wei, H. Jian, X. Tang, J. Yang, L. Hu, L. Chen, J. Dai, X. Zhu, Y. Sun, Enhanced thermoelectric properties in Cu-doped c-Axis-Oriented $Ca_3Co_4O_{9+\delta}$ thin films, J. Am. Ceram. Soc. 96 (2013) 2396–2401, https://doi.org/10.1111/jace.12415.

[54] J. Buršík, M. Soroka, K. Knížek, J. Hirschner, P. Levinský, J. Hejtmánek, Oriented thin films of $Na_{0.6}CoO_2$ and $Ca_3Co_4O_9$ deposited by Spin-coating method on Polycrystalline substrate, Thin Solid Films 603 (2016) 400–403, https://doi.org/10.1016/j.tsf.2016.02.056.

[55] B. Paul, J. Lu, P. Eklund, Nanostructural tailoring to Induce flexibility in thermoelectric $Ca_3Co_4O_9$ thin films, ACS Appl. Mater. Interfaces 9 (2017) 25308–25316, https://doi.org/10.1021/acsami.7b06301.

[56] O. Bubnova, Z.U. Khan, A. Malti, S. Braun, M. Fahlman, M. Berggren, X. Crispin, Optimization of the thermoelectric figure of merit in the conducting polymer Poly(3,4-ethylenedioxythiophene), Nat. Mater. 10 (2011) 429–433, https://doi.org/10.1038/nmat3012.

[57] A. Besganz, V. Zöllmer, R. Kun, E. Pál, L. Walder, M. Busse, Inkjet printing as a flexible technology for the deposition of thermoelectric Composite structures, Procedia Technol 15 (2014) 99–106, https://doi.org/10.1016/j.protcy.2014.09.043.

[58] H. Fang, B.C. Popere, E.M. Thomas, C.-K. Mai, W.B. Chang, G.C. Bazan, M.L. Chabinyc, R.A. Segalman, Large-scale Integration of flexible materials into Rolled and Corrugated thermoelectric Modules, J. Appl. Polym. Sci. 134 (2017) 44208, https://doi.org/10.1002/app.44456.

[59] A. Chen, D. Madan, P.K. Wright, J.W. Evans, Dispenser-printed planar Thick-film thermoelectric energy generators, J. Micromechanics Microengineering. 21 (2011) 104006, https://doi.org/10.1088/0960-1317/21/10/104006.

[60] S.J. Kim, J.H. We, B.J. Cho, A Wearable thermoelectric generator Fabricated on a glass Fabric, Energy Environ. Sci. 7 (2014) 1959–1965, https://doi.org/10.1039/c4ee00242c.

9

3.4 Combination of laser and thermal sintering of thermoelectric Ca$_3$Co$_4$O$_9$ films

Mario Wolf, Lena Rehder, Frank Steinbach, Marvin Abt, Richard Hinterding, Ludger Overmeyer and Armin Feldhoff

Combination of Laser and Thermal Sintering of Thermoelectric Ca$_3$Co$_4$O$_9$ Films

Mario Wolf[1],*, Lena Rehder[1], Frank Steinbach[1], Marvin Abt[2], Richard Hinterding[1], Ludger Overmeyer[2,3], and Armin Feldhoff[1],*

Supporting Information
available online

Dedicated to Prof. Dr. rer. nat. Jürgen Caro on the occasion of his 70th birthday

The manufacturing technology of thermoelectric materials is laborious and expensive often including complex and time-intensive preparation steps. In this work, a laser sintering process of the oxide-based thermoelectric material Ca$_3$Co$_4$O$_9$ is investigated. Samples based on spray-coated Ca$_3$Co$_4$O$_9$ were prepared and subsequently sintered under various laser parameters and investigated in terms of the microstructure and thermoelectric properties. Here, the combination of laser sintering and subsequent thermal sintering proved to be a promising concept for the preparation of thermoelectric films. Laser sintering can thus make a great contribution in improving the processing of thermoelectric materials, especially when films are applied that cannot be sintered under pressure.

1 Introduction

The demand for electrical energy continues to grow, featuring an increasing desire to reduce the vast amount of wasted energy, especially in form of heat. A simple and environmentally friendly method is the conversion of wasted heat into usable electricity with thermoelectric materials [1–3]. The major advantage of *energy harvesting* via thermoelectric generators (TEGs) are their reliability in direct power conversion without moving parts, thus they can operate long term without need of exchange. However, TEGs have been used only in niche applications, like space exploration or microelectronics [4, 5], because performance is too low for wide commercial application compared to the competition. Additionally, the cost and slow production of thermoelectric materials and TEGs also prevent a wide-ranging utilization of thermoelectric power conversion [6, 7].

The thermoelectric energy conversion is based on the coupling of thermal and electronic currents within the thermoelectric material. Eq. (1) shows the underlying transport equation. When a voltage U and a temperature difference ΔT are applied at a material with the cross-sectional area A and a length l, the electrical current I_{el} and the entropy current I_S are coupled via a material tensor, containing the three main thermoelectric parameters: The isothermal electrical conductivity σ, the Seebeck coefficient α and the open-circuited entropy conductivity Λ_{OC} [8, 9].

$$\begin{pmatrix} I_{el} \\ I_S \end{pmatrix} = \frac{A}{l} \begin{pmatrix} \sigma & \sigma\alpha \\ \sigma\alpha & \sigma\alpha^2 + \Lambda_{OC} \end{pmatrix} \begin{pmatrix} U \\ \Delta T \end{pmatrix} \qquad (1)$$

The performance of a thermoelectric material can then be described by the figure of merit zT, which reflects the conversion efficiency of the thermoelectric material. It is determined as the quotient of the power factor $\sigma\alpha^2$ and the entropy conductivity Λ_{OC} (Eq. (2)) [10–12].

[1]Mario Wolf, Lena Rehder, Frank Steinbach, Richard Hinterding, Prof. Dr. rer. nat. habil. Armin Feldhoff
mario.wolf@pci.uni-hannover.de,
armin.feldhoff@pci.uni-hannover.de
Leibniz University Hannover, Institute of Physical Chemistry and Electrochemistry, Callinstraße 3A, 30167 Hannover, Germany.

[2]Marvin Abt, Prof. Dr.-Ing. Ludger Overmeyer
Institute for Integrated Production Hannover, Hollerithallee 6, 30419 Hannover, Germany.

[3]Prof. Dr.-Ing. Ludger Overmeyer
Institute of Transport and Automation Technology, An der Universität 2, 30823 Garbsen, Germany.

$$zT = \frac{\sigma \alpha^2}{\Lambda_{\mathrm{OC}}} \qquad (2)$$

Recently, the concept of optimizing the power factor $\sigma \alpha^2$ instead of focusing on the figure of merit zT arose in the thermoelectric community [3, 13]. The power factor directly determines the achievable maximum electrical power output of a material [14], which can be equally or more important than the conversion efficiency based on the zT value. As a result, focusing on improvement of the isothermal electrical conductivity σ and the Seebeck coefficient α can be advantageous for specific desired applications.

The most common thermoelectric materials utilized so far, such as Bi_2Te_3 [15], bring major drawbacks in their toxicity and poor thermal stability, hindering an application at elevated temperatures in air. As a result, various kinds of promising materials are investigated and improved including intermetallic phases such as Zintl [16, 17] and half-Heusler phases [18, 19], oxides [20, 21] and polymers [22]. From these, oxide-based materials are the most promising for applications at high temperatures, due to their good thermal stability in air atmosphere. Within this group, calcium cobaltite ($Ca_3Co_4O_9$, CCO) proved to be the best candidate [23, 24]. CCO is characterized by a layered crystal structure, consisting of electrically conducting CoO_2 layers and poorly conducting Ca_2CoO_3 layers that cause phonon scattering [3]. As these two subsystems exhibit incommensurable lattice parameters b_1 and b_2, the structure is described in a 4-dimensional superspace group [25]. For the thermoelectric properties of CCO, the production process plays an important role [26–28]. A high energy sintering step is required to ensure a good electrical conductivity. For this, various methods like hot pressing [29, 30], conventional sintering [31], spark plasma sintering (SPS) [32], cold sintering [33, 34] and pressureless sintering methods [35] have been investigated. However, all of these established techniques are usually quite long procedures or restricted to small amounts per sintering step.

Additionally, optimization of the manufacturing technology of materials (especially films) and TEGs is also in the focus of research. Here, printing processes and additive manufacturing are promising for fast and rapid production. Rösch et al. [36] produced a printed origami TEG, consisting of poly-3,4-ethylenedioxythiophene (PEDOT) nanowires and TiS on a thin, flexible substrate. At a temperature difference of 30 K, an electrical power output of 50 µW cm^{-2} was achieved. Kim et al. [4] fabricated a flexible screen-printed TEG based on Bi_2Te_3 and Sb_2Te_3 by printing respective pastes on the substrate via a screen-printing process and rolling up the thermocouples. An electrical output power of 4 mW cm^{-2} at a temperature difference of 50 K was achieved. Glatz et al. [37] fabricated a micro-TEG for non-planar surface applications based on copper and nickel. The fabrication process consists of four photolithography steps and four electrochemical deposition steps. Here, an electrical power output of 25 nW cm^{-2} at a temperature

difference of 32 K was achieved. The utilization of printing processes for oxide-based materials is also promising. In a previous work [38], the authors presented a fast and simple fabrication process for an oxide-based thermoelectric generators from a combination of spray coating and laser patterning. The prototype was based on CCO and Ag on a ceramic substrate, making it applicable at high temperatures. The produced prototype achieved an electrical power density of up to 1.65 µW cm^{-2} at a temperature difference of 100 K and a power factor of the CCO layer of 0.06 µV cm^{-1}K^{-2}. The electrical conductivity was highly limited by the high porosity and poor sintering of the CCO layer. For this process, the established sintering techniques described above are insufficient for a rapid and fast production of well sintered oxide-based thermoelectric films.

In this work, laser sintering as an alternative as well as an addition to the commonly used thermal sintering processes is therefore investigated. For this, various parameters of the utilized CO_2 laser were analyzed in terms of their influence on the microstructure and resulting electrical conductivity. Selective laser sintering (SLS) has already been investigated and is an established preparation method for other kinds of materials, especially metallic and polymeric ones, but also some ceramic materials [39–41]. For laser sintering, layers of powdered materials are usually used, which are then rapidly heated and consolidated by the laser [39]. This can be done layer after layer, building up 3-dimensional bodies. The biggest advantages of this process are the fast and rapid production and the absence of any binder [39, 41]. For SLS, usually particle sizes around 40–100 µm are considered optimal, although smaller particles can result in a better surface density and overall quality, when the particles are fixed onto the substrate to avoid agglomeration due to static force [39]. For ceramic materials, Mu et al. recently presented protonic ceramic films with a thickness of up to 200 µm and a grain size between 2 and 5 µm [41, 42]. Due to the fast and rapid process of laser processes, a laser sintering of thermoelectric materials can also be highly advantageous and significantly improve the manufacturing technology for thermoelectric materials and TEGs. Especially for the preparation of thin films, a laser sintering process can be promising for rapid production and a reduction of the high manufacturing costs.

2 Experimental Section

2.1 Sample Preparation

CCO powder was purchased from CerPoTech (Tiller, Norway) and was used as a spray coating paste by dispersing 30 wt % in isopropyl alcohol with agitation and ultrasonication. The CCO is characterized by platelets with dimensions about 500 nm in a,b-direction and about 30 nm in c-direction. SEM micrographs of the powder are shown in the Supporting Information (Fig. S1). The paste was applied to

a two-layer flexible low-temperature co-fire ceramic substrate (LTCC, DuPont 951X) with an effective substrate thickness of 440 µm via spray coating (Sogolee Airbrush HP-200). The coated substrate was dried on a heating plate at 373 K after each step. A CO_2-laser (Epilog Fusion 32 M2 Dual, 75 W maximum power, spot diameter 80 µm) was then used for laser sintering of the CCO layer. Tab. 1 shows the different laser parameters. The parameters were chosen similar to a work of Mu et al. [42], who used a power between 2 and 10 W and a defocus up to 20 mm. As the decomposition of CCO starts at approximately 1200 K in air [43], the high power of the laser can obviously result in a rapid decomposition and phase separation. As a result, a significantly higher scan speed of 200 mm s^{-1} (compared to around 1 mm s^{-1} used by Mu et al. [42]) was used here. In Tab. 1, a cycle describes the number of times the laser has passed the sample. Samples A–D have been prepared 1) via laser treatment with the respective parameters and 2) via laser treatment followed by a thermal sintering step (5 h at 873 K and 1033 K for 2 h with a heating and cooling rate of 3 K min^{-1} according to our previous work [38]). For comparison, a thermally sintered reference sample of the CCO layer spray-coated onto the LTCC substrate was prepared analogously. By this, a comparison of pure thermal sintering, pure laser sintering and combination of laser sintering and thermal sintering can be achieved. Additionally, a CCO bulk sample for comparison of the electrical conductivity, Seebeck coefficient and power factor was prepared by pressing of 1 g of CCO and subsequent sintering at 1073 K for 10 h.

Table 1. Details of the laser sintering of the CCO layers. Samples A–D were prepared with the displayed laser parameters. Every sample has been additionally prepared with a subsequent thermal sintering to investigate the combination of laser and thermal sintering at 873 K for 5 h and 1033 K for 2 h. A thermally sintered reference was prepared for comparison.

Sample	Cycles	Scanning speed [mm s^{-1}]	Power [W]	Focus distance [mm]
Reference	–	–	–	–
A	1	200	11.25	0.0
B	1	200	7.5	10.0
C	1	200	7.5	15.0
D	10	200	7.5	17.5

2.2 Characterization

The CCO layers on the LTCC substrates were characterized as-produced by X-ray diffraction (XRD, Bruker D8 Advance with Cu-K$_\alpha$ radiation) to investigate crystallinity and identify possible decomposition processes. Additionally, grazing incidence XRD patterns were measured at a fixed angle of 4° for the X-ray source and are included in the

supporting information (Fig. S2). Microstructural characterization was done via a field-emission scanning electron microscope (FE-SEM, JEOL JSM-6700F). Fractured samples were used for SEM analysis. Additionally, the films were analyzed by a field-emission transmission electron microscope (FE-TEM, JEOL JEM-2100F-UHR) equipped with an energy dispersive X-ray spectrometer (EDXS, Oxford Instruments INCA200 TEM) for elemental analysis. For TEM analyses, cross-section views were prepared by infiltrating the sample with epoxy resin followed by polishing and grinding to achieve sufficient sample thickness. Scanning TEM (STEM) micrographs and selected area diffraction (SAED) in TEM mode were both done at 200 kV. The isothermal electrical conductivity σ was measured using a home-made modified measurement cell with a horizontal tube furnace (Carbolite) and KEITHLEY 2100 Digit Multimeters in a modified van-der-Pauw setup based on the description of Indris [44]. The Seebeck coefficient α was measured as a function of the temperature with a ProboStat A setup from NorECs with an ELITE thermal system and KEITHLEY 2100 Digit Multimeters.

3 Results and Discussions

3.1 X-ray Diffraction

In Fig. 1, the normalized XRD patterns of the CCO layers are shown. Fig. 1a compares the thermally sintered reference with the pure laser sintered samples. After laser sintering, the XRD patterns still show the presence of the CCO layer, but the intensity of all reflections are significantly lower and the background becomes very noisy. Additionally, the 0020 and 0040 reflections that correspond to the a,b-dimensions of the CCO platelets strongly decreases after laser treatment. This can be explained by a strongly decreasing crystallinity due to the high power of the laser. As a result, the reflections of the substrate also become more apparent. After laser treatment, an additional reflection at approximately 41.5° can be seen, especially in samples A and D. This could be explained by the formation of $Ca_3Co_2O_6$, which can be formed by the decomposition of CCO. As this reflection is especially intense in samples A and D, the corresponding reflections of CCO are less pronounced in the normalized XRD pattern. Grazing incidence XRD patterns of the films have been also measured and are included in the Supporting Information (Fig. S2). Interestingly, the grazing incidence XRD pattern do not show the formation of $Ca_3Co_2O_6$ on the surface after laser treatment, but also show the strongly decreasing overall crystallinity and vanishing 0020 and 0030 reflections of the platelets. Additionally, only sample C shows the 1101 reflection. This could be explained by the laser parameters, as sample C was treated by the lowest power and simultaneously highest focus distance, which should result in the least impact on the film. Although the platelets were also mostly destroyed,
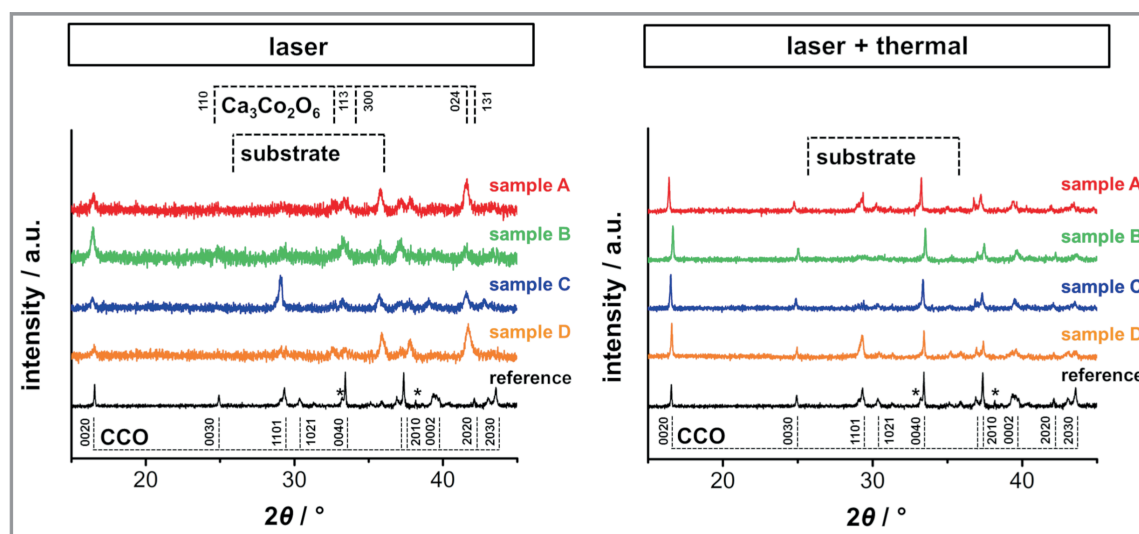
Figure 1. Normalized XRD patterns of thermally sintered reference and samples A–D after a) only laser sintering and b) the combination of laser sintering and thermal sintering. Literature reflections and indices of the $Ca_3Co_4O_9$ reference correspond to the superspace group Cm (0 1 – p 0) [25]. The reflections of the substrate have been extracted from a measurement of the pure LTCC substrate. The asterisk corresponds to minor impurities of $CaCo_2O_4$. After laser sintering, the crystallinity of the samples is reduced, but the reflections of the CCO can still be identified. After subsequent thermal sintering, the crystallinity is restored.

smaller particles could still be present and show the 1101 reflections, which does not correspond to the a,b-dimension of the platelets.

In Fig. 1b, the same comparison is shown for the combination of laser sintering and thermal sintering. Again, all XRD patterns confirm the presence of the CCO layer. The peak intensity for all samples after laser sintering and thermal sintering is relatively higher and sharper than the samples sintered only via laser treatment, which indicates that the thermal sintering restored the crystallinity of the CCO film. Additionally, the intensity of the 1101 reflection differs significantly, as it is strongly pronounced in samples A and D, while it is only implied for samples B and C. While large CCO platelets can be seen in all samples, the samples B and C show less of the smaller particles covering the platelets compared to samples A and D, which could be responsible for the intensity of the 1101 reflection.

3.2 Microstructural Analyses

SEM analysis of the thermally sintered reference sample, the laser sintered sample C and the same sample prepared via a combination of laser sintering and thermal sintering are shown in Fig. 2. The thermally sintered reference sample shows typical CCO platelets with dimension about 500 nm up to 1–2 µm in the a,b-dimension (Fig. 2a, b). The film shows a high porosity, featuring large pores with several µm in size (see Supporting Information Fig. S3). After laser treatment, the typical CCO particles cannot be identified anymore (Fig. 2c, d). Here, a network of melted particles

can be seen in the micrographs. As no defined particles can be seen here, the laser treatment could lead to a melting of the film resulting in an amorphous region on top of the film. This assumption corresponds to the strongly decreasing reflection intensity in the XRD pattern (cf. Fig. 1) and absence of the 0020 and 0030 reflections in the grazing incidence XRD pattern (Fig. S2). The other samples A, B and D show a similar behavior of a melted particle network with slight differences based on the varying laser parameters (see Supporting Information, Fig. S4). After subsequent thermal sintering, the CCO platelets can be seen again (Fig. 2e, f). Compared to the thermally sintered reference, larger platelets up to several µm in a,b-dimension and a slightly denser network could be achieved (Fig. S3–S5). The samples A, B and D again similarly show large CCO platelets after sintering (see Fig. S5).

The layer thickness of all prepared samples has been analyzed via cross-sectional SEM images, which is shown in Fig. 3. The cross-sectional SEM micrographs of sample C after laser sintering (Fig. 3a) and combination of laser and thermal sintering (Fig. 3b) show the porous CCO layer on top of the LTCC substrate. Fig. 3c shows a comparison of the layer thickness of all prepared samples according to cross-sectional SEM micrographs. The layer thickness and the error bars were determined as the median of the layer thickness at various points alongside the samples. Because the spray coating and all sintering steps are done pressureless, the samples show a strong topography and the error bars of the resulting values for the layer thickness are comparably large. After laser sintering, the layer thickness slightly decreases for all samples, as the laser treatment also
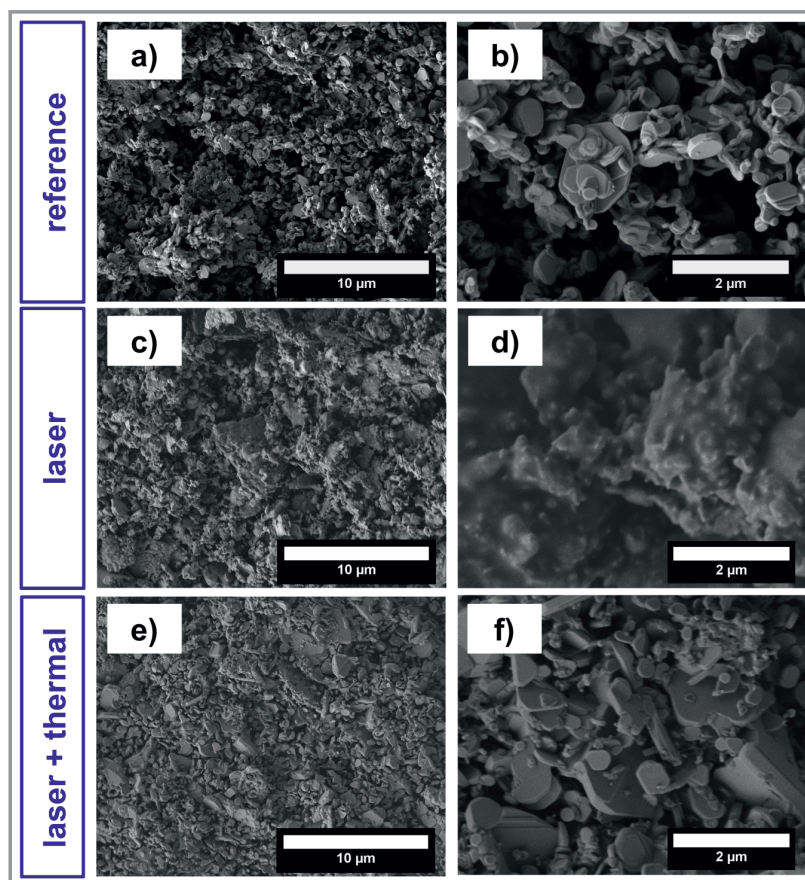
Figure 2. Top-view SEM micrographs of sample C after a,b) thermal sintering (reference), c,d) laser sintering and e,f) combination of laser sintering and thermal sintering. The micrographs prove a melting of the CCO particles after laser sintering and show a denser sintered CCO network with larger platelets after the combination of laser and thermal sintering.

agglomerations of much smaller and spherical particles compared to the typical CCO platelets underneath (Fig. 4a, b). However, the EDXS elemental mapping in still shows a mostly homogeneous distribution of Ca and Co, similar to the typical CCO, but with some red or green spots. Therefore, no complete decomposition of CCO into CaO and Co_3O_4, the typical decomposition products [43], can be found. The few green and red spots that can be identified indicate a starting phase separation of Ca and Co due to the high energy of the laser. Therefore, we assume the formation of some other Ca-Co-O phases such as $Ca_3Co_2O_6$ or $CaCo_2O_4$ [43, 45] alongside separated CaO and presumably CoO or Co_3O_4 after the laser treatment, corresponding to the finding of the XRD analyses.

After subsequent thermal sintering, the first 2–3 µm seem to be less porous compared to the area underneath and are characterized by large platelets with a homogeneous distribution of Ca and Co (Fig. 4c, d), showcasing a better sintering of the particles within the laser treated area. Selected area electron diffraction (SAED) of the top film of spherical particles (Fig. 5b) exhibit a diffuse diffraction near the main beam, indicating amorphous regions analogously to the findings of the XRD patterns. The CCO platelets underneath do not show a diffuse diffraction (Fig. 5c). These results indicate that a laser treatment before thermal sintering results in much smaller, spherical and amorphous regions that show an initial sintering process. The subsequent thermal sintering then results in a denser area with well sintered, larger CCO particles. This however only occurs in the first 2–3 µm of the film, while the rest of the film seems to be mostly unaffected. Compared to other selective laser sintering processes of ceramics [41, 42], this is a quite low impacted area, probably due to the high scanning speed of 200 mm s^{-1} and high focus distance of the laser, which, however, is required to avoid a decomposition of CCO, which presumably already started at the high scanning speed used, as indicated by the small red and green spots.

results in an ablation of particles and agglomerates. As the ablated parts may just drop onto the film again, the layer becomes even rougher, leading to an even bigger error bar. The subsequent thermal sintering leads to an additional slight shrink of all layers. For samples A and B, the shrinkage is quite low and similar to the reference sample, while in samples C and D the layer thickness shows a stronger decrease. This indicates that the subsequent thermal sintering of samples C and D leads to a denser CCO film as a result of the previous laser treatment. The cross-sectional SEM micrographs (Fig. S5) support this by showing denser layers of particle networks compared to the thermally sintered reference.

To further analyze the laser sintering process of the CCO layer, TEM analyses of the laser-sintered sample C as well as the combination of laser and thermal sintering of the same sample were done, shown in Fig. 4. After laser sintering, the top 2–3 µm of the CCO film are characterized by
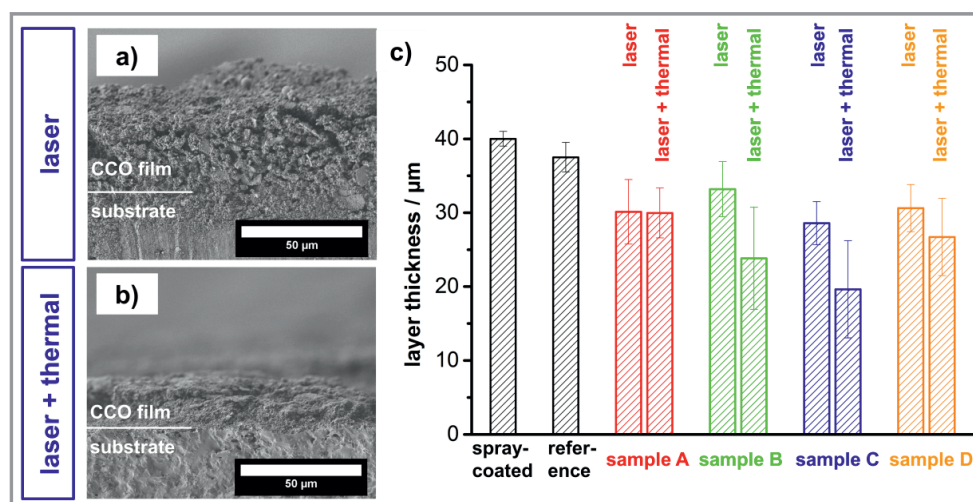
Figure 3. Layer thickness analyses of the prepared samples. Cross-sectional SEM micrographs of sample C after a) laser sintering and b) combination of laser sintering and thermal sintering. c) Comparison of the layer thickness of the spray-coated CCO film, the thermally sintered reference sample and samples A–D after laser sintering and the combination of laser and thermal sintering.
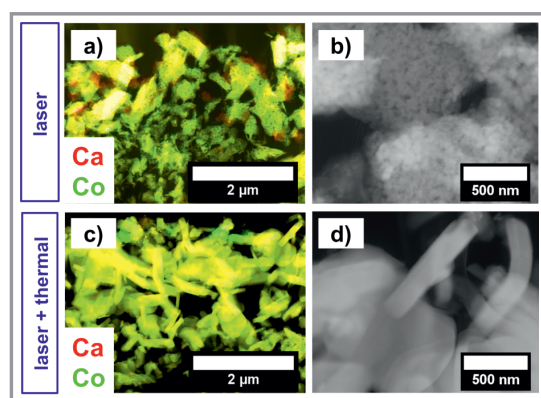

Figure 4. Cross-sectional STEM analysis of a,b) laser-sintered sample and c,d) combination of laser and thermal sintering in sample C. The EDXS elemental distributions in a) and c) show homogeneous distributions of Ca (red) and Co (green). The high-resolution STEM annular dark-field micrograph of the laser-sintered sample in b) exhibits small spherical particles in the first 2–3 μm of the CCO film, with the typical platelet particles underneath. After subsequent thermal sintering, the respective 2–3 μm can be still identified, characterized by large sintered CCO platelets, shown in d).

3.3 Thermoelectric Characterization

Fig. 6 presents the electrical conductivity of measured samples. In Fig. 6a, the comparison of an as-prepared spray-coated CCO layer, the pure laser-sintered sample C, a conventional thermally sintered reference sample and the combination of laser and thermal sintering is shown. By pure laser sintering, the electrical conductivity increases by 2 to 3 orders of magnitude compared to the pristine spray-coated CCO layer, proving the initial sintering due to the laser treatment. The electrical conductivity of a thermally sintered reference sample is around 2 to $4 \, \mathrm{S \, cm^{-1}}$ (cf. [38]). Via combination of laser and thermal sintering, the resulting electrical conductivity is again up to one order of magnitude higher. This is shown in Fig. 6b in detail. Here, sample C exhibits the highest electrical conductivity of approximately $18 \, \mathrm{S \, cm^{-1}}$ at 773 K. Samples A and B also show an increased electrical conductivity, while sample D exhibits roughly the same values as the pure thermally sintered reference sample. The higher electrical conductivity as a consequence of the combination of laser sintering and thermal sintering is in good agreement with the findings of the microstructural characterization. The resulting denser layer with well sintered particles in the top 2 to 3 μm is highly beneficial for the electrical conductivity. However, due to the remaining layer being mostly unchanged and therefore highly porous with smaller, poorly sintered platelets, the film is still characterized by a lower electrical conductivity compared to the bulk CCO sample.

In Fig. 6c, the measured Seebeck coefficient α of the thermally sintered reference, the prepared Samples A–D and a CCO bulk sample for comparison are shown. The samples B and C show a slightly increased Seebeck coefficient while samples A and D are characterized by a slightly decreased Seebeck coefficient. Consequently, samples B and C achieved a higher power factor up to $0.4 \, \mathrm{\mu W \, cm^{-1} K^{-2}}$ compared to the thermally sintered reference. The prepared CCO bulk sample still shows a higher power factor up to $1.5 \, \mathrm{\mu W \, cm^{-1} K^{-2}}$ as a result of the higher electrical conductivity and higher Seebeck coefficient. The values of the

3.4. Laser sintering of calcium cobaltite

Chemie
Ingenieur
Technik

Research Article

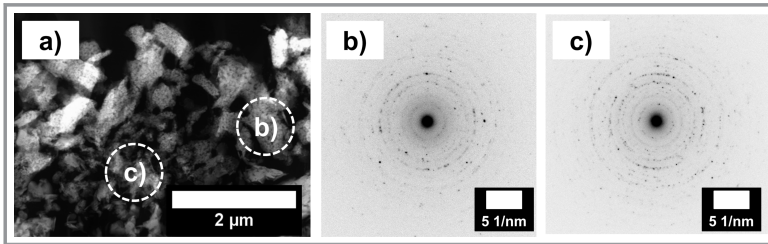**These are not the final page numbers!** ↘↘

7

Figure 5. SAED analyses of the laser-sintered sample C. a) Cross-sectional STEM annular dark-field micrograph with marked spots for SAED. SAED within the laser treated area b) shows diffuse diffraction near the primary beam (radius approximately 3.2 1/nm around the primary beam), supporting the hypothesis of amorphous regions due to the high power of the laser. Underneath the first 2 to 3 µm, the SAED in c) does not show this diffuse diffraction.

prepared CCO bulk sample are in the typical range compared to reported values for undoped CCO at this temperature [26, 28, 46].

3.4 Influence of Laser Parameters

Overall, the laser treatment resulted in melted and sintered networks of mostly amorphous particles (see Fig. S4). A higher laser power (sample A) and multiple cycles (sample D) both resulted in a strongly melted network and high topography of the film. A lower focus distance (sample B) also resulted in a stronger melted network, compared to a higher focus distance (sample C). After subsequent sintering, the crystallinity of all films could be restored, resulting in large CCO platelets (see Fig. S5). However, the preparation with the higher power (sample A) or with higher amount of cycles (sample D) did not result in an increase of the thermoelectric properties, while the samples prepared with 7.5 W and one cycle
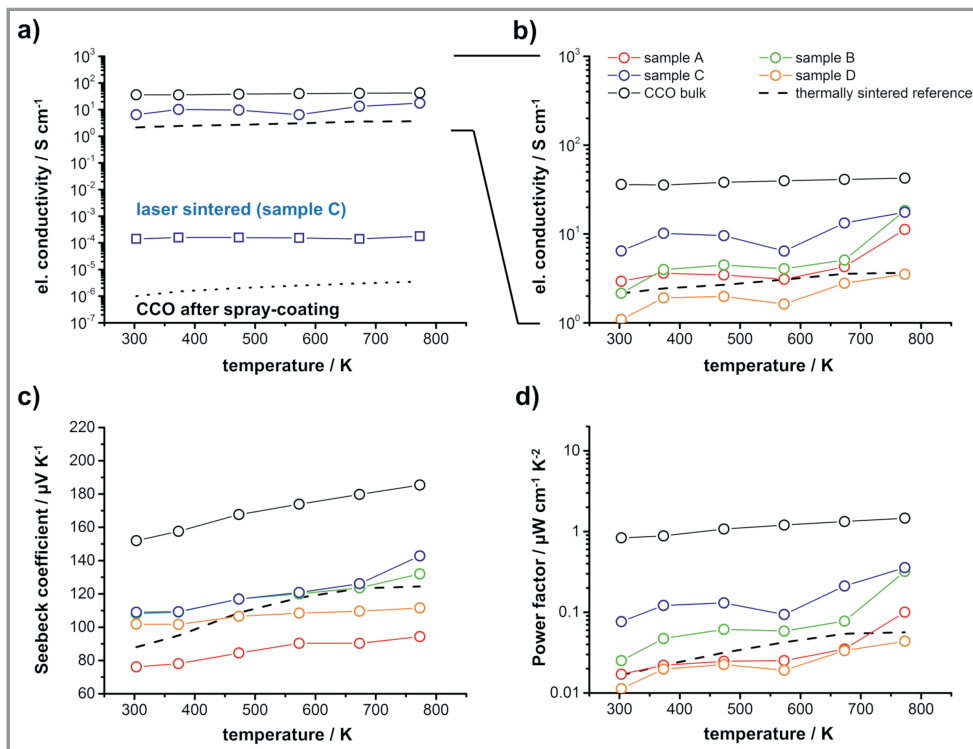

Figure 6. Temperature-dependent electrical conductivity σ, Seebeck coefficient α and calculated power factor of the prepared samples. a) Comparison of spray-coated CCO film, reference sample, laser sintering and combination of laser and thermal sintering. b) Electrical conductivity and c) Seebeck coefficient of samples A–D after combination of laser and thermal sintering and comparison to the thermally sintered reference sample. The resulting electrical conductivity and consequently the power factor of the samples B and C shown in d) is increased compared to the thermally sintered reference.

(samples B, C) both showed a noteworthy increase in the electrical conductivity, resulting in a peak power factor of $0.4\,\mu\mathrm{W\,cm^{-1}K^{-2}}$ at 773 K, which corresponds to an increase of approximately one order of magnitude compared to the thermally sintered reference. Additionally, a higher focus distance of 15 mm (sample C) showed slightly better results compared to 10 mm focus distance (sample B). Based on the TEM microstructural analyses of sample C, via the investigated laser parameters mainly the top 2 to 3 μm of the film were influenced by the laser treatment, as a result of the high scanning speed. However, this resulted in a strongly increased electrical conductivity after subsequent thermal sintering, due to a denser layer with larger and well sintered CCO particles. This shows the potential of a laser sintering process in the manufacturing of ceramic thermoelectric films. Via further investigation and variation of the vast amount of laser parameters, the influence of the parameters can be investigated in more details and the resulting thermoelectric properties may be further enhanced.

4 Conclusions

A promising optimization for manufacturing of oxide-based thermoelectric materials is presented by laser sintering of a CCO layer. The laser sintering of a spray-coated CCO layer mostly impacted the top 2 to 3 μm of the film, resulting in much smaller, spherical, amorphous regions after laser treatment. Via a subsequent thermal sintering, the crystallinity within this 2 to 3 μm could be restored and the film was characterized by a denser layer and larger CCO platelets. As a result, the film showed a strongly increased electrical conductivity of approximately $18\,\mathrm{S\,cm^{-1}}$, resulting in a power factor of $0.4\,\mu\mathrm{W\,cm^{-1}K^{-2}}$ at 773 K. A stand-alone laser sintering without subsequent thermal sintering did not result in increased properties. Nevertheless, these results prove the potential of a supporting laser sintering in the manufacturing of ceramic thermoelectric films and, consequently, the manufacturing of TEGs.

Supporting Information

Supporting Information for this article can be found under DOI: https://doi.org/10.1002/cite.202100128.

References

[1] J. He, T. M. Tritt, *Science* **2017**, *357 (6358)*, eaak9997. DOI: https://doi.org/10.1126/science.aak9997
[2] A. J. Minnich, M. S. Dresselhaus, Z. F. Ren, G. Chen, *Energy Environ. Sci.* **2009**, *2 (5)*, 466–479. DOI: https://doi.org/10.1039/b822664b
[3] M. Wolf, R. Hinterding, A. Feldhoff, *Entropy* **2019**, *21*, 1058. DOI: https://doi.org/10.3390/e21111058
[4] S. J. Kim, J. H. We, B. J. Cho, *Energy Environ. Sci.* **2014**, *7 (6)*, 1959–1965. DOI: https://doi.org/10.1039/c4ee00242c
[5] L. E. Bell, *Science* **2008**, *321 (5895)*, 1457–1461. DOI: https://doi.org/10.1126/science.1158899
[6] R. He, G. Schierning, K. Nielsch, *Adv. Mater. Technol.* **2018**, *3 (4)*, 1700256. DOI: https://doi.org/10.1002/admt.201700256
[7] M. Orrill, S. LeBlanc, *J. Appl. Polym. Sci.* **2017**, *134 (3)*, 44256. DOI: https://doi.org/10.1002/app.44256
[8] A. Feldhoff, *Entropy.* **2020**, *22*, 803. DOI: https://doi.org/10.3390/e22080803
[9] H. U. Fuchs, *Energy Harvest. Syst.* **2014**, *1 (3–4)*, 1–18. DOI: https://doi.org/10.1515/ehs-2014-0011
[10] A. Feldhoff, *Energy Harvest. Syst.* **2015**, *2 (1–2)*, 517. DOI: https://doi.org/10.1515/ehs-2014-0040
[11] H. U. Fuchs, *The Dynamics of Heat – A Unified Approach to Thermodynamics and Heat Transfer*, 2nd ed., Springer-Verlag, New York **2010**.
[12] A. F. Ioffe, *Semiconductor Thermoelements, and Thermoelectric Cooling.*, 1st ed., Info-Search Ltd., London **1957**.
[13] D. Narducci, *Appl. Phys. Lett.* **2011**, *99 (10)*, 102104. DOI: https://doi.org/10.1063/1.3634018
[14] M. Bittner, N. Kanas, R. Hinterding, F. Steinbach, J. Räthel, M. Schrade, K. Wiik, M. Einarsrud, A. Feldhoff, *J. Power Sources.* **2019**, *410–411*, 143–151. DOI: https://doi.org/10.1016/j.jpowsour.2018.10.076
[15] H. Mamur, M. R. A. Bhuiyan, F. Korkmaz, M. Nil, *Renewable Sustainable Energy Rev.* **2018**, *82*, 4159–4169. DOI: https://doi.org/10.1016/j.rser.2017.10.112
[16] F. Gascoin, S. Ottensmann, D. Stark, S. M. Haïle, G. J. Snyder, *Adv. Funct. Mater.* **2005**, *15 (11)*, 1860–1864. DOI: https://doi.org/10.1002/adfm.200500043
[17] J. Shuai, J. Mao, S. Song, Q. Zhang, G. Chen, Z. Ren, *Mater. Today Phys.* **2017**, *1*, 74–95. DOI: https://doi.org/10.1016/j.mtphys.2017.06.003
[18] J. S. Poon, *Metals (Basel)* **2018**, *8 (12)*, 989. DOI: https://doi.org/10.3390/met8120989
[19] H. Zhu et al., *Nat. Commun.* **2018**, *9 (1)*, 1–9. DOI: https://doi.org/10.1038/s41467-018-04958-3
[20] J. W. Fergus, *J. Eur. Ceram. Soc.* **2012**, *32 (3)*, 525–540. DOI: https://doi.org/10.1016/j.jeurceramsoc.2011.10.007
[21] N. Kanas, S. P. Singh, M. Rotan, M. Saleemi, M. Bittner, A. Feldhoff, T. Norby, K. Wiik, T. Grande, M.-A. Einarsrud, *J. Eur. Ceram. Soc.* **2018**, *38 (4)*, 1592–1599. DOI: https://doi.org/10.1016/j.jeurceramsoc.2017.11.011
[22] L. M. Cowen, J. Atoyo, M. J. Carnie, D. Baran, B. C. Schroeder, *ECS J. Solid State Sci. Technol.* **2017**, *6 (3)*, N3080–N3088. DOI: https://doi.org/10.1149/2.0121703jss
[23] V. Rogé, F. Delorme, A. Stolz, A. Talbi, N. Semmar, J. Perrière, F. Giovannelli, E. Millon, *Mater. Chem. Phys.* **2019**, *221*, 361–366. DOI: https://doi.org/10.1016/j.matchemphys.2018.09.069
[24] F. Delorme, F. Giovannelli, *J. Electroanal. Chem. Interfacial Electrochem.* **2018**, *40*, 107–114. DOI: https://doi.org/10.1007/s10832-018-0109-2

[25] Y. M. Iyazaki, M. O. Noda, T. O. Ku, M. K. Ikuchi, Y. I. Shii, *J. Phys. Soc. Jpn.* **2002**, *71 (2)*, 491–497. DOI: https://doi.org/10.1143/JPSJ.71.491

[26] M. Bittner, L. Helmich, F. Nietschke, B. Geppert, O. Oeckler, A. Feldhoff, *J. Eur. Ceram. Soc.* **2017**, *37 (13)*, 3909–3915. DOI: https://doi.org/10.1016/j.jeurceramsoc.2017.04.059

[27] S. Bresch, B. Mieller, C. Selleng, T. Stöcker, R. Moos, T. Rabe, *J. Electroceramics.* **2018**, *40 (3)*, 225–234. DOI: https://doi.org/10.1007/s10832-018-0124-3

[28] S. Bresch, B. Mieller, D. Schoenauer-Kamin, R. Moos, F. Giovanelli, T. Rabe, *J. Appl. Phys.* **2019**, *126 (7)*, 075102. DOI: https://doi.org/10.1063/1.5107476

[29] N. Puri, R. P. Tandon, A. K. Mahapatro, *Ceram. Int.* **2018**, *44 (6)*, 6337–6342. DOI: https://doi.org/10.1016/j.ceramint.2018.01.024

[30] H. Wang, X. Sun, X. Yan, D. Huo, X. Li, J. G. Li, X. Ding, *J. Alloys Compd.* **2014**, *582*, 294–298. DOI: https://doi.org/10.1016/j.jallcom.2013.07.145

[31] K. Koumoto, R. Funahashi, E. Guilmeau, Y. Miyazaki, A. Weidenkaff, Y. Wang, C. Wan, *J. Am. Ceram. Soc.* **2013**, *96 (1)*, 1–23. DOI: https://doi.org/10.1111/jace.12076

[32] J. G. Noudem, M. Prevel, A. Veres, D. Chateigner, J. Galy, *J. Electroceramics.* **2009**, *22 (1–3)*, 91–97. DOI: https://doi.org/10.1007/s10832-008-9421-6

[33] J. Guo, R. Floyd, S. Lowum, J. P. Maria, T. Herisson De Beauvoir, J. H. Seo, C. A. Randall, *Annu. Rev. Mater. Res.* **2019**, *49*, 275–295. DOI: https://doi.org/10.1146/annurev-matsci-070218-010041

[34] A. Moraes dos Santos, D. Thomazini, M. V. Gelfuso, *Ceram. Int.* **2020**, *46 (9)*, 14064–14070. DOI: https://doi.org/10.1016/j.ceramint.2020.02.206

[35] T. Schulz, J. Töpfer, *J. Alloys Compd.* **2016**, *659*, 122–126. DOI: https://doi.org/10.1016/j.jallcom.2015.11.001

[36] A. G. Rösch, A. Gall, S. Aslan, M. Hecht, L. Franke, M. M. Mallick, L. Penth, D. Bahro, D. Friderich, U. Lemmer, *npj Flex. Electron.* **2021**, *5 (1)*, 1–8. DOI: https://doi.org/10.1038/s41528-020-00098-1

[37] W. Glatz, S. Muntwyler, C. Hierold, *Sens. Actuators, A* **2006**, *132 (1)*, 337–345. DOI: https://doi.org/10.1016/j.sna.2006.04.024

[38] M. Wolf, M. Abt, G. Hoffmann, L. Overmeyer, A. Feldhoff, *Open Ceram.* **2020**, *1*, 100002. DOI: https://doi.org/10.1016/j.oceram.2020.100002

[39] R. D. Goodridge, C. J. Tuck, R. J. M. Hague, *Prog. Mater. Sci.* **2012**, *57 (2)*, 229–267. DOI: https://doi.org/10.1016/j.pmatsci.2011.04.001

[40] M. Schmidt, M. Merklein, D. Bourell, D. Dimitrov, T. Hausotte, K. Wegener, L. Overmeyer, F. Vollertsen, G. N. Levy, *CIRP Ann.* **2017**, *66 (2)*, 561–583. DOI: https://doi.org/10.1016/j.cirp.2017.05.011

[41] S. Mu, H. Huang, A. Ishii, Z. Zhao, M. Zou, P. Kuzbary, F. Peng, K. S. Brinkman, H. Xiao, J. Tong, *J. Power Sources Adv.* **2020**, *4*, 100017. DOI: https://doi.org/10.1016/j.powera.2020.100017

[42] S. Mu et al., *Solid State Ionics* **2018**, *320*, 369–377. DOI: https://doi.org/10.1016/j.ssi.2018.03.023

[43] M. Sopicka-Lizer, P. Smaczyński, K. Kozlowska, E. Bobrowska-Grzesik, J. Plewa, H. Altenburg, *J. Eur. Ceram. Soc.* **2005**, *25 (12)*, 1997–2001. DOI: https://doi.org/10.1016/j.jeurceramsoc.2005.03.222

[44] S. Indris, *Perkolation von Grenzflächen in Nanokristallinen Keramischen Kompositen*, 1st ed., Cuvillier Verlag, Göttingen **2001**.

[45] H. Tran, T. Mehta, M. Zeller, R. H. Jarman, *Mater. Res. Bull.* **2013**, *48 (7)*, 2450–2456. DOI: https://doi.org/10.1016/j.materresbull.2013.02.060

[46] R. Hinterding, Z. Zhao, M. Wolf, M. Jakob, O. Oeckler, A. Feldhoff, *Open Ceram.* **2021**, *6*, 100103. DOI: https://doi.org/10.1016/j.oceram.2021.100103
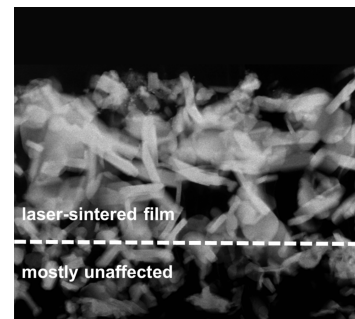
10

Combination of Laser and Thermal Sintering of Thermoelectric Ca$_3$Co$_4$O$_9$ Films

Mario Wolf*, Lena Rehder, Frank Steinbach, Marvin Abt, Richard Hinterding, Ludger Overmeyer, Armin Feldhoff*

Research Article: Laser sintering as promising alternative and addition sintering process in manufacturing of thermoelectric materials is investigated by laser treatment of a ceramic Ca$_3$Co$_4$O$_9$ film. The microstructure and the thermoelectric properties are analyzed to evaluate the effect of the laser and compared to conventional thermal sintering methods. .... ■

laser-sintered film

mostly unaffected

Supporting Information
available online

Supporting Information

Combination of laser and thermal sintering of thermoelectric Ca$_3$Co$_4$O$_9$ films

Mario Wolf[a], Lena Rehder[a], Frank Steinbach[a], Marvin Abt[b], Richard Hinterding[a], Ludger Overmeyer[b, c], Armin Feldhoff[a]

Fig. S1 shows the SEM micrographs of the purchased CCO powder. The CCO particles are in form of platelets with dimensions of about 200-500 nm in a,b-direction (with some larger platelets up to 1 µm) and 20-30 nm in c-direction.
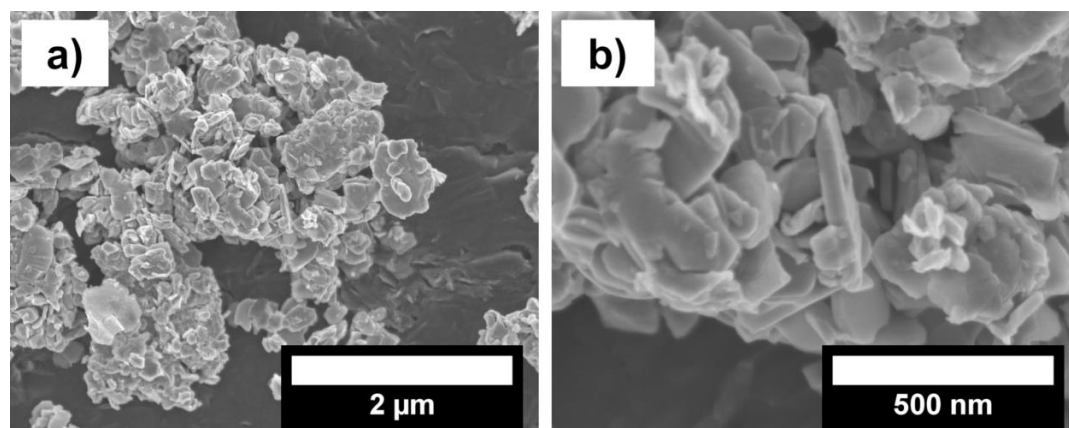

Fig. S1. SEM micrographs of as-received CCO powder. The CCO is characterized by platelets with dimension of about 200-500 nm in a,b-direction and a thickness of about 20-30 nm.

Fig. S2 displays the as-prepared gracing incidence XRD patterns of the laser treated samples A-D and the samples A-D prepared via combination of laser and thermal sintering. Both compared to gracing incidence XRD pattern of a thermally sintered CCO reference. After laser treatment, especially the 0020 and 0040 reflections, that corresponds to the elongation of the platelets in the a,b-direction, vanish. After subsequent thermal sintering, these reflections become more visible to the growth of the platelets. The asterisks in b) correspond to minor CaO impurities, that could be found in sample A and C, most likely due to some decomposition at the laser treated surface.
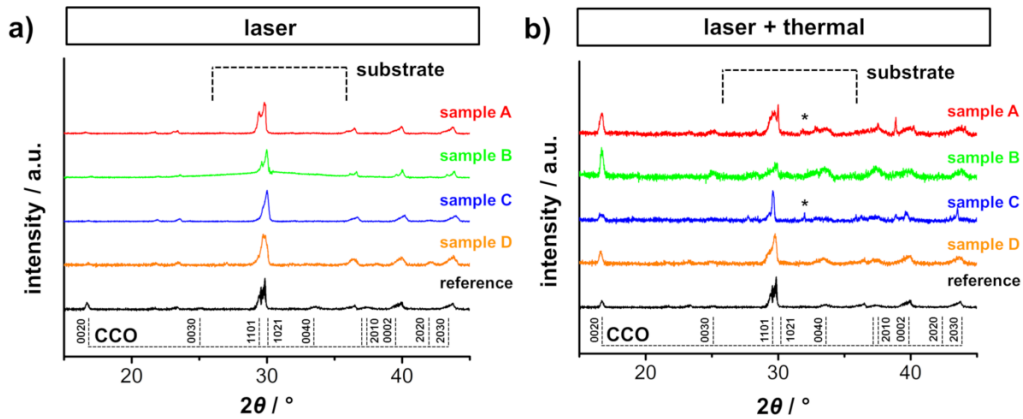
1

Fig. S2. Grazing incidence XRD patterns of a) laser treated samples A-D and b) via combination of laser and thermal sintering prepared samples A-D, both compared to gracing incidence XRD pattern of thermally sintered CCO reference. The XRD patterns were measured via a detector scan with the X-ray source fixed at an angle of 4°. The Asterisks in b) most likely correspond to small CaO impurities found at the surface of sample A and C. The increasing intensity of the 0020 reflection after a combination of laser and thermal sintering correspond to the larger CCO platelets on top of the film.

Fig. S3 shows SEM micrographs of the thermally sintered reference sample. The top view (left) shows the CCO platelets, mostly with dimensions around 500 nm, but some larger particles around 1-2 µm can be seen. Alongside the cross-sectional views, the high porosity of the film can be seen, featuring large pores in the range of several µm.
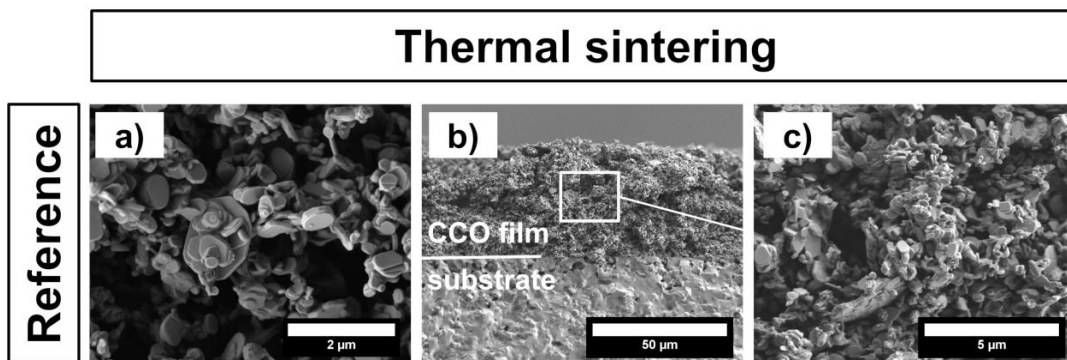

Fig. S3. SEM micrographs of the thermally sintered reference. The left micrograph shows SEM top-view and the two right show SEM cross-sectional view.

2

Fig. S4 shows the SEM microstructure of the laser sintered samples A-D. The top view micrographs of all samples show the beginning sintering process on the top of the film. Especially for samples B-D, the film seems to be less porous on top compared to the reference samples in the main manuscript. Overall, all samples show a similar behavior of melted and sintered networks, but show slight differences according to the varying laser parameters: Sample D shows a strongly melted network and a high topography, most likely due to the high amount of cycles (10) despite a high focus distance of 17.5 mm. Sample B and C were prepared with the same power and same amount of cycles, but different focus distance. As a result, sample B (focus distance 10 mm) show a stronger melted network compared to sample C (focus distance 15 mm). Sample A was prepared at a higher power (11.25 W), also showing a melted network and a rough surface with high topography due to the high power of the laser. The cross-sectional views show the rough topography of the CCO layers after laser treatment. The layer thickness varies between 25-35 μm for all samples.

Fig. S5 shows the SEM microstructure of the laser sintered and thermally sintered samples A-D. The top-view micrographs show the large CCO platelets, similar to the pure thermally sintered reference sample, but more sintered networks can be observed. Additionally, especially sample C shows a denser CCO film with less large pores that can be seen compared to the other samples. The layer thickness is somewhat lower and varies between 20-30 μm. Remarkably, the sample B and C both show a significant shrinkage from a layer thickness of about 33 μm and 30 μm after laser sintering to about 25 μm and 20 μm after subsequent thermal sintering, respectively.
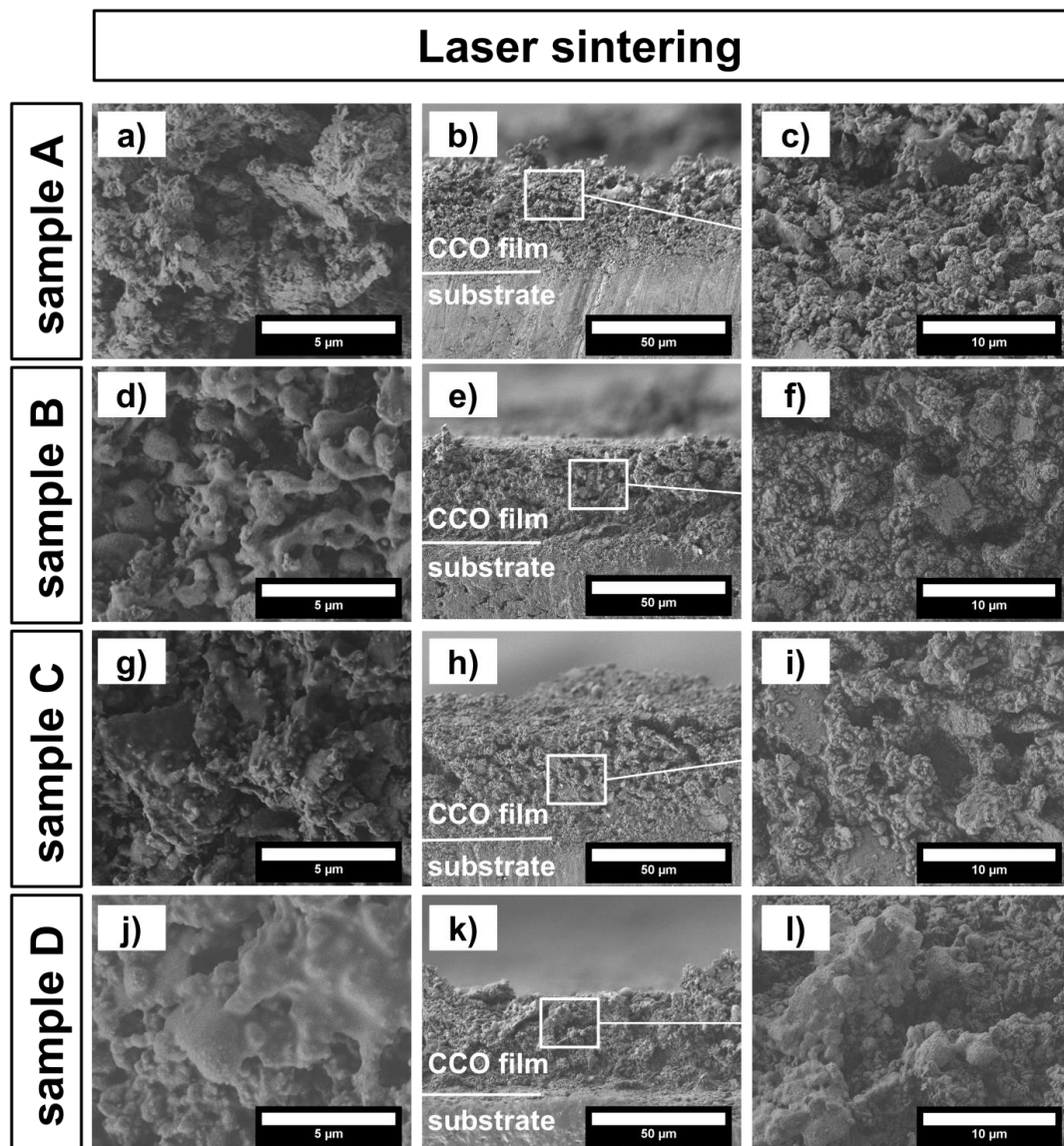
3

Fig. S4. SEM micrographs of laser sintered samples A-D. The left column shows SEM top-view and the two right columns show SEM cross-sectional view of the respective samples.
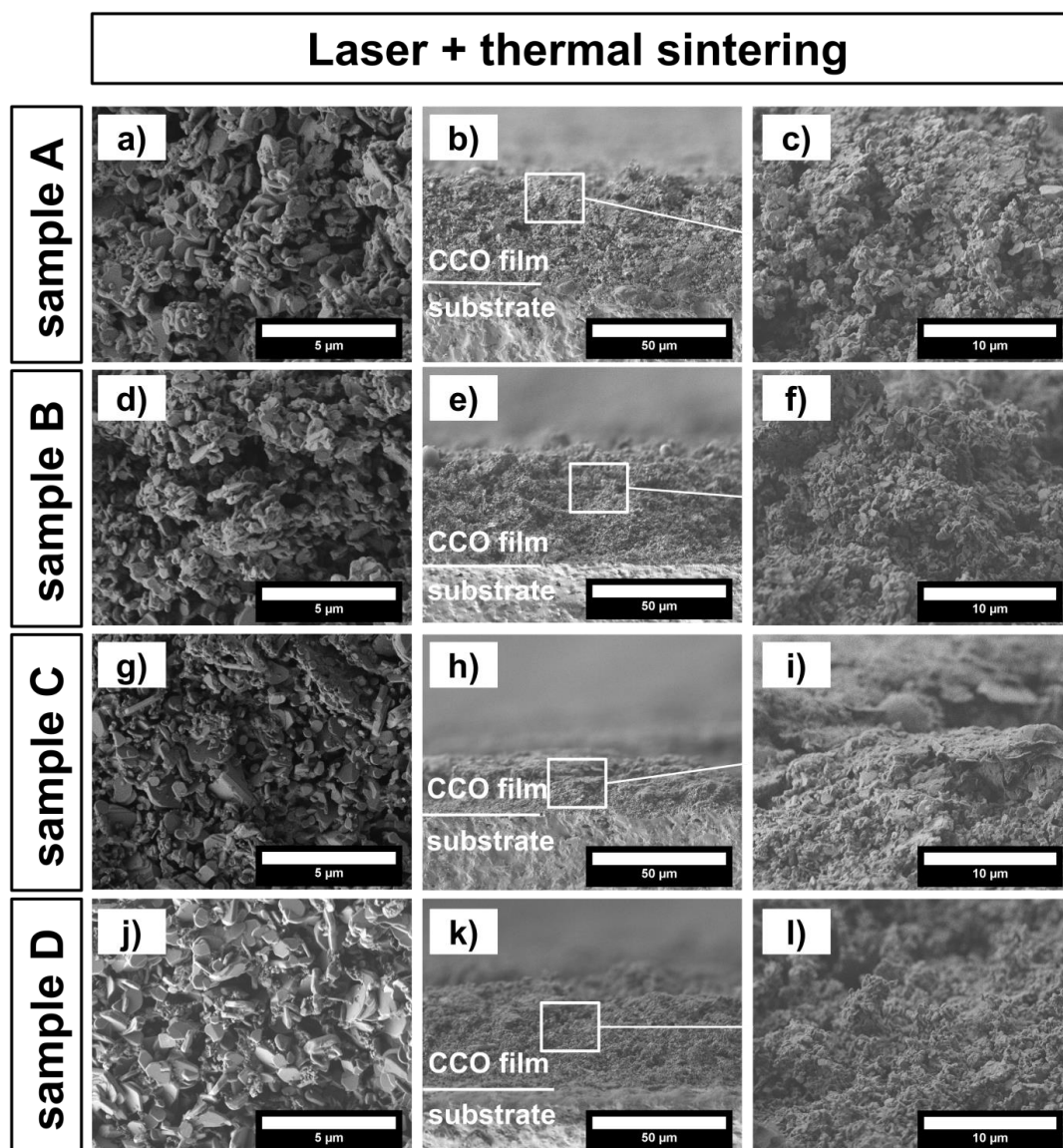
Fig. S5. SEM micrographs of laser sintered and thermally sintered samples A-D. The left columns show SEM top-view and the two right columns show SEM cross-sectional view of the respective samples.

5

4. Conclusions and Outlook

In this work, both the material research and improvement as well as the investigation of new manufacturing processes for thermoelectric generators (TEGs) have been illuminated. Within the material research, a new look on the importance of conversion efficiency and electrical power output has been presented, opening paths to individual optimization depending on the desired application. Furthermore, a new manufacturing concept for the production of TEGs combining additive and subtractive methods in combination with the utilization of promising laser-induced processes have been shown.

The concept of thermoelectric materials optimized for a high power factor instead of a high figure of merit has drawn uprising attention in recent years. In order to achieve an overview on the already established materials from various material classes through the eyes of this concept, a special review utilizing Ioffe plots to evaluate and compare different materials focussing on high-temperature applications was devised. By using the Ioffe plots, the full picture of the thermoelectric properties of a material can be revealed, not only comparing the figure of merit but also the respective power factor and electrical conductivity. This may result in some promising candidates that have been overlooked until now, especially to achieve a high electrical power output. In a theoretical work, based on finite elemente method (FEM) simulations, the mentioned concept to optimize either for a high figure of merit or a high power factor could also be transferred to the design of TEGs. For their optimization, the general concept is to optimize the geometries of the n- and p-type materials to maximize the figure of merit, which, however, not necessarily also leads to a maximized electrical power output of the TEG. This means that for both, material development as well as TEG design, the concept of optimization toward high electrical power output instead of a high conversion efficiency is an important task, opening up both a path to new materials as well as designs.

As an example for optimization of the conversion efficiency, a hybrid material consisting of the most promising oxide-based material $Ca_3Co_4O_9$ (CCO) combined with a polymeric (Matrimid) and a metallic phase (Ag) was prepared and characterized. The resulting hybrid material featured heteromaterial interfaces leading to an exceptionally low thermal conductivity as a result of the strongly reduced mean-free path of the phonons. On the downside, the thermal stability of the hybrid material was strongly reduced due to the introduction of a polymeric phase. However, as a result of this work, additional investigations on hybrid materials with CCO and anisotropic oxide materials were performed, achieving increased zT values compared to pure CCO. Designing hybrid materials for thermoelectric applications therefore is a promising concept that can be further investigated in the future by adding various different phases to tune individual properties or to combine with other techniques such

as doping or nanostructuring.

As an example for an optimization of the power factor, the mostly overlooked Cu-Ni alloy was investigated. Naturally, the comparatively high thermal conductivity results in a fairly low zT for this material, but due to the high electrical conductivity and the moderate Seebeck coefficient, the resulting power factor even surpasses the values of the established half-Heusler compounds. The investigated alloying with Sn and W as heavier elements proved the potential of this alloys, as small amounts of both elements result in an increase in both the power factor as well as the figure of merit. Due to the availability and the vast amount of suitable processing technology for metals, such simple alloys are especially interesting for fast and scalable manufacturing technologies such as printing or additive manufacturing.

A combination of spray-coating and laser structuring was presented as a new concept for the manufacturing of TEGs. Here, a porous layer of CCO was applied on a low-temperature co-fire ceramic (LTCC) substrate and subsequently partly ablated using a CO_2-laser to achieve a TEG structure. Within the spray-coating process, the thickness of the resulting layer can be controlled and varied between 10 and 40 μm. On the back side of the substrate, an Ag layer was applied in the same manner and the legs were contacted over the edges, resulting in a prototype TEG. After sintering of the layers, a maximum power output of 1.6 μW cm^{-2} at a hot-side temperature of 673 K and a temperature difference of 100 K could be achieved. Compared to previously reported printed TEGs, this first CCO-based prototype therefore reached a higher electrical power output compared to the polymer or metal-based prototypes but a lower electrical power output than Bi_2Te_3-based prototypes. The developed process was performed with a simple CCO dispersion without the need of any additives that can decrease the resulting performance. However, the resulting CCO layer still only reached about 5 % of the electrical conductivity of the undoped bulk material due to the high porosity of the layer. Here, the biggest optimization potential is located in gaining a higher densification of the layer and therefore a higher electrical conductivity. Compared to undoped bulk CCO, a possible enhancement of one order of magnitude for the resulting electrical conductivity and therefore the resulting electrical power output may be achieved. Due to the adaptability of the developed process, it can also be transferred to various other kinds of materials and substrates.

The most limiting remaining process step was the need of a thermal sintering step to ensure the electrical conductivity of the layers. As a possible alternative or addition, a laser sintering process of the CCO layer was investigated. Here, first sintering steps could be easily achieved by a laser treatment of the pristine spray-coated CCO layer. The microstructural characterization showed a beginning sintering processes of the CCO particles already after short treatment with a CO_2-laser at low power around 10 W. However, the X-ray diffraction pattern also proved a strongly decreasing crystallinity of the particles and, for some laser parameters, even a decomposition of the CCO. After subsequent thermal sintering, the crystallinity can be restored. Via TEM analyses, the indicated decreasing crystallinity after laser sintering could be proven by showing amorphous regions. Overall, the resulting electrical conductivity could be increased via a combination of laser sintering and thermal sintering compared to only thermal sintering of the film. This shows the potential of laser treatment as an addition to traditional thermal sintering. The interaction between the laser and the sample, however, is a complex process that has to be further investigated in an stand-alone project in terms of optimizing the resulting thermoelectric properties.

For further investigation of the material development for manufacturing of TEGs, all found aspects play an important role. Obviously, the described optimization towards either a high power conversion or a high electrical power output also impacts the material choice for manufacturing of TEGs. The developed manufacturing route for a CCO/Ag based TEG can be further improved by gaining a higher densification but also by transferring it to other material systems. The also investigated Cu-Ni alloy is a promising candidate with the aim of a high electrical power output, as the manufacturing of metals is less limited and already established for electronic structures. Generally, the utilization of fast and scalable printing as well as laser-induced processes is a promising path to decrease the costs of TEGs and therefore increase their viability for wide application. The concept of laser sintering can be a powerful tool as an alternative to thermal sintering, which is a hardly limiting step in fast production of TEGs.

Publications and Conferences

Publications included in this work

1. High power factor vs. high zT - A review of thermoelectric materials for high temperature application

   <u>Mario Wolf</u>, Richard Hinterding and Armin Feldhoff

   Entropy 21 (11) **2019**, 1058

2. Geometry optimization of thermoelectric modules: Deviation of optimum power output and conversion efficiency

   <u>Mario Wolf</u>, Alexey Rybakov, Richard Hinterding and Armin Feldhoff

   Entropy 22 (11) **2020**, 1233

3. Low thermal conductivity in thermoelectric oxide-based multiphase composites

   <u>Mario Wolf</u>, Kaan Menekse, Alexander Mundstock, Richard Hinterding, Frederik Nietschke, Oliver Oeckler and Armin Feldhoff

   Journal of Electronic Materials 48 (11) **2019**, 7551-7561

4. Cu-Ni-based alloys from nanopowders as potent thermoelectric materials for high power output applications

   <u>Mario Wolf</u>, Jan Flormann, Timon Steinoff, Gregory Gerstein, Florian Nürnberger, Hans Jürgen Maier and Armin Feldhoff

   submitted to *Alloys*, November **2021**

5. Combined spray-coating and laser structuring of thermoelectric ceramics

   Marvin Abt, <u>Mario Wolf</u>, Armin Feldhoff, Ludger Overmeyer

   Journal of Materials Processing Technology 275 **2020**, 116319

6. Ceramic-based thermoelectric generator processed via spray-coating and laser structuring

   <u>Mario Wolf</u>, Marvin Abt, Gerd Hoffmann, Ludger Overmeyer and Armin Feldhoff

   Open Ceramics 1 **2020**, 100002

7. Combination of laser and thermal sintering of thermoelectric $Ca_3Co_4O_9$ films

   <u>Mario Wolf</u>, Lena Rehder, Frank Steinbach, Marvin Abt, Richard Hinterding, Ludger Overmeyer and Armin Feldhoff

   Chemie Ingenieur Technik 94 **2021**, 1-10

Publications not included in this work:

1. Role of doping agent degree of sulfonation and casting solvent on the electrical conductivity and morphology of PEDOT:SPAES thin films

   Daniela V. Tomasino, <u>Mario Wolf</u>, Hermes Farina, Gianluca Chiarello, Armin Feldhoff, Marco Aldo Ortenzi and Valentina Sabatini

   Polymers 13 **2021**, 658

2. Ceramic composites based on $Ca_3Co_4O_{9+\delta}$ and $La_2NiO_{4+\delta}$ with enhanced thermoelectric properties

   Richard Hinterding, Zhijun Zhao, <u>Mario Wolf</u>, Matthias Jakob, Oliver Oeckler and Armin Feldhoff

   Open Ceramics 6 **2021**, 100103

3. Improved thermoelectric properties in ceramic composites based on $Ca_3Co_4O_9$ and $Na_2Ca_2Nb_4O_{13}$

   Richard Hinterding, <u>Mario Wolf</u>, Matthias Jakob, Oliver Oeckler and Armin Feldhoff

   Open Ceramic, 8 **2021**, 100198

4. Evaluation of Cu-Ni-based alloys for thermoelectric energy conversion

   Timon Steinhoff, <u>Mario Wolf</u>, Florian Nürnberger, Gregory Gerstein and Armin Feldhoff

   Materials Science Forum, 1016 MSF **2021**, 107-112

Contributions to conferences:

1. Oxide/polymer-composites for thermoelectric application

   <u>Mario Wolf</u>, Kaan Menekse, Alexander Mundstock, Frederik Nietschke, Oliver Oeckler and Armin Feldhoff

   Bunsentagung 2018 - Kinetics in the Real World, Deutsche Bunsen-Gesellschaft (DBG), Hannover (Germany), 10th-12th May (**2018**) (Poster)

2. Printed oxide-based thermogenerators

   <u>Mario Wolf</u>, Marvin Abt, Ludger Overmeyer and Armin Feldhoff

   ZFM Festkörpernachmittag, Hannover (Germany), 6th July (**2018**) (Talk)

3. Combined spray-coating and laser structuring as unique fabrication method for thermoelectric generators

   <u>Mario Wolf</u>, Marvin Abt, Ludger Overmeyer and Armin Feldhoff

   17th European Conference on Thermoelectrics (ECT), European Thermoelectric Society (ETS), Limassol (Cyprus), 23th-25th September (**2019**) (Talk)

4. Scalable fabrication of thermoelectric generators by combining spray-coating and laser structuring

   Mario Wolf, Marvin Abt, Ludger Overmeyer and Armin Feldhoff

   1st Virtual Conference on Thermoelectrics (VCT), International Thermoelectric Society (ITS), 21th-23th July (**2020**) (Talk)

5. Thermoelectric composite ceramics based on anisotropic oxides

   Richard Hinterding, Zhijun Zhao, Mario Wolf, Matthias Jakob, Oliver Oeckler, Armin Feldhoff

   1st Virtual Conference on Thermoelectrics (VCT), International Thermoelectric Society (ITS), 21th-23th July (**2020**) (Poster)

6. Thermoelectric composite ceramics based on anisotropic oxides

   Richard Hinterding, Zhijun Zhao, Mario Wolf, Matthias Jakob, Oliver Oeckler, Armin Feldhoff

   Electroceramics, European Ceramic Society (ECerS), 25th-27th August (**2020**) (Talk)

7. Scalable fabrication of thermoelectric generators by combining spray-Coating and laser structuring

   Mario Wolf, Marvin Abt, Armin Feldhoff and Ludger Overmeyer

   Materials Science and Engineering 2020 (MSE), German Materials Society (DGM), 22th-25th September (**2020**) (Talk)

8. Combining spray-coating and laser structuring: A new approach for processing of thermoelectric generators

   Mario Wolf, Marvin Abt, Armin Feldhoff and Ludger Overmeyer

   45th International Conference and Expo on Advanced Ceramics and Composites, American Ceramic Society (ACerS), 8th-12th February (**2021**) (Talk)

9. Combination of $Ca_3Co_4O_9$ with anisotropic oxides in thermoelectric composite ceramics

   Richard Hinterding, Zhijun Zhao, Mario Wolf, Matthias Jakob, Oliver Oeckler and Armin Feldhoff

   45th International Conference and Expo on Advanced Ceramics and Composites, American Ceramic Society (ACerS), 8th-12th February (**2021**) (Talk)

10. Thermoelectric properties of composite ceramics based on $Ca_3Co_4O_9$ and large plate-like oxides

    Richard Hinterding, Zhijun Zhao, Mario Wolf, Matthias Jakob, Oliver Oeckler and Armin Feldhoff

    96th DKG Annual Meeting, Deutsche Keramische Gesellschaft e.V. (DKG), 19th-21th April (**2021**) (Talk)

11. Ceramic-based thermoelectric generator via spray-coating and laser structuring

    <u>Mario Wolf</u>, Marvin Abt, Armin Feldhoff and Ludger Overmeyer

    96th DKG Annual Meeting, Deutsche Keramische Gesellschaft e.V. (DKG), 19th-21th April (**2021**) (Poster)

12. Evaluation of Cu-Ni-based alloys for thermoelectric energy conversion

    Armin Feldhoff, Timon Steinhoff, <u>Mario Wolf</u>, Florian Nürnberger and Gregory Gerstein

    THERMEC 2021 - International Conference on Processing and Manufacturing of Advanced Materials, THERMEC International Committee, 10th-14th May (**2021**) (Talk)

13. High power factor versus high zT in thermoelectric materials and generators

    Armin Feldhoff, <u>Mario Wolf</u> and Richard Hinterding

    Materials Challenges in Alternative and Renewable Energy 2021 combined with the 4th Annual Energy Harvesting Society Meeting, American Ceramic Society (ACerS), 18th-23th July (**2021**) (Talk)

Curriculum Vitae

Personal data

Date of birth:	03.04.1993
Place of birth:	Hoya, Germany
Nationality:	german
Martial status:	unmarried, no children

Higher education

since 07/2017   **Leibniz University Hannover**

Submission of the doctoral thesis:
"Physico-Chemical Material Development for the Manufacturing of Thermoelectric Generators"

04/2015 – 06/2017   **Master of Science Material- und Nanochemie
Leibniz University Hannover**

Master Thesis: "Poröse Metallstrukturen zur katalytischen Anwendung – ein bionischer Ansatz"

10/2011 – 03/2015   **Bachelor of Science Chemie
Leibniz University Hannover**

Bachelor Thesis: "Synthese und Analyse von elektrogesponnen Fäden"

Education

09/2003 – 06/2011   **Johann-Beckmann-Gymnasium Hoya**
Degree: Abitur

09/2002 – 08/2003   **Orientierungsstufe Hoya**

09/1999 – 08/2002   **Grundschule Bücken**